Dynamics in the Upper Solar Convection Zone

by

Marc Lyle DeRosa

B.A., Johns Hopkins University, 1994

M.S., University of Colorado, 1997

A thesis submitted to the

Faculty of the Graduate School of the

University of Colorado in partial fulfillment

of the requirements for the degree of

Doctor of Philosophy

Department of Astrophysical and Planetary Sciences

2001

This thesis entitled:
Dynamics in the Upper Solar Convection Zone
written by Marc Lyle DeRosa
has been approved for the Department of Astrophysical and Planetary Sciences

Juri Toomre

Nicholas H. Brummell

Peter A. Gilman

Jeffrey B. Weiss

Ellen G. Zweibel

Date

The final copy of this thesis has been examined by the signatories, and we find that both the content and the form meet acceptable presentation standards of scholarly work in the above mentioned discipline.

DeRosa, Marc Lyle (Ph.D., Astrophysical and Planetary Sciences)

Dynamics in the Upper Solar Convection Zone

Thesis directed by Professor Juri Toomre

The differential rotation of the sun, as deduced from helioseismology, exhibits a prominent layer of radial shear near the top of the convection zone. This shearing boundary layer just below the solar surface is composed of convection possessing a broad range of length and time scales, including granulation, mesogranulation, and supergranulation. Such turbulent convection is likely to influence the dynamics of the deep convection zone in ways that are not yet fully understood. We seek to assess the effects of this near-surface shear layer through two complementary studies, one observational and the other theoretical in nature. Both deal with turbulent convection occurring on supergranular scales within the upper solar convection zone.

We characterize the horizontal outflow patterns associated with solar supergranulation by individually identifying several thousand supergranules from a 45°-square field of quiet sun. This region is tracked for a duration of six days as it rotates across the disk of the sun, using full-disk ($2''$ pixels) SOI-MDI images from the SOHO spacecraft of line-of-sight Doppler velocity imaging the solar photosphere at a cadence of one minute. This time series represents the first study of solar supergranulation at such high combined temporal and spatial resolution over an extended period of time. The outflow cells in this region are observed to have a distribution of sizes, ranging from 14–20 Mm across, while continuously evolving on time scales of several days. Such evolution manifests itself in the form of cell merging, fragmentation, and advection, as the supergranules and their associated network of convergence lanes respond to the turbulent convection occurring a short distance below the photosphere.

We have also conducted three-dimensional numerical simulations of turbulent compressible convection within thin spherical shells located near the top of the convection zone. Vigorous fluid motions possessing several length and time scales are driven by imposing the solar heat flux and differential rotation at the bottom of the domain. The convection patterns form a connected network of downflow lanes in the surface layers that break up into more plume-like structures with depth. The regions delineated by this downflow network enclose broad upflows that fragment into smaller structures near the surface. We find that a negative radial gradient of angular velocity Ω is maintained against diffusion in these simulations by the tendency for the convective motions to partially conserve their angular momentum in radial motion. This behavior suggests that similar dynamics may be responsible for the decrease of Ω with radius as deduced from helioseismology within the upper shear layer of the solar convection zone.

Dedication

To my parents, Pete and Cindy, and to my sister Lisa.

Acknowledgements

The research presented in this thesis simply would not have been completed without the guidance, encouragement, and wisdom of my advisor and mentor, Juri Toomre. Starting with the first summer following my arrival in Boulder, and extending throughout the intervening years up to the present time, Juri has stimulated my interest in the rich fields of solar physics and astrophysical fluid dynamics while providing perspective, insight, and sage advice at several critical junctures along the way. His cheerful nature, sparkling wit, and unending generosity have made this experience a truly enjoyable one.

I would like to acknowledge several members of the solar group here at CU, including Deborah Haber, Sacha Brun, Nic Brummell, Brad Hindman, and Jason Lisle, who have shaped my understanding of the solar interior through several helpful discussions. I am indebted in particular to Mark Miesch, Tom Clune, and Julian Elliott for their long, arduous hours spent programming and debugging the ASH computer code. Special mention also goes to Kelly Cline, who endured varied mood swings and other eccentric behavior as my officemate for the last three years, as well as to Anne Hammond and Gwen Dickinson for their attention to detail and the behind-the-scenes work necessary to keep things running smoothly.

It is also necessary to mention several folks residing at outside institutions for their part in this research. Analysis of the numerical simulations presented in Chapter 5 progressed largely due to several long sessions with Peter Gilman of HAO, whose broad experience with fluid flows of all flavors within spherical shells was (and continues to be) a huge asset. Additionally, Dick Shine of Lockheed-Martin graciously provided his ideas and experience (and perhaps most importantly, his computer code) associated with correlation tracking methods. Tom Duvall, Rick Bogart, and John Beck of the SOI-MDI Team at Stanford assisted in part in the processing and subsequent analysis of the large MDI dataset of the near-surface solar velocity field. Without their contributions, the research of Chapter 3 would never have advanced to its current state. Support for this research was provided by NSF grants ATM–9731676, ECS–9217394, and GRT–9355046, and NASA grants NAG 5–8133 and NAG 5–7996.

Memories of my time in Boulder will always be associated with the many friends with whom I have spent countless hours playing softball and volleyball, watching movies, playing poker, rooting for the Broncos, Rockies, and Avs, hiking, and eating steak. A few deserve special mention. Marc Swisdak, whom I met within a week of arriving in Boulder, is an associate and close friend anyone would be lucky to have, and I will always be grateful for his kindness, gracefulness, and his amazing ability to remember almost anything. I would also like to recognize my housemates Eli Michael and Jason Tumlinson for making it through the last several months without getting too annoyed living with someone who was probably a little too stressed out. Many thanks go out to Amanda Sickafoose, who has shown me the merits of having a take-charge attitude in life, and to Matt Beasley, for always being so effervescently happy and for showing me how to effectively dispose of disposable income.

Finally, I am truly grateful for having such a wonderful family. My sister, Lisa, must be commended for having grown up with an older brother who was probably somewhat overbearing at times, and for managing nevertheless to turn into a top-notch person who will undoubted be extremely successful at any endeavor she tries. Lastly, I am truly indebted to my parents, Pete and Cindy, who have provided a positive environment filled with direction, encouragement, motivation, and love in which a rather shy kid could develop the confidence and determination to realize his dreams.

Contents

Tables

Table

Figures

Figure

Chapter 1

INTRODUCTION: THE DYNAMIC SOLAR CONVECTION ZONE

Our sun is the nearest star to earth and the most massive object in the solar system. Most of this mass is concentrated near its center (the *core*), where the matter is hot and dense enough to permit the fusion of its abundant supply of hydrogen into helium. The energy produced via these thermonuclear reactions slowly diffuses through the *radiative interior* until it enters the *convection zone*, a layer roughly 200 Mm (where 1 Mm equals 1000 km) thick occupying about the outer 30% of the sun by radius. In this region, the entropy and temperature gradients are superadiabatic and therefore unstable to convective overturning motions; thus, it is energetically favorable for fluid to rise buoyantly by extracting energy from the ambient thermal field. Once the heat reaches the surface of the sun (the *photosphere*), it escapes through the tenuous *solar chromosphere* and *corona* and into outer space.

The focus of this thesis is the dynamics within the upper layers of the solar convection zone. The convection zone as a whole contains fluid motions that vary over widely ranging yet distinct length and time scales, all of which interact in complex ways. In this introductory chapter, we first examine in §1.1 what has been learned about the convection zone from observations of the photosphere, including from results of helioseismic inversions. In §1.2 we describe the current state of numerical modeling efforts which elucidate some of the dynamical processes present when compressible fluids are subject to rotation and stratification. Finally, we develop and motivate the research presented in this thesis in §1.3.

1.1 OBSERVATIONS OF THE SOLAR SURFACE

1.1.1 Differential Rotation of the Surface and Interior

Observations of the solar photosphere show that the sun possesses a *differential rotation* in which the equatorial regions rotate faster than the poles. Measurements of Doppler shifts of photospheric absorption lines (Howard & Harvey 1970; Snodgrass & Ulrich 1990) indicate that the surface plasma at the equator has a rotation period of 25 days, while in the polar regions it is about 33 days. Alternatively, measuring the rotation rate of sunspots and other surface features as they rotate across the disk of the sun (Ward 1966; Howard et al. 1984; Snodgrass & Ulrich 1990; Zappalà & Zuccarello 1991) also show a similar differential rotation profile, except that these rotation rates are found to be faster than the plasma rate by a few percent at each latitude. This systematic difference in rotation rates most likely indicates that the sub-surface layers rotate faster than the surface, as the magnetic features reflect an average of angular velocity as weighted over their radial extent.

The existence of approximately 10^7 resonant acoustic modes of oscillation makes it possible to probe the solar interior in some detail using *helioseismology* (e.g. Ulrich 1970; Gough & Toomre 1991). Helioseismology involves the measurement and analysis of the oscillation frequencies of these normal modes, as measured at the surface, in order to infer properties of the medium through which the waves have traveled. Waves of different frequencies provide information over a range of depths and latitudes, from which it is possible to construct detailed maps of structure and large-scale flows within the interior of the sun. For example, inversions of *global modes* are used to infer the dependence of density, pressure, temperature, and sound speed with both radius and latitude, whereas their rotational splittings provide estimates of the angular velocity field throughout much of the sun, as shown in Figure 1.1 for example.

Over the last seven years, two major research efforts have provided nearly uninterrupted observations of the solar photosphere from which the oscillation frequencies can be measured. The Global Oscillation Network Group (GONG) operates a series of six identical Doppler imaging instruments distributed approximately equally in longitude around the earth. The data from the six observing sites are subsequently combined to form one continuous dataset on which helioseismic inversions can be performed. In a complementary fashion, the Michelson Doppler Imager (MDI), one of several instruments on board the Solar and Heliospheric Observatory (SOHO) spacecraft, also provides continuous observations of the line-of-sight surface velocity field. From its vantage point in space, MDI does not suffer from atmospheric seeing effects and weather-related interruptions which can affect the data from the GONG project. On the other hand, the ground-based GONG instruments are more accessible and can be upgraded as more advanced instruments become available. Together, the virtually uninterrupted coverage and high temporal resolution of the data provided by both projects enables the precise measurements of oscillation frequencies necessary for detailed helioseismic analyses.

Global helioseismic inferences of angular velocity deduced from both GONG and MDI data indicate that the surface differential rotation pattern of fast equatorial rotation relative to the poles largely holds throughout the bulk of the convection zone, such that radial gradients of angular velocity are small (Thompson et al. 1996; Schou et al. 1998). Figure 1.2 shows that there exists a layer of radial shear, known as the *tachocline* (Spiegel & Zahn 1992), located at the interface between the bottom of the convection zone and the stably stratified radiative interior underneath. Much recent attention has focused on the tachocline region, as it is thought to be the seat of the global solar magnetic dynamo. In the near-surface layers, helioseismology also reveals the existence of another shear layer occupying the outer 35 Mm or 5% of the sun. This upper shear layer contains negative radial gradients in angular velocity, lending credence

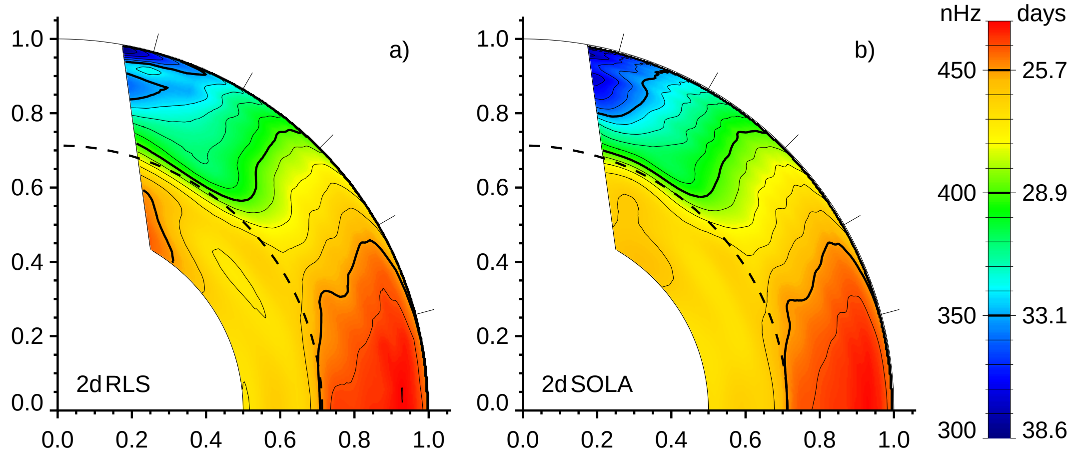

Figure 1.1: Average rotation rates $\Omega/2\pi$ as a function of radius and latitude inferred from two different helioseismic analyses applied to MDI velocity images. (adapted from Fig. 5 of Schou et al. 1998).

to the notion that subsurface fluid layers rotate faster near the surface, much as was inferred by comparing the tracer and spectroscopic rotation rates.

1.1.2 Dynamics in the Near-Surface Layers

High-resolution observations of the photosphere indicate that the upper shear layer contains several spatially coincident yet distinct modes of convection. White light images show a mottled pattern known as *granulation* (e.g. Bray et al. 1984; Roudier et al. 1991), representing the tops of near-surface convection cells, called *granules*. The granulation pattern is observed to cover the entire visible surface, with individual granules being recognizable for about 5–10 minutes and typically measuring about 1 Mm across. In addition, images of the line-of-sight velocity field reveal larger scales of convection such as *mesogranulation* (measuring 5 Mm across, existing for several hours) (November et al. 1981) and *supergranulation* (25–30 Mm, 1 day) (Leighton et al. 1962), which also cover the visible surface of the sun while coexisting with the granulation pattern.

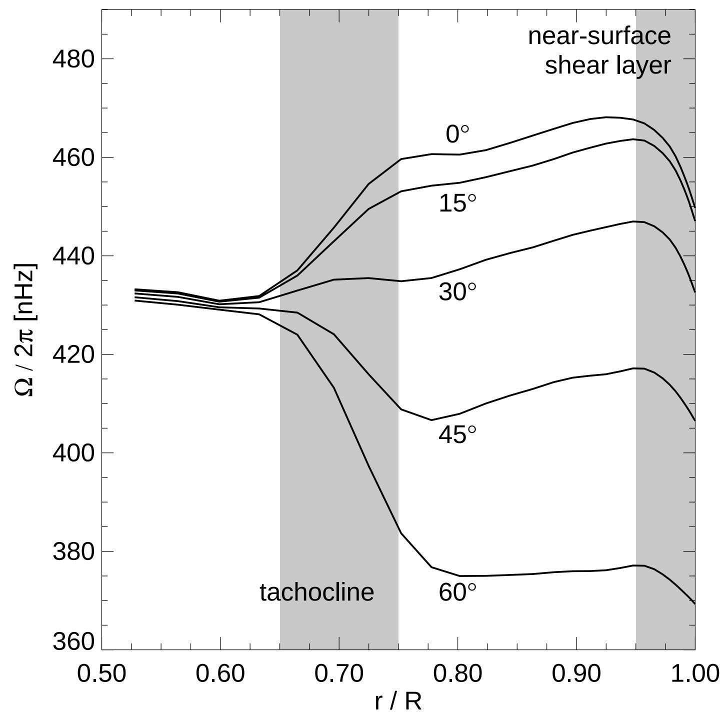

Figure 1.2: Average rotation rates $\Omega/2\pi$ inferred from the helioseismic inversion of over 4 years of GONG data using the RLS technique (adapted from Howe et al. 2000). Shear layers (*shaded*), evidenced by variations of Ω with radius, are observed near the base of the convection zone as well as near the surface. The gradients of Ω in that near-surface shear layer at high latitudes is somewhat sensitive to the inversion method and data sets used (e.g. see Fig. 1.1 and Schou et al. 1998).

Time-distance and *ring-diagram* techniques are two examples of *local helioseismology*, in which helioseismic analyses are applied to more localized regions of the sun. Both methods have revealed flow patterns in the near-surface layers having a spatial scale larger than that of supergranulation. By partitioning the visible surface into smaller sections, it is possible to infer the dependence with position and depth of quantities such as temperature and average flow velocities by measuring the oscillation frequencies of high-degree modes. Time-distance analyses indicate that persistent poleward meridional flows of order 20 m s^{-1} occupy at least a 20 Mm-deep layer below the photosphere (Giles et al. 1998). The return flow, which must be located at a level deeper than to which the time-distance analysis is sensitive, has not yet been detected. Synoptic maps of the horizontal velocity field inferred from ring-diagram analyses show extended regions of organized flow patterns evolving on time scales on the order of one day, while longer temporal averages show banded zonal flows which propagate toward the equator over the course of several years (Haber et al. 2000). The ring-diagram analyses have revealed that the meridional circulations can possess an evolving double-celled structure with latitude in the northern hemisphere, while that in the south is single-celled (Haber et al. 2001).

In response to these various motions, small-scale magnetic elements present in the photosphere are observed to be systematically advected by granular and supergranular flows (Berger et al. 1998; Hagenaar et al. 1999). As a result, individual filaments of emergent flux interact frequently with other magnetic elements, either merging with or annihilating other elements, depending on polarity. At the same time, larger regions of intense magnetic field, including sunspot pairs and plage regions, can persist for time periods ranging between a few days and several months. Sunspots in particular form regular patterns which cycle every 22 years as indicated by the timing, latitude, and polarity of emerging sunspot pairs. At the beginning of each sunspot cycle, pairs first appear in mid-latitude regions with an approximate east-west orientation. Sunspot pairs in the northern hemisphere generally have the opposite polarity of pairs in the southern hemisphere, but throughout each cycle the polarity remains the same for a given hemisphere. As the cycle progresses, pairs emerge in increasing numbers at latitudes progressively closer to the equator. After about 11 years, the sunspots at the equator become fewer in number while the next cycle begins as sunspots reappear at mid-latitudes. The spots of the new cycle have their polarity reversed from the spots of the previous cycle, making the total cycle time about 22 years.

We have described several ordered phenomena, such as differential rotation, supergranulation, and the 22-year magnetic cycle, which coexist with the quickly evolving and highly turbulent fluid motions within the convection zone. A detailed picture of how such persistent flows and magnetic fields interact with the more intermittent fluid motions is just beginning to emerge. Dynamical effects which are not yet accessible to observations can only be examined with the aid of analytical models and numerical simulations of turbulent convection, which we now review briefly.

1.2 SIMULATIONS OF TURBULENT CONVECTION

1.2.1 Mean-Field Hydrodynamic Models of the Convection Zone

With the rapid advancement of computer technology, especially over the past two decades, theoretical modeling of turbulent convection is now playing an increasingly larger role in gaining a better understanding of convection zone dynamics. Solar observations not only provide many clues toward such understanding, but also serve as goals to which the theoretical models strive to attain.

Due to the complexity and vigor of the turbulence within the convection zone, not all dynamically relevant scales of motion can be explicitly resolved in the same simulation. The most widely adopted approach is to assume a separation of scales, whereby large-scale or long-lived phenomena of interest, such as the differential rotation, are typically represented by globally averaged quantities. Perturbations superposed on these mean quantities thus describe more local phenomena. Such scale separation is achieved by filtering the relevant physical equations in space or time, and then solving only the averaged equations. Obtaining a solvable set of equations requires one to somehow approximate how the dynamics of the unresolved scales of motion affect those scales which are explicitly resolved. Given the usually intricate dependencies between large- and small-scale dynamics of a turbulent system, however, it may not be clear what treatment of the small-scale effects is appropriate. Furthermore, it may not even be clear that an appropriate dividing line between small- and large-scale motions exists, since the very nature of turbulence is that it is characterized by a wide range of scales of motion. Despite these limitations, such scale-separation treatments are widely used to investigate the intricate dynamics occurring within the solar convection zone.

The broad class of *mean-field models*, which typically contain only at most a few resolved large scales of motion, provided the first theoretical picture of convection zone dynamics. Such calculations suggested that the effects of unresolved motions are likely to make important contributions to large-scale dynamics. For example, velocity correlations associated with turbulent eddies, commonly known as *Reynolds stresses*, were found to be very effective in transporting angular momentum throughout the convection zone and are therefore likely to play an important role in achieving the solar differential rotation profile. By adjusting the functional forms of the Reynolds stress terms it was possible to obtain models which compare favorably to the observed solar surface rotation, meridional circulation, and temperature profiles (Durney & Roxburgh 1971; Kitchatinov & Rüdiger 1993). However, other choices led to very different profiles, and there is no evident basis for preferring some functional forms over others. Many of these models also produced cylindrically symmetric angular velocity profiles in the interior, a result now contradicted by helioseismic inferences. One notable exception is the model of Kitchatinov & Rüdiger (1995), which was able to produce an interior differential rotation profile similar to that inferred from helioseismic inversions. The main drawback of the mean-field approaches continues to be the ad hoc parameterization of small-scale effects.

1.2.2 Multi-Mode Hydrodynamical Simulations

The continual advancement of computing technology has enabled simulations of three-dimensional systems that explicitly resolve a diverse spectrum of size scales, rather than only the largest few. Several recent compressible convection simulations exhibit rich structures, such as narrow downflow plumes and concentrated vorticity fields coexisting with large-scale circulation (e.g. Brummell et al. 1995), suggesting that the gross parameterizations of small-scale dynamical source terms typically employed in mean-field treatments are physically inappropriate. However, the disparity between the largest and smallest size scales of motion in the convection zone continues to present severe challenges for modeling, as local dissipative processes operate on size scales that are at least a factor of 10^6 smaller than the depth of the convection zone itself. Current computer technology can explicitly resolve only 10^3 size scales in each of the three physical dimensions when memory, data storage, and time-stepping limitations are considered. In terms of the *Reynolds number* R_e (ratio of inertial to dissipative forces), the largest current models have $R_e = 10^4$, which is much lower than the value of $R_e = 10^{12}$ thought to exist within the solar convection zone. Values of other nondimensional parameters of these simulations, such as the *Rayleigh number* R_a (ratio of buoyancy driving to dissipative forces), *Taylor number* T_a (ratio of Coriolis to viscous forces), and *Prandtl number* P_r (ratio of viscous to thermal diffusion) are similarly removed from the parameter regime applicable to the actual sun. As a result, issues of scale separation and closure still exist, although to a lesser degree than in mean-field models since these more detailed simulations explicitly resolve a much broader range of scales. Three-dimensional models serve as useful analogs for the real convection zone because many physical effects relevant to the dynamics on a global scale are present to some degree.

Solar convection zone simulations have employed several different strategies to cope with the disparity of scales. One approach seeks to study the global dynamics of a spherical system by approximating the convection zone as a fluid confined to a rotating spherical shell. The available computational degrees of freedom are used to explicitly model the largest scales of motion, while net contributions resulting from motions occurring on sub-grid scales are approximated.

We now discuss global simulations of convection in rotating spherical shells. Unlike mean-field models, the largest size scales associated with convection are now explicitly resolved in these simulations. The first extensive research in this area was performed by Gilman (1977, 1978a,b), who modeled a Boussinesq fluid (where the fluid is largely incompressible except for density perturbations coupled with gravitational effects) at $R_e \approx 100$, $T_a = 10^5$, and $P_r = 1$. Simulations having Rayleigh numbers between 10^4 and 10^5 were computed for various combinations of temperature and velocity boundary conditions. For $R_a \lesssim 5 \times 10^4$ these models exhibited solar-like surface differential rotation profiles, with zonal velocities faster at the equator than at mid- to high latitudes. Such differential rotation was achieved by the equatorward transport of angular momentum by Coriolis forces and Reynolds stresses working against diffusion. For $R_a \gtrsim 5 \times 10^4$, the transport of angular momentum away from the equator by poleward meridional flows became strong enough to reverse the sense of the differential rotation profile, such that the angular velocity of equatorial latitudes became slower than at higher latitudes.

Compressibility was later included into these spherical shell models (Glatzmaier & Gilman 1981; Glatzmaier 1984, 1985; Gilman & Miller 1986) via the *anelastic approximation*, first adapted from meteorology to the stellar context by Gough (1969). These anelastic models exhibited convective structures possessing a wide range of spatial and temporal scales. The most prominent velocity structures that emerged were the so-called *banana cells*, visible as fluid rolls elongated in latitude oriented perpendicular to the equator. For the more highly stratified models that were considered, a necessary condition for surface differential rotation was that the rotational influence, characterized by T_a, must be large enough to allow angular momentum to be deposited in equatorial regions by Coriolis-driven Reynolds stresses. In addition, the unresolved motions need to transport heat more efficiently than momentum, suggesting a P_r less than unity. However, the solutions with strong enough rotation to produce a surface equatorial acceleration also had the angular velocity nearly constant on cylinders aligned with the axis of rotation, which we now know is not the case within the actual solar convection zone.

The advent of high-performance, massively parallel computing platforms provides access to more turbulent regimes, allowing simulations with much lower diffusivities (and thus higher R_e and R_a) to be carried out. The models of Miesch et al. (2000) and Elliott et al. (2000) represent the most turbulent simulations of a global variety performed to date. In these simulations, combinations of flow parameters and boundary conditions were found which produced a more solar-like differential rotation, breaking the tendency for a cylindrically symmetric angular velocity profile. The increased turbulence in these simulations was accompanied by a breakup of the banana cell structures and a more complex evolution of convective structures than found in the earlier, less turbulent simulations. As the driving was increased, however, the rotation profiles tended to revert back to being aligned on cylinders. In these simulations the level of turbulence is still substantially lower than in the actual sun, and it remains to be seen how even more turbulent driving affects the dynamics within these systems.

Parallel computing opportunities have also permitted local studies of the turbulent dynamics of rotating fluids. In contrast to the scale-separation approach, this strategy distributes the computational degrees of freedom over the smallest scales of motion, thereby precluding the need for parameterizing unresolved effects. As a result, the computational domains are more restricted in overall size, and are usually Cartesian rather than spherical, but do not include any sub-grid scale approximations found in the global simulations described earlier. However, any large-scale structures that do form are limited by the size of the domain and thus may not be representative of a larger system. Because the combined effects of small-scale motions at or near the scale of dissipation have a significant effect on the global dynamics, these models are still of great interest.

Turbulent, compressible fluids in a Cartesian domain have been modeled by Cattaneo et al. (1991), with effects due to rotation later included by Brummell et al. (1996, 1998). Rotational effects on an f-plane are included by inclining the axis of rotation with respect to the thermal stratification, effectively representing different latitudinal positions on a sphere. These models are characterized by a more laminar thermal boundary layer at the upper surface covering a deeper turbulent interior. Of interest in the solar case is the behavior at $P_r < 1$, where compact plumes of downwelling fluid span the full vertical extent of the fluid layer. These coherent downflows, however, contribute little to the overall vertical transport of energy as their upward heat flux is largely balanced by the downward transport of kinetic energy. The primary energy transport is therefore accomplished by the smaller-scale, more turbulent motions of the system. Simulations with a moderate rotational influence were found to drive a mean flow (although it is rather modest when compared to the kinetic energy of the convection), owing to the tilting of downflowing structures toward the rotation vector.

Another class of local simulations designed to provide insight into granular convection in the near-surface layers has been performed by Stein & Nordlund (1998, 2000). The fully compressible fluid equations are solved, including the effects of ionization and radiative transfer which are important for the near-photospheric layers. Their domain is a 6 Mm $\times$ 6 Mm wide and 3 Mm deep Cartesian box, which is large enough to contain many granules but only encompasses a relatively shallow layer of convection near the surface of the sun. However, these models do produce some extremely realistic results in the appearance and evolution of granulation. The granulation pattern is shown to be thermally driven, with radiatively cooled matter being transported downward in the network of dark lanes separating individual granules. In addition, these granulation simulations produce photospheric absorption line profiles, acoustic oscillation frequencies and excitation characteristics in close agreement with measurements of comparable quantities determined from observations of actual granulation.

1.2.3 Models Including Magnetic Effects

The inclusion of magnetic effects into hydrodynamic convection models adds another level of both complexity and realism. It is believed that both the large-scale and small-scale photospheric magnetic field structures are merely the surface manifestation of magnetism produced by the *solar dynamo* (Parker 1979) thought to be operating within the solar convection zone and possibly just below its base in the overshoot layer. The observed 22-year pattern of sunspot emergence during each solar activity cycle, as characterized by Hale's polarity laws, must be directly linked to a *global solar dynamo* operating within the sun. On smaller scales, filaments of magnetic flux are observed to emerge through the photosphere and are advected horizontally in response to the organized granulation and supergranulation flow patterns. Because these small-scale flux elements possess less ordered behavior than larger magnetic structures such as sunspots and appear to be unaffected by the 22-year global magnetic cycle, they may be the result of a *local solar dynamo* that is at least partially distinct from the global dynamo (e.g. Cattaneo 1999). Any dynamical picture must account for both the organized large-scale dynamo activity and the small-scale magnetic filaments.

Shear flows such as the interior differential rotation profile are extremely efficient at stretching out poloidal magnetic field into toroidal field. For sustained dynamo action to occur in the sun, however, there must exist a mechanism which regenerates poloidal field from toroidal field; otherwise, the toroidal magnetic field which results from the differential rotation of the solar interior would eventually diffuse away. One promising way such poloidal field may be created is known as the α-effect, and operates via the cyclonic twisting of toroidal field by turbulent convective fluid motions, as originally suggested by Parker (1955a). The earliest models which investigated the feasibility of the α-effect in producing a solar-like global magnetic cycle were of the mean-field type. Such models showed that dynamo action is indeed possible for systems containing both shear and rotation-induced helical motions (e.g. Stix 1976), but have trouble reproducing the relative strength of magnetic features observed on the sun. This effect occurs because strong magnetic fields tend to inhibit the small-scale helical motions that may be responsible for the α-effect, a process known as *α-quenching*.

We now know from helioseismology that a strong region of radial shear is located at the base of the convection zone within the tachocline, and it is within this region that the strongest toroidal magnetic fields are believed to be formed. The existence of this shear layer led to the idea of *interface dynamos* (Parker 1993), a class of mean-field models which contain a layer of convection placed immediately above a stably stratified overshoot layer containing shearing flows. The flows within the shear layer produce the toroidal field, while the poloidal field necessary to complete the dynamo cycle is regenerated within the convection zone. Because the region of storage is spatially distinct from the region where the α-effect occurs, the quenching problem is avoided; however, there must now exist a mechanism that transports the magnetic flux between each region. Toroidal magnetic structures naturally drift upward into the convecting layer due to their magnetic buoyancy (Parker 1955b), where some fraction is converted into poloidal field via the α-effect. Transporting this poloidal field back down into the shear layer is more problematic, and is accomplished by turbulent diffusion in some of the most recent interface dynamo models (e.g. Charbonneau & MacGregor 1997). These models are successful in reproducing waves of antisymmetric dynamo activity reminiscent of the 22-year sunspot cycle, but suffer from the drawback that the resulting dynamo behavior depends strongly on the details of the α-effect, which results from unresolved turbulent motions that can only be approximated in such a mean-field model.

Another mechanism which is able to regenerate poloidal field from toroidal field stems from the Coriolis force acting on large-scale concentrations of toroidal flux. Such dynamo models, called *Babcock-Leighton* or *flux-transport* dynamos, require magnetic structures within the convection zone large enough and long-lived enough to be influenced by the Coriolis force. To avoid the quenching problem, the Babcock-Leighton dynamos must also rely upon a mechanism to transport the poloidal flux down into the tachocline. Recent mean-field models (e.g. Dikpati & Charbonneau 1999) show that the advection of poloidal flux by a solar-like meridional circulation may be a viable mechanism, as suggested by their ability to produce realistic dynamo activity.

One drawback of the Babcock-Leighton models, which also applies to the α-effect models described above, is that the magnetism generated by most of these models does not feed back on the shearing flows in any way, and thus it is unclear how these prescribed flows are affected by the presence of a magnetic field within the domain. This problem suggests the need for dynamically consistent models which solve for both the flow velocities and the magnetic fields. Such full MHD simulations of Boussinesq fluids have been computed by Gilman & Miller (1981) and Gilman (1983), with compressibility added later by Glatzmaier (1984, 1985). For the relatively laminar parameter regimes considered, however, it was found in both the Boussinesq and compressible simulations that waves of dynamo activity tended to propagate poleward rather than toward the equator. In addition, these simulations could not reproduce the alternating polarity observed in the solar dynamo with each new sunspot emergence cycle. More turbulent simulations are just beginning to be attempted.

The highly organized patterns of sunspot and active region emergence associated with the 22-year magnetic cycle suggest that portions of the toroidal field must rise coherently through the convection zone and emerge at the surface. Simulations of thin flux tubes rising through a convectively unstable spherical shell (e.g. Moreno-Insertis 1986; D'Silva & Choudhuri 1993; Fan et al. 1993) reproduce many of the observed characteristics of bipolar active regions, including the emergence and tilt angles of sunspot pairs. These simulations, while encouraging, only consider thin flux tubes and thus neglect effects associated with the tube thickness. Such effects may be important, as three-dimensional magnetic structures within the solar convection zone may be subject to several MHD instabilities which may cause their destruction before they ever reach the photosphere. For example, vortical motions within these flux tubes may cause their fragmentation, after which they are likely to be shredded by the surrounding vigorous convection (Schüßler 1979; Longcope et al. 1996). Structures which manage to remain coherent are subject to kink instabilities which also may enhance their dissipation (Linton et al. 1996; Fan et al. 1999). In addition, strong downflow plumes within the convection may prevent some tubes from emerging at all, as such fast downwelling fluid motions can counteract their rising and pump the magnetic flux back into the tachocline (Tobias et al. 1998).

Theoretical modeling of turbulent fluids has provided valuable insight toward our understanding of convection zone dynamics. These simulations have identified likely mechanisms for sustaining the observed solar differential rotation profile and the global dynamo, even though severe approximations and parameterizations were used in most cases. These results suggest that the differential rotation throughout the solar interior is almost certainly achieved by the influence of rotation on the turbulent motions located within the solar convection zone, while the global solar dynamo is believed to occur via the interaction of magnetic field with strong shearing motions within the tachocline and with the turbulent fluid motions of the convection zone. While much attention has been focused on the relevant processes occurring within the bulk of the convection zone and the tachocline region below, the dynamics occurring in the upper shear layer immediately below the photosphere have not been studied in as much detail. This thesis seeks to address this area.

1.3 SUMMARY OF RESEARCH PRESENTED IN THIS THESIS

This thesis is devoted to a study of the upper shear layer within the solar convection zone, which forms the transition region between the deep convection zone interior and the photosphere. This layer is visible in helioseismic inversions as a region of radial gradients in angular velocity which occupy about the outer 5% (or 35 Mm) of the sun. The upper shear layer is of great interest because the multiple modes of convection contained therein are likely to influence both the dynamics of the deeper convection zone as well as the photosphere in ways that are not yet well understood. Convection on supergranular size and time scales in particular may be weakly influenced by rotation, facilitating the transport of angular momentum. In combination with such rotational effects, the large horizontal and radial extent of supergranular flows suggest that they most likely play the largest role in the dynamics of this shearing boundary layer.

We first seek to characterize the supergranulation pattern using correlation tracking methods applied to observations of line-of-sight Doppler velocity to identify supergranular outflows on the surface. Chapter 2 is devoted to an overview of surface flow measurements, including a description of the correlation tracking technique and an assessment of the systematic and random errors associated with this technique. We then in Chapter 3 apply correlation tracking methods to one 45°-square region of quiet sun to generate flow maps of horizontal velocity for a duration of six days, representing the longest uninterrupted time series of solar supergranulation studied to date. Distributions of supergranular sizes and lifetimes are obtained after directly identifying individual supergranules on each image in the time series. The intricate evolution of the supergranulation pattern is evident in the numerous examples of cell emergence, disappearance, fragmentation, and merging events, as well as in the systematic advection of intercellular lanes.

This observational study is complemented in Chapters 4 and 5 by global numerical simulations of turbulent convection within thin spherical shells. Such simulations approximate the conditions present in the upper solar convection zone as solar-like stratification, rotation, and thermal forcing profiles are imposed. We find that convection subject to solar-like density gradients naturally produces convective structures on multiple scales, the smallest of which is analogous in size to solar supergranulation. We investigate the influence of these supergranular-like convection cells on the global differential rotation and meridional circulation contained within the thin shells, including their contribution to the maintenance of shearing flows within the domain. Finally, concluding remarks and future directions associated with this research are presented in Chapter 6.

Chapter 2

SURFACE FLOW MEASUREMENTS

2.1 AN OVERVIEW OF SURFACE FLOWS

Observations of the velocity field at the solar surface play a vital role in the quest to understand how the turbulent convection within the sun transports energy and momentum throughout its interior. The dynamics of convection are responsible for sustaining large-scale features such as the global differential rotation and meridional circulation profiles, as well as more localized phenomena such as granulation, mesogranulation, and supergranulation. We will here use measurements of horizontal velocities to analyze flows on supergranular size scales. Measurements of surface flows fall into three general categories: those determined by direct Doppler measurements of the surface fluid, those inferred from helioseismic inversions, and those obtained by following tracers. We now examine each measurement technique in some detail.

2.1.1 Direct Doppler Methods

Flows can be detected by direct Doppler methods by observing the shifts of photospheric spectral lines. These measurements are possible since the Doppler shifts of these lines are proportional to the line-of-sight velocity of the emitting plasma. By measuring variations of the same spectral line across the solar disk, one obtains a map of line-of-sight velocities with position. Images of this kind are collectively referred to as *Dopplergrams* or *velocity images*. A sample velocity image is presented in Figure 2.1.

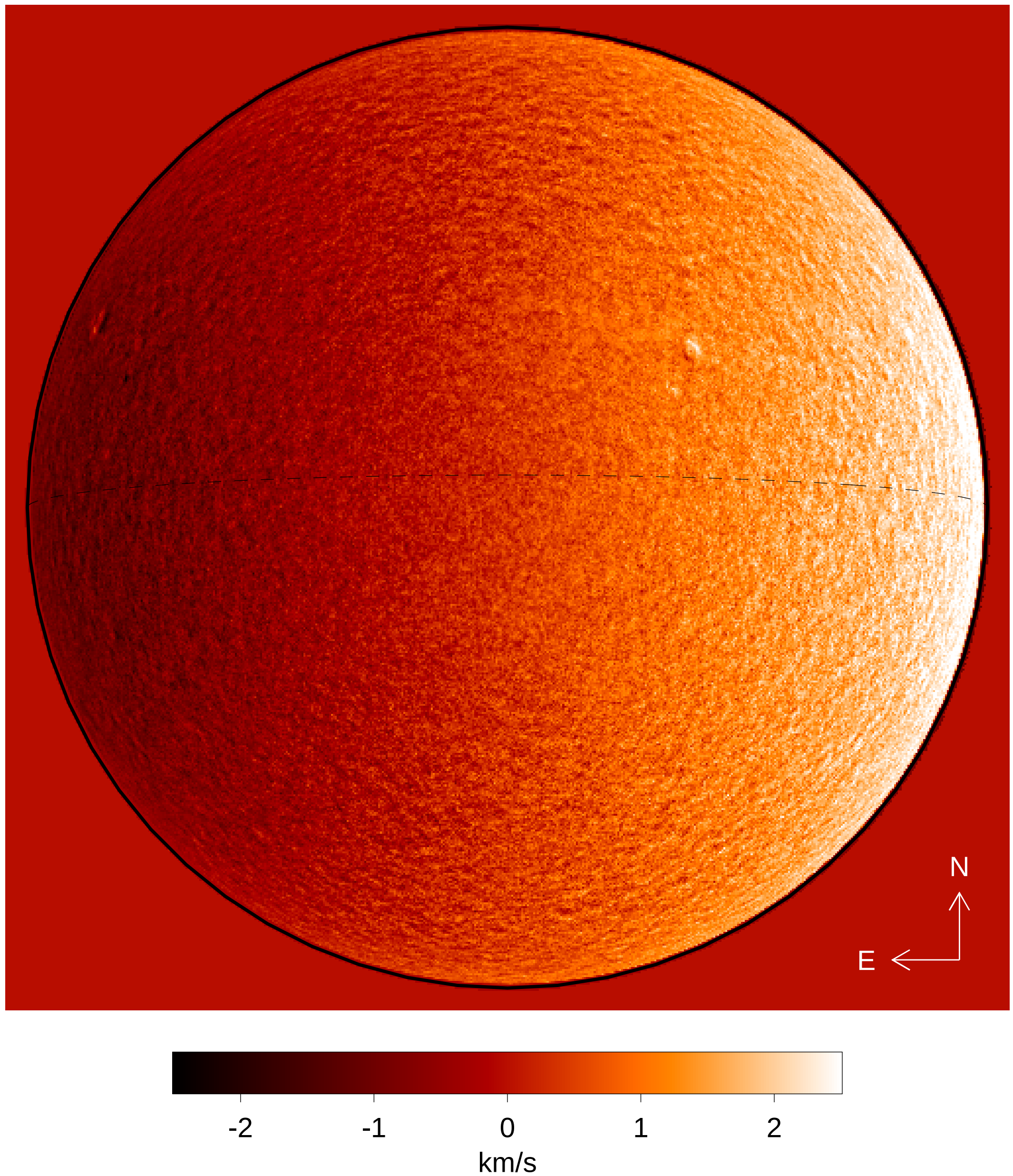

Figure 2.1: An image of line-of-sight velocity of the photosphere taken by MDI (see §2.2.1) on 1999 May 7, $00^{\mathrm{h}}01^{\mathrm{m}}$ UT. The solar equator is indicated by a dashed line. Approaching (negative) velocities are dark, while receding (positive) velocities are bright.

Some of the more groundbreaking discoveries in solar physics have been made using velocity images (initially by photographic means), including the first detection of solar supergranulation (Leighton et al. 1962) and of mesogranulation (November et al. 1981). In addition, the frequencies of acoustic oscillations, which form the basis for helioseismology, are most easily measured using time series of velocity images. Furthermore, measurements of large-scale velocity patterns, such as the surface differential rotation profile (Snodgrass 1984; Snodgrass & Ulrich 1990) and torsional oscillations (Howard & LaBonte 1980; LaBonte & Howard 1982), have been performed using time series of velocity images.

In Figure 2.1 the Doppler signal resulting from rotation is immediately apparent as the large-scale gradient of color across the image. Superposed on the rotation signal are a network of supergranular outflows, which appear as small perturbations to the overall rotation velocity. Supergranules are cellular flows in which the fluid diverges horizontally from a central region, and are recognizable on the velocity image as an association of dark and light regions. The side of each supergranule closest to disk center is dark (relative to the rotation signal) since this side of the outflow is largely approaching the observer. Similarly, the side of the supergranule closer to the limb is light due to its velocity of recession relative to the observer. These dark/light associations were first identified as outflows and attributed to solar convection by Leighton et al. (1962). Also visible in the image are two sunspots, one above and to the right of disk center, and the other at about the same latitude near the east limb.

Using direct Doppler measurements to measure horizontal flows is problematic for several reasons. First, since only fluid motions moving toward or away from the observer are measured, the spherical nature of the sun causes the proportion of radial to horizontal velocities projected into the line-of-sight to vary with the angular distance from disk center. This geometric effect makes measurements of horizontal flow fields difficult near disk center (where only a small amount of the horizontal velocity is projected into the line-of-sight) as well as near the limb (where foreshortening effects come into play). In addition, only one of the two horizontal velocity components are available, as motions moving parallel to the limb move transverse to the observer and are therefore not projected into the line-of-sight Doppler velocity. Furthermore, one needs to make some assumptions about the nature of the flow field in order to separate the radial flow contributions from the horizontal components to the projected line-of-sight velocity.

2.1.2 Local Helioseismic Techniques

Helioseismic techniques are used to infer the global characteristics of the solar interior after observing acoustic oscillations visible over the entire photosphere. By observing smaller regions of the sun and analyzing waves which propagate into and out of these regions, researchers are able to determine more localized properties of the sun. As a result, such analysis techniques are termed *local helioseismology*. One such measurement is of the bulk horizontal velocity of the fluid as averaged over the region of interest, as the frequencies of waves traveling through a moving medium will be Doppler shifted by an amount proportional to the bulk flow speed. This principle is used in both time-distance and ring-diagram techniques.

Time-distance helioseismology (Duvall et al. 1993; D'Silva 1996; Duvall et al. 1997) uses a time series of velocity images to measure the travel times of acoustic modes propagating along subsurface ray paths. The method involves computing the cross-correlation function between the data at two points separated by varying distances and times. The locations in space-time where the correlation is high indicate the upper turning points of acoustic modes after having traversed their subsurface ray paths. The difference in travel times between two counter-propagating waves traversing the same ray path in opposite directions indicates the presence of a bulk flow, since waves traveling against the flow take longer to traverse the same distance than waves traveling with the flow. These travel-time differences can be used to construct a map of fluid velocities not only at the surface but also over a range of depths. This technique has been used to measure flows in both quiet sun and under sunspots (Duvall et al. 1996), as well as to characterize meridional flows near the surface and at depth (Giles et al. 1997; Giles 1999).

Ring-diagram analysis (Hill 1988) is based on the multi-dimensional power spectra of the normal modes of oscillation computed from time series of velocity images. After tracking a localized region of the solar photosphere in a frame corotating with the sun, these time series are then Fourier decomposed, thereby transforming the (x, y, t) velocity data into (k_x, k_y, ω) frequency data. The nested trumpet-like structures which appear as maxima in frequency space indicate the eigenfrequencies of the oscillations. Projections of these structures in the (k_x, ω)-plane yield the familiar (ℓ, ν) diagram, but projections in the (k_x, k_y)-plane yield a series of concentric rings, for which this analysis technique is named. Horizontal flows within the localized region both near the surface and at depth cause displacements in the locations of the rings, which are then be used to infer the magnitude and direction of such flows (Schou & Bogart 1998; Basu et al. 1999; Haber et al. 2000).

2.1.3 Tracer-Type Measurements

Near-surface flows can also be measured by following recognizable features embedded in a time series of images from frame to frame as they move around. Although only motion transverse to the line-of-sight can be detected, such techniques have proven useful for characterizing several aspects pertaining to granulation, mesogranulation, and supergranulation (Title et al. 1995; Strous & Simon 1998).

Feature tracking and correlation tracking are the two tracer-type techniques most commonly used in practice. The main difference between the two methods is that feature tracking requires the identification of structures embedded in the flow. Horizontal velocities are then determined by identifying the same structures in subsequent images in the time series, measuring their horizontal displacements, and then converting these displacements to a velocity. Alternatively, correlation tracking compares the topology of the images surrounding predetermined measurement gridpoints with the topology in the vicinity of the same gridpoints in subsequent images. Horizontal velocities are then calculated by determining the optimal displacement such that the topology maximally coincides.

The main drawback of both feature tracking and correlation tracking is that changes in appearance may be interpreted as proper motions. For example, changes in the shape of an object due to its evolution may affect the velocities measured by feature tracking and correlation tracking methods. In addition, the shape of an object rotating across the solar disk may appear to change even if it is not evolving, as projection effects may alter how the object is viewed by an observer. In either case, a tracer-type measurement algorithm may interpret these changes as proper motions and ascribe spurious velocities to the region of interest. Furthermore, the underlying assumption that the tracers are passive floaters in the fluid may be incorrect, as the proper motions of tracers may be somewhat different than the actual velocity of the fluid. Despite these drawbacks, tracer-type methods are useful for measuring several different aspects of solar surface flows.

Chapter 3 will examine the general properties of the flow field on supergranular scales by having applied the correlation tracking method to features present in time series of velocity images. We begin here by describing in detail how the near-photospheric flow maps are obtained from time series of observational data, and then in §2.3 discuss the sensitivities of the correlation tracking approach.

2.2 OBTAINING SURFACE FLOW FIELDS FROM MDI DATA

The flow field on supergranular scales can be deduced by applying correlation tracking to mesogranule-sized structures evident in time series of velocity images. Such features have been shown to sense the supergranular flow field quite well, even near disk center (see §3.1) where the contrast of individual mesogranules is small (DeRosa & Toomre 1998). With this method, we are able to measure both horizontal components of the near-surface velocity field for several supergranular lifetimes. We begin here by briefly describing the MDI instrument, which provides the velocity time series to which the data processing scheme is applied. Then we summarize the data processing steps leading up to the application of the correlation tracking technique described in §2.2.2.

2.2.1 The MDI Instrument on SOHO

The Solar and Heliospheric Observatory (SOHO) spacecraft provides extended, uninterrupted observations of the sun by viewing our star from the L_1 Lagrangian point located approximately 1.5×10^6 km sunward from earth. The suite of 12 instruments on SOHO observe the solar interior and atmosphere as well as the solar wind from a vantage point where images and measurements free of atmospheric seeing effects can be obtained. Furthermore, the Doppler velocity of that position relative to the sun only changes slowly in time, unlike in near-earth orbits, and this relative stability leads to greatly enhanced sensitivity in Doppler measurements.

One of the instruments on SOHO, the Michelson Doppler Imager (MDI) (Scherrer et al. 1995), was designed so that helioseismic techniques applied to its images could be used to probe the interior structure of the sun. Such analyses are performed using Doppler and intensity observations of the photosphere with high spatial and temporal resolution, providing precision measurements of the many resonant mode frequencies. From its space-based location, MDI is able to provide data undistorted by the earth's atmosphere and uninterrupted by diurnal gaps, allowing helioseismologists to observe the solar interior in greater detail than previously possible. Such rapid, undistorted time series are also ideal for the measurement and analysis of surface flows considered here.

MDI is able to provide images of continuum intensity, line-of-sight velocity, and line-of-sight magnetic field by sampling the radiation field at 75 mÅ intervals surrounding the mid-photospheric 6768 Å absorption line of Ni I. After passing through the telescope, the light travels through a series of fixed filters and two tunable Michelson interferometers which are able to provide filtergrams anywhere in the vicinity of the absorption line. Images of the sun at five equally spaced wavelengths are then linearly combined to compute the observables listed above. The full sun can be imaged simultaneously onto a 1024×1024-pixel CCD detector (with $2''$ pixels), or a higher resolution field (with $0.6''$ pixels) can be projected onto the same detector. Telemetry constraints limit the quantity of data which gets beamed back to earth, but dedicated campaigns in each of the last five years have provided continuous coverage of velocity and sometimes intensity and magnetic field at a cadence of one minute for a duration of several months. We use data from these so-called *Dynamics Campaigns* providing full-disk data with few interruptions to perform our study of supergranular surface flows.

2.2.2 Isolating the Mesogranules

We use the line-of-sight velocity images observed by MDI in full-disk mode ($2''$ pixels) during the 1999 Dynamics Campaign at a cadence of one minute. These time series are processed so that the evolving mesogranular pattern can be used to track surface flow on supergranular size scales. To accomplish this objective, one $45°$-square region of photospheric plasma is tracked and remapped onto a latitude-longitude coordinate system as it rotates across the disk of the sun, as illustrated in Figure 2.2. The pixel size in the remapped images is equivalent to 1.46 Mm in both latitude and longitude, which is approximately equal to the instrument pixel scale of $2''$ at disk center. The entire region is tracked rigidly at a synodic rate of $13.5°$ day^{-1}, which is slightly faster than the Carrington rate of $13.2°$ day^{-1} and equal to the average supergranular rate over the latitudinal extent of the region as measured by Snodgrass & Ulrich (1990).

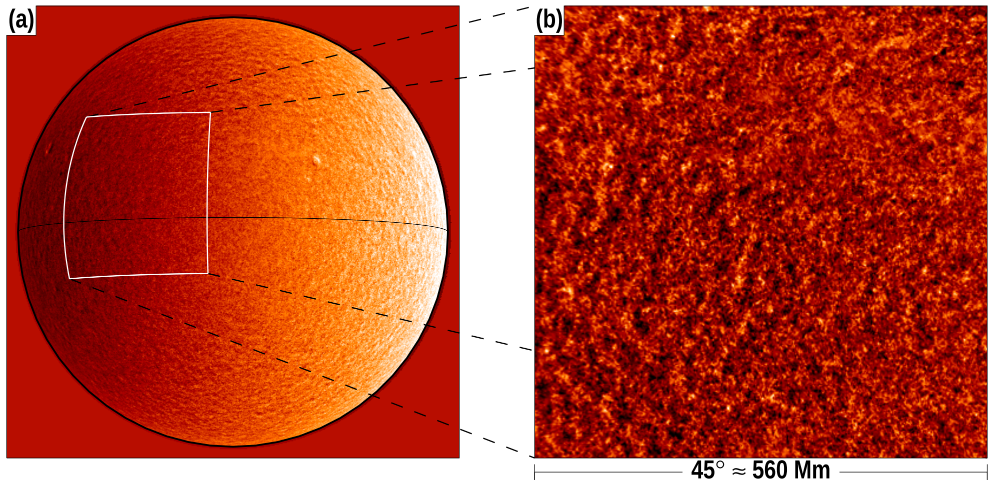

Figure 2.2: The first step in the data processing sequence. (a) The full-disk line-of-sight velocity image observed by MDI on 1999 May 7, $00^{\mathrm{h}}01^{\mathrm{m}}$ UT, scaled to ± 2500 m s^{-1}. The equator is indicated by the solid black line crossing the image. (b) The 45°-square region enclosed in white in (a) after remapping to a latitude-longitude coordinate system, and scaled to ± 800 m s^{-1}. The Doppler signal due to solar rotation, visible in (a) as the large horizontal gradient of velocity across the solar disk, is removed as part of the remapping process. In both images, approaching velocities are dark and receding bright.

The time series spans approximately six days, or about as long as a 45°-square region centered in latitude near the equator remains accessible to our analysis on the solar disk. Although all points in the tracked region remain on the earth-facing side of the sun for longer than six days, most of that additional time places the regions within about 25° of the limb where geometric foreshortening effects blur the objects of interest.

During the remapping stage, the large Doppler signal resulting from the overall rotation of the sun is removed by subtracting an empirical fit to the observed differential rotation profile. This empirical fit is formed by averaging together 60 consecutive full-disk images (spanning one hour) and then fitting a planar surface to the resulting average image. A circular mask is used so that pixels falling outside the solar disk do not contribute to the fit. This surface fit is subtracted from each full-disk MDI velocity image before the remapping occurs.

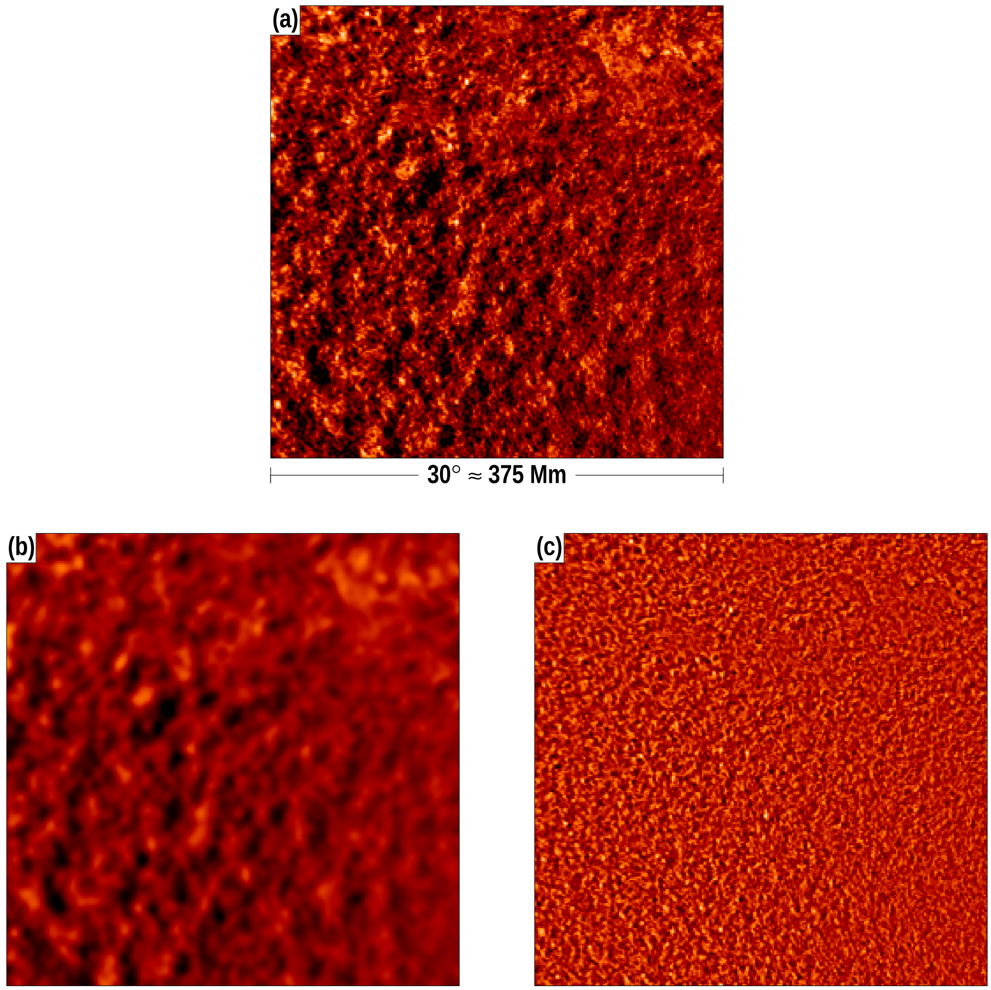

Figure 2.3: The next step in the data processing sequence. (a) The central 30° portion of Fig. 2.2b after the acoustic oscillations have been attenuated using a low-pass temporal filter. (b) The image in (a) after 7.3-Mm Gaussian smoothing, and (c) the residual of (a) and (b). Such filtering effectively separates the supergranules in (b) from the mesogranules in (c). All three images are scaled to ± 500 m s^{-1}, with approaching velocities dark and receding velocities bright.

To separate the radial velocity signal (arising from the acoustic oscillations) from the horizontal velocities (resulting from supergranulation and mesogranulation), we apply a low-pass temporal filter to the time series. The filter consists of taking a 31-minute weighted average using a tapered Gaussian filter to attenuate the high-frequency acoustic oscillations. The weighting function (derived from Libbrecht & Zirin 1986) is

$$W(\delta t) = \exp\left(-\frac{\delta t^2}{2\tau^2}\right) - \exp\left(-\frac{\Delta t^2}{2\tau^2}\right)\left[1 + \frac{\Delta t^2}{2\tau^2} - \frac{\delta t^2}{2\tau^2}\right], \tag{2.1}$$

where δt is the time difference from the central observing time, $\tau = 8$ minute is the half-width of the filter, and $\Delta t = 16$ minute is the half-length of the filter. This weighting function has the property that $W = \frac{dW}{d(\delta t)} = 0$ for $\delta t = \pm\Delta t$. For these parameters, typical p-mode oscillation amplitudes are reduced by a factor of 500 compared to the longer-lived mesogranular and supergranular signals.

At this stage, it is assumed that the remaining structure in the velocity images originates primarily from the horizontal motions of the supergranular, mesogranular, and marginally resolved granular outflows. Mesogranules appear as small-scale undulations superposed on the supergranular outflows, as can be seen in Figure 2.3*a*. The next step in the data processing sequence is to separate the mesogranular component from the supergranular component by applying a spatial Gaussian filter of width 7.3 Mm (equivalent to 5 pixels) to each of the individual images comprising the time series. Retaining the low frequencies produces an image of the supergranular pattern as in Figure 2.3*b*, whereas the high-frequency image contains the mesogranules as in Figure 2.3*c*. The sum of these two components yields the original unfiltered image. The filter width was chosen so that the locations of individual supergranules in the field are difficult to determine by inspecting only the mesogranular component. Once time sequences of mesogranular component are available, flow maps are obtained by applying the correlation tracking technique.

2.3 THE CORRELATION TRACKING TECHNIQUE

2.3.1 The Correlation Tracking Algorithm

We now describe the correlation tracking algorithm and its sensitivities. Correlation tracking methods, as applied to solar images, were primarily developed by members of the Lockheed-Martin Solar and Astrophysics Laboratory, most notably Neal Hurlburt, Dick Shine, and Alan Title (Title et al. 1995). The algorithm presented here is the result of several rounds of fine-tuning, both on their part (Hurlburt et al. 1995) and ours.

The correlation tracking algorithm takes as input two equally sized images $I_1(x, y)$ and $I_2(x, y)$, where in this notation integer values of the pixel coordinates x and y index the pixels in the two images. We now identify N coordinates in the image field as gridpoints at which to measure the local displacement of the features embedded in the two images. Note that while it is possible for the measurement gridpoints to be located at fractional pixel coordinates, it is computationally more sensible to have them located at integer pixel coordinates. In practice, the gridpoints form a regularly spaced array. We denote each measurement gridpoint by the pixel coordinates (x_n, y_n), where the variable $n = 1, 2, \cdots, N$ indexes the measurement gridpoints.

At each gridpoint (x_n, y_n), the goal is to calculate the optimal displacement $(\delta x, \delta y)$ such that the topology of the pixels in the neighborhood of (x_n, y_n) in image I_1 best coincide with the topology of the pixels in the neighborhood of the corresponding gridpoint on image I_2. Because we consider only those pixels in the neighborhood of each gridpoint, the optimal displacement thus calculated serves as a measurement of the movement of the features in the immediate area of the gridpoint. This optimal displacement is determined by shifting the pixels in the neighborhood of each gridpoint by varying amounts and determining the relative displacement of the best overlap. In this formulation, the pixels closer to the gridpoint are weighted more heavily than pixels farther out, as characterized by the e-folding width σ of the spatial weighting function. The mathematical details of the algorithm have been omitted here, but are presented in Appendix A for the interested reader. The end result is an array of displacements $(\delta x, \delta y)$ at each measurement gridpoint, which can be converted into a velocity after dividing by the time separation between I_1 and I_2. Note that the spatial resolution of the resulting velocity field is determined by σ, and not by the gridpoint spacing. In practice the flow maps are spatially oversampled by a factor of two or four in each dimension.

2.3.2 Calibrating the Algorithm

To detect supergranular outflows, the algorithm needs to be able to detect displacements as small as 0.004 pixels, equivalent to a structure having a velocity of 100 m s^{-1} given the spatial and temporal resolution of the MDI full-disk solar data. We can assess the accuracy and precision of the correlation tracking algorithm by shifting sample images by known amounts, and then applying the correlation tracking algorithm to the original and shifted image pairs. Before describing the results of these calibration tests, we first briefly describe the Fourier shifting algorithm.

2.3.2.1 The Fourier Shifting Scheme

Shifting the sample images is performed by the Fourier shift technique, whereby the image is reconstructed at shifted gridpoints once the two-dimensional Fourier spectrum of the image is known. The Fourier shifting scheme was chosen since it incorporates global information, whereas the interpolation performed as part of the correlation tracking technique is local. Given a two-dimensional $2M \times 2N$-pixel image $I(x, y)$ indexed by $x = 0, 1, \cdots, 2M-1$ and $y = 0, 1, \cdots, 2N-1$, the discrete forward and inverse Fourier transforms are given by

$$\hat{I}(\omega_p, \omega_q) = \frac{1}{4MN} \sum_{x=0}^{2M-1} \sum_{y=0}^{2N-1} I(x, y)\, e^{-i\omega_p x}\, e^{-i\omega_q y} \qquad \text{(forward transform)} \qquad (2.2)$$

and

$$I(x, y) = \sum_{p=0}^{2M-1} \sum_{q=0}^{2N-1} \hat{I}(\omega_p, \omega_q)\, e^{i\omega_p x}\, e^{i\omega_q y}, \qquad \text{(inverse transform)} \qquad (2.3)$$

where the spatial frequencies ω_p and ω_q are defined

$$\omega_p = \frac{\pi p}{M} \qquad \text{and} \qquad \omega_q = \frac{\pi q}{N}. \tag{2.4}$$

To determine $I(x + \delta x, y + \delta y)$, we simply evaluate equation (2.3) at the shifted points $x + \delta x$ and $y + \delta y$:

$$I(x + \delta x, y + \delta y) = \sum_{p=0}^{2M-1} \sum_{q=0}^{2N-1} \hat{I}(\omega_p, \omega_q)\, e^{i\omega_p (x+\delta x)}\, e^{i\omega_q (y+\delta y)} \tag{2.5}$$

$$= \sum_{p=0}^{2M-1} \sum_{q=0}^{2N-1} \left[\hat{I}(\omega_p, \omega_q)\, e^{i\omega_p \delta x}\, e^{i\omega_q \delta y}\right] e^{i\omega_p x}\, e^{i\omega_q y}. \tag{2.6}$$

Consequently, obtaining the transformed image $\hat{I}(\omega_p, \omega_q)$ allows one to calculate the shifted image $I(x + \delta x, y + \delta y)$ by taking the inverse transform of $\hat{I}(\omega_p, \omega_q)$ modulated by the function $e^{i\omega_p \delta x} e^{i\omega_q \delta y}$.

2.3.2.2 Assessing the Accuracy and Precision of Correlation Tracking

The calibration experiments were performed on the two 384×384-pixel images shown in Figure 2.4. Image A (Fig. 2.4*a*) is the superposition of 100,000 two-dimensional Gaussian functions whose positions, amplitudes, and widths in each the two directions were randomly chosen. The amplitudes were allowed to be of either sign. Image B (Fig. 2.4*b*) is a 45°-square (heliographic) region of mesogranulation centered approximately just north of disk center, which was originally observed by MDI and processed so that the mesogranules are evident, as described in §2.2.2.

To assess the accuracy and precision of correlation tracking, we shift the two sample images by several amounts ranging from 0.001 to 0.4 pixels, and then apply the correlation tracking algorithm to each shifted image and its unshifted parent image. As stated earlier, we need to detect shifts as small as 0.004 pixels, but the behavior of the algorithm at large shifts is also of interest. For each such pair of images, the correlation tracking algorithm computes the optimal shift at each gridpoint in a 48×48 array of measurement gridpoints. These gridpoints are spaced 8 pixels apart, with the

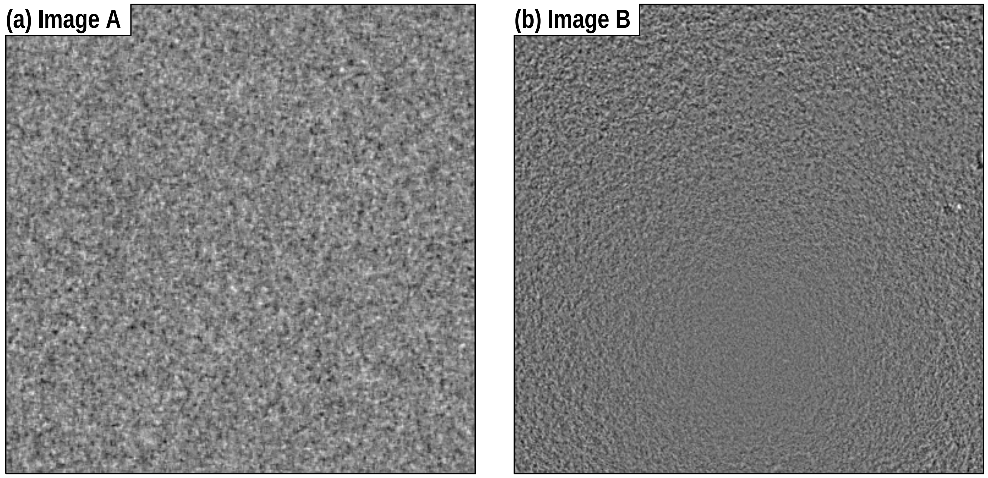

Figure 2.4: Sample images used for the correlation tracking calibration tests: (a) Image A, an image of 100,000 Gaussian structures whose sign, size, height are randomly chosen to approximate the mesogranulation pattern; (b) Image B, a 45°-square image of mesogranulation similar to those analyzed in the next chapter.

e-folding distance σ also chosen to be 8 pixels. Because the overlap between neighboring subimages is small, each of the $48^2 = 2304$ displacements measured by the correlation tracking algorithm at each gridpoint thus serves as a (mostly) independent measurement of the actual shift in each case.

In Figure 2.5 is shown a series of scatter diagrams containing the results of shifting Image A by several amounts in the positive x-direction. In each panel, the optimal displacement $(\delta x, \delta y)$ for each measurement gridpoint is plotted as a point, with the blue cross characterizing a two-dimensional Gaussian fit to the distribution of optimal displacements. The red cross in each panel indicates the amount each image was actually shifted. Comparing the locations of the two crosses therefore yields the systematic error associated with the correlation tracking algorithm, while the arm length of each blue cross, indicating the 2σ width of the Gaussian fit in the x- and y-directions, represents the random error.

As shown in Figure 2.5, we find that for Image A the correlation tracking algo-

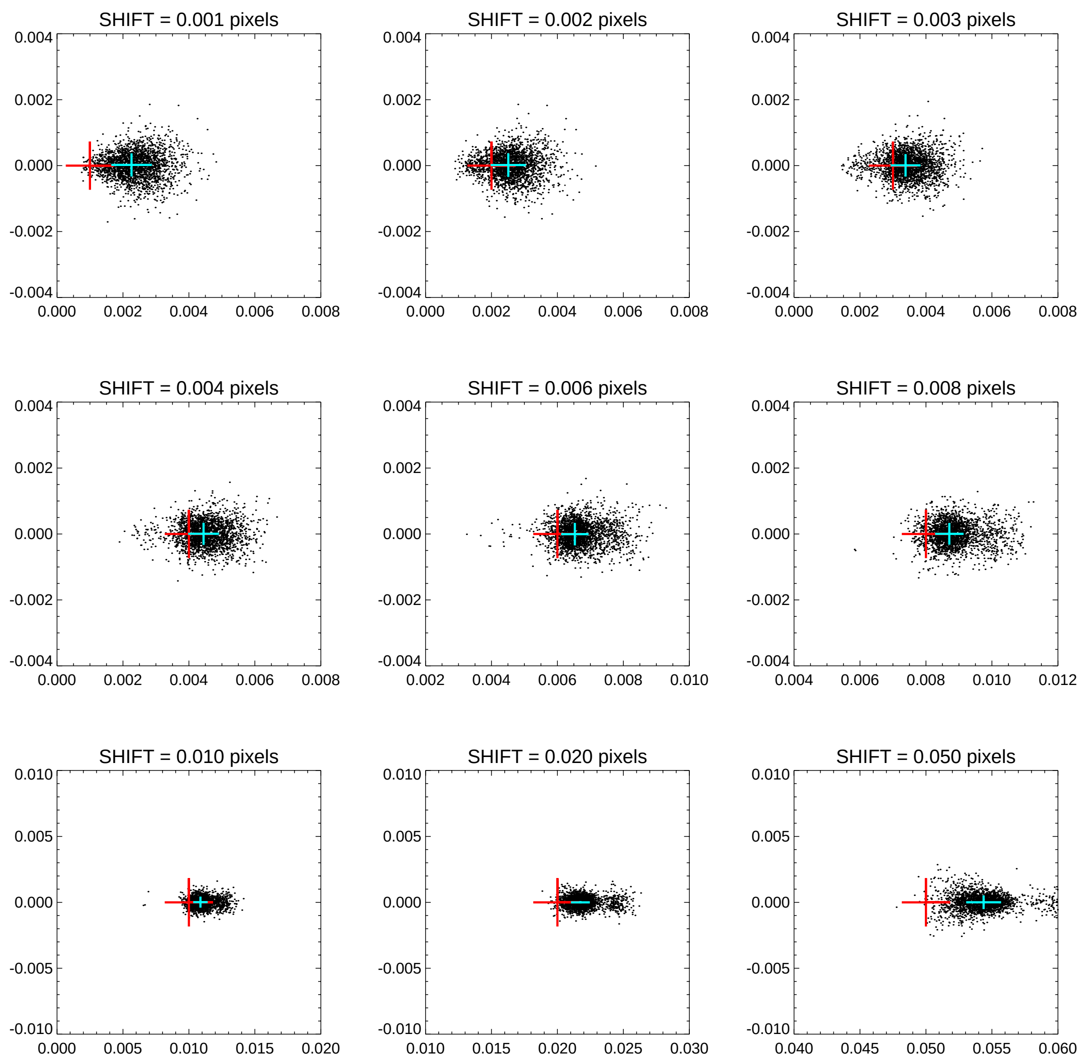

Figure 2.5: Scatter diagrams of the x- and y-displacements computed by applying the correlation tracking technique to Image A (Fig. 2.4a). Each panel contains data from each of nine shifts in the x-directions as indicated on top of each panel. The dots represent the displacement measured by the correlation tracking algorithm for each of the 2304 measurement gridpoints, while the known shift is plotted as a red cross. The blue cross represents a two-dimensional Gaussian fit to the data, with the length of the arms indicating the 2σ level in the x- and y-directions. Note that the overall scales for the images in the bottom row have been broadened.

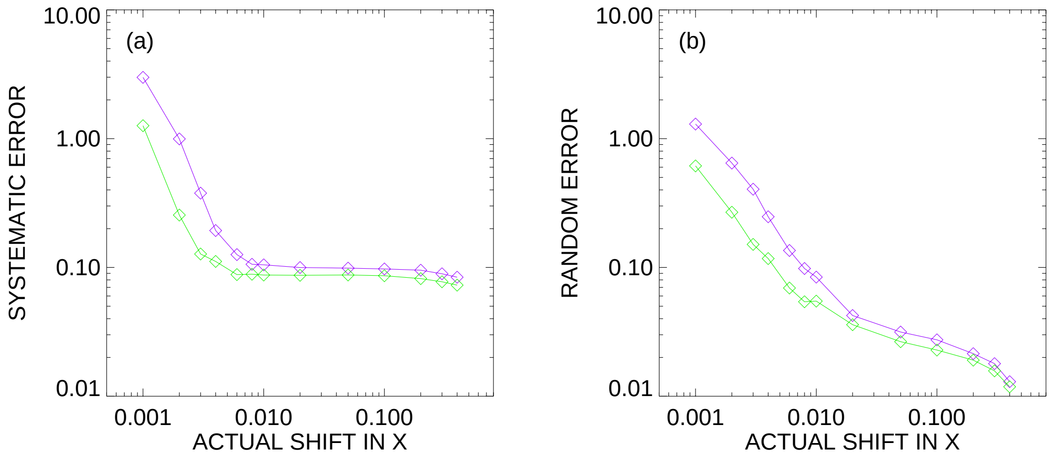

Figure 2.6: Systematic (a) and random (b) errors for the correlation tracking algorithm applied to Images A (*green*) and B (*purple*) of Fig. 2.4.

rithm measures an average shift in the x-direction that is systematically larger than the actual shift, ranging from about 10% for the largest shifts to a factor of 2.5 for the case of the 0.001-pixel shift. These results for Image A are also shown in green in Figure 2.6a, wherein the systematic errors are plotted as a function of the known shift. The ordinate is defined by

$$\text{systematic error} = \frac{\text{measured shift}}{\text{actual shift}} - 1, \tag{2.7}$$

corresponding to the percentage increase of the measured shift relative to the actual shift.

We believe the systematic errors are caused by the difficulty of the algorithm to accurately locate the optimal displacement. As discussed in Appendix A, for each measurement gridpoint (x_n, y_n) the algorithm searches $(\delta x, \delta y)$-space for the displacement which minimizes a merit function $m(\delta x, \delta y)$. This function is equal to the squared difference between two subimages shifted by the relative shift $(\delta x, \delta y)$. If the function m is somewhat lumpy in the area of the global minimum, the algorithm may settle into a local minimum in the vicinity of the global minimum, rather than the global minimum, causing the merit degradation problem described in §A.5. In all nine scatter diagrams, a large fraction (over 90%) of the gridpoints were flagged for merit degradation.

Figure 2.6*b* shows the random error in the x-direction for each measurement, equal to the width of the Gaussian fit in the x-direction divided by the actual shift. We find the random errors of the correlation tracking algorithm are generally smaller than 10% for shifts of 0.005 pixels or larger. This scatter most likely results from inaccuracies in the interpolation scheme used to perform the image shifting. When analyzing real solar data, we find that both spatially and temporally averaging the flow maps until the resulting flows become coherent will attenuate the random error produced by the algorithm. We discuss such averaging further in §3.1. The random errors in the y-direction are less than those in the x-direction, as shown for Image A by the blue crosses in Figure 2.5.

We have performed the same calibration experiments on Image B, containing the solar mesogranulation pattern of Figure 2.4*b*. We find that both the systematic and random errors for Image B are slightly larger than those for Image A, but otherwise shows the same general trends. These errors are plotted in purple in Figure 2.6. We note that the region surrounding disk center of Image B, corresponding to the washed-out area of the image in Figure 2.4*b* just below center, causes a contrast gradient in the mesogranulation pattern that is not present in Image A. This contrast gradient may be the source of an additional source of systematic error seen in the correlation tracking flow maps, as discussed further in §3.1.4.

The results of these simple calibration studies show that correlation tracking can effectively measure the proper motions of moving patterns and features contained in sample images down to displacements of about 0.004 pixels. For shifts of 0.005 pixels and 0.05 pixels, the systematic errors in these correlation tracking measurements are limited to about 10%. The random errors steadily descrease from 10% for a 0.005-

pixel shift to less than 2% for a shift of 0.05 pixels. The high temporal cadence of the time series of solar data permits spatial and temporal averaging which reduces the random noise level below the strength of the coherent signal of interest. In the next chapter, we use the correlation tracking technique to measure the near-surface velocity field experienced by solar mesogranulation.

Chapter 3

THE NATURE OF SOLAR SUPERGRANULATION

We use near-photospheric flow fields to study surface convection on size scales on the order of solar supergranulation and larger. The flow fields are obtained by applying the correlation tracking method described in Chapter 2 to the mesogranulation pattern extracted from time series of MDI velocity images. The time series discussed in this chapter is of a 45°-square region centered on the equator observed from 1999 April 14–20 during the April 1999 Dynamics Campaign of MDI.

We first provide an overview of the flow fields deduced by correlation tracking, and their relation to other determinations of the surface velocity field. An anomalous flow of unknown origin present in the flow fields is also discussed. In §3.2 we provide a more dynamical description of solar supergranulation, before formally characterizing the distributions of supergranular sizes and lifetimes in §3.3. We present in §3.4 the results of our efforts to search for larger-scale flows by applying correlation tracking to the supergranular flow pattern. Finally, we present concluding remarks in §3.5.

3.1 ASSESSING CORRELATION TRACKED FLOW MAPS

3.1.1 Properties of the Flow Maps

As described in §2.2 and §2.3, our dataset is a time series of one corotating region of quiet sun measuring 45° on a side. Each image in the time series was extracted from an MDI full-disk velocity image and remapped onto a latitude-longitude grid with a

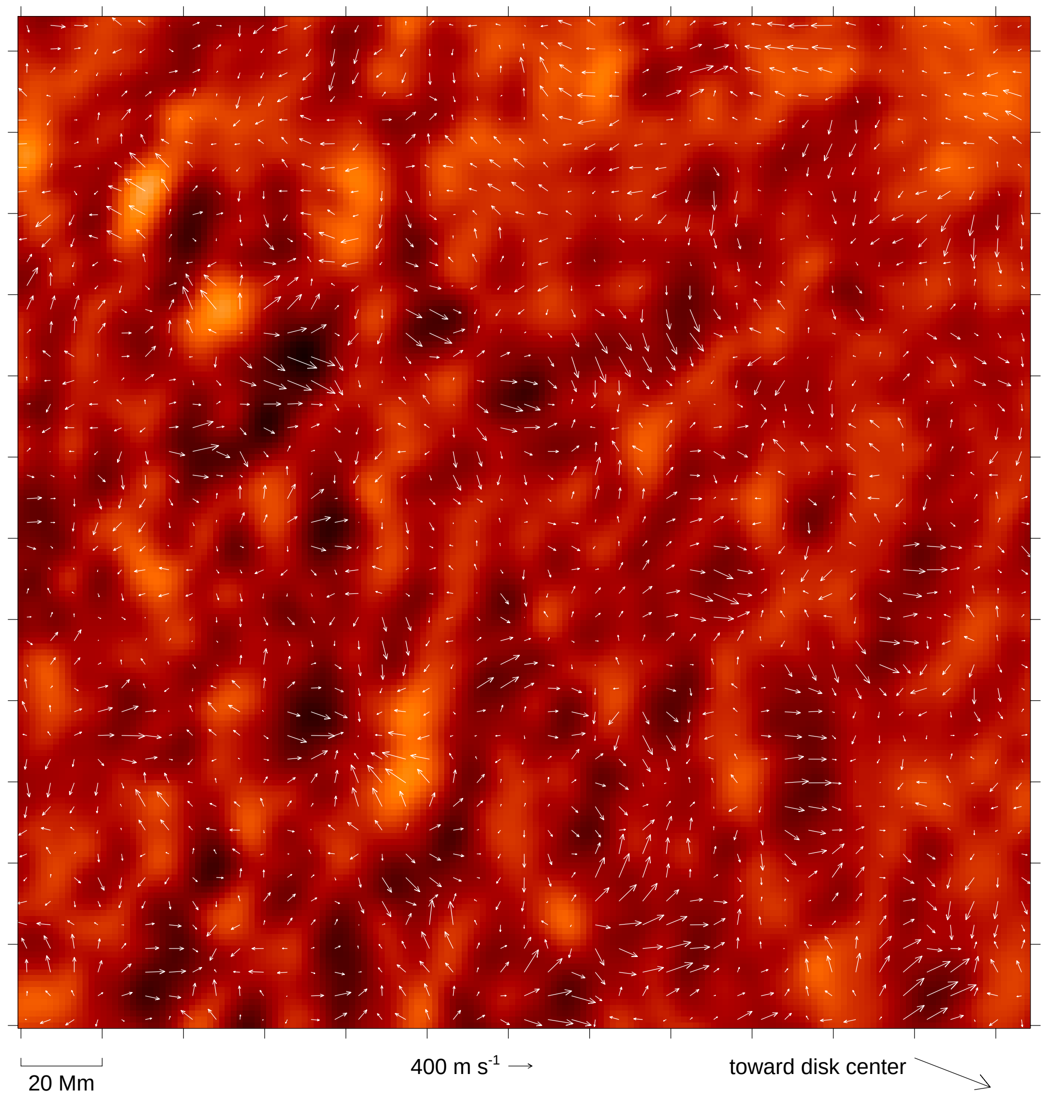

Figure 3.1: A 4-hr averaged flow map, generated by applying correlation tracking methods to a time series of mesogranules, is superposed as a pattern of arrows on the corresponding time-averaged, line-of-sight velocity image. This 20°-square region is centered heliographically on (b, ℓ)=(7.5°N, 30°E), with the direction toward disk center from the center of the image as indicated. The background velocity image has been smoothed in the same manner as Fig. 2.3b to bring out the supergranules, and is scaled to ±500 m s^{-1}, with approaching velocities dark and receding velocities light. The arrow field has an rms velocity of 194 m s^{-1}, and is spatially oversampled by a factor of four relative to the gridpoint neighborhood size σ.

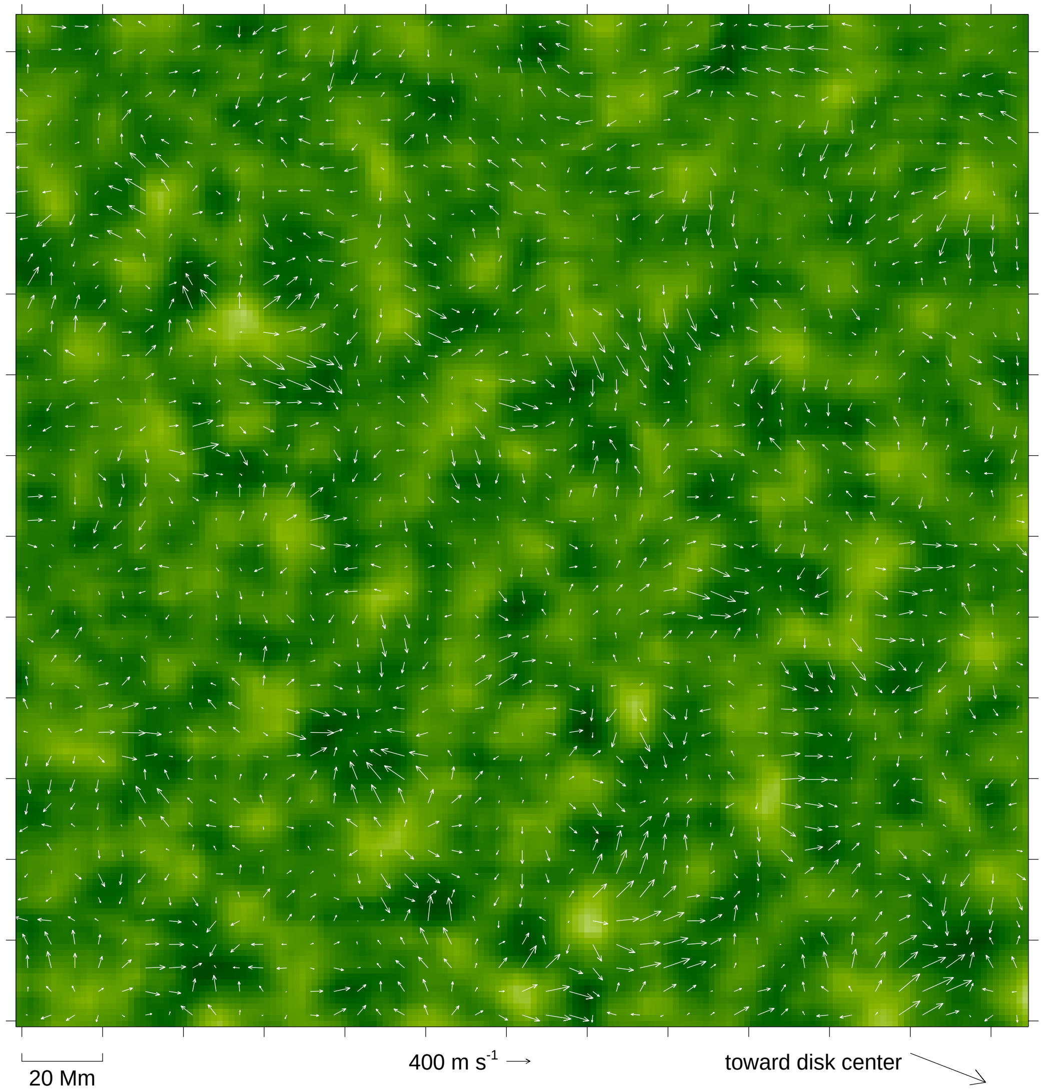

Figure 3.2: The same 4-hr averaged flow map of Fig. 3.1 is superposed on an image of its horizontal divergence. Regions of negative divergence (convergence) are dark and positive divergence light.

pixel spacing of 1.46 Mm in each direction. The temporal cadence of the time series is one minute. The images were then filtered (using a high-pass 7.3 Mm Gaussian kernel) to reveal the mesogranulation pattern, after which the correlation tracking algorithm is applied to obtain a time series of surface flow maps. For this study, we set the size of the measurement gridpoint neighborhood at $\sigma = 8$ pixels or 11.7 Mm (see §2.3 for the formal definition of σ), equal to approximately two mesogranule diameters. The measurement gridpoints are spaced 2 pixels or 2.92 Mm apart, such that the spatial resolution of the flow maps is oversampled by a factor of four in each dimension. The oversampling allows the resulting flow fields to be spatially averaged in order to reduce some of the random noise introduced by the correlation tracking algorithm.

We now examine these correlation tracked flow fields and make comparisons with other horizontal velocity determinations. Figure 3.1 shows a 4-hr averaged flow field, superimposed as a pattern of arrows on the corresponding 4-hr averaged image of line-of-sight velocity that has been smoothed to show only the supergranulation pattern. The flow map contains several prominent outflow sites of diameter 20–30 Mm which coincide with the supergranules evident in the velocity image. Also present are diverging lanes, where fluid motions spread out on either side of an essentially linear feature. These lanes can result from several supergranules packed closely enough such that the spatial resolution of the flow map is insufficient to discern the area of converging fluid in the intercellular region.

Visually studying time series of flow map arrows can be somewhat confusing, so we typically compute the horizontal divergence D of each flow map in our time series and instead analyze time series of the scalar field D. The horizontal divergence D is defined as

$$D(x, y) = \frac{\partial u_x}{\partial x} + \frac{\partial u_y}{\partial y}, \tag{3.1}$$

which is computed directly from the horizontal flow field (u_x, u_y) using second-order finite differences to approximate the spatial derivatives. Individual supergranules, which by definition are cells of horizontal outflow, are consequently identified more easily from images of D than from the preceding flow fields, as such outflow features now appear as local maxima in divergence. The divergence image computed from the flow field of Figure 3.1 is displayed as the background image in Figure 3.2.

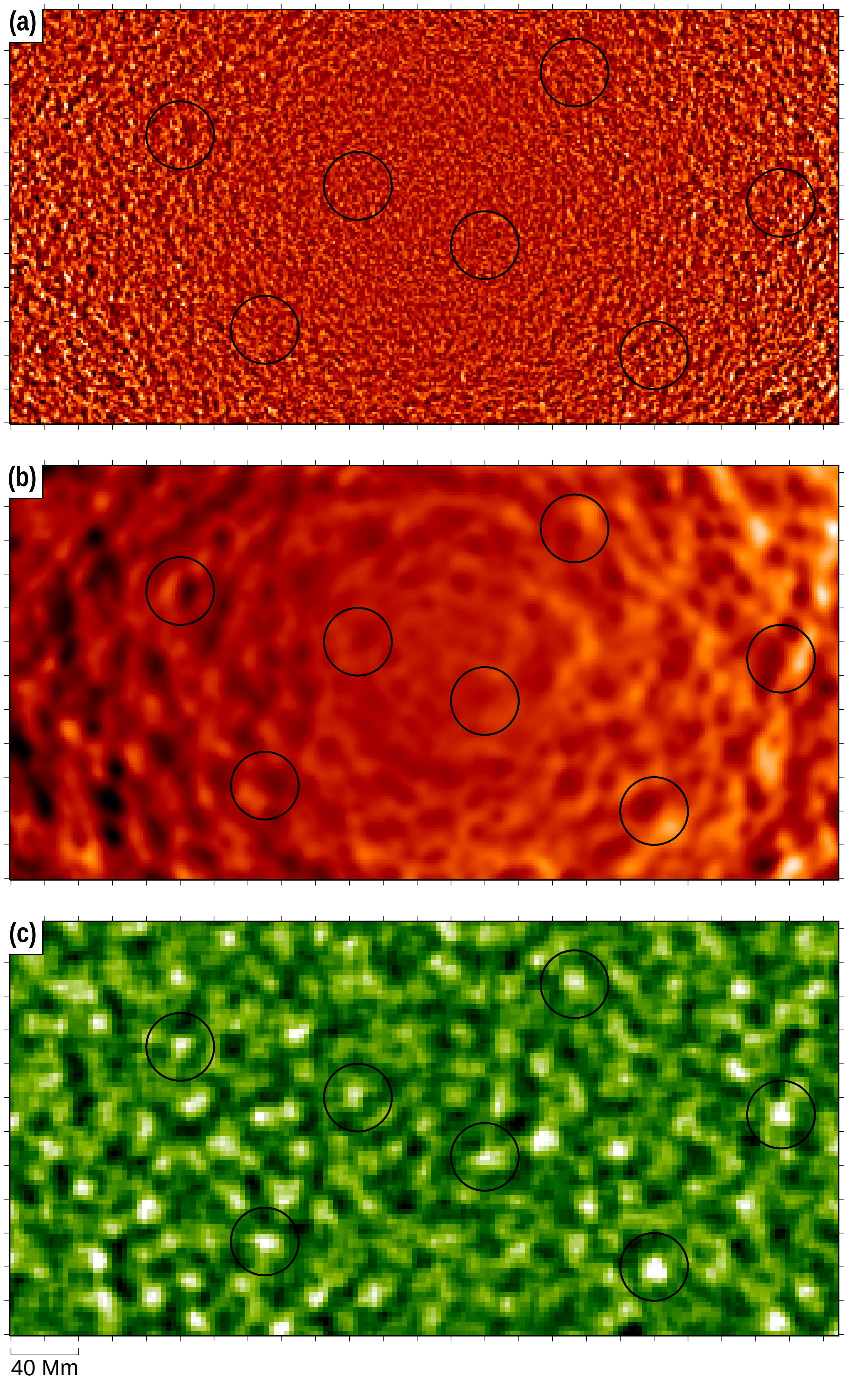

Figure 3.3: A $40^\circ \times 20^\circ$ field of mesogranulation (*a*) and supergranulation (*b*) as seen in images of Doppler velocity, accompanied by the corresponding image of horizontal divergence (*c*) deduced from correlation tracking. All three images are centered on disk center. The locations of several prominent supergranules, most clearly seen in the divergence image, are circled in all three images.

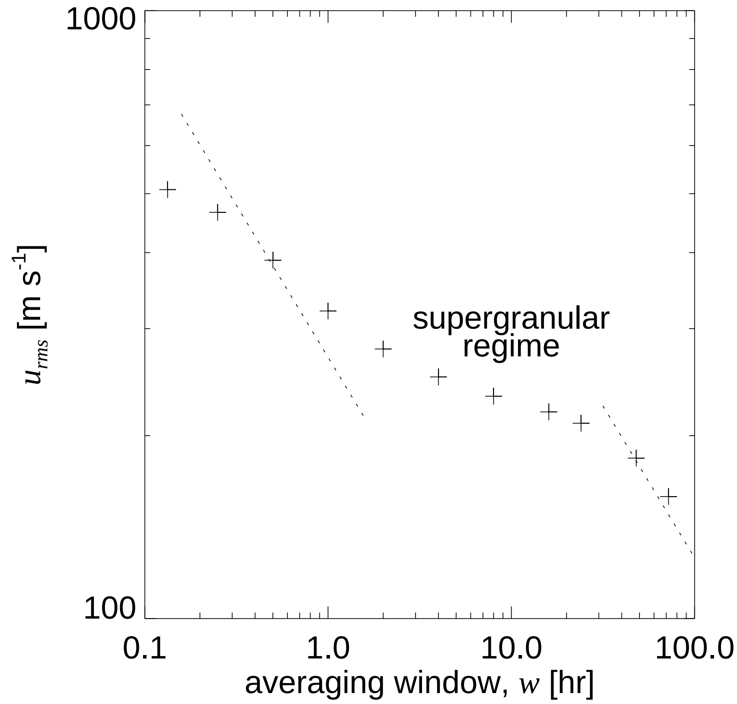

Figure 3.4: The rms velocity u_{rms} as a function of the temporal averaging window w. Temporal averages of random velocity vectors would fall off as $u_{rms} \sim w^{-\frac{1}{2}}$, indicated by the dotted lines. The flatter parts of the spectrum reflect the existence of features with lifetimes of order w. To see the supergranular outflows, we need to average for about 4 hr to obtain a coherent signal.

One advantage of applying correlation tracking to mesogranules is that we can still reliably detect outflows located near disk center where the line-of-sight velocity signal from horizontal fluid motions fades out. Figure 3.3 shows the velocity field in the disk center region for one day in May 1999. The top two panels are Doppler images showing the mesogranulation and supergranulation patterns respectively. One can see that the detection of supergranules directly from the velocity images becomes increasingly more difficult as one approaches the center of the disk due to their lower contrast. While the mesogranules also show lower contrast levels, they remain coherent enough to be recognizable in correlation studies. The bottom panel in Figure 3.3 is an image of horizontal divergence calculated directly from the horizontal flow field deduced from correlation tracking. The locations of several prominent supergranules, as revealed most clearly in the divergence image, are circled in each of the three images.

The flow maps are averaged in time (typically for several hours) so that only the longer-lived flows remain, but also to reduce the random error of the flow maps. One source of random error originates from the algorithm itself, as discussed in §2.3. In calibration tests there, the algorithm is found to have a random noise level of approximately 10% for flows on the order of 100 m s^{-1}; averaging for several hours or more will reduce this error below 1%. In addition to the random noise component, it is not well known how the residual signal originating from granulation pattern manifests itself in the flow fields. With $2''$ pixels, individual granules are at best marginally resolved in our data, though larger resolved structures associated with solar granulation (such as exploding granules) may still be present. We do not filter the data in any way that specifically targets the granulation pattern, though the temporal filtering designed to attenuate the acoustic oscillations also attenuates much of the granulation signal.

Time-averaging will abate the effects of both the residual granulation signal and the algorithmic noise in the velocity images. In Figure 3.4 is plotted the rms velocity as a function of the time-averaging window for a sample time series of flow maps. Flatter regions of this curve indicate that the flow field contains temporally coherent features at those time scales, while the steeper portions of the curve indicate incoherence on those time scales. In this study, an averaging window of at least 4 hr (corresponding to 240 flow maps) is used because much of the random noise present in the data is reduced while preserving the evolution of individual supergranules, a phenomenon we believe occurs on time scales much longer than 4 hr.

3.1.2 Comparison With Direct Doppler Images

To understand how well the flow maps generated by correlation tracking sense the actual horizontal velocity field, we can compare the disk-center-directed component

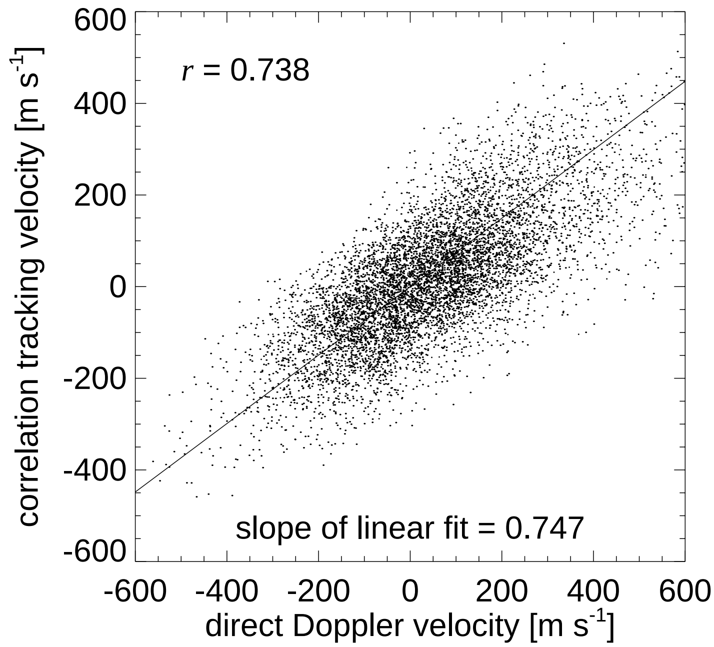

Figure 3.5: A scatter diagram showing the correlation in Fig. 3.1 between the line-of-sight velocity and the disk-center-directed component of the correlation tracking flow field. A linear fit to the data is shown, with its slope indicating that the correlation tracking velocities underrepresent the velocities measured in the velocity image by about 25%.

of each flow vector in the flow maps with its corresponding line-of-sight velocity as measured directly from the velocity image. Using Figure 3.1 as an example, which is centered heliographically at about $(b, \ell)=(7.5°\mathrm{N}, 30°\mathrm{E})$ so that disk center is below and to the right in the figure, we can see how well the two velocity measurements agree.

Figure 3.5 reveals a strong correlation between the disk-center-directed velocities measured by correlation tracking and those in the corresponding velocity image. As seen in Figure 3.1, the strong outflow sites present in the flow map are coincident with the supergranules present in the Doppler image, while other regions of slower mesogranular advection correspond to regions in the velocity images where no organized supergranular outflows exist. The correlation coefficient (defined in Burr 1974, for example) is found to be $r = 0.720$, which quantifies the visual impression that the two velocity measurements agree well.

The line in Figure 3.5 is a linear fit to the data showing the correspondence between the correlation tracking and direct Doppler measurements of velocity. The slope of the line indicates that the velocities derived from the correlation tracking calculation underrepresent the velocities indicated on the velocity image by about 25%. Systematic errors of this order of magnitude should be taken into account when interpreting correlation tracking flow maps.

3.1.3 Comparison With Time-Distance Results

We now describe a study (see also DeRosa, Duvall, & Toomre 2000) where outflow sites detected using our correlation tracking technique are compared to travel-time differences measured by time-distance analysis. This study uses a 2048-min sequence of velocity images observed by MDI using its high-resolution ($0.6''$ pixels) field-of-view taken from 1997 January 16–18.

As stated in §2.1.2, time-distance analysis is performed by computing travel-time differences between counterpropagating waves. Such travel-time differences arise due to the effects of bulk fluid motions on the waves, as the mode frequencies will be Doppler shifted when the waves are propagating upstream or downstream relative to a bulk flow. In this study, we examine the travel-time differences between f modes (gravity waves which propagate along the surface of the sun) traveling toward or away from each measurement location.

The time-distance analysis was performed by first blocking the 2048-min time series into four 512-min sequences. For each block of data, travel-time differences were measured between f modes traveling toward and away from each measurement location. The timing measurements were averaged radially over an annulus with inner and outer radii of 3.72 Mm and 8.67 Mm surrounding each measurement location, and then aver-

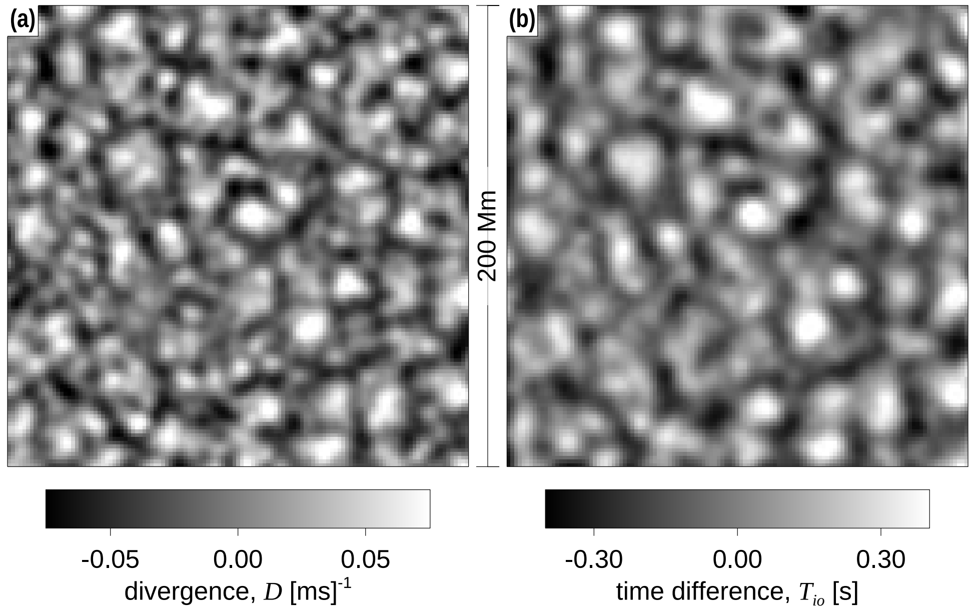

Figure 3.6: Comparison between the correlation tracking and time-distance helioseismology techniques: (a) the image of divergence D calculated from correlation tracking measurements of the near-surface velocity field for one of the 512-min blocks; (b) the image of travel time differences T_{io} measured using time-distance helioseismology for the same block.

aged azimuthally in space to remove all directional dependence. Finally, the data were averaged in time over each 512-min block to increase the signal-to-noise ratio. The end result is a map of travel-time differences $T_{io}(x, y)$ as a function of position, where the subscript "*io*" indicates that the sense of the difference is times from incoming waves minus times from outgoing waves.

As a result of the directional averaging, extrema in T_{io} correspond to locations where the flow is divergent or convergent (such as supergranular outflows or their associated intercellular lanes). For example, maxima in T_{io} indicate places where f modes approaching from any direction, on average, take longer to traverse the same ray path than the corresponding outgoing f modes, signifying a horizontal outflow. Consequently, T_{io} should be proportional to the horizontal divergence D of the near-surface flow field, which can be computed directly using equation (3.1) on correlation tracking flow maps

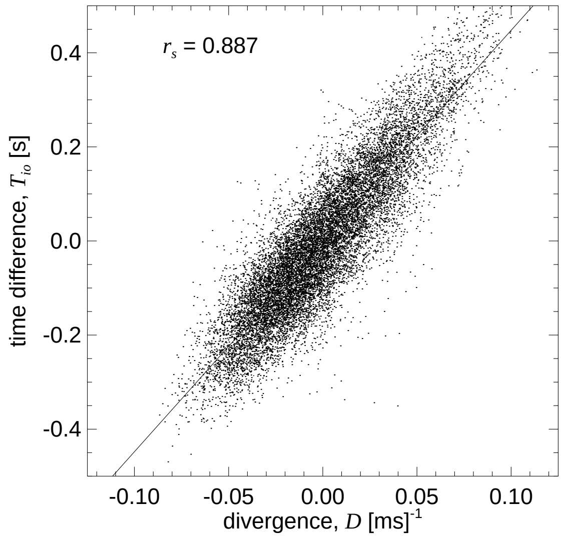

Figure 3.7: Scatter diagram of the travel-time vs. the divergence data shown in Fig. 3.6. The best-fit line, having a vertical intercept and slope of -2.01×10^{-4} and 4.48 respectively, is determined from regression.

derived from the same data.

To test this hypothesis, we compared maps of D and T_{io} for each of the four 512-min blocks of data. Figure 3.6 shows the results for one of the 512-min blocks, after artificially degrading the spatial resolution of the divergence map to match that of the time-distance results. The accompanying scatter diagram of T_{io} vs. D in Figure 3.7 shows the correlation between the two images. The correlation coefficient for this block evaluates to $r = 0.887$, and as averaged over all four blocks becomes $\bar{r} = 0.890$. The statistical interpretation of this result is that 79.2% (equal to $\bar{r}^2$) of the scatter in D and T_{io} can be explained by the fact that a linear relationship exists between the two variables.

This result indicates that the time-distance flow maps, which are sensitive to bulk fluid motions occurring near the solar surface, are proportional to the motions of the

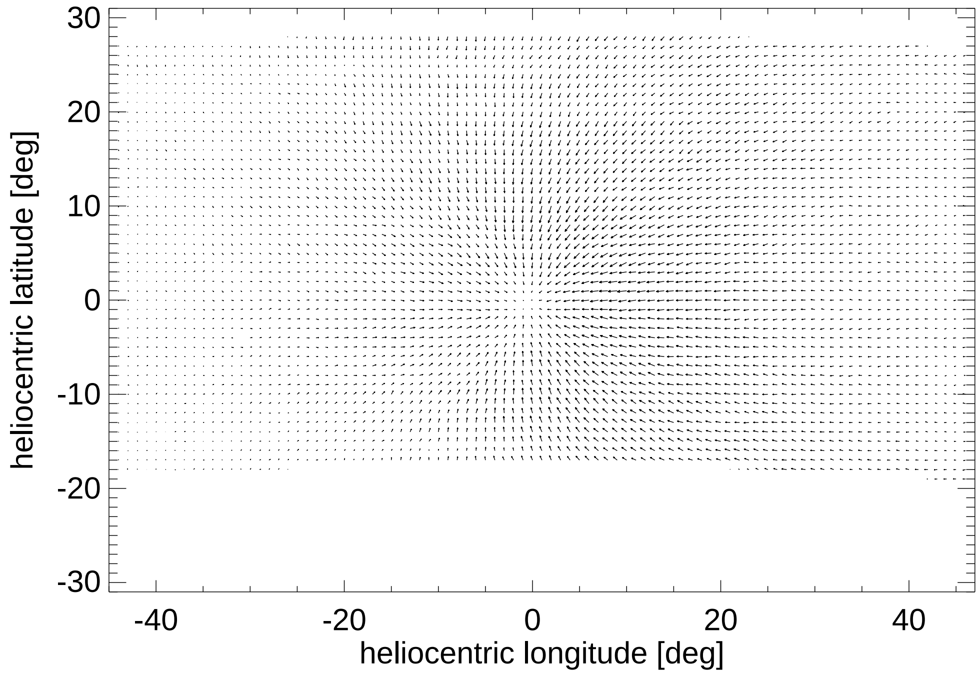

Figure 3.8: Anomalous large-scale flow present in the mesogranulation correlation tracking results, remapped in a heliocentric frame where the disk center point is always placed at the origin. As a result, the April 1999 dataset, which is at fixed heliographic coordinates, rotates from east to west across this coordinate system. The flow map arrows are on the scale of 200 m s^{-1}.

mesogranule pattern velocities, as deduced from correlation tracking. The additional similarity between these flows and those measured directly from Doppler images imply that we can reliably detect fluid motions associated with solar supergranulation using the correlation tracking technique.

3.1.4 The Anomalous Flow Directed Toward Disk Center

We now discuss another source of systematic error associated with the correlation tracking flow maps. When applying correlation tracking to the mesogranular time series observed by the full-disk field-of-view of MDI, we find that superimposed on the supergranular outflow pattern is a larger-scale flow of order 200 m s^{-1} directed everywhere toward disk center (from the vantage point of MDI). To characterize this anomalous flow, we have remapped each flow field in the April 1999 time series onto a heliocentric coordinate system and then averaged in time over the entire dataset. The heliocentric coordinate system is defined such that the origin always coincides with disk center. The time-averaged results are shown in Figure 3.8.

Attempts to discover the origin of this anomalous flow have suggested only that it is a result of the changing contrast gradient of the mesogranular features with heliocentric distance. This contrast gradient is primarily a geometric effect, since the changing viewing angle across the solar disk causes a variation in the amount of the proportion of the horizontal velocity projected into the line-of-sight. It is thought that random noise present in the images coupled with such a contrast gradient produces a non-zero average when the optimal displacement vectors are computed by the correlation tracking algorithm. As a result, this asymmetry introduces a spurious displacement at each measurement gridpoint, thereby biasing the resulting flows in the direction of the asymmetry. Such random variations in the mesogranular data, which we suspect are the cause of the anomalous flow, can result from instrumental noise, unresolved granulation, or even the signal resulting from residual acoustic oscillations.

Several artificial datasets have been constructed in order to study the anomalous flow, but to date we not been able to reproduce the effect. It is also not known whether the spurious velocities are present only using data from the MDI instrument, which is known to be slightly astigmatic, or whether flow maps computed using data from other instruments show the same effect. Flow fields determined by other authors using correlation tracking on data observed by ground-based instruments routinely had their mean flows removed because the pointing of these instruments was not known as precisely as with MDI. The resulting pointing jitter introduces a registration error of an unknown amount between each consecutive image in the time series, which the correlation tracking algorithm subsequently interprets as a real displacement. This effect is not a problem for MDI as its pointing accuracy is much higher than that of ground-based instruments.

Because the magnitude of such an anomalous flow is approximately the same order of magnitude as the supergranular outflows, it makes analysis of the flow maps more difficult. However, because the spatial scale of the anomalous flow is much larger than that of the supergranulation pattern, we typically remove the empirically determined average of Figure 3.8 from our flow fields, which adequately reduces this level of systematic error below the supergranular outflow signal. The flow fields shown in Figures 3.1 and 3.2 have had such an average removed. The anomalous flow is also present in flow maps calculated using the high-resolution field-of-view of MDI, which were used to perform the comparison with the time-distance results. However, the smaller pixel size of the high-resolution data allows us to use a smaller gridpoint neighborhood size σ when applying the correlation tracking method, which reduce the contrast gradient across each measurement gridpoint cell. As a result, the anomalous flow magnitudes are proportionally smaller.

In spite of the anomalous flow, we believe that correlation tracking is an effective method of deducing the locations of supergranular outflows from time series of line-of-sight velocity images. We are able to measure both components of the horizontal velocity field across most of the disk, including the disk-center region where horizontal velocities cannot be measured directly. We have also shown that our flow maps compare favorably with direct Doppler and time-distance measurements of the near-surface horizontal velocity field. We now use the flow maps determined by correlation tracking to examine the dynamics of the supergranular flow field in more detail, both qualitatively in the next section and quantitatively in §3.3.

3.2 A DYNAMICAL PICTURE OF SUPERGRANULATION

The flow maps determined from this dataset, consisting of about six days of data, represent the longest uninterrupted time series of solar supergranulation to date. The 4-hr temporal cadence allows us to study the evolution of supergranular flows with unprecedented temporal resolution. Since supergranules are primarily defined by their velocity structure, one way to examine these outflow patterns is by placing passive floaters ("corks") in our horizontal flow fields and observing their motions in response.

Figure 3.9 shows a time series of horizontal divergence images, computed from correlation tracked flow fields of the April 1999 dataset. Cork locations as a function of time are overplotted in red as they are advected horizontally by the evolving flow field. Initially, the corks are distributed uniformly across the field-of-view. However, on time scales of about 8–12 hr, the corks within each supergranule are advected away from the cell centers at speeds of about 500 m s^{-1} toward lanes of convergence which occur where neighboring outflows meet. This cleaning-out process is illustrated in the top row of images in Figure 3.9, where most corks in the field have reached the nearest convergence lane within 12 hr. Collectively, these corks trace out a network defining supergranule boundaries, or in some cases, the corks outline regions of the flow field containing several supergranules. Once within a convergence lane, the corks begin to travel along the lanes at much slower speeds toward collection points in the network. The effect of this slower migration toward network interstices is evident in Figure 3.9, where by the end of the time series the connected network present at the $t = 12$ hr mark has split into multiple fragments each containing corks approaching their respective collection points. Note that the corks are permitted to coincide, accounting for the (false) impression that the total number of corks in the figure decreases with time.

While the corks are approaching the collection points, the flow field continues to evolve. Occasionally, a new supergranular outflow emerges at a location which was

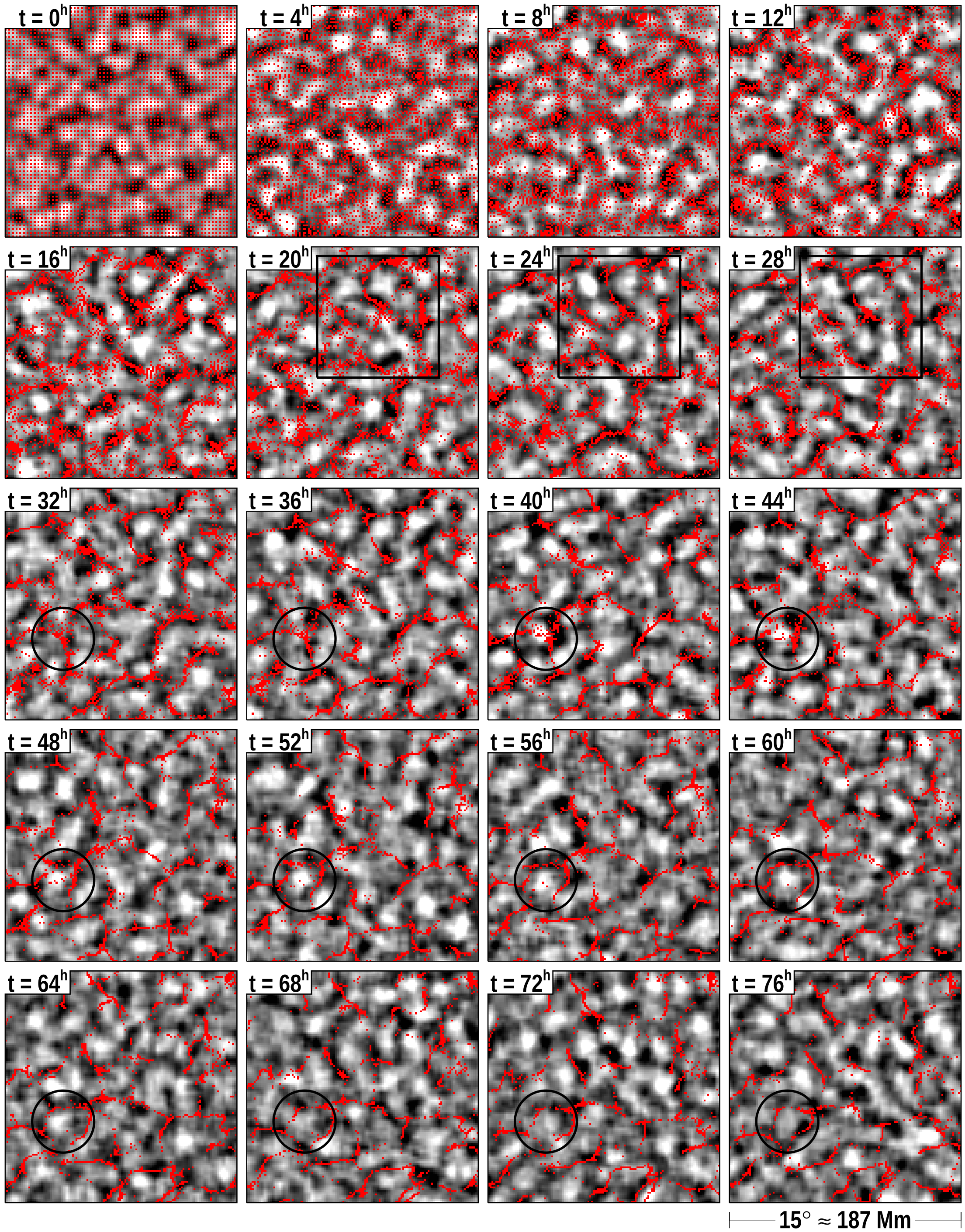

Figure 3.9: A 15°-square region from the April 1999 dataset showing cork locations (*red*) superimposed on the corresponding horizontal divergence images (*gray scale*). The corks are first advected toward cell boundaries on time scales of 12 hr, after which they travel toward boundary intersections on longer time scales. The regions enclosed in the circle show the emergence of a long-lived supergranule which suddenly appears at one of the network intersections. The boxed regions are enlarged in Fig. 3.12.

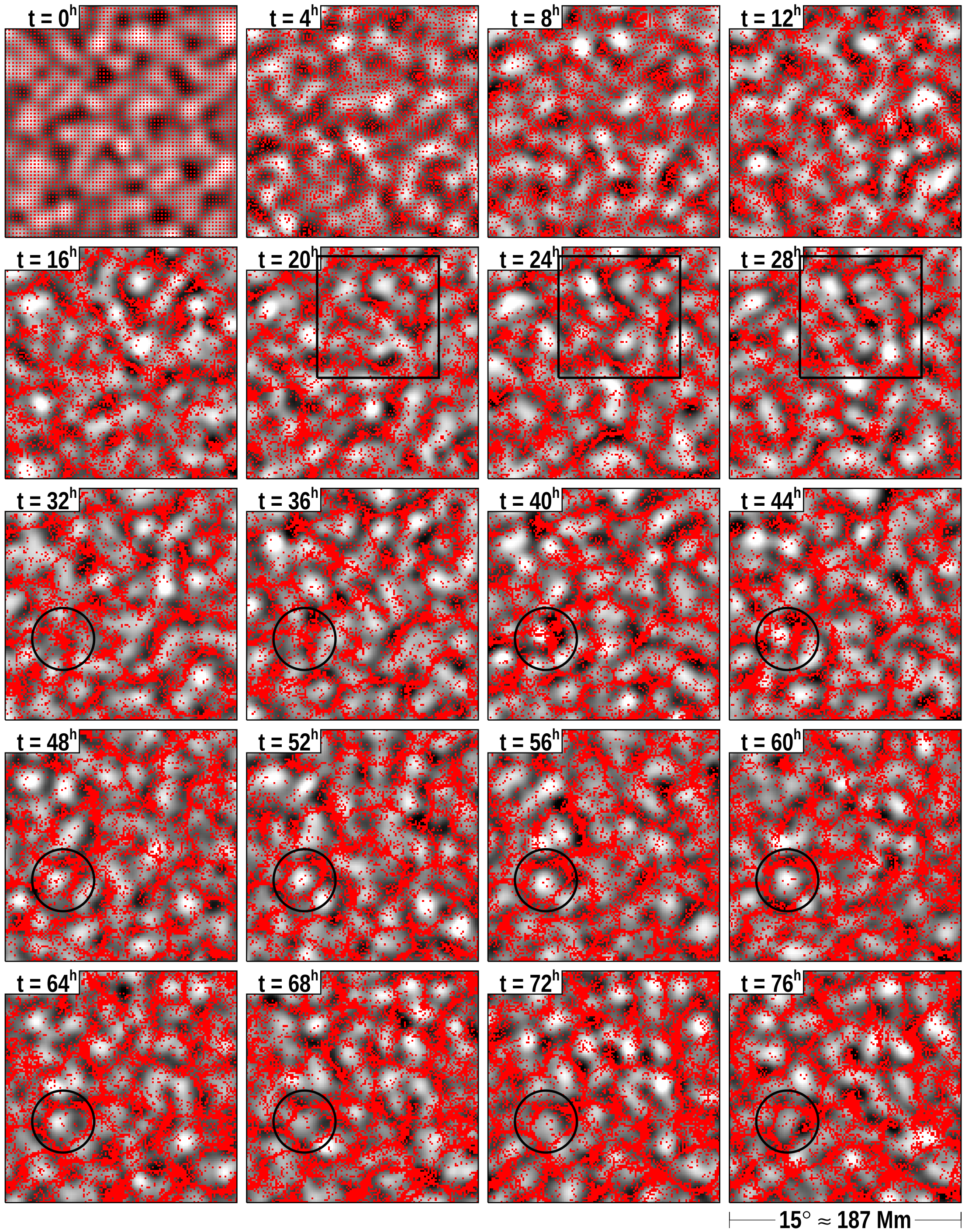

Figure 3.10: The same time series as in Fig. 3.9, but here additional corks have been added at random locations with time, emphasizing the newly formed convergence lanes which have appeared after the initial 12-hr clean-out time. The time series continues in Fig. 3.11, where the supergranule in the circle can be seen to survive for about two days. The boxed regions are enlarged in Fig. 3.12.

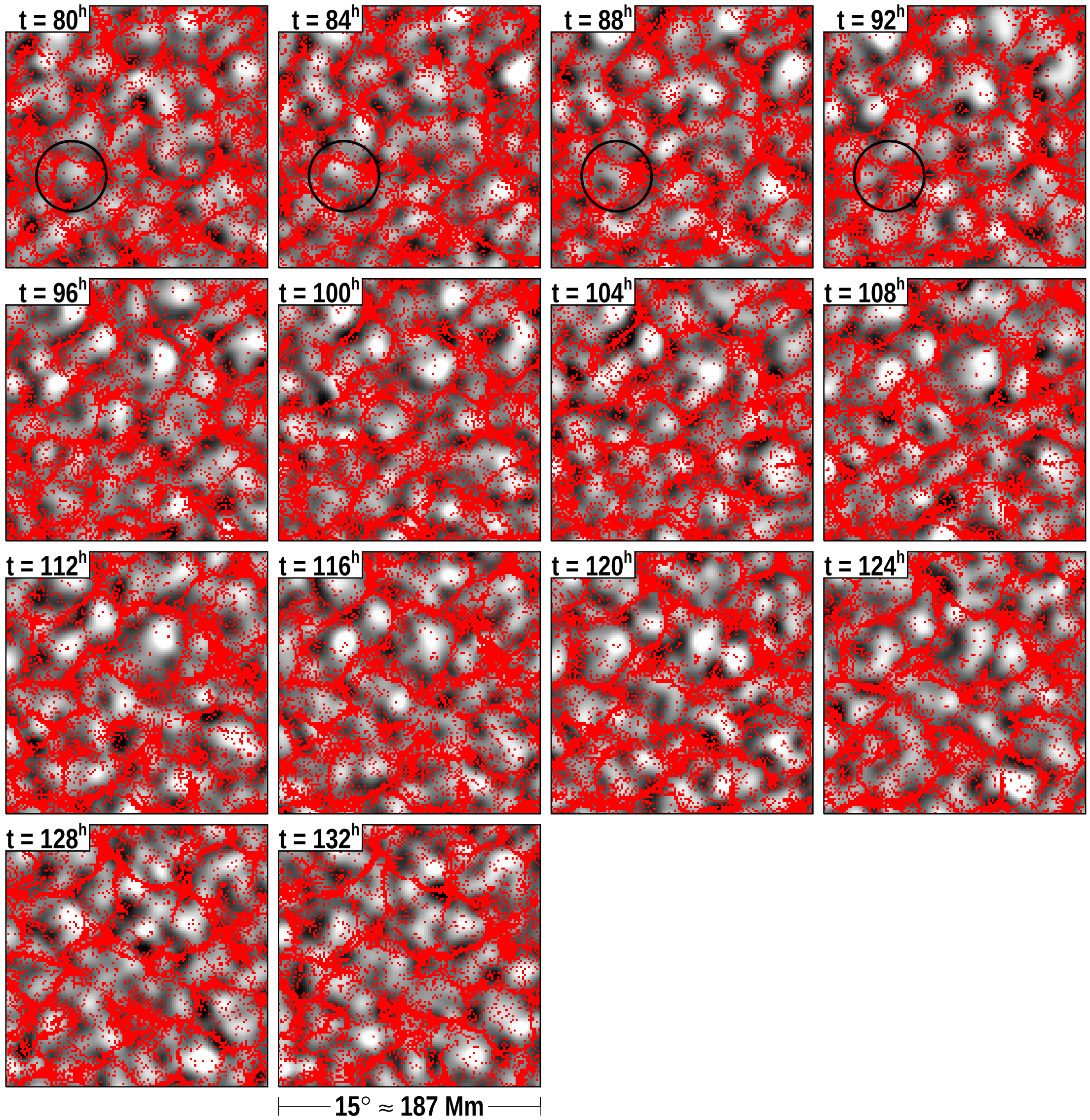

Figure 3.11: A continuation of the time series of Fig. 3.10.

formerly part of the network, as in the circled regions of Figure 3.9. At $t = 36$ hr, the corks in the circled region trace out a portion of the network where three lanes intersect. Four hours later, a new supergranule appears, as indicated by the bright spot in the divergence image. Over the following 12 hr, the corks are advected away from this new outflow center until they reach the edge of the emergent supergranule.

New supergranules appearing via such emergence events are less common than

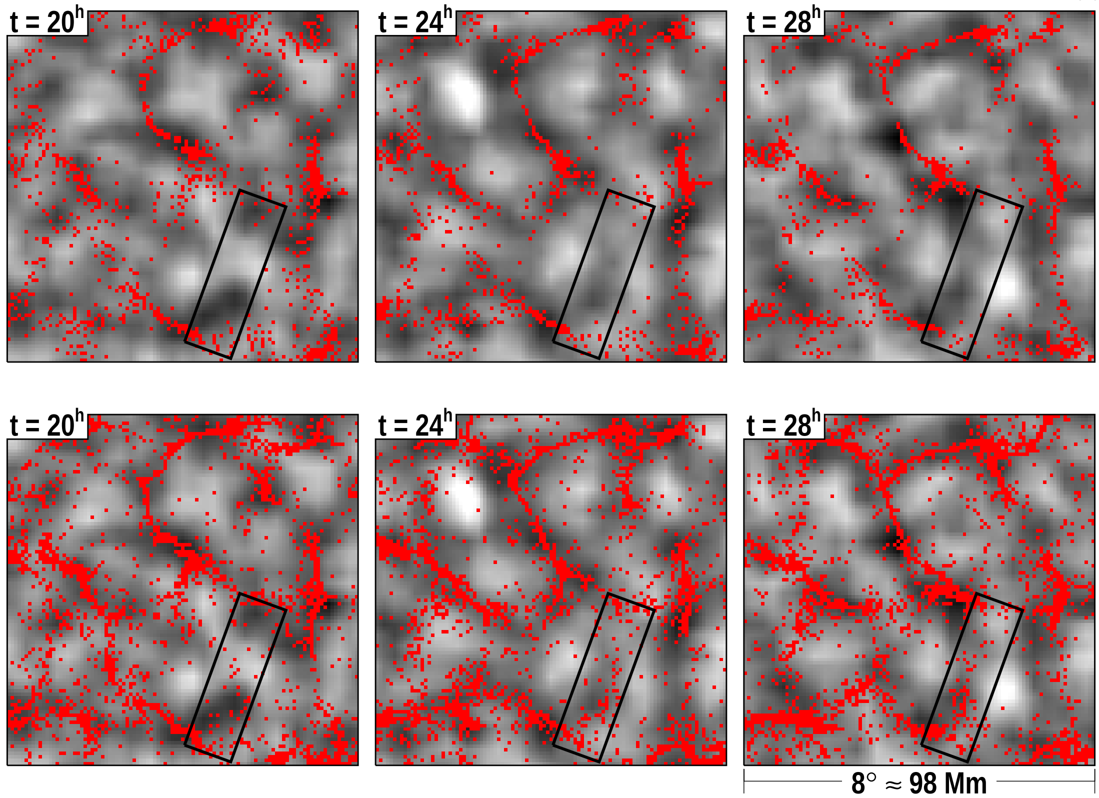

Figure 3.12: A comparison between the cork movies of Figs. 3.9 (*top row*) and 3.10 (*bottom row*) showing the different cork responses to the formation of a new convergence lane (*black box*). By adding corks continuously throughout the time series in the lower sequence, convergence lanes which form after the initial 12-hr clean-out time become populated with corks, whereas these lanes appear free of corks when additional corks are not added, as in the upper sequence. The panels here correspond to the regions enclosed in the square boxes of Figs. 3.9 and 3.10.

those that result from the fragmentation of existing supergranules into multiple cells, as new convergence lanes are continually forming within existing supergranular outflows. These new lanes would not be populated by corks if they were to form after the initial 12-hr cleaning-out period, as no corks remain within the adjoining outflow cells to populate the newly formed convergence lanes. To remove this dependence on the initial time at which the corks are placed into the flow field, we have adopted the approach of placing additional corks at random locations continually throughout the time series,

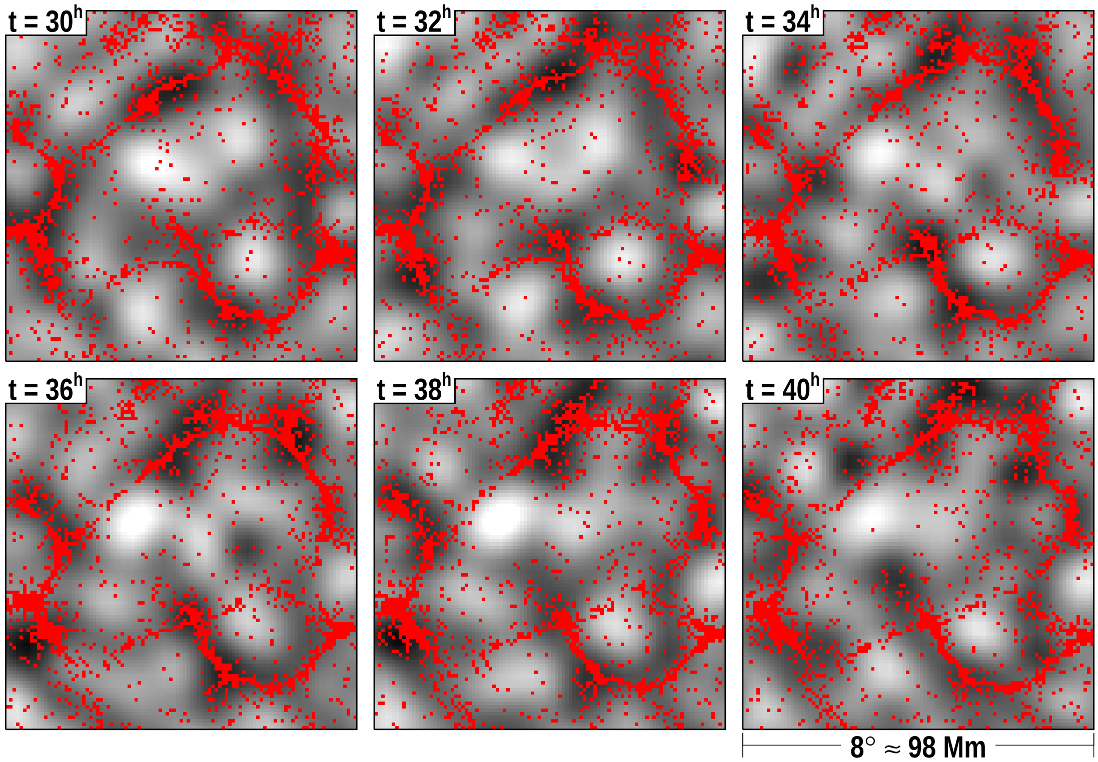

Figure 3.13: A time series showing a large cell outlined by corks which contains several smaller coutflow centers which evolve on time scales of several hours. These smaller outflows are separated by weaker convergence lanes which do not exist long enough to get populated by corks. For this time series, corks were continually introduced into the flow field.

as illustrated by Figures 3.10 and 3.11. There, we show the same time series as in Figure 3.9, except that additional corks are introduced at a rate such that the number of new corks introduced over each 6-hr interval is equal to the number of corks present initially. These added corks serve to outline convergence lanes formed after the initial 12-hr cleaning-out period, as illustrated in the close-up images of Figure 3.12.

From Figures 3.9–3.12 it is evident that some of the regions surrounded by the cork boundaries contain several peaks in divergence separated by weaker convergence lanes. Both the weaker lanes and associated outflow centers typically evolve on time scales much shorter than the 12 hr it takes the flow to clean out corks in any individual

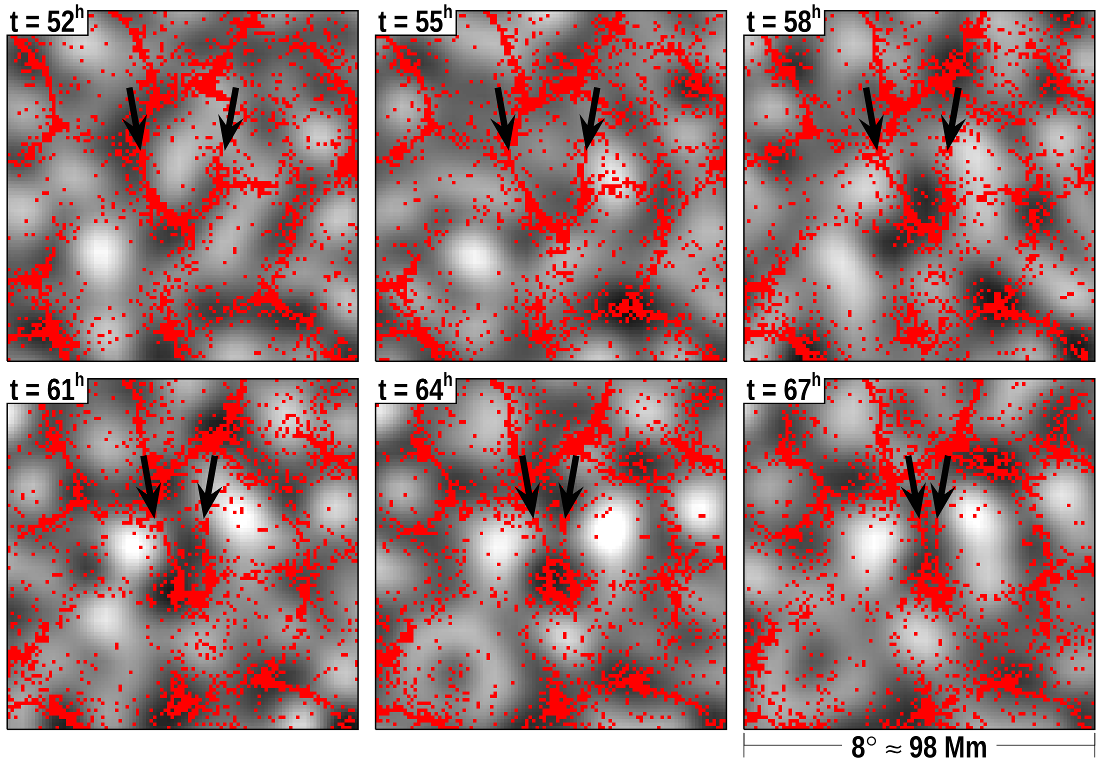

Figure 3.14: A time series showing two convergence lanes (indicated by the arrows) which are advected horizontally by the evolving flow field. For this time series, corks were continually introduced into the flow field.

cell, and are often intermittent in nature. A weak convergence lane may, for example, either become more established or disappear completely, and in the process undergo several weakenings and strengthenings. Such evolution is evident in Figure 3.13, where we show a large structure outlined by corks containing several smaller outflow centers. Consequently, if one considers the network of all convergence lanes, both weak and strong, as defining supergranular boundaries, then the typical sizes and lifetimes of supergranulation are much smaller and much shorter than the cork network would suggest.

If a convergence lane becomes strong relative to its neighboring outflow cells, it will generally persist until a stronger feature appears nearby. Figure 3.14 shows a pair of

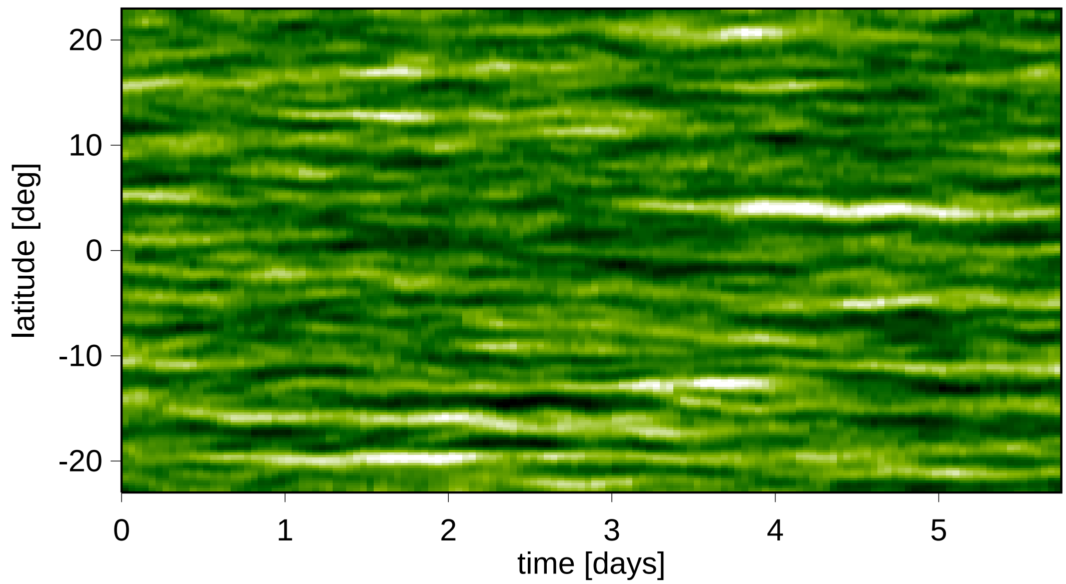

Figure 3.15: A space-time cut across 45° of latitude of horizontal divergence for the April 1999 dataset. Horizontal structures represent persistent outflow cells, with their lengths proportional to their lifetimes.

outflow lanes which are advected horizontally in response to strengthening supergranules in the surrounding region. In the first panel, arrows indicate two existing convergence lanes which partially enclose a supergranule. As this supergranule weakens, two stronger supergranules emerge on either side, whose outflows cause the two convergence lanes to move laterally in response until the original cell vanishes.

Such dynamic behavior, including the emergence, fragmentation, and lane advection events described above, is prevalent in the supergranular flow fields deduced by correlation tracking. The flow field also contains many outflow cells which survive for several days and coexist with other more quickly evolving outflows. For example, the cell circled in Figures 3.10 and 3.11 survives for about two days. We also show in Figure 3.15 a space-time cut of horizontal divergence extracted from the same dataset. The bright horizontal structures represent outflow cells which persist at the same location, with the lengths of such structures indicative of their lifetimes. It is evident that outflow cells with lifetimes of at least 36 hr are plentiful, accompanied by other outflow cells having much shorter lifetimes.

Throughout this section, we have illustrated several modes of evolution associated with supergranular outflows detected at the solar surface, including instances of cell emergence, merging, and fragmentation. The associated network of convergence lanes also changes constantly, as the network continually reorganizes itself in response to nearby evolving outflows as well as to the turbulent motions occurring beneath the surface. In addition to the regions where the flow pattern evolves quickly, we also find features which persist for much longer time periods. In the next section, we substantiate the qualitative impressions described here by measuring the distribution of supergranular cell sizes and lifetimes after identifying individual outflows on our flow maps.

3.3 MEASURING SUPERGRANULAR SIZES AND LIFETIMES

3.3.1 Correlation Sizes and Lifetimes

The classical technique for measuring supergranular properties involves computing spatial and temporal correlation functions of photospheric and chromospheric data. Separations between the maxima of spatial correlation functions yield an average separation of the supergranules evident in the data. Using line-of-sight velocity images, the average separation between supergranular cell centers is 32 Mm, as originally found by Leighton et al. (1962) and Simon & Leighton (1964) and confirmed by several later studies (e.g. Wang & Zirin 1989).

Such correlation analyses can also be applied to quiet-sun images of surface magnetic flux, which effectively outline supergranular boundaries, since small-scale concentrations of magnetism visible at the photosphere are quickly advected horizontally by supergranular outflows (Schrijver et al. 1997; Hagenaar et al. 1999; Lisle et al. 2000). This network has been observed in the chromosphere using emission in Ca II K as a proxy for magnetic field. Correlation studies of this chromospheric network yield average cell sizes of 30–35 Mm (Simon & Leighton 1964; Singh & Bappu 1981; Hagenaar et al. 1997) in agreement with the measurements of supergranular cell sizes derived from velocity images.

Spatial correlation and power spectral analyses applied to high resolution horizontal flow maps by November (1994) also give a horizontal length scale of 32 Mm for supergranulation, but these and other more recent flow map studies (e.g. Shine et al. 2000) show that most supergranules contain several smaller divergence centers having an average separation of about 7 Mm, consistent with mesogranular separation distances. The correlation tracked flow maps of this study also show large outflow cells containing smaller divergence centers, confirming the impression that broad outflows associated with supergranulation are comprised of several smaller divergence centers.

Cell lifetimes can also be determined by computing temporal correlation functions among successive images in a time series. The rate at which the function declines from its central maximum yields a measurement of the average lifetime of the supergranules in the field of view. Simon & Leighton (1964) were able to measure the average cell lifetime of the Ca II K network cells to be 20 hr, equal to the length of time required for temporal correlations of successive images to drop by a factor of e^{-1} from its initial value. However, Wang & Zirin (1989) argue that proper motions and evolutionary changes in individual supergranules in the field of view may bias the correlation lifetime toward shorter values, due to the possibility that supergranules may alter their appearance or location without losing their identity, and thus the actual supergranular lifetime may be even longer than 20 hr. These effects occur on shorter time scales than typical supergranular lifetimes, and are also reflected in the shape of the temporal correlation function. Indeed, we have already demonstrated the existence of several supergranules having lifetime of at least 36 hr (e.g. in Fig. 3.15) in our data.

3.3.2 The Direct Identification Method

While correlation and power spectral analysis methods are useful for obtaining a general idea of supergranular cell sizes and lifetimes, we propose that measurements of such quantities should take into account the more complex phenomenology by which individual supergranules form and evolve. Events similar to those described in §3.2, where supergranular cells frequently merge and fragment, are observed to occur much more frequently than cases where individual supergranules simply emerge, persist, and disappear all without interacting with other outflow cells. In order to account for such intricate evolutionary behavior, we have devised a pattern recognition algorithm that identifies the outflow centers on each divergence image in our time series, from which the detailed life histories of all supergranules in the dataset can be determined. This information is then used to compile a statistical database of the sizes and lifetimes of all supergranules present in the April 1999 dataset.

Before identifying the supergranules, we attenuate the random noise in the divergence data by applying selected spatial and temporal filters. The data are averaged in time using boxcar filters with widths Δt of 4 hr, 6 hr, and 8 hr, and using spatial smoothing using Gaussian kernels with widths w of 5.8 Mm, 8.8 Mm, and 14.6 Mm. Such filtering operations are generally consistent with the effective spatial and temporal resolution of the data, so we do not believe the filtering causes much loss of information. We realize that such filtering will sometimes artificially blur together some of the distinct objects we seek to identify, and as a result we assess the effects such filtering may have on the resulting size and lifetime distributions in what follows.

On each filtered divergence image, we identify *supergranular outflow cores*, defined mathematically as a contiguous grouping of pixels for which the local curvature (i.e. second derivative) of divergence in all horizontal directions is negative. By this definition, the pixels comprising each outflow core contain exactly one local maximum in divergence. The identity of individual objects is established by matching outflow cores which fully or partially overlap on successive images. To be considered supergranules, the cores must cover at least 50 Mm^2 in area (equal to 6 pixels) and survive for at least 4 hr, thresholds which are consistent with the effective spatial and temporal resolution of the data.

Figure 3.16 shows both the flow field and the corresponding outflow cores. The full 45°-square field from which the figure originates contains approximately 400 outflow cores, and by implication the same number of supergranules. The cores cover about 20% of the total area of the image, so that the full area of each supergranule is approximately five times that of its corresponding outflow core, assuming the supergranular pattern fills the available area. When tabulating the areas of individual supergranules below, we multiply the core sizes by the appropriate filling factor, determined by comparing the area covered by the cores to the total area in the field.

To further illustrate the core identification scheme, we now show in Figures 3.17 and 3.18 the evolving cork network (colored red) of Figures 3.10 and 3.11, except that the divergence images have been replaced by colored tiles representing the outflow cores. Each core is assigned a solid color (other than red) at random for as long as it is continuously recognizable on successive images. We find that the core identification scheme performs quite well, as most regions outlined by the corks contain objects, and objects which overlap in subsequent images have been assigned the same color. The black object circled in Figures 3.17 and 3.18, for example, retains its identity for about 48 hr until it disappears.

In the cases where objects merge or split, the largest fragment is chosen to retain the identity of the outflow core. Such a process is illustrated in Figure 3.19, where the two fragments inside the circle merge together for a short time and then split up again. After the cells have merged, at $t = 36$ hr one large cell (colored purple) exists at the location previously occupied by two smaller cells. The large cell retains the color of the

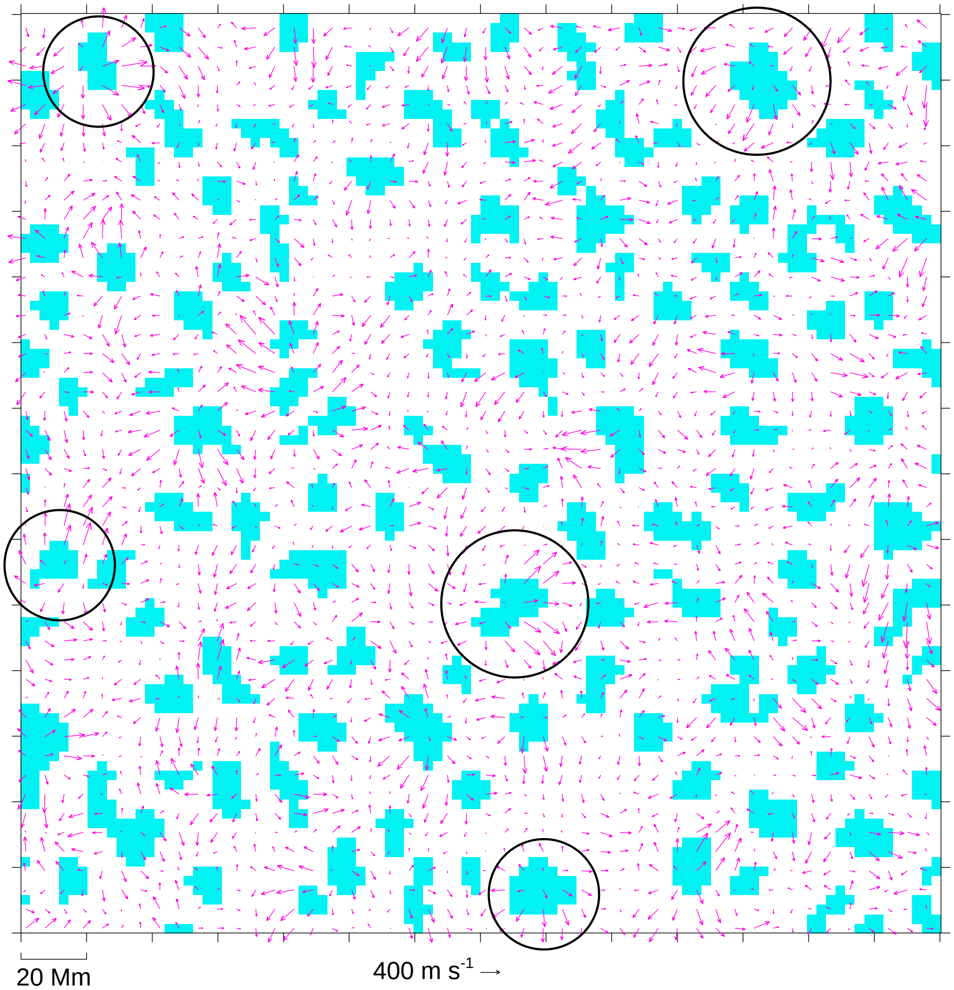

Figure 3.16: A 23°-square field of supergranule outflow cores (*blue*), with the corresponding averaged flow field (*red arrows*) overlaid. Each outflow core is represented by a contiguous group of pixels. Several prominent supergranules possessing well defined outflows are circled. The arrow scale is 400 m s^{-1}, the tick marks are spaced 20 Mm apart, and the field is approximately 23° square. The data were filtered using 2-hr temporal boxcar and 8.8-Mm spatial Gaussian smoothing functions prior to the identification of the outflow cores. The field is centered in space at (b, ℓ)=(12°N, 38°E) and in time at 11$^{\mathrm{h}}$00$^{\mathrm{m}}$ on 14 Apr 1999.

largest of the two fragments which merged together. After 8 hr have elapsed, the large cell splits back into two smaller cells. Again, the largest fragment retains the identity of the original cell. The other (smaller) fragment is assigned a new identity and color.

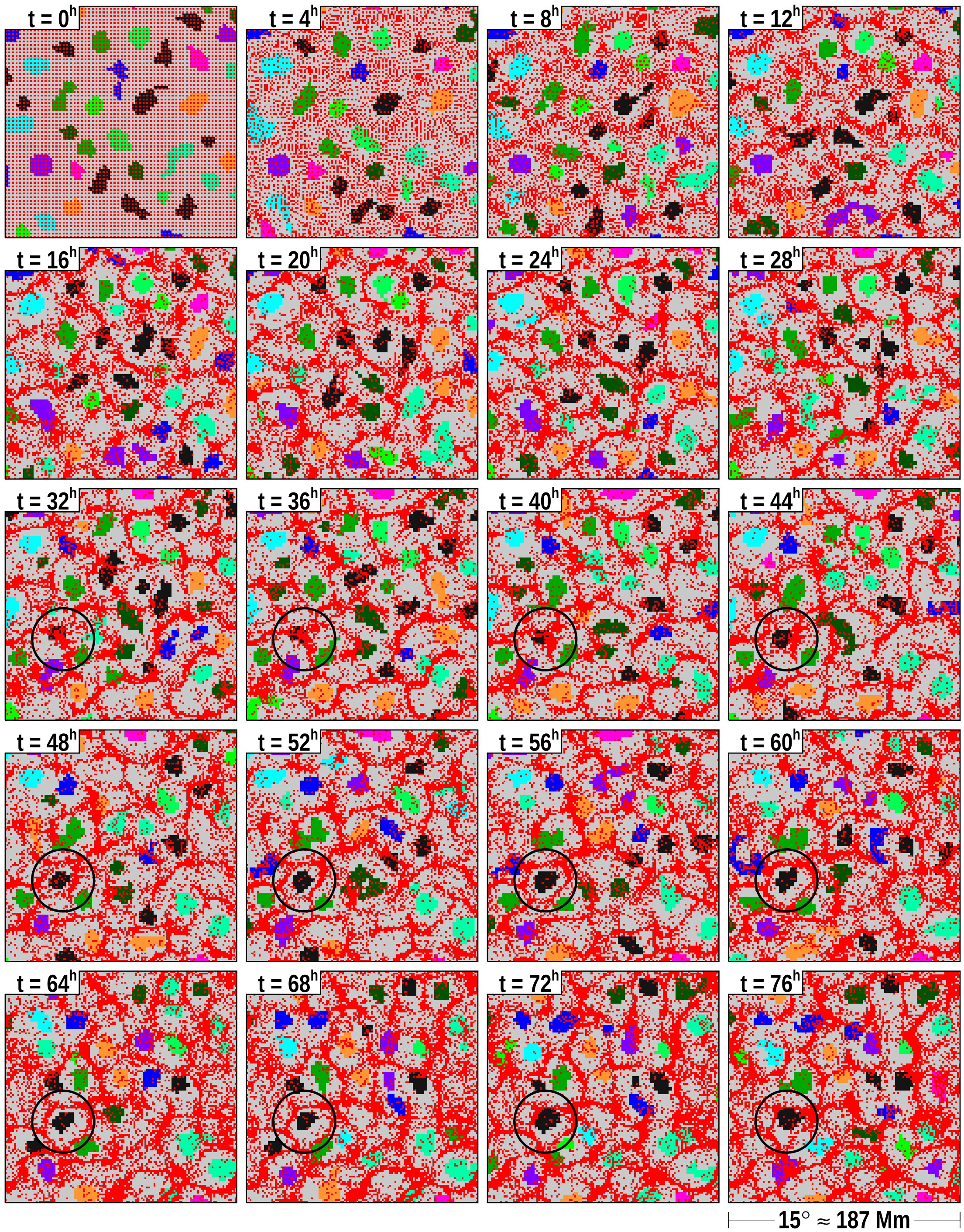

Figure 3.17: A time series of cork positions (*red*) relative to the outflow cores (*colored tiles*). Outflow cores recognizable on successive images are assigned the same solid color throughout their lifetime; however, the colors are chosen randomly, making it possible for different objects to have the same color. The time series shown here and continued in Fig. 3.18 is the same as in Figs. 3.10 and 3.11. The long-lived object enclosed in the circle is the same as identified in Figs. 3.10 and 3.11.

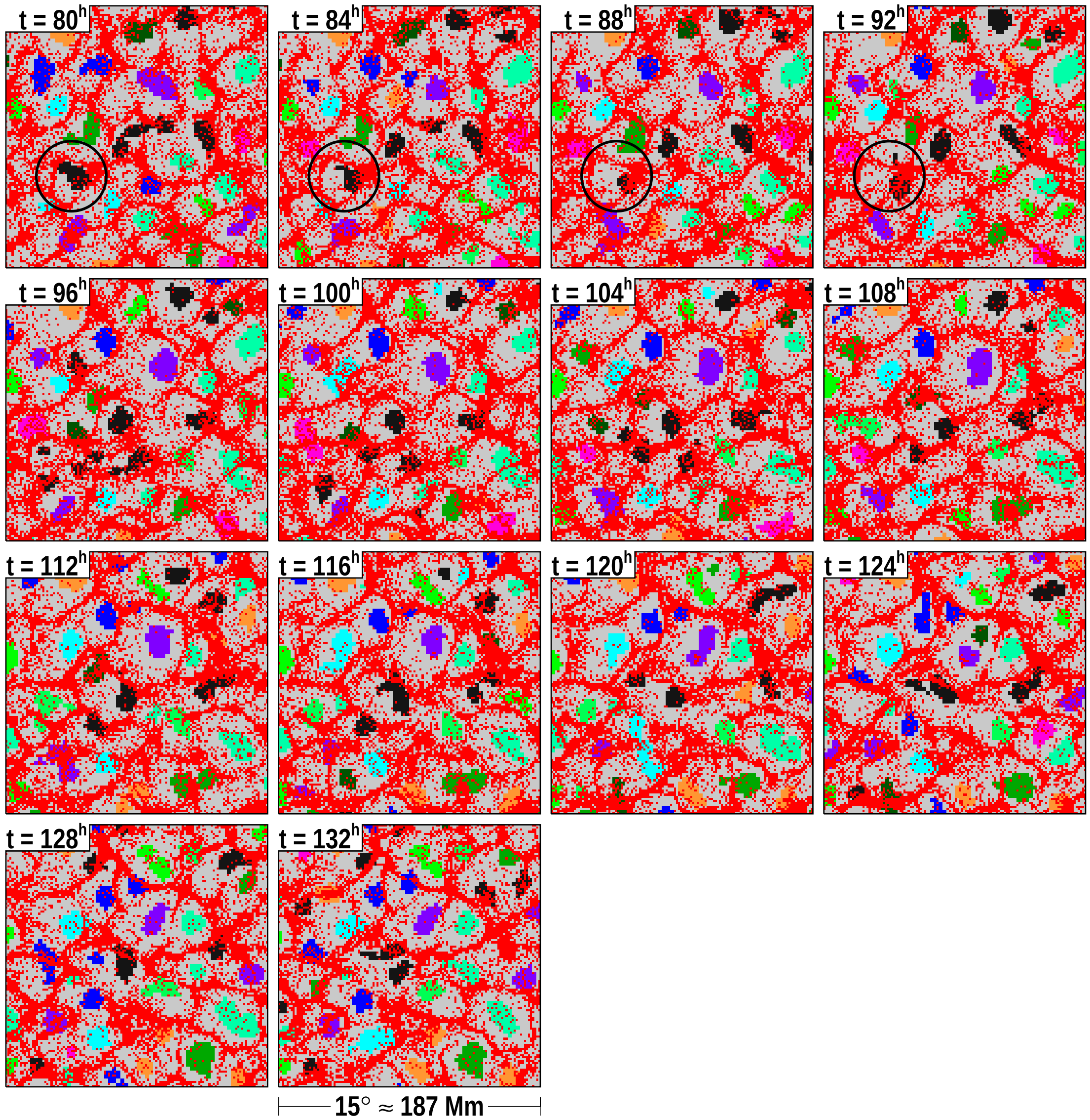

Figure 3.18: A continuation of the time series of Fig. 3.17.

In this way, each outflow core in the six-day dataset can be assigned a unique identity, from which its lifetime and average area can be determined. We now have the information necessary to compile statistics on the supergranulation pattern, as deduced from their outflow cores. As discussed earlier, we assume that the area of an individual supergranule is directly proportional to the area of its outflow core. Figure 3.20 shows the distribution of average supergranular areas, defined as the average area of each

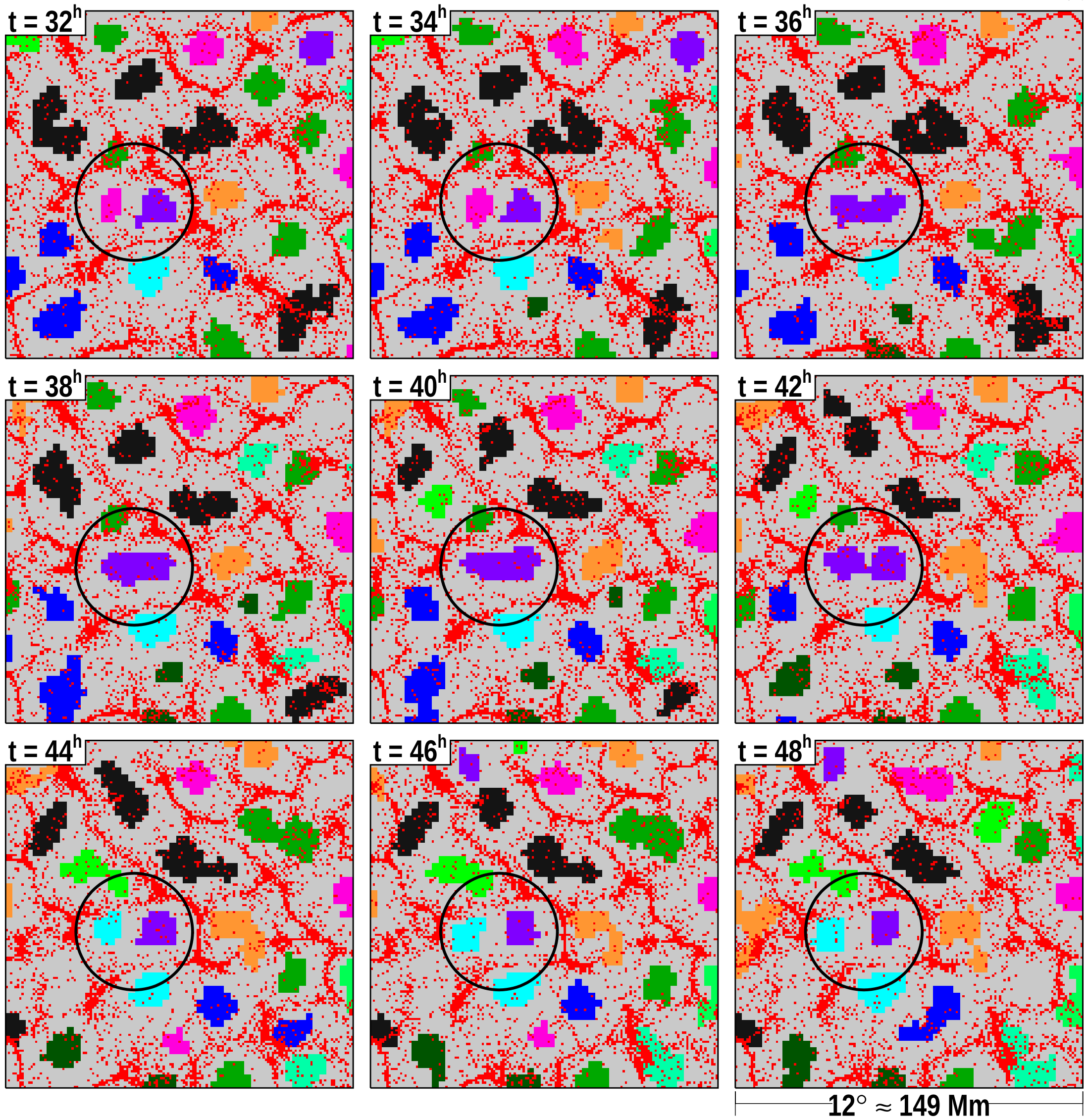

Figure 3.19: An enlarged region illustrating splitting and merging events. The objects enclosed in the circle merge together at $t = 36$ hr, and subsequently dissociate at $t = 44$ hr.

supergranule throughout its lifetime. The dotted line represents the best-fit Gaussian function,

$$N(A)\,dA = C\exp\left(-\frac{z^2}{2}\right) \qquad \text{where} \qquad z = \frac{A - \langle A\rangle}{B}\,dA, \tag{3.2}$$

where the mean, width, and height, are respectively denoted by $\langle A\rangle$, B, and C. The dis-

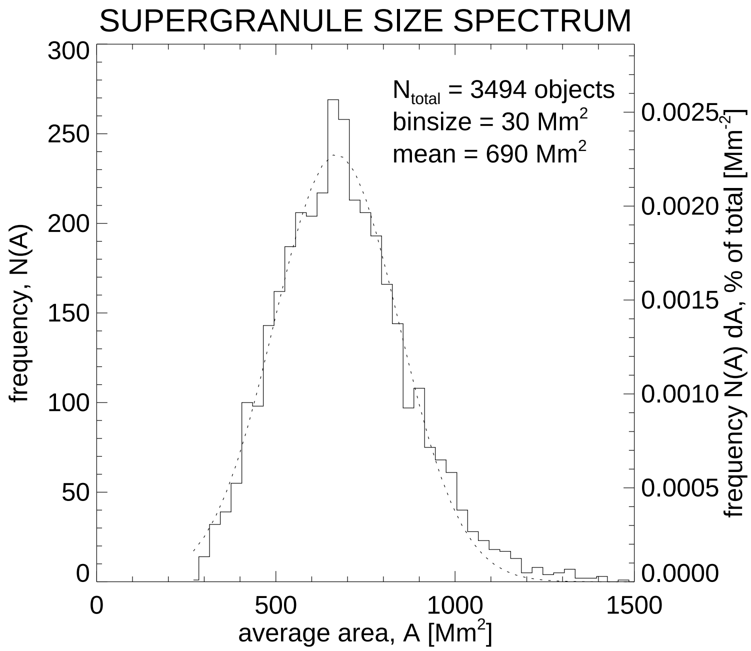

Figure 3.20: Average size distribution $N(A)$ for the N_{total} supergranules identified in the April 1999 dataset. The area A is defined as the area of the entire supergranule (not just the outflow core) as averaged over the lifetime of each object. The outflow cores were identified after applying 4-hr temporal boxcar and 8.8-Mm spatial Gaussian filters to the time series. The dotted line is the best-fit Gaussian function [see eq. (3.2)] with $\langle A \rangle = 669$ Mm^2, $B = 174$ Mm^2, and $C = 239$.

tribution was compiled using time series of divergence data from the April 1999 dataset after smoothing by 4-hr temporal boxcar and 8.8-Mm spatial Gaussian filters. Figure 3.20 indicates that supergranules have an average area $\langle A \rangle$ of 669 ± 174 Mm^2, which is approximately equivalent to a linear extent of $\sqrt{\langle A \rangle}$=22–29 Mm across. However, as one would expect, this result is sensitive to the degree of spatial smoothing applied to the data before identifying the outflow cores. Figure 3.21 shows the dependence of the mean sizes $\sqrt{\langle A \rangle}$ on the spatial smoothing width w for each of the temporal and spatial smoothing combinations. One would expect average sizes to increase with more smoothing, and this is indeed realized. Extrapolating down to zero smoothing, we find

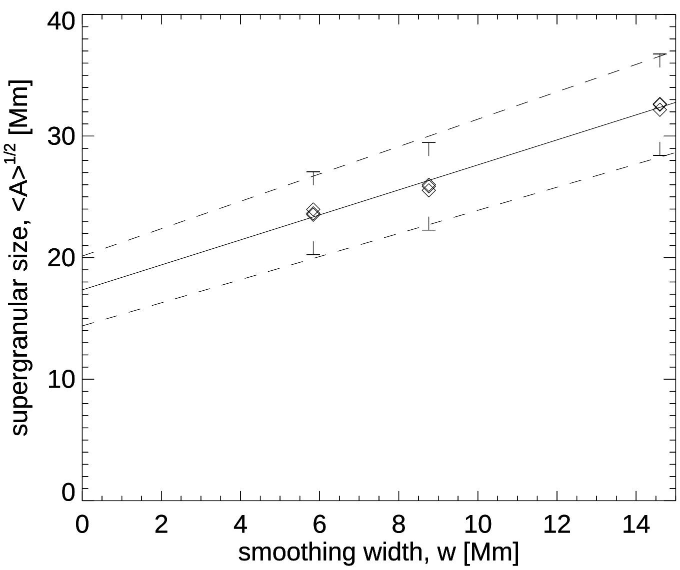

Figure 3.21: Dependence of the mean supergranular sizes $\sqrt{\langle A\rangle}$ on the width w of the Gaussian kernel used to spatially smooth the divergence images. Extrapolating down to zero smoothing gives a supergranular size of 17 ± 3 Mm across.

that supergranules have an average size of 14–20 Mm across. The amount of temporal filtering appears to have little effect on the characteristic supergranular cell size.

One study of this sort has already been performed by Hagenaar et al. (1997), wherein the Ca II K network were used to determine supergranular boundaries. They find a mean cell size of 13–18 Mm, in agreement with our result and approximately half the average cell size measured using correlation analysis techniques. Hagenaar et al. (1997) argue that this discrepancy arises because the correlation measurement preferentially weights the largest cells when computing the average cell size. Direct inspection of the Ca II K network supports this result, in that while cells of order 32 Mm (the average cell size found using classical corrleation analysis techniques) certainly exist, many smaller cells can also be found. We believe that the same rules applicable to the chromospheric Ca II K network also apply to the outflows found by our direct identification method.

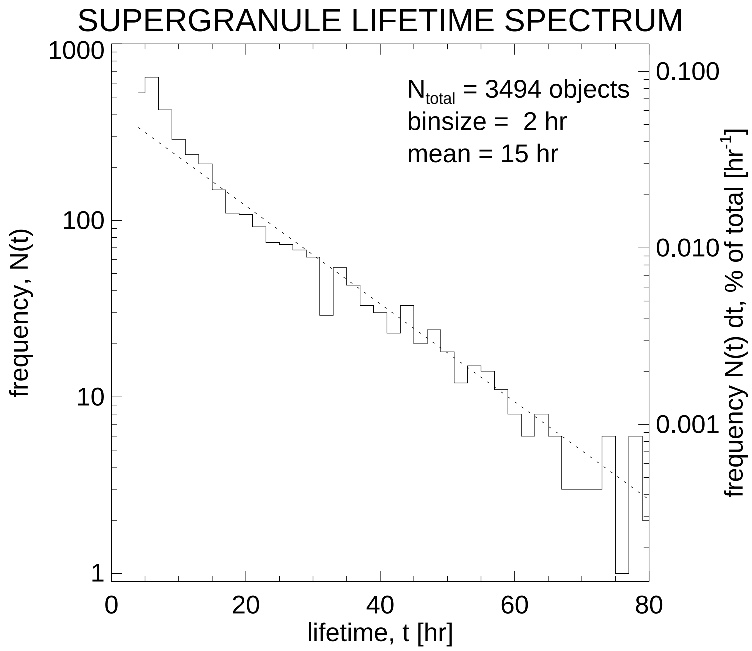

Figure 3.22: Distribution of supergranular lifetimes $N(t)$ for the N_{total} supergranules identified in the April 1999 dataset. The lifetime t is equal to the number of consecutive frames in which each object can be identified. The outflow cores were identified after applying 4-hr temporal boxcar and 8.8-Mm spatial Gaussian filters to the time series. The dotted line is the best-fit exponential function [see eq. (3.3)] with the intercept $C = 434$ and $\tau = 16$ hr.

Figure 3.22 shows the distribution of supergranular lifetimes for the April 1999 dataset, along with the best-fit exponential function,

$$N(t)\,dt = Ce^{-t/\tau}\,dt, \tag{3.3}$$

where the intercept and mean lifetime are denoted by C and τ respectively. The supergranules identified by our method have a mean lifetime of $\tau = 16$ hr, or 25% less than the correlation lifetime of 20 hr. However, this mean value may obscure the fact that amidst the many short-lived supergranules there exist several cells which survive for multiple days, suggesting that the pattern as a whole cannot be adequately characterized by a single time scale. In addition, approximately 10% of the supergranules

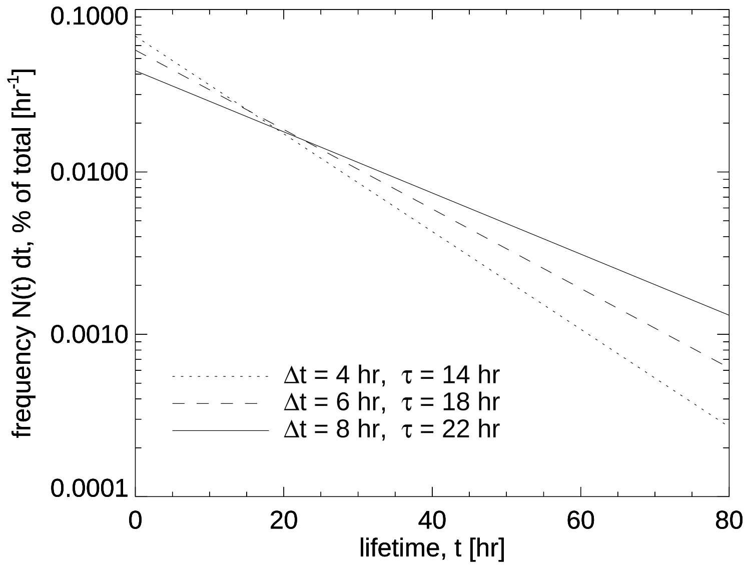

Figure 3.23: Dependence of the distribution of supergranular lifetimes $N(t)$ on the temporal averaging window Δt.

present in this dataset appear on either the first or last image in the time series, such that the actual lifetimes of these objects are longer than those values used in compiling the lifetime histogram of Figure 3.22. Consequently, we believe the distribution in the figure is biased toward shorter supergranular lifetimes. We included these extra cells in the distribution because removing them would bias the results even more so toward shorter lifetimes, for longer-lived supergranules have a greater probability of appearing on either the first or last image in the time series than do those supergranules with shorter lifetimes.

The effect of the temporal averaging is shown in Figure 3.23, displaying the supergranular lifetime distributions for several values of Δt for $w = 8.8$ Mm. With greater temporal averaging, the slope of the distribution function becomes flatter due to the merging of short-lived cells into longer-lived cells. Note that the smallest value of Δt for which a lifetime distribution is plotted is Δt=4 hr, corresponding to the minimum amount of temporal averaging one needs to perform in order to reduce the random noise

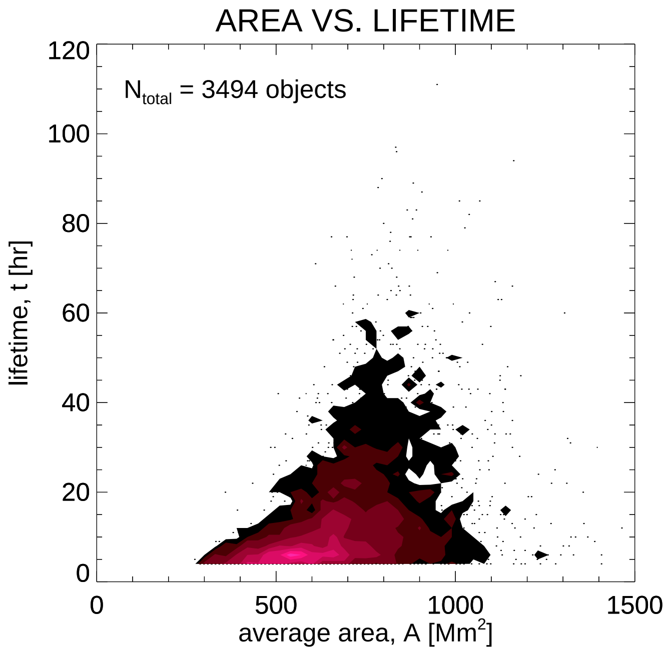

Figure 3.24: The distribution N(A,t) as a function of the average supergranular area A vs. lifetime t for the N_{total} supergranules identified in the April 1999 dataset. The shaded contours appear at values of N=2, 5, 10, 20, 30, 40, 50, and 60. The dots represent locations in coordinate space where $N = 1$.

level in the divergence signal below the supergranular outflow signal (see Fig. 3.4). We also find that the amount of spatial smoothing has little effect on the lifetime distribution functions.

Figure 3.24 shows the distribution of supergranular cells as a function of average area A and lifetime t. The general trend is for larger cells to live longer, although we note that the longest lived cells are not the largest. This effect may be caused by the propensity for extremely large cells to fragment into smaller cells at some point during their existence.

3.4 FLOWS ON LARGER SCALES

It is evident that the pattern of supergranulation possesses a broad range of scales of motion in time and space, as shown both by the heuristic impressions provided by the cork studies in §3.2 as well as by the statistical analysis of the previous section. We now attempt to measure surface flows occurring on larger spatial scales than that of supergranulation, including differential rotation, meridional circulation, and possibly giant cell circulations. Such large-scale flows detected at the surface would likely span a significant fraction of the convection zone, and thus would provide another way to probe the solar interior. These flows would be large enough to interact with the solar differential rotation profile and might play a role in the 22-yr global magnetic cycle.

Several other studies using a variety of techniques have detected large-scale flows both near the surface and at depth. Ring-diagram analyses (Haber et al. 2000) of time series of MDI velocity data have shown extended regions of organized flows on the order of 25–50 m s^{-1} which vary on time scales of about one day. Longer temporal averages (of at least nine days) show bands of zonal flows of order 20 m s^{-1} which migrate toward the equator and appear to vary with changes in solar activity. Such long temporal averages also contain persistent poleward-directed meridional flows of order 20 m s^{-1} in both hemispheres and extending to depths of at least 10 Mm below the surface. Similar meridional flows were also measured using time-distance analyses (Giles et al. 1998) applied to two months of MDI data, with poleward flows detected as deep as 20 Mm. In addition, spectral decompositions of line-of-sight velocity images reveal large-scale banded flow patterns at the surface which persist for several solar rotations (Beck et al. 1998; Ulrich 1998). Such flow patterns are distinct from the torsional oscillations discovered earlier by Howard & LaBonte (1980) and are not associated with regions of surface magnetic activity.

The supergranular flow fields discussed throughout this chapter, which were de-

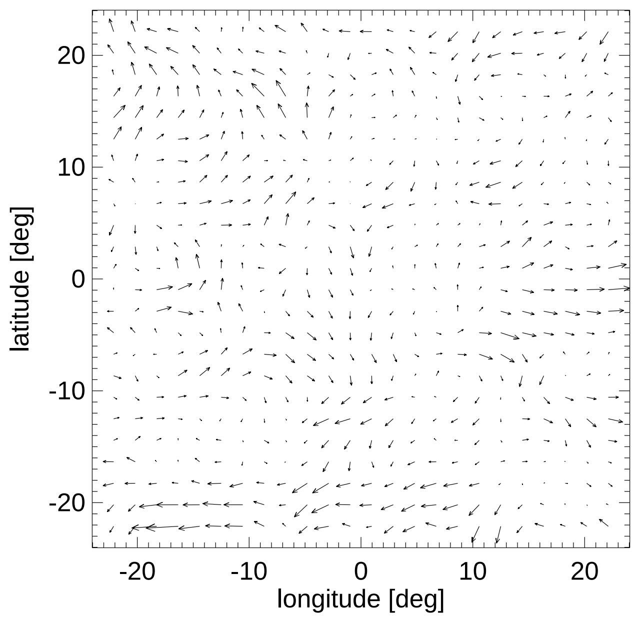

Figure 3.25: Six-day averaged flow field deduced by applying correlation tracking to 8-hr averaged images of horizontal divergence. The flow field arrows have an rms velocity of 22 m s^{-1} and are scaled to 50 m s^{-1}.

duced from applying correlation tracking to images of mesogranulation, presumably also include a large-scale velocity component. Unfortunately, the speed of the outflows (200–500 m s^{-1}) combined with the 200 m s^{-1} anomalous flow pattern (see §3.1.4) obscure the contribution to the flow maps arising from large-scale flows, which we expect to have velocities of at most 50 m s^{-1}. However, if the supergranular pattern itself is horizontally advected by flows on larger scales, it may be possible to measure such large-scale flows by applying the correlation tracking algorithm to the horizontal divergence images, themselves produced from correlation tracked flow maps. We now discuss the results of this effort.

We have shown that supergranules in quiet sun regions are on average about 20 Mm across. Using the supergranules as tracers for the correlation tracking technique

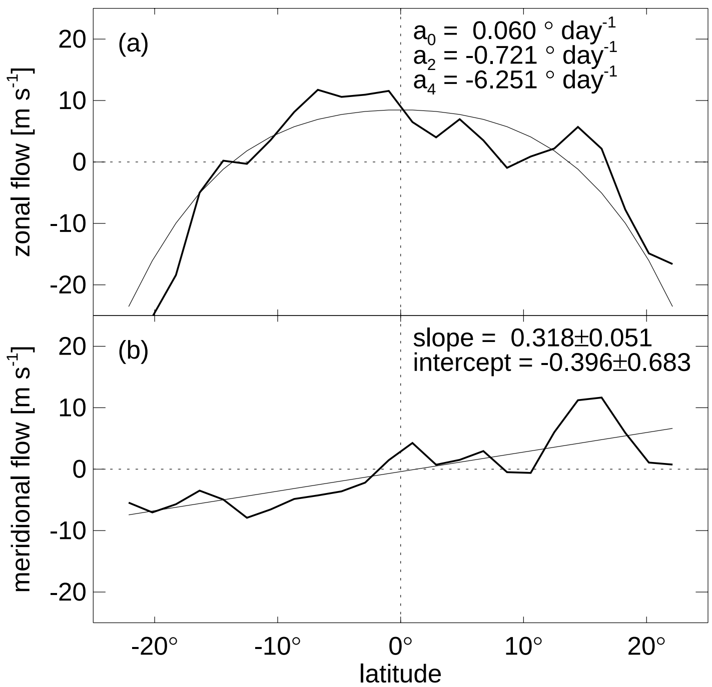

Figure 3.26: Longitudinally averaged zonal and meridional flows from Fig. 3.25. The fit parameters for the zonal flow are of the functional form $\Omega(\lambda) = a_0 + a_2 \sin^2(\lambda) + a_4 \sin^4(\lambda)$, where λ denotes latitude. The equatorial rate a_0 is relative to the tracking rate of the dataset of 13.5° day^{-1} synodic. The fit to the meridional flow is linear with latitude. Negative velocities indicate eastward/southward flows while positive values correspond to westward/northward flows.

therefore requires the size of the gridpoint neighborhood σ to be at least this size. In practice, we find that setting σ to be about twice the size of the tracers works best, so we here set σ=47 Mm, equivalent to a heliographic distance of 3.8°. Figure 3.25 shows the resulting flow field obtained by applying correlation tracking to supergranular outflow patterns present in the divergence data. The resulting flow field is averaged over the full duration of the time series, or about six days. The flow field arrows are binned spatially so that the distance separating neighboring arrows is 23 Mm or 1.9°. Both spatial and temporal averaging are necessary to attenuate the random errors present in the resulting flow maps.

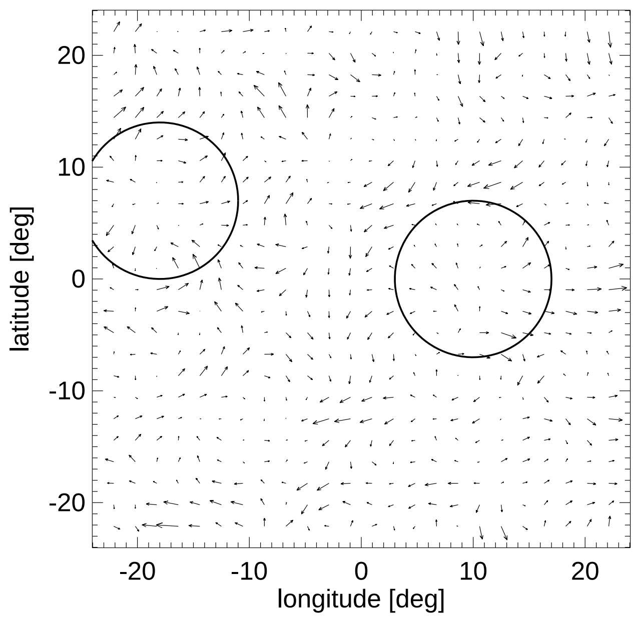

Figure 3.27: Residual large-scale flow field, formed by subtracting the fits to the longitudinally averaged zonal and meridional flows of Fig. 3.25 from the flow field of Fig. 3.25. Two organized outflows are enclosed in circles. The flow map vectors are scaled to 50 m s^{-1}, and are spatially oversampled by a factor of two.

From the flow field of Figure 3.25, we first compute longitudinal averages of the zonal and meridional components. The zonal average, displayed in Figure 3.26, contains the differential rotation profile of the supergranulation pattern minus the mean rate of 13.5° day^{-1} (synodic) at which the dataset was originally tracked. We have fitted the zonal flow to a function of the form

$$\Omega(\lambda) = a_0 + a_2 \sin^2 \lambda + a_4 \sin^4 \lambda, \tag{3.4}$$

where the differential rotation rate Ω is a function of latitude λ. After adding back in the tracking rate of the region, the equatorial rate a_0 deduced from these data corresponds to a sidereal rate of 14.5° day^{-1} or 466 nHz, which is slower than the equatorial rate for supergranules of 2.972 μrad s^{-1} or 473 nHz quoted by Snodgrass & Ulrich (1990),

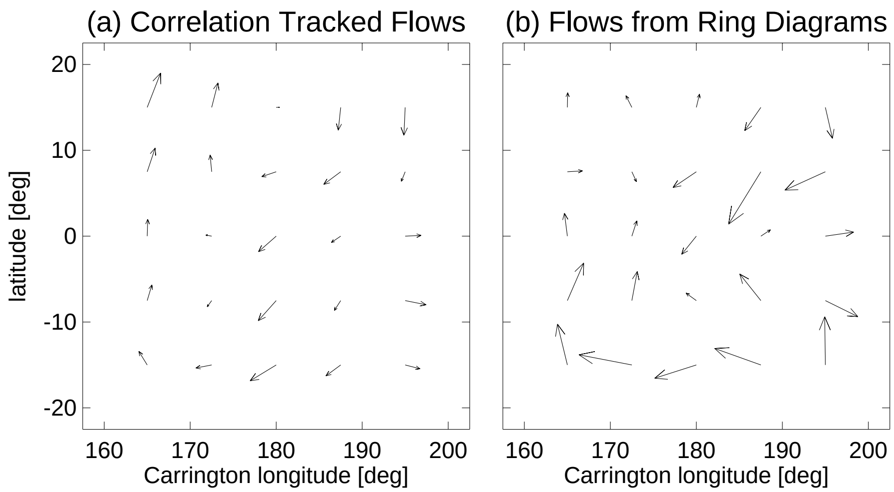

Figure 3.28: A comparison between the large-scale flow field of Fig. 3.27 (a) with ring-diagram results (b) for the same region. The correlation tracked flow field has been spatially averaged to match the spatial resolution of the ring-diagram analysis.

but higher than the equatorial rate deduced spectroscopically ($a_0 = 2.851$ μrad s^{-1} or 454 nHz) and from magnetic tracers ($a_0 = 2.879$ μrad s^{-1} or 458 nHz) in the same data. In addition, their supergranular rotation rate also decreases much more rapidly than ours, corresponding in our units to $a_2 = -2.40°$ day^{-1} (versus the $a_2 = -0.721°$ day^{-1} for this dataset as indicated in Fig. 3.26). As a result, we conclude that our method for measuring differential rotation only partially senses the true supergranular rotation rate.

The lower panel of Figure 3.26 shows the meridional flow as averaged over longitude. We detect a poleward meridional flow symmetric about the equator, to within the error of the coefficients of the linear fit. At latitudes of $\pm 20°$ the flow has attained speeds of approximately 5–10 m s^{-1}, which may be slightly slower by about a factor of two than other measurements of the surface meridional flow, such as those performed using time-distance (e.g. Giles et al. 1997) and ring diagram (e.g. Haber et al. 2000) analyses. We are not able to detect the asymmetry present in the meridional flow seen

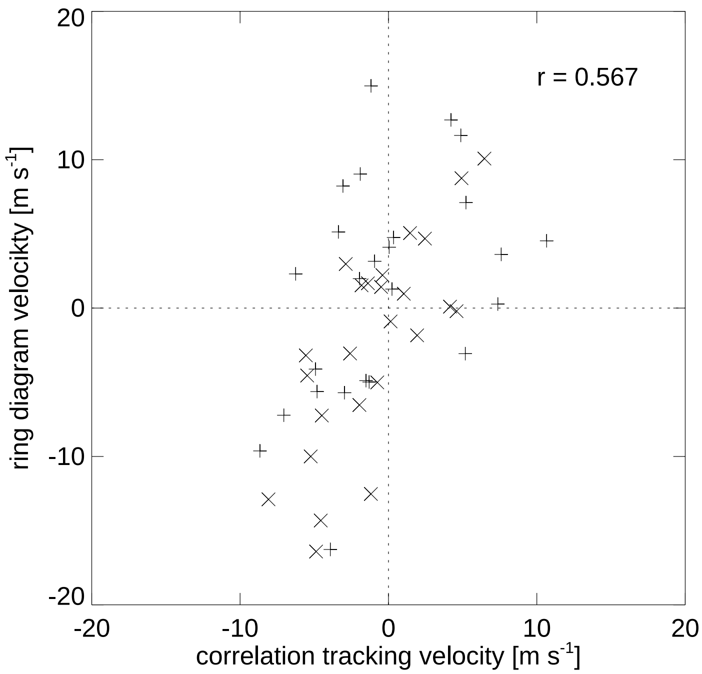

Figure 3.29: A scatter diagram comparing the large-scale flow field deduced by correlation tracking Fig. 3.28*a* to the ring-diagram results Fig. 3.28*b* for the same region. Both the correlation between the x-component (*crosses*) and the y-component (*plusses*) are shown. The correlation coefficient is $r = 0.567$.

in both the time-distance and ring diagram analyses which causes the zero-crossing of the meridional flow velocity to occur at about 5° of latitude north of the equator. We note, however, that both studies use substantially longer datasets to make their measurements of the meridional flow speeds, and it is possible that with greater temporal coverage the meridional flow measurement attained using this scheme may approach the results found in these other studies.

We now examine the residual flow field, shown in Figure 3.27, formed by removing the fits of Figure 3.26 from the large-scale flow field of Figure 3.25. Several regions of organized fluid motions on scales of 10°–20° are evident in this residual flow field, including two regions (circled in the figure) suggestive of large-scale outflows. These divergent flows are approximately 10° or about 120 Mm across and have outflow velocities on the order of 30 m s^{-1}.

We believe the flows of Figure 3.27 are of solar origin for two reasons. First, the flow field possesses a high amount of spatial coherence down to the resolution limit of the data. Furthermore, our results compare favorably with ring-diagram results for the same region, as shown in Figure 3.28. The flow vectors determined from ring-diagram analysis are obtained by performing helioseismic inversions on 15°-square time series of Doppler velocity images. These square regions are typically separated by 7.5° in longitude and latitude. For direct comparison, we show in Figure 3.28*a* the residual flow field deduced by correlation tracking from Figure 3.27 after reducing the resolution to match that of the corresponding ring-diagram flow vectors for the April 1999 dataset, shown in Figure 3.28*b*. A scatter diagram comparing the two methods is shown in Figure 3.29, and while there is some scatter in the data, the points appear to be correlated. The correlation coefficient is $r = 0.567$ as indicated in the figure.

We find that velocity features associated with solar supergranulation are advected by large-scale horizontal zonal and meridional flows, and as a result these flows can be measured applying the correlation tracking technique to the supergranular flow field. The supergranules in the April 1999 dataset possess a fast differential rotation profile relative to spectroscopic and magnetic features, with a meridional circulation of ± 10 m s^{-1} between -20° and 20° of latitude. In addition, organized flow patterns on scales of 10°–20° are evident in the residual flow field, after the longitudinally averaged zonal and meridional flows are removed.

3.5 CONCLUSIONS

We have presented in this chapter evidence that the near-photospheric velocity field on supergranular and larger scales is extremely complex, containing fluid motions possessing a wide range of length and time scales. Using the correlation tracking technique applied to full-disk MDI velocity images, we are able to study the horizontal flow field associated with solar supergranulation for time periods as long as six days with a combined spatial and temporal resolution unavailable before MDI. We find significant evolution of the supergranular flow field on time scales as short as 6 hr as convergence lanes are observed to appear and disappear and be horizontally advected by stronger elements of the flow field. Amongst these quickly evolving flows are persistent features which survive for time periods of 36 hr or more, encompassing not only long-lived supergranules but also velocity patterns evident in the large-scale flow maps deduced from tracking the supergranular pattern. A complete understanding of these surface patterns requires knowledge of how these structures are formed and interact within the bulk of convection zone. To this end, we now turn to detailed three-dimensional convection models of a stratified fluid confined to rotating spherical shells which are designed to simulate aspects the supergranular layer of the upper solar convection zone.

Chapter 4

NUMERICAL MODELING OF SPHERICAL SHELLS OF CONVECTION

4.1 NUMERICAL MODELING OF ANELASTIC FLUIDS

Observations of supergranular and larger-scale flow fields, such as those presented in Chapter 3, together with measurements of the smaller-scale patterns of mesogranulation and granulation, provide the only direct look at the turbulent motions which occupy the underlying convection zone. Such observations indicate this convection is extremely complex, forming coherent features such as networks of upflows and downflows possessing a broad range of length and time scales. These vigorous overturning motions are permeated by magnetic structures of all sizes, ranging from small flux tubes to large-scale magnetic patterns associated with active regions and sunspots observed at the surface. To investigate further the dynamics of such turbulent flows on supergranular and larger scales, we now turn to three-dimensional numerical simulations of convection occupying thin spherical shells located immediately below the solar surface.

The simulations described in the next chapter are carried out using the anelastic spherical harmonic (ASH) code. The ASH code solves the anelastic equations of hydrodynamics describing a compressible fluid confined to a rotating spherical shell heated from below. The complex structures and intricate behavior of the resulting convection requires high spatial resolution, and the flows must be studied over extended periods of time for statistical equilibration to be achieved. As a result, the ASH code is designed to run efficiently on massively parallel architectures such as the Cray T3E and SGI Origin 2000 machines (Clune et al. 1999). This multi-processor version was devised by Tom Clune, Mark Miesch, and Julian Elliott, although the numerical approach to this problem was first implemented by Gary Glatzmaier in the early 1980's (Glatzmaier 1984).

The ASH code employs a pseudo-spectral approach, where all fluid velocities and state variables are projected onto orthogonal basis functions in each of the three spatial dimensions. The radial structure of the solution variables is represented by an expansion based on Chebyshev polynomials, while variations in the latitudinal and longitudinal directions are expanded over spherical harmonic basis functions Y_ℓ^m, characterized by the angular degree ℓ and azimuthal order m. This discretization scheme ensures that the horizontal resolution is uniform everywhere on a sphere when all (ℓ, m)-pairs for a given maximum degree $\ell_{\max}$ are retained in the modal expansion. Conversely, the simplest finite-difference scheme, where computational gridpoints are distributed along lines of latitude and longitude, suffers from the problem that the spatial resolution varies with latitude such that the gridpoints are more closely spaced near the poles compared to equatorial regions (colloquially known as the *pole problem*).

As the name implies, the ASH code solves an approximate form of the Navier-Stokes equations known as the anelastic equations. The anelastic approximation (Gough 1969) allows us to handle the effects of compressibility while filtering out acoustic perturbations which would otherwise severely limit the size of the computational time step. This approximation is valid when the convective fluid velocities are subsonic, which in turn implies that the stratification of the fluid is only slightly superadiabatic. The filtering is achieved by insisting that the time derivative of density vanishes in the continuity equation, or thereby that the divergence of the momentum be zero, or that the momentum vector be solenoidal. This approximation is effectively equivalent to allowing pressure disturbances to equilibrate instantaneously, forcing the system to evolve on convective rather than sound-speed time scales. It is therefore implicitly assumed that sound waves do not play a significant role in the dynamical evolution of the system, which is in agreement with the expectation that the coupling of convection, stratification, and rotation are the major dynamical influences throughout the bulk of the convection zone.

As with the temporal scales of motion, fully resolving all spatial scales of motion in a numerical simulation is infeasible at this time, as the dynamically active scales in the solar convection zone range from 10^2 Mm (depth of the zone) to 10^{-4} Mm (typical dissipation scale), thereby encompassing a factor of 10^6 in scale. However, current simulations can cope with a range of only about 10^3 in each of three dimensions. Consequently, the ASH code adopts the common approach of parameterizing the transport properties resulting sub-grid scale (SGS) turbulent eddies and resolving only the largest scales of convection, thus becoming a large eddy simulation (LES).

All LES-SGS simulations require a prescription for representing the effects of SGS convective motions not explicitly resolved in the model. Such a scheme may incorporate characteristics of the resolved flows into their functional forms (see the reviews by Canuto 1996; Lesieur 1997; Canuto & Christensen-Dalsgaard 1998), or may simply enhance the molecular (viscous and thermal) diffusivities. We have adopted the latter approach for simplicity, yet recognize that this aspect requires considerable attention in the future. The main drawback of this scheme is that the enhanced diffusion draws energy from larger resolved scales of motion which should be unaffected by such dissipative effects. In one alternative approach, known as hyperviscosity, one allows the enhanced eddy diffusivities to act on fourth (or higher) order derivatives of the velocity field, thereby confining the diffusive effects more toward the smaller end of the spectrum. Another class of SGS models involves adding extra stress terms to the equations of motion. Evolution equations for these additional contributions can then be constructed once functional forms for the correlations between second-order variables are specified using some kind of a closure hypothesis. As is true of all LES-SGS studies, one hopes that the specific form by which the SGS motions are parameterized has a relatively small effect on the global dynamics of the system.

Time-stepping in the ASH code is performed using an implicit second-order Crank-Nicholson procedure for the linear terms and a fully explicit second-order Adams-Bashforth procedure for the nonlinear terms. Because the explicit time-stepping procedure cannot be performed in the spectral domain, this scheme necessitates conversions between the physical and spectral representations during each time step when switching between solving the implicit and explicit terms in the evolution equations. However, the benefits gained by avoiding the pole problem prevalent in finite difference representations outweigh the added computational time spent in performing the transformations between the physical and spectral domains.

4.2 THE ASH CODE: EQUATION SUMMARY

4.2.1 Fluid Flow in a Rotating Frame

We first set down the equations valid for a fully compressible, rotating fluid before introducing the anelastic approximation. We choose to operate in spherical polar coordinates (r, θ, ϕ), where r is the radius at each point, and θ and ϕ are respectively the polar (latitude) and azimuthal (longitude) angles. The fluid is rotating with respect to an inertial frame at constant angular velocity $\boldsymbol{\Omega}$, such that

$$\boldsymbol{\Omega} = \Omega \cos\theta\, \hat{\boldsymbol{r}} - \Omega \sin\theta\, \hat{\boldsymbol{\theta}}, \tag{4.1}$$

as illustrated in Figure 4.1. All symbols appearing in this section are defined in Table 4.1 for convenience, and most have their usual meanings in a fluid dynamical context. The fluid equations express the conservation of mass (mass continuity),

$$\frac{\partial \rho}{\partial t} + \boldsymbol{\nabla} \cdot (\rho \boldsymbol{u}) = 0, \tag{4.2}$$

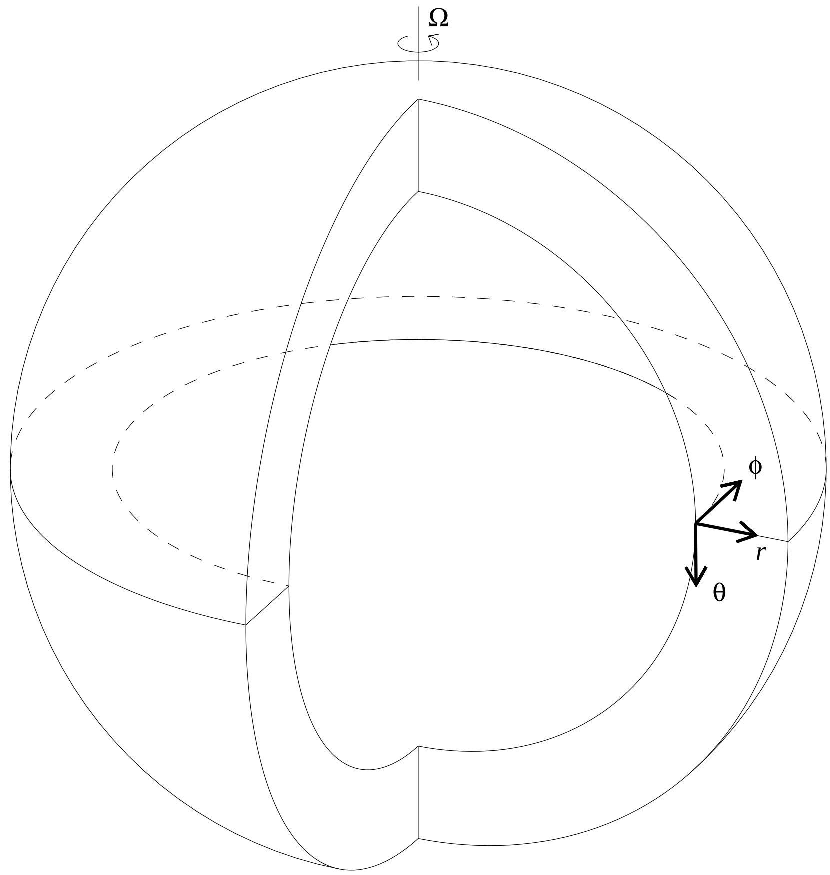

Figure 4.1: The spherical shell domain in partial cutaway to show the empty interior.

the conservation of momentum,

$$\rho\left[\frac{\partial \boldsymbol{u}}{\partial t}+(\boldsymbol{u}\cdot\boldsymbol{\nabla})\boldsymbol{u}\right]=-\boldsymbol{\nabla}p-\rho g\,\hat{\boldsymbol{r}}+2\rho(\boldsymbol{u}\times\boldsymbol{\Omega})+\boldsymbol{\nabla}\cdot\underline{\underline{\boldsymbol{\mathcal{D}}}}, \tag{4.3}$$

and the conservation of internal energy,

$$\rho T\left[\frac{\partial s}{\partial t}+(\boldsymbol{u}\cdot\boldsymbol{\nabla})s\right]=-\boldsymbol{\nabla}\cdot\boldsymbol{q}_{\mathrm{eff}}+\Phi. \tag{4.4}$$

In the momentum conservation equation, it is customary for the gravitational acceleration term to contain contributions from both centrifugal acceleration and classical Newtonian gravitational acceleration. For the solar models considered here, however, the centrifugal acceleration (of order $\Omega^2 R_\odot$) is several orders of magnitude smaller than

Table 4.1: Definitions of symbols appearing in §4.2.

Symbol	Gaussian Unit	First Appears	Definition
c_p	erg g^{-1} K^{-1}	equation (4.8)	specific heat at constant pressure
c_v	erg g^{-1} K^{-1}	γ def below	specific heat at constant volume
$\underline{\underline{\boldsymbol{\mathcal{D}}}}$	g cm^{-3} s^{-1}	equation (4.3)	viscous stress tensor
$\underline{\underline{\boldsymbol{e}}}$	s^{-1}	equation (4.5)	strain rate tensor
g	cm s^{-2}	equation (4.3)	Newtonian gravitational acceleration
p	erg cm^{-3}	equation (4.3)	pressure
$\boldsymbol{q}$	erg cm^{-2} s^{-1}	equation (4.8)	diffusive heat flux
$\boldsymbol{q}_{\mathrm{eff}}$	erg cm^{-2} s^{-1}	equation (4.4)	effective heat flux
$\boldsymbol{q}_{\mathrm{turb}}$	erg cm^{-2} s^{-1}	equation (4.8)	turbulent heat flux
r	cm	§4.2.1 intro	radius
$\hat{\boldsymbol{r}}$	dimensionless	equation (4.3)	radial unit vector
s	erg g^{-1} K^{-1}	equation (4.4)	specific entropy
T	K	equation (4.4)	temperature
t	s	equation (4.2)	time
$\boldsymbol{u}$	cm s^{-1}	equation (4.2)	velocity
$\underline{\underline{\boldsymbol{\delta}}}$	dimensionless	equation (4.5)	Kronecker delta
γ	dimensionless	equation (4.10)	ratio c_p/c_v of specific heats
κ_r	cm ^{2} s^{-1}	equation (4.8)	radiative diffusivity
κ_s	cm ^{2} s^{-1}	equation (4.8)	turbulent thermal diffusivity
θ	dimensionless	§4.2.1 intro	polar angle
ν	cm^2 s^{-1}	equation (4.7)	kinematic viscosity
ν_{eff}	cm^2 s^{-1}	equation (4.5)	effective kinematic viscosity
ν_{turb}	cm^2 s^{-1}	equation (4.7)	turbulent kinematic viscosity
ρ	g cm^{-3}	equation (4.2)	density
Φ	erg cm^{-2} s^{-1}	equation (4.4)	viscous heating
ϕ	dimensionless	§4.2.1 intro	azimuthal angle
$\boldsymbol{\Omega}$	s^{-1}	equation (4.3)	angular velocity of reference frame

the Newtonian gravity (of order $\dfrac{GM_\odot}{R_\odot^2}$), where $R_\odot$ and $M_\odot$ are the solar radius and mass. In order to use simple spherical harmonic expansions, we ignore centrifugal effects in these models, thereby rendering the surfaces of constant gravitational potential spherical: $\boldsymbol{g} = -g\,\hat{\boldsymbol{r}}$. Note that this assumption precludes Eddington-Sweet circulations (e.g. Tassoul 1978).

The viscous stress tensor $\underline{\underline{\boldsymbol{\mathcal{D}}}}$ appearing in equation (4.3) is defined as

$$\underline{\underline{\boldsymbol{\mathcal{D}}}} = 2\rho\nu_{\text{eff}}\left[\underline{\underline{\boldsymbol{e}}} - \frac{1}{3}(\boldsymbol{\nabla}\cdot\boldsymbol{u})\,\underline{\underline{\boldsymbol{\delta}}}\right], \tag{4.5}$$

while the viscous heating term Φ appearing in equation (4.4) can be written

$$\Phi = 2\rho\nu_{\text{eff}}\left[\underline{\underline{\boldsymbol{e}}} : \underline{\underline{\boldsymbol{e}}} - \frac{1}{3}(\boldsymbol{\nabla}\cdot\boldsymbol{u})^2\right], \tag{4.6}$$

where in both equations (4.5) and (4.6) the tensor $\underline{\underline{\boldsymbol{e}}}$ is the strain rate tensor and is itself a function of $\boldsymbol{u}$.

In accordance with our SGS formulation, we define the effective viscosity ν_{eff} as

$$\nu_{\text{eff}} = \nu + \nu_{\text{turb}}, \tag{4.7}$$

where ν_{turb} is the turbulent eddy viscosity which accounts for viscous transport by convective motions not formally resolved in the simulation. In the above hydrodynamic equations, the true viscosity ν has been replaced by ν_{eff}. Additionally, we also must account for the transport of heat by the SGS turbulence. We therefore define

$$\boldsymbol{q}_{\text{eff}} = \boldsymbol{q} + \boldsymbol{q}_{\text{turb}} = \underbrace{-\kappa_r\rho c_p\boldsymbol{\nabla}T}_{\boldsymbol{q}}\underbrace{-\kappa_s\rho T\boldsymbol{\nabla}s}_{\boldsymbol{q}_{\text{turb}}}, \tag{4.8}$$

where we have explicitly taken into account the smoothing out of entropy gradients by unresolved SGS motions by having the eddy thermal diffusivity κ_s acting on $\boldsymbol{\nabla}s$. Ideally, if the simulation were to resolve all relevant scales of motion, the turbulent contributions to ν_{eff} and $\boldsymbol{q}_{\text{eff}}$ would be superfluous. However, fully resolved global simulations of relevance to the sun are currently unattainable.

The heat flux $\boldsymbol{q}$ appearing in equation (4.8) should contain contributions from both radiative diffusion and thermal conduction. For the sun, the energy flux due to thermal conduction is much smaller than the fluxes from radiative diffusion or convection (e.g. Spitzer 1962; Hansen & Kawaler 1994) and is thus ignored in these models. Furthermore, the radiative flux is assumed to take the form of a Fick-type diffusion law,

$$\boldsymbol{q} = -\kappa_r\rho c_p\boldsymbol{\nabla}T. \tag{4.9}$$

Equations (4.2)–(4.4) are to be solved for the following seven quantities: the four state variables ρ, p, T, s, and the three components of $\boldsymbol{u}$. However, equations (4.2)–(4.4) comprise only five independent relations. Since only two of the state variables are independent, the system is closed by first specifying an equation of state relating the state variables ρ, p, and T, and then deriving an equation for s.

In the simulations presented here, we assume the fluid is a perfect gas, thereby ignoring the effects of ionization. The equation of state is therefore

$$p = \frac{\gamma - 1}{\gamma} c_p \rho T. \tag{4.10}$$

The specific entropy is then

$$s = c_p \left(\frac{1}{\gamma} \ln p - \ln \rho \right), \tag{4.11}$$

valid to within an arbitrary constant determined by specifying the value of s given reference values of p and ρ. Equations (4.2)–(4.4), (4.10), and (4.11) now form a complete set of equations describing a compressible fluid in a spherical geometry.

4.2.2 The Anelastic Approximation

Compressibility clearly plays an important role in the dynamics of the solar convection zone, as the fluid density varies by several orders of magnitude across the layer. The density drops by a factor of approximately 100 between $0.90R_\odot$ and $0.99R_\odot$, which encompasses the upper region of the convection zone considered in this thesis. We therefore apply the anelastic approximation to the fully compressible fluid equations in order to accommodate a solar-like density stratification in our simulations. As discussed earlier, sound waves and other pressure disturbances which operate on time scales faster than the time scale of the convection are filtered out in this formulation, since including such dynamics would otherwise limit the size of the computational time step.

The main assumption of the anelastic approximation is that such temporal filtering is valid when the convective motions are subsonic, which occurs when the radial entropy gradient responsible for driving the convection departs only slightly from the marginally stable entropy gradient (that is, when $\left|\dfrac{ds}{dr}\right| \ll 1$). We now estimate the degree of superadiabaticity at a given radius within the solar convection zone using simplified mixing-length arguments to estimate the heat transport of a convectively unstable parcel of fluid.

We first define the dimensionless parameter ϵ as

$$\epsilon = -\frac{\lambda}{c_p}\frac{ds}{dr}, \tag{4.12}$$

where ϵ characterizes the superadiabaticity of the fluid in terms of the entropy gradient. To make ϵ dimensionless, we normalize the entropy gradient by choosing c_p as the entropy scale and the mixing length λ as the characteristic length scale. The negative sign in equation (4.12) ensures that ϵ is positive, since superadiabatically stratified (convectively unstable) fluids have negative entropy gradients. We assume that the superadiabatic stratification $\dfrac{ds}{dr}$ is prescribed throughout the convection zone, even though the very motions which it supposedly drives most assuredly feed back and alter the stratification.

Now consider an isolated fluid parcel, initially in equilibrium with its surroundings, rising through the convectively unstable medium characterized by entropy gradient $\dfrac{ds}{dr}$. The motion of this parcel is driven by the excess heat it possesses after rising a radial distance λ. Equating the kinetic energy of the parcel with this heat excess, we have

$$\frac{\rho v^2}{2} = -\lambda\rho T\,\frac{ds}{dr}, \tag{4.13}$$

where v is the upward radial velocity of the parcel, and T and ρ are representative values of the temperature and density of the fluid. Solving for v and substituting the definition of ϵ from equation (4.12) into equation (4.13), we obtain

$$v = (2\epsilon c_p T)^{\frac{1}{2}}\,. \tag{4.14}$$

The flux of energy $F_{\rm conv} = \dfrac{1}{2}\rho v^3$ carried radially outward by these convective motions is therefore equal to

$$F_{\rm conv} = \rho \left(\epsilon c_p T\right)^{\frac{3}{2}} , \tag{4.15}$$

where factors of order unity have been omitted from our estimate. We now determine the degree of superadiabaticity ϵ necessary for convection to transport the entire solar luminosity $L_\odot$ through the convection zone by equating $F_{\rm total} = F_{\rm conv}$, which implies

$$\frac{L_\odot}{4\pi r^2} = \rho \left(\epsilon c_p T\right)^{\frac{3}{2}} , \tag{4.16}$$

and solving for ϵ. We thus have

$$\epsilon = \frac{1}{c_p T}\left(\frac{L_\odot}{4\pi r^2 \rho}\right)^{\frac{2}{3}} . \tag{4.17}$$

We can also estimate the typical Mach number M_a achieved by these convective flows. By definition,

$$M_a = \frac{v}{c_s}, \tag{4.18}$$

where the adiabatic sound speed c_s is given by

$$c_s = \left(\frac{\gamma p}{\rho}\right)^{\frac{1}{2}} . \tag{4.19}$$

Substituting the expressions for v and c_s from equations (4.14) and (4.19) into equation (4.18) gives

$$M_a = \left(\frac{\epsilon c_p \rho T}{\gamma p}\right)^{\frac{1}{2}} = \left(\frac{\epsilon}{\gamma - 1}\right)^{\frac{1}{2}} , \tag{4.20}$$

where the last equality follows from the ideal gas law, equation (4.10). Equation (4.20) implies that convective motions driven by a fluid for which ϵ is small do not approach the speed of sound.

Table 4.2 lists values for v, ϵ, and M_a calculated using equations (4.14), (4.17), and (4.20) for several radii within the convection zone. Values for T and ρ are taken from

Table 4.2: Estimates of v, ϵ, and M_a using a mixing-length approach as calculated from equations (4.14), (4.17), and (4.20) assuming $L_\odot = 3.90 \times 10^{33}$ erg s^{-1}, $R_\odot = 6.96 \times 10^{10}$ cm, and $c_p = 4 \times 10^{8}$ erg g^{-1} K^{-1}. The temperature T and density ρ are taken from Model S of Christensen-Dalsgaard et al. (1993). In this model, the base of the convection zone sits at $r = 0.73 R_\odot$.

r [$R_\odot$]	T [K]	ρ [g cm^{-3}]	v [m s^{-1}]	ϵ	M_a
0.73	2.1×10^{6}	1.6×10^{-1}	130	1×10^{-7}	4×10^{-4}
0.75	1.8×10^{6}	1.3×10^{-1}	140	1×10^{-7}	4×10^{-4}
0.80	1.4×10^{6}	8.8×10^{-2}	150	2×10^{-7}	5×10^{-4}
0.85	9.9×10^{5}	5.2×10^{-2}	170	4×10^{-7}	7×10^{-4}
0.90	6.2×10^{5}	2.6×10^{-2}	200	8×10^{-7}	1×10^{-3}
0.94	3.5×10^{5}	1.0×10^{-2}	270	3×10^{-6}	2×10^{-3}
0.96	2.2×10^{5}	5.3×10^{-3}	330	6×10^{-6}	3×10^{-3}
0.97	1.6×10^{5}	3.1×10^{-3}	400	1×10^{-5}	4×10^{-3}
0.98	1.0×10^{5}	1.4×10^{-3}	510	3×10^{-5}	7×10^{-3}
0.99	4.7×10^{4}	3.2×10^{-4}	830	2×10^{-4}	2×10^{-2}
0.999	1.3×10^{4}	1.2×10^{-6}	5300	3×10^{-2}	2×10^{-1}

an advanced one-dimensional solar model used extensively in helioseismology (Model S of Christensen-Dalsgaard et al. 1993). Table 4.2 shows that ϵ is no greater than about 10^{-4} (and thus $M_a \lesssim 10^{-2}$) throughout the bulk of the convection zone, and so the convective motions driven at greater depths are expected to be decidedly subsonic. Only within the last 1% by radius does ϵ approach unity. Above $0.99R_\odot$, the rapidly decreasing density and temperature profiles lead to faster fluid motions involving smaller spatial and temporal scales. In addition, the recombination of electrons with helium and hydrogen nuclei release latent heat which then must be transported outward by the convection. As a result, the stratification must become more superadiabatic to transport the requisite amount of energy, rendering the anelastic approximation less valid.

4.2.3 Scaling of the Fully Compressible Fluid Equations

Because the convective motions are subsonic and the superadiabaticity within the convection zone is small, we expect that the resulting departures of the thermodynamic state variables from their spherically averaged means should also be small. Therefore, we perform a formal scale analysis on the fully compressible fluid equations (4.2)–(4.4) introduced in §4.2.1 to separate the spherically symmetric mean state from the fluctuations resulting from the convection. We express each state variable f as the sum of a spherically symmetric mean quantity $\hat{f}(r,t)$ and a fluctuating quantity $f'(r,\theta,\phi,t)$:

$$\begin{aligned} p(r,\theta,\phi,t) &= \hat{p}(r,t) + p'(r,\theta,\phi,t), \\ \rho(r,\theta,\phi,t) &= \hat{\rho}(r,t) + \rho'(r,\theta,\phi,t), \\ T(r,\theta,\phi,t) &= \hat{T}(r,t) + T'(r,\theta,\phi,t), \\ s(r,\theta,\phi,t) &= \hat{s}(r,t) + s'(r,\theta,\phi,t). \end{aligned} \tag{4.21}$$

The perturbations to the state variables result from convective motions driven by the superadiabatic stratification of the layer, which we have previously characterized by the parameter ϵ defined in equation (4.12). We therefore assume $\dfrac{f'}{\hat{f}}$ is of order ϵ for any quantity f in equation (4.21).

For low Mach number flows the time scale on which pressure and density perturbations get smoothed out is much faster than the time scale of the convective motions, since such perturbations dissipate on sound-speed time scales. We perform such temporal filtering by assuming

$$\frac{\partial \rho'}{\partial t} = 0 \tag{4.22}$$

in the mass continuity equation.

The resulting anelastic equations consist of a set of equations describing the mean state, and a system of dynamic equations which governs the evolution of the fluctuating quantities. The details of the formal scale separation, which include the derivations of equations (4.23)–(4.33) which follow, are presented in §B.1 of Appendix B. We assume that the diffusivities ν_{eff}, κ_r, and κ_s are functions of $\hat{\rho}$ (and thus r) only, while the parameters γ and c_p are assumed constant throughout the domain.

The mean momentum equation becomes

$$\frac{d(\hat{p}+\hat{p}_{\text{turb}})}{dr} = -\hat{\rho} g, \tag{4.23}$$

where the quantity $\hat{p}_{\text{turb}}(r,t)$ represents the small departure from hydrostatic equilibrium caused by the combined effect of turbulent motions in the system. The mean equations of state are

$$\hat{p} = \frac{\gamma-1}{\gamma}\, c_p \hat{\rho} \hat{T}, \tag{4.24}$$

$$\frac{d\hat{s}}{dr} = c_p \left(\frac{1}{\gamma \hat{p}} \frac{d\hat{p}}{dr} - \frac{1}{\hat{\rho}} \frac{d\hat{\rho}}{dr} \right). \tag{4.25}$$

Upon initialization, the equations (4.23)–(4.25) are solved to determine the mean state, with the turbulent pressure $\hat{p}_{\text{turb}} = 0$ since the system is started from rest. Because there are only three equations but four unknown mean variables, one of them is therefore undetermined. Consequently, we take the approach of prescribing the entropy gradient $\dfrac{d\hat{s}}{dr}$, and then solving equations (4.23)–(4.25) to determine the other mean variables $\hat{p}$, $\hat{\rho}$, and $\hat{T}$. Note that the gravitational acceleration g can either be assumed constant throughout the layer, or can be prescribed along with the entropy gradient if the self-gravity of the mean state is deemed important.

The equations governing the evolution of the dynamic quantities $\boldsymbol{u}$ and s are:

$$\hat{\rho}\frac{\partial \boldsymbol{u}}{\partial t} = 2\hat{\rho}(\boldsymbol{u} \times \boldsymbol{\Omega}) - \hat{\rho}(\boldsymbol{u} \cdot \boldsymbol{\nabla})\boldsymbol{u} - \boldsymbol{\nabla} p' - \rho' g\, \hat{\boldsymbol{r}} + \boldsymbol{\nabla} \cdot \underline{\underline{\hat{\boldsymbol{\mathcal{D}}}}} \tag{4.26}$$

and

$$\hat{\rho}\hat{T}\frac{\partial s'}{\partial t} = \boldsymbol{\nabla} \cdot \hat{\boldsymbol{q}}_{\text{eff}} - \hat{\rho}\hat{T}(\boldsymbol{u} \cdot \boldsymbol{\nabla})(\hat{s} + s') + \hat{\Phi}, \tag{4.27}$$

where the anelastic viscous stress tensor $\underline{\underline{\hat{\boldsymbol{\mathcal{D}}}}}$ and the anelastic viscous heating term $\hat{\Phi}$ are defined

$$\underline{\underline{\hat{\boldsymbol{\mathcal{D}}}}} = 2\hat{\rho}\nu_{\text{eff}} \left[\underline{\underline{\boldsymbol{e}}} - \frac{1}{3}(\boldsymbol{\nabla} \cdot \boldsymbol{u})\, \underline{\underline{\boldsymbol{\delta}}} \right] \tag{4.28}$$

and

$$\hat{\Phi} = 2\hat{\rho}\nu_{\text{eff}}\left[\underline{\underline{\boldsymbol{e}}} : \underline{\underline{\boldsymbol{e}}} - \frac{1}{3}(\boldsymbol{\nabla} \cdot \boldsymbol{u})^2\right], \tag{4.29}$$

and where the anelastic heat flux $\hat{\boldsymbol{q}}_{\text{eff}}$ is defined as

$$\hat{\boldsymbol{q}}_{\text{eff}} = -\kappa_r \hat{\rho} c_p \boldsymbol{\nabla}(\hat{T} + T') - \kappa_s \hat{\rho}\hat{T}\boldsymbol{\nabla}(\hat{s} + s'). \tag{4.30}$$

The evolution of the system given by equations (4.26)–(4.27) are subject to the following three constraints:

$$\boldsymbol{\nabla} \cdot (\hat{\rho}\boldsymbol{u}) = 0, \tag{4.31}$$

$$\frac{p'}{\hat{p}} = \frac{\rho'}{\hat{\rho}} + \frac{T'}{\hat{T}}, \tag{4.32}$$

$$\frac{s'}{c_p} = \frac{p'}{\gamma\hat{p}} - \frac{\rho'}{\hat{\rho}}. \tag{4.33}$$

4.2.4 Energetics of the Anelastic Equations

For future reference, we now list the equations describing the kinetic and internal energy budgets of the system, while relegating the detailed derivations to §B.2 in Appendix B. The equation describing the conservation of kinetic energy density $\mathcal{E}_k = \dfrac{\hat{\rho}\boldsymbol{u} \cdot \boldsymbol{u}}{2}$ is

$$\frac{\partial \mathcal{E}_k}{\partial t} = -\boldsymbol{u} \cdot \boldsymbol{\nabla} p' - \rho' g \boldsymbol{u} \cdot \hat{\boldsymbol{r}} + \boldsymbol{u} \cdot \left(\boldsymbol{\nabla} \cdot \underline{\underline{\hat{\boldsymbol{\mathcal{D}}}}}\right) + \boldsymbol{\nabla} \cdot \left[\boldsymbol{u}\left(\frac{\hat{\rho}\boldsymbol{u} \cdot \boldsymbol{u}}{2}\right)\right]. \tag{4.34}$$

The terms on the right-hand side of equation (4.34) all represent sources or sinks of kinetic energy due to work respectively done by pressure gradient forces, buoyancy forces, shear stresses, and by inertial forces.

The equation describing the conservation of internal energy density $\mathcal{E}_s = \hat{\rho}\hat{T}s'$ is

$$\frac{\partial \mathcal{E}_s}{\partial t} = \boldsymbol{\nabla} \cdot \hat{\boldsymbol{q}}_{\text{eff}} + \boldsymbol{u} \cdot \boldsymbol{\nabla} p' + \rho' g \boldsymbol{u} \cdot \hat{\boldsymbol{r}} - c_p \boldsymbol{\nabla} \cdot (\hat{\rho} T' \boldsymbol{u}) + \hat{\Phi}. \tag{4.35}$$

As with the kinetic energy equation, each of the terms on the right-hand side of equation (4.35) represents either a source or sink of internal energy. The first term on the right-hand side represents the transport of flux via temperature/entropy gradients throughout the domain. The next two terms denote the extraction of heat from the thermal field by pressure-gradient and buoyancy forces. The fourth and fifth terms represent the heat generated by volume expansion and viscous dissipation, while the sixth term may be interpreted as the radial transport of enthalpy.

The sum of equations (4.34) and (4.35) yields the following equation describing the total energy budget of the system:

$$\frac{\partial(\mathcal{E}_k + \mathcal{E}_s)}{\partial t} = \boldsymbol{\nabla} \cdot \left(\boldsymbol{u} \cdot \underline{\underline{\hat{\boldsymbol{\mathcal{D}}}}}\right) + \boldsymbol{\nabla} \cdot \left[\boldsymbol{u}\left(\frac{\hat{\rho}\boldsymbol{u} \cdot \boldsymbol{u}}{2}\right)\right] + \boldsymbol{\nabla} \cdot \hat{\boldsymbol{q}}_{\text{eff}} - \boldsymbol{\nabla} \cdot (c_p \hat{\rho} T' \boldsymbol{u}). \tag{4.36}$$

4.2.5 Streamfunction Formalism

To solve the anelastic evolution equations (4.26) and (4.27), we recognize that the mass flux is solenoidal, which permits the quantity $\hat{\rho}\boldsymbol{u}$ to be written in terms of poloidal and toroidal streamfunctions W and Z,

$$\hat{\rho}\boldsymbol{u} = \boldsymbol{\nabla} \times (\boldsymbol{\nabla} \times W\,\hat{\boldsymbol{r}}) + \boldsymbol{\nabla} \times Z\,\hat{\boldsymbol{r}} \tag{4.37}$$

such that equation (4.31) is automatically satisfied. We now replace the anelastic momentum equation (4.26) with three scalar equations describing the evolution of W, $\dfrac{\partial W}{\partial r}$, and Z. They are the radial component of the momentum equation,

$$-\frac{\partial}{\partial t}(\nabla_\perp^2 W) = -\frac{\partial p'}{\partial r} - \hat{\rho} g + \hat{\boldsymbol{r}} \cdot \left[\boldsymbol{\nabla} \cdot \underline{\underline{\hat{\boldsymbol{\mathcal{D}}}}}\right] + \hat{\rho}\,\hat{\boldsymbol{r}} \cdot \Big[2(\boldsymbol{u} \times \boldsymbol{\Omega}) - (\boldsymbol{u} \cdot \boldsymbol{\nabla})\boldsymbol{u}\Big], \tag{4.38}$$

the horizontal divergence of the momentum equation,

$$-\frac{\partial}{\partial t}\left[\frac{\partial}{\partial r}(\nabla_\perp^2 W)\right] = -\nabla_\perp^2 p' + \boldsymbol{\nabla}_\perp \cdot \left[\boldsymbol{\nabla} \cdot \underline{\underline{\hat{\boldsymbol{\mathcal{D}}}}}\right] + \hat{\rho}\boldsymbol{\nabla}_\perp \cdot \Big[2(\boldsymbol{u} \times \boldsymbol{\Omega}) - (\boldsymbol{u} \cdot \boldsymbol{\nabla})\boldsymbol{u}\Big], \tag{4.39}$$

and the radial component of the curl of the momentum equation,

$$\begin{aligned} -\frac{\partial}{\partial t}(\nabla_\perp^2 Z) = {} & \hat{\boldsymbol{r}} \cdot \left[\boldsymbol{\nabla} \times (\boldsymbol{\nabla} \cdot \underline{\underline{\hat{\boldsymbol{\mathcal{D}}}}})\right] - \hat{\rho}\,\hat{\boldsymbol{r}} \cdot [\boldsymbol{\nabla} \times (\boldsymbol{u} \cdot \boldsymbol{\nabla})\boldsymbol{u}] \\ & + 2(\boldsymbol{\Omega} \cdot \boldsymbol{\nabla})\hat{\rho} u_r + \frac{2\hat{\rho}\Omega u_\theta \sin\theta}{r}. \end{aligned} \tag{4.40}$$

In the above equations, the horizontal Laplacian operator is defined

$$\nabla_\perp^2 = \frac{1}{r^2 \sin\theta} \frac{\partial}{\partial\theta}\left(\sin\theta \frac{\partial}{\partial\theta}\right) + \frac{1}{r^2 \sin^2\theta} \frac{\partial^2}{\partial\phi^2}, \tag{4.41}$$

while the horizontal divergence of a vector $\boldsymbol{A}$ is defined

$$\boldsymbol{\nabla}_\perp \cdot \boldsymbol{A} = \frac{1}{r\sin\theta} \frac{\partial(\sin\theta\, A_\theta)}{\partial\theta} + \frac{1}{r\sin\theta}\frac{\partial A_\phi}{\partial\phi}. \tag{4.42}$$

Equations (4.38)–(4.40), together with the anelastic energy equation (4.27), form the evolution equations solved by the ASH code. Detailed derivations of these equations are provided in §B.3 of Appendix B.

4.3 THE ASH CODE: NUMERICAL IMPLEMENTATION

We now summarize the discretization scheme and parallel implementation of the ASH code, following the more detailed presentation of Miesch (1998).

4.3.1 Angular Discretization

The first step in the pseudo-spectral method is to express all dependent variables as a projection over orthogonal basis functions. For the angular dependence, the basis functions are the spherical harmonics Y_ℓ^m,

$$Y_\ell^m(\theta,\phi) = C_\ell^m P_\ell^m(\cos\theta)\, e^{im\phi}, \tag{4.43}$$

where the functions P_ℓ^m are the associated Legendre functions, and where the constants C_ℓ^m are defined

$$C_\ell^m = (-1)^m \left[\frac{2\ell+1}{4\pi}\frac{(\ell-m)!}{(\ell+m)!}\right]^{\frac{1}{2}}. \tag{4.44}$$

The spherical harmonic functions are characterized by the angular degree ℓ and azimuthal order m. All dependent variables $f(r,\theta,\phi,t)$ in the problem are expressed as linear combinations of the spherical harmonics,

$$f(r,\theta,\phi,t) = \sum_{\ell=0}^{\infty}\sum_{m=-\ell}^{\ell} f_\ell^m(r,t) Y_\ell^m(\theta,\phi), \tag{4.45}$$

where the spectral coefficients $f_\ell^m(r,t)$ are found by the formula

$$\begin{aligned} f_\ell^m(r,t) &= \int_0^{2\pi} d\phi \int_0^{\pi} \sin\theta \, d\theta \, Y_\ell^{m*}(\theta,\phi) \, f(r,\theta,\phi,t) \\ &= C_\ell^m \int_0^{\pi} \sin\theta \, d\theta \, P_\ell^m(\cos\theta) \int_0^{2\pi} d\phi \, e^{-im\phi} \, f(r,\theta,\phi,t). \end{aligned} \tag{4.46}$$

Equation (4.46) constitutes the continuous spherical harmonic transform formula.

Numerical simulations are of course discretized, either by having a discrete grid in physical space or by limiting the number of mode coefficients in spectral space. To maximize the accuracy of the transforms, Gaussian quadrature techniques are utilized in evaluating the integrals of equation (4.46), where continuous integrals are approximated as weighted sums over predetermined collocation points (θ_i, ϕ_j) known as Gaussian abscissae. The Gaussian abscissae depend only on the number of collocation points and the orthogonal basis used in the expansion. Using Gaussian quadrature, the spherical harmonic transform of equation (4.46) becomes

$$\begin{aligned} f_\ell^m(r,t) &= C_\ell^m \sum_{i=1}^{N_\theta} w_i P_\ell^m(\cos\theta_i) \sum_{j=1}^{N_\phi} w_j e^{-im\phi_j} f(r,\theta_i,\phi_j,t) \\ &= \sum_{i=1}^{N_\theta} \sum_{j=1}^{N_\phi} w_i w_j Y_\ell^{m*}(\theta_i,\phi_j) f(r,\theta_i,\phi_j,t), \end{aligned} \tag{4.47}$$

where N_θ and N_ϕ are the number of collocation points used in the θ and ϕ directions. In this formula, the Gaussian abscissae in ϕ are the Fourier collocation points ϕ_j, where

$$\phi_j = \frac{2\pi j}{N_\phi} \qquad \text{where} \qquad j = 1, 2, \cdots, N_\phi, \tag{4.48}$$

having weights w_j of

$$w_j = \frac{1}{N_\phi}. \tag{4.49}$$

The Gaussian abscissae in θ are the Legendre collocation points θ_i, where

$$\theta_i = \text{zeroes of } P_{N_\theta}(\cos\theta) \qquad \text{with} \qquad i = 1, 2, \cdots, N_\theta, \tag{4.50}$$

having weights w_i of

$$w_i = \frac{2}{[\sin^2\theta_i \, P'_{N_\theta}(\cos\theta_i)]^2}. \tag{4.51}$$

In equations (4.50) and (4.51), the functions $P_\ell(\cos\theta)$ are the Legendre functions of the first kind, with

$$P'_{N_\theta} = \left.\frac{dP_{N_\theta}(\cos\theta)}{d(\cos\theta)}\right|_{\theta=\theta_i}. \tag{4.52}$$

The values N_θ and N_ϕ determine the angular resolution in physical space in both the latitudinal and longitudinal directions. To ensure that the horizontal resolution is even everywhere on a spherical surface, we set $N_\phi = 2N_\theta$, and truncate the spherical harmonic expansion of equation (4.45) at a maximum angular degree ℓ_{max}, wherein all modes for which $0 \le \ell \le \ell_{\text{max}}$ and $-\ell_{\text{max}} \le m \le \ell_{\text{max}}$ are used in the expansion. To attenuate aliasing errors when evaluating the nonlinear terms in the evolution equations, we also choose ℓ_{max} to satisfy

$$N_\theta \ge \frac{3\ell_{\text{max}} + 1}{2}. \tag{4.53}$$

4.3.2 Radial Discretization

As with the angular discretization, the radial discretization is handled in a similar fashion. The radial dependence of each field is evaluated only at discrete collocation points, and is transformed to spectral space using Gaussian quadrature. Each coefficient $f_\ell^m(r,t)$ is expanded over the set of Chebyshev polynomials T_n of order n, where

$$T_n(x) = \cos(n \arccos x). \tag{4.54}$$

While the T_n appear trigonometric, they are in fact polynomials in x defined on $(-1, 1)$. The physical radii r_k are scaled to the Chebyshev gridpoints x_k by

$$r_k = \frac{1}{2}\Big[(r_1 + r_2) + (r_2 - r_1)x_k\Big], \tag{4.55}$$

where r_1 and r_2 are respectively the radii of the lower and upper boundary of the physical domain such that they map to -1 and 1 in the Chebyshev domain.

Each discrete function $f_\ell^m(r_k,t)$ can be expressed as a truncated series

$$f_\ell^m(r_k,t) = \frac{2}{N_r-1}\sum_{n=1}^{N_r} \epsilon_n f_{\ell n}^m(t) T_{n-1}(x_k), \tag{4.56}$$

where the spectral coefficients $f_{\ell n}^m$ are found by evaluating

$$f_{\ell n}^m = \sum_{k=1}^{N_r} w_k T_{n-1}(x_k) f_\ell^m(x_k,t). \tag{4.57}$$

The Chebyshev collocation points x_k are

$$x_k = \cos\left(\frac{(k-1)\pi}{N_r-1}\right), \tag{4.58}$$

while the weights w_k are

$$w_k = \frac{\epsilon_k \pi}{N_r-1}. \tag{4.59}$$

In this formula and in equation (4.56), the constant ϵ_k is equal to 1, unless $k=1$ or $k=N_r$, for which $\epsilon_k = \dfrac{1}{2}$.

4.3.3 Temporal Discretization and Parallel Implementation

When transformed to spectral space, the ASH code evolution equations (4.27) and (4.38)–(4.40) are of the form

$$\frac{\partial y}{\partial t} = \mathcal{L} + \mathcal{N}, \tag{4.60}$$

where $\mathcal{L}$ and $\mathcal{N}$ respectively designate linear and nonlinear source terms.[1] Generally, these source terms can be a function of any of the dependent variables W, Z, p, and s as well as a function of the independent variables r, θ, ϕ, and t.

The time-stepping for both the linear and nonlinear source terms is performed simultaneously using a combination of the Crank-Nicholson scheme for the linear source

[1] Although the Coriolis terms are linear, they are grouped with the nonlinear source terms $\mathcal{N}$ in the ASH code time-stepping algorithm.

terms $\mathcal{L}$ and the Adams-Bashforth scheme for the nonlinear source terms $\mathcal{N}$. Both methods are accurate to second-order. By combining the two methods (see Appendix C), we discretize equation (4.60) to obtain

$$\frac{y_{i+1} - y_i}{\Delta t_i} = \left(1 + \frac{1}{2}\frac{\Delta t_i}{\Delta t_{i-1}}\right)\mathcal{N}_i - \left(\frac{1}{2}\frac{\Delta t_i}{\Delta t_{i-1}}\right)\mathcal{N}_{i-1} + \Theta\mathcal{L}_{i+1} + (1-\Theta)\mathcal{L}_i, \tag{4.61}$$

where subscripts are used to denote the index of the time step. For example, y_i denotes the value of y at the most recently computed time step (occurring at time t_i) and y_{i+1} denotes the yet-to-be-computed value of y at the next time step. The time separation between subsequent time steps is $\Delta t_i = t_{i+1} - t_i$.

After rewriting, equation (4.61) becomes

$$y_{i+1} - \Delta t_i \Theta \mathcal{L}_{i+1} = y_i + \Delta t_i \left[\left(1 + \frac{1}{2}\frac{\Delta t_i}{\Delta t_{i-1}}\right)\mathcal{N}_i - \left(\frac{1}{2}\frac{\Delta t_i}{\Delta t_{i-1}}\right)\mathcal{N}_{i-1} + (1-\Theta)\mathcal{L}_i\right]. \tag{4.62}$$

Since the term $\mathcal{L}_{i+1}$ is linear, we may write $\mathcal{L}_{i+1} = \mathcal{A}' y_{i+1}$, where $\mathcal{A}'$ is a matrix operator. Equation (4.62) now becomes the matrix equation

$$\mathcal{A} y_{i+1} = \mathcal{B}, \tag{4.63}$$

where

$$\mathcal{A} = 1 - \Delta t_i \Theta \mathcal{A}' \tag{4.64}$$

and

$$\mathcal{B} = y_i + \Delta t_i \left[\left(1 + \frac{1}{2}\frac{\Delta t_i}{\Delta t_{i-1}}\right)\mathcal{N}_i - \left(\frac{1}{2}\frac{\Delta t_i}{\Delta t_{i-1}}\right)\mathcal{N}_{i-1} + (1-\Theta)\mathcal{L}_i\right]. \tag{4.65}$$

The updated fields y_{i+1} are determined by solving the matrix equation (4.63) once $\mathcal{A}$ and $\mathcal{B}$ are calculated.

We now summarize the main loop of the ASH code:

- At the beginning of each iteration, the dependent variables y_i begin in (r, ℓ, m)-space.

- Spatial derivatives of the dependent variables are evaluated. First, each quantity is transformed to (n, ℓ, m)-space via a Chebyshev transform, then the derivatives are evaluated using Chebyshev recursion relations, and then the derivatives are transformed back to (r, ℓ, m)-space via an inverse Chebyshev transform.

- The linear term $\mathcal{L}_i$ is evaluated in (r, ℓ, m)-space.

- The dependent variables y_i are transformed to (r, θ, ϕ)-space via an inverse Legendre transform (to go from ℓ to θ) and an inverse Fourier transform (to go from m to ϕ).

- The nonlinear term $\mathcal{N}_i$ is evaluated in (r, θ, ϕ)-space.

- The nonlinear term $\mathcal{N}_i$ is transformed back to (r, ℓ, m)-space via a forward Legendre transform and a forward Fourier transform.

- The quantity $\mathcal{B}$ of equation (4.65) is evaluated, now that we have available the terms $\mathcal{L}_i$, $\mathcal{N}_i$, and $\mathcal{N}_{i-1}$, with the latter term saved over from the previous time step.

- The quantity $\mathcal{A}$ of equation (4.64) is calculated.

- The matrix equation (4.63) is solved for y_{i+1} using LU-decomposition.

As stated at the beginning of this chapter, the ASH code runs efficiently on massively parallel architectures such as the Cray T3E and Origin 2000 machines (Clune et al. 1999). These machines are of the distributed-memory configuration, where each processor has its own local memory bank independent of the other processors. Such a configuration requires to the programmer to devise sensible algorithms responsible for evenly splitting up the workload (load-balancing) and coordinating interprocessor communication when information is needed by multiple processors.

The most computationally intensive steps of the flowchart above involve global operations such as the spectral transforms and the solution of the matrix equation. The strategy adopted by the ASH code is to perform all transforms between the physical and spectral domains in-processor so as to avoid interprocessor communication during the transform. However, such a scheme requires frequent global transposes in order to arrange the data such that the dimension of the transform is local.

Chapter 5

SUPERGRANULAR CONVECTION IN THIN SHELL MODELS

5.1 INTRODUCTION

Helioseismology has shown that the latitudinally varying angular velocity profile observed at the surface is largely maintained throughout the bulk of the convection zone (Thompson et al. 1996; Schou et al. 1998). The angular velocity is nearly constant along radial lines, particularly at mid-latitudes, as seen in Figure 5.1. However, regions of strong radial shear (shown shaded) exist near both the bottom and the top of the convection zone, and these shear layers are thought to play important roles in the dynamics of the convection zone. The tachocline region at the base of the convection zone has commanded much recent attention as it is likely the seat of the global solar dynamo. Portions of the strong toroidal magnetic fields thought to be generated by the shearing motions within the tachocline will likely rise buoyantly through the convection zone in a coherent fashion until they reach the surface. Such magnetic structures are believed to produce the observed large-scale patterns of magnetic activity visible at the photosphere, including sunspots and bipolar active regions, that comprise the 22-year solar magnetic activity cycle. This flux may also contribute to the production of small-scale magnetic field elements seen at the photosphere, including bright points, pores, and the magnetic carpet, although these features are more likely the result of local dynamo action closer to the surface.

Prior to their emergence, the small-scale filamentary magnetic structures must

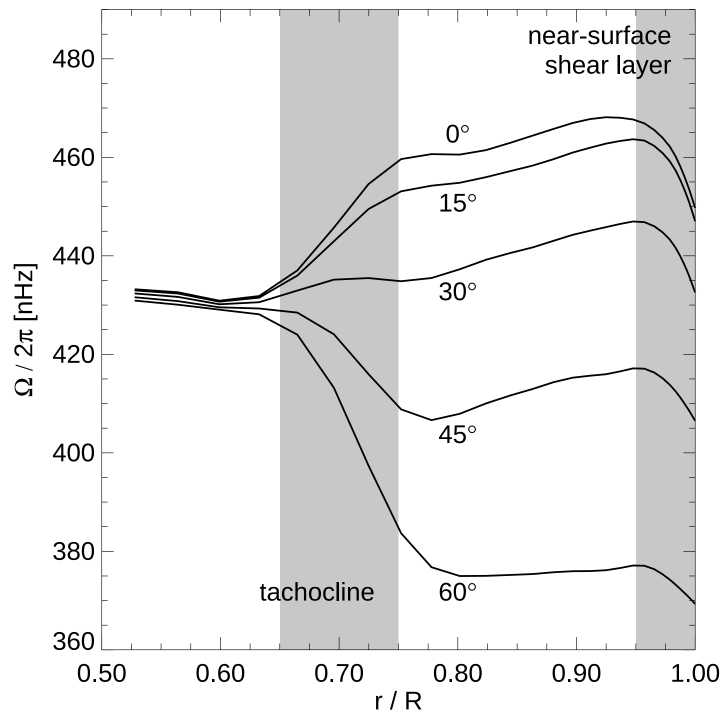

Figure 5.1: Average rotation rates $\Omega/2\pi$ inferred from the helioseismic inversion of over 4 years of GONG data using RLS inversions (adapted from Howe et al. 2000). Shear layers (*shaded*), evidenced by variations of Ω with radius, are observed near the base of the convection zone as well as near the surface, with the latter region extending from 0.95–1.00 R (where R is the radius of the sun). The gradients of Ω in that near-surface shear layer at high latitudes is somewhat sensitive to the inversion method and data sets used (e.g. see Schou et al. 1998).

be at least partially influenced by the dynamics within the upper shear layer of the solar convection zone. The stratification within this region serves to drive vigorous motions possessing a wide range of spatial and temporal scales, visible at the surface as the convective patterns of supergranulation, mesogranulation, and granulation (Spruit et al. 1990). The outflows associated with such convective motions are observed to readily advect emergent magnetic flux toward intercellular lanes and concentrate these fields on scales small enough for dissipation to occur. It is not yet known to what degree large-scale magnetic structures such as sunspots and active regions are impacted by the turbulent convection occurring near the surface. In addition to reconfiguring magnetic flux, these convective motions facilitate the transport of angular momentum along both radial and latitudinal velocity gradients, and are likely to influence the dynamics of the bulk of the convection zone in ways that are not yet understood. The relatively large horizontal and radial extent of supergranular flows in particular suggest that they play a prominent role in the dynamics within this shearing boundary layer, as such motions may be weakly influenced by rotational effects that create the Reynolds stresses necessary for efficient turbulent transport of angular momentum within the layer.

Velocity features larger than the spatial scale of solar supergranulation are also evident (e.g. Giles et al. 1998; Haber et al. 2000) in the upper shear layer. Banded zonal velocity features which propagate in latitude are visible in long-term observations of the photosphere (LaBonte & Howard 1982; Hathaway et al. 1996; Howe et al. 2000), suggesting a weak organization on larger spatial scales. Helioseismic observations indicate a steady, longitudinally averaged, meridional flow toward the poles having speeds of order 20 m s^{-1}, extending to depths of at least 20 Mm below the visible surface (Giles et al. 1998; Haber et al. 2000). The return flow necessary to satisfy mass conservation has not yet been detected. Despite the slower fluid velocities associated with such large-scale flow patterns, fluid motions in the meridional plane can still effectively redistribute angular momentum and couple widely separated regions within the solar convection zone.

To understand more clearly some of the physical processes occurring within the upper shear layer of the solar convection zone, we have constructed numerical simulations of a compressible fluid confined to a thin spherical shell located near the top of the convection zone. These simulations constitute the first global simulations of solar convection at a resolution high enough to begin to explicitly resolve fluid motions on supergranular scales. Such calculations are performed using the ASH computer code described in Chapter 4, which runs efficiently on massively parallel computer platforms such as the Cray T3E and Origin 2000 machines (Clune et al. 1999). The complex structures and intricate behavior of the resulting convection require high spatial resolution, and the flows must be studied for long periods of time for statistical equilibrium to be achieved.

In constructing these simulations, we have adopted the viewpoint that the angular velocity profile seen in helioseismic observations is maintained within the bulk of the convection zone, somewhere below the bottom boundary of our models, where the combined effects of convection and rotation create a net equatorward transport of angular momentum. Numerical simulations of the full convection zone suggest that such transport is achieved by Reynolds stresses and large-scale meridional circulation, all working against diffusion (e.g. Miesch et al. 2000; Elliott et al. 2000; Brun & Toomre 2001). From this perspective, we are essentially assuming that the global differential rotation profile is not substantially affected by the convection within our thin shells, and thus can be imposed via the velocity boundary condition applied to the lower boundary. We can therefore only explore the effects of such differential rotation within a thin spherical layer of convection, but are able to investigate some of the ingredients associated with the formation of shearing boundary layers analogous to the near-surface shear layer of the sun.

After discussing the initialization of the four thin shell simulations in §5.2, we begin in §5.3 by illustrating the velocity patterns and time evolution of the multiple-scale convection driven within our simulations. We then in §5.4 examine the energy balance responsible for the resulting axisymmetric differential rotation and meridional circulation profiles and discuss the role of the convective motions in their maintenance. We conclude with a discussion of the solar implications of these simulations and present ideas for future research in §5.5.

Table 5.1: A summary of the parameters of the thin shell convection simulations. The differences between Case *S2* and the other three simulations are set in bold.

	Case *S1*	Case *S2*	Case *S3*	Case *D2*
Radial Extent	0.94–0.98 R	0.94–0.98 R	0.94–0.98 R	**0.90**–0.98 R
Thickness [Mm]	28	28	28	**56**
Velocity BC's at Top	stress-free impenetrable	stress-free impenetrable	stress-free impenetrable	stress-free impenetrable
Velocity BC's at Bottom	no-slip **uniform rot.** impenetrable	no-slip differential rot. impenetrable	no-slip differential rot. impenetrable	no-slip differential rot. impenetrable
Entropy BC's at Top	constant entropy	constant entropy	constant entropy	constant entropy
Entropy BC's at Bottom	constant flux	constant flux	constant flux	constant flux
Ang. velocity Ω_0 [nHz]	410	410	410	410
Rot. period P [days]	28.2	28.2	28.2	28.2
$\nu_{\rm top}$ [cm^2 s^{-1}]	1×10^{12}	1×10^{12}	$\mathbf{5 \times 10^{11}}$	1×10^{12}
$\kappa_{\rm top}$ [cm^2 s^{-1}]	1×10^{12}	1×10^{12}	$\mathbf{2 \times 10^{12}}$	1×10^{12}
Density contrast	7.5	7.5	7.5	**18**
Prandtl number P_r	1	1	$\mathbf{\frac{1}{4}}$	1
Taylor number T_a	5.4×10^3	5.4×10^3	5.4×10^3	2.1×10^5
Reynolds number R_e	1.4×10^2	1.4×10^2	1.4×10^2	2.2×10^2
Rayleigh number R_a	1.9×10^4	1.9×10^4	1.9×10^4	5.4×10^5
Supercriticality $\frac{R_a}{R_{a,0}}$	40	100	200	500
Averaging Interval [days]	140	140	30	36
$N_r \times N_\theta \times N_\phi$ $\ell_{\max}$ Ang. Periodicity	64×512×1024 340 four-fold	64×512×1024 340 four-fold	**128**×512×1024 340 four-fold	**128**×512×1024 340 four-fold

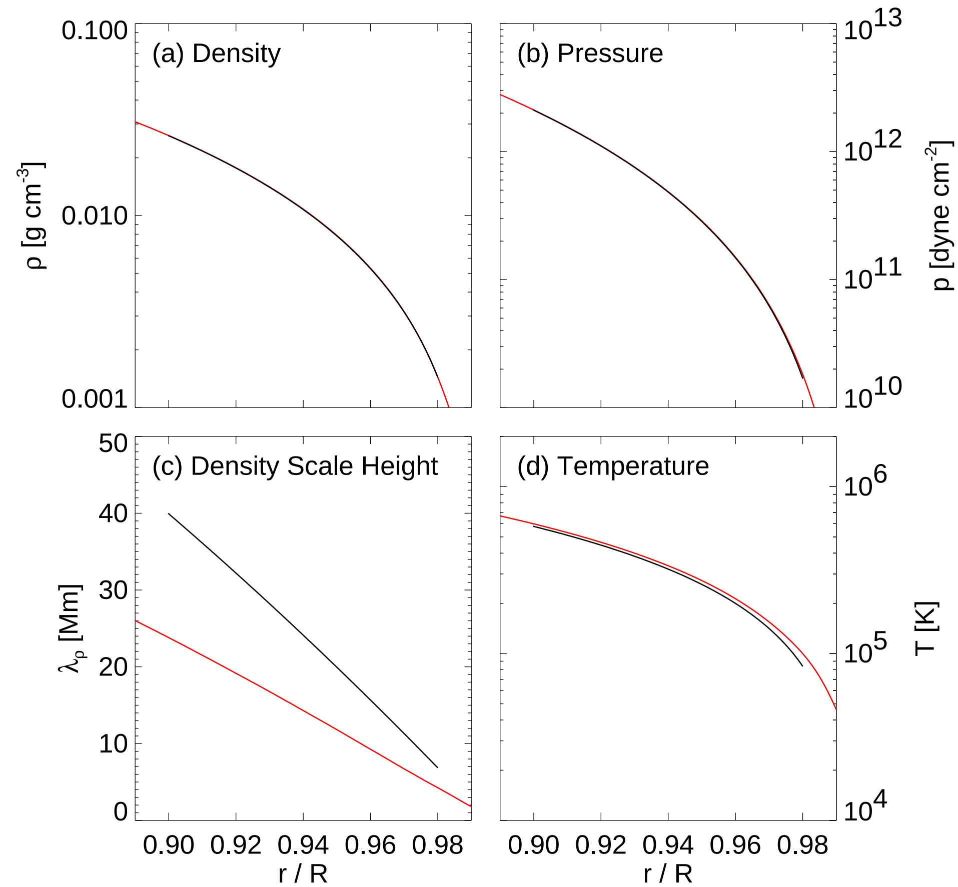

Figure 5.2: The radial profiles of (*a*) density, (*b*) pressure, (*c*) density scale height, and (*d*) temperature as a function of proportional radius used upon initialization of the simulations (*black*), compared with the corresponding values taken from a one-dimensional solar structure model (*red*).

5.2 SUMMARY OF SIMULATION PARAMETERS

5.2.1 Initialization of the Spherically Symmetric Mean State

We have constructed three shallow shell simulations (Cases *S1*, *S2*, and *S3*) that span a radial extent of 0.94–0.98 R, equivalent to a shell thickness of 28 Mm. The remaining simulation (Case *D2*) spans 0.90–0.98 R or 56 Mm, and is accordingly twice as thick as the three shallow shell simulations but otherwise equivalent to Case *S2*.

We simulate the angular velocity profile established within the deep convection zone by imposing a differentially rotating no-slip lower boundary on Cases *S2*, *S3*, and *D2*. For comparison purposes, the lower boundary of Case *S1* is maintained at a uniform rate equal to the angular velocity Ω_0 of the computational frame, with all other attributes equivalent to Case *S2*. In all four cases, the upper boundary is stress-free and both the lower and upper boundaries are impenetrable. The parameters of the four thin shell simulations are summarized in Table 5.1.

As discussed in the previous chapter, the anelastic equations of motion are advanced in time by the ASH code using a pseudo-spectral approach, wherein functions of θ and ϕ are expanded over spherical harmonic functions characterized by angular degree ℓ and azimuthal order m. Functions of radius are projected onto Chebyshev polynomials characterized by radial order n. The four simulations presented here are calculated using spherical harmonic functions with $\ell_{\max} \leq 340$, so that horizontal scales as small as about 10 Mm are explicitly resolved. The highest order Chebyshev polynomial used is $n = 64$ in Cases *S1* and *S2*, and $n = 128$ in Cases *S3* and *D2*. Since we expect the resulting convection to have a limited longitudinal scale and seek computational economics, we impose a four-fold azimuthal symmetry by keeping every fourth m value in the spherical harmonic expansion. Such an imposed symmetry is primarily noticeable only in the higher latitude regions, where the convergence of meridional lines near the poles limits the longitudinal scale of the convective structures to sizes smaller than are present at lower latitudes.

During initialization, the radial profiles of density $\hat{\rho}(r)$, temperature $\hat{T}(r)$, and pressure $\hat{p}(r)$ are determined by jointly solving the equation of hydrostatic equilibrium (4.23) and the mean equations of state (4.24) and (4.25), given radial profiles of the gravitational acceleration $g(r)$ and specific entropy gradient $\frac{d\hat{s}}{dr}$ throughout the domain. We specify the initial entropy gradient to have a slightly superadiabatic value (e.g. $-\frac{d\hat{s}}{dr} = 10^{-7}$), while the function $g(r)$ is taken from the one-dimensional solar model of Brun et al. (1999). The initial values of $\hat{\rho}(r)$, $\hat{T}(r)$, and $\hat{p}(r)$ obtained in this way are shown in Figure 5.2 to compare favorably with the structure model, with the slight discrepancy in density resulting in a greater density scale height λ_ρ in our simulations than in the structure model.

With our current angular resolution, we are able to place the upper boundary of each simulation at 0.98 R and thus accommodate the intricate convective structures driven by the imposed solar-like stratification. Above this radius, the even greater degree of stratification is likely to drive modes of convection that are smaller in physical size and thus below our current resolution limit. In addition, the anelastic approximation is likely to break down as the convection becomes less efficient and typical convective velocities become a significant fraction of the speed of sound. Furthermore, the ionization zone of hydrogen is located above 0.98 R in the sun, suggesting that both the ideal gas equation of state and the diffusive treatment of radiative effects currently used in these calculations become inappropriate above this level. Consequently, the upper boundary of all four simulations is located at 0.98 R.

The ASH code is a LES-SGS simulation and thus requires a prescription to account for the transport of energy and momentum by turbulent motions not explicitly resolved. We have adopted the simplest approach of enhancing the molecular values of the viscous and thermal diffusivities, while recognizing that such an SGS treatment is unlikely to capture all dynamical effects of small-scale turbulence. The eddy diffusivities $\nu_{\rm eff}(r)$ and $\kappa_s(r)$ used in these simulations are chosen to vary inversely as the square root of the mean density profile, so that $\beta = \frac{1}{2}$ in

$$\nu_{\rm eff} = \nu_{\rm top} \left(\frac{\hat{\rho}}{\hat{\rho}_{\rm top}}\right)^{-\beta} \qquad \text{and} \qquad \kappa_s = \kappa_{\rm top} \left(\frac{\hat{\rho}}{\hat{\rho}_{\rm top}}\right)^{-\beta}. \tag{5.1}$$

This particular value of β was chosen to allow some variation of the dissipation scale with the density scale height λ_ρ, but at the same time to prevent numerical instabilities near the bottom of the domain where the dissipation length scale is smallest. We note that as computing technology becomes more advanced, the parameterization of SGS transport effects in simulations of highly turbulent fluids should become less of an issue because such global simulations will be able to explicitly resolve more of the energy transport at small dynamical scales. Nevertheless, we fully acknowledge that our SGS prescription is somewhat inadequate and requires considerable attention in the future.

The free parameters ν_{top} and κ_{top} in equation (5.1) are the viscous and thermal diffusivities at the upper boundary, and their ratio determines the Prandtl number $P_r = \dfrac{\nu_{\text{top}}}{\kappa_{\text{top}}} = \dfrac{\nu_{\text{eff}}}{\kappa_s}$ of each simulation. Cases *S1*, *S2*, and *D2* each have $P_r = 1$, while Case *S3* is constructed with $P_r = \frac{1}{4}$ in order to investigate a turbulent fluid which diffuses heat more readily than momentum. The lower Prandtl number of Case *S3* is achieved by increasing κ_{top} by a factor of 2 while simultaneously decreasing ν_{top} by a factor of 2, relative to Case *S2*.

The thermal driving in all cases is accomplished by setting the heat flux at the lower boundary equal to the solar value, while the upper boundary is held at constant entropy. The radiative diffusivity $\kappa_r(r)$ throughout the domain is taken from the structure model used above; however, we note that the radiative heat flux is several orders of magnitude smaller in our simulations than convective heat flux throughout the bulk of the domain. We have artificially increased the thermal eddy diffusivity κ_s near the boundaries in order to prevent the formation of thin diffusive thermal layers with a radial extent below our current radial resolution. This enhanced κ_s is applied only to the spherically symmetric component of the thermal field. Steep entropy gradients would otherwise be required to carry the imposed heat flux, since the radial velocities are forced to vanish, and so too the convective transport of heat near the boundaries. This enhanced κ_s profile turns out to play a sensitive role in determining the nature of the convection near the top of the thin shell simulations.

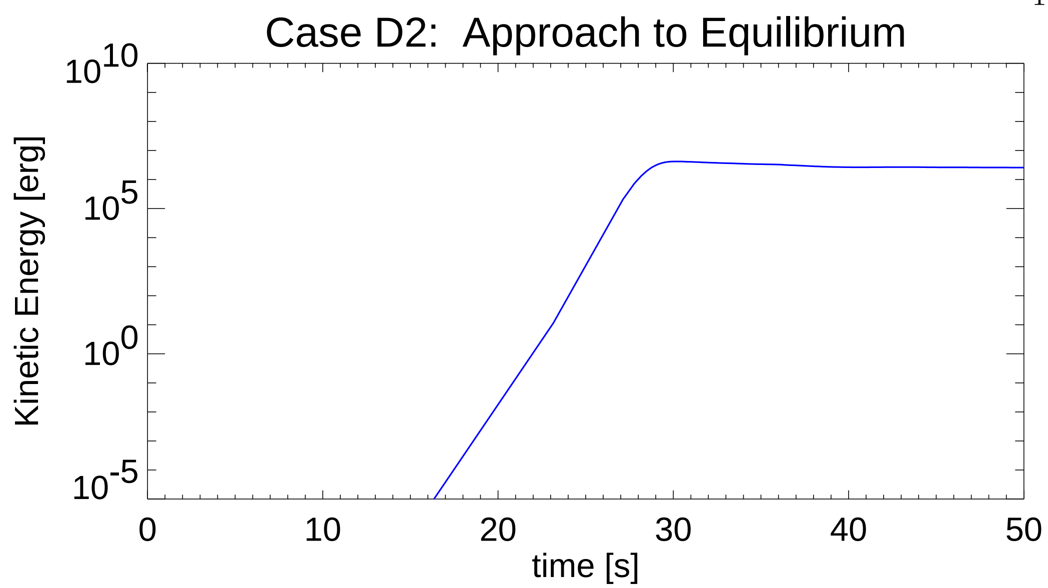

Figure 5.3: The domain-averaged kinetic energy as a function of time for Case *D2*. The ramp-up time of about 30 days from seed entropy perturbations is typical of the simulations considered here.

5.2.2 Approach to Thermal Equilibrium

Once the spherically symmetric mean state has been arranged, small seed perturbations are introduced into the fluctuating entropy field s', and the simulations advanced in time using the evolution equations (4.26) and (4.27). The seed entropy perturbations are soon reflected in the fluctuating density field ρ', whose variations quickly provide the unstable density imbalance that buoyantly accelerates the fluid from rest. After an initial period of adjustment during which the convection kinetic energy ramps up (typically about 30 days, as shown in Fig. 5.3 for Case *D2*), an approximate thermal equilibrium is reached.

In total thermal equilibrium, the outward energy transport in these simulations must be achieved by a balance of radiative, kinetic, enthalpy, and eddy diffusive fluxes,

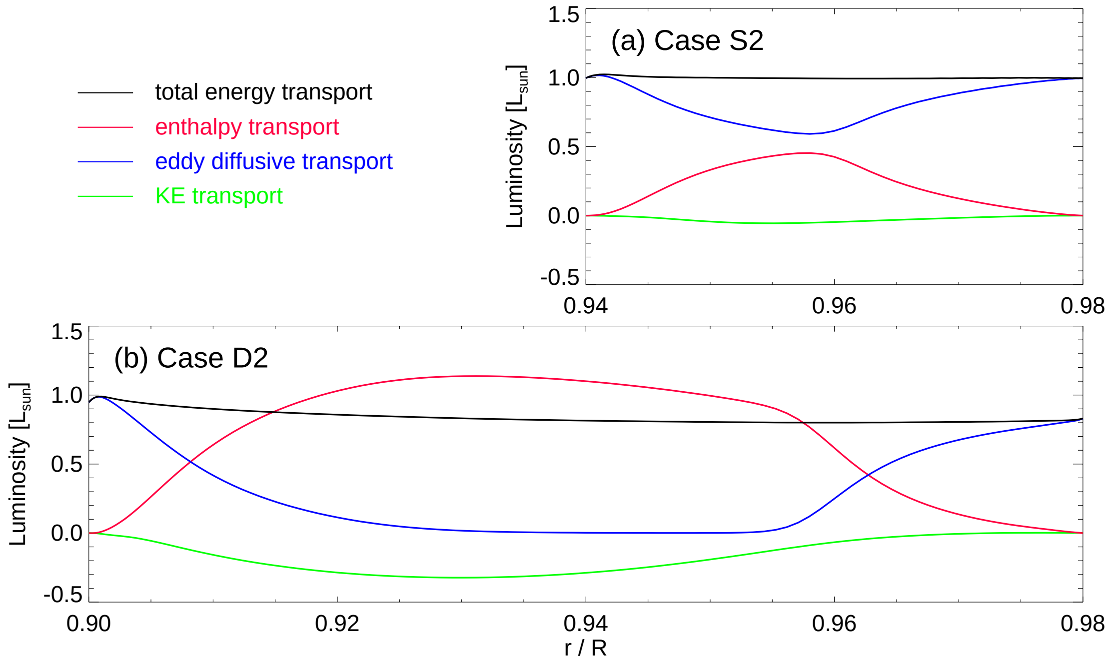

Figure 5.4: The time-averaged spherically symmetric energy balance within Cases *S2* and *D2* as a function of radius, showing the percentage of $L_\odot$ carried by kinetic energy F_k, enthalpy F_e, and by unresolved eddies F_u. The radiative flux F_r (not shown) is negligible in both cases.

as represented by the following:

$$F_k = u_r\left(\frac{\hat{\rho}u^2}{2}\right), \tag{5.2}$$

$$F_e = u_r\hat{\rho}c_p(T' - \langle T'\rangle), \tag{5.3}$$

$$F_r = -\kappa_r\hat{\rho}c_p\frac{\partial(\hat{T}+T')}{\partial r}, \tag{5.4}$$

$$F_u = -\kappa_s\hat{\rho}\hat{T}\frac{\partial(\hat{s}+s')}{\partial r}, \tag{5.5}$$

where the kinetic, enthalpy, radiative, and unresolved eddy fluxes are denoted by F_k, F_e, F_r, and F_u respectively. The quantity $T' - \langle T'\rangle$ appearing in the definition of F_e is the temperature excess relative to the mean (spherically symmetric) value of the temperature field at each radial level. In a true steady state, the total energy transport at each radius within the domain must equal the energy influx at the lower boundary, which in terms of luminosity is equivalent to the total solar luminosity $L_\odot$:

$$4\pi r^2(F_k + F_e + F_r + F_u) = L_\odot. \tag{5.6}$$

Figure 5.4 shows the time-averaged energy transport within Cases *S2* and *D2* as a function of radius at a late stage in the simulations. In both cases, the energy transport achieved by unresolved eddies reflects the enhanced profile of κ_s applied to the spherically symmetric entropy gradient. The function κ_s is determined during initialization and is typically about 3 orders of magnitude larger at the top than the corresponding $\kappa_{\rm top}$ felt by the convection. The radial energy transport within Cases *S1* and *S3* is qualitatively similar to Case *S2*.

5.3 GENERAL FLOW CHARACTERISTICS

5.3.1 Multi-Scale Convection

The convective flow patterns in these simulations are intricate, containing complex evolving structures occurring on multiple size scales. We illustrate the velocity patterns in Figures 5.5 and 5.6 by showing the radial velocity for Cases *S2* and *D2* at several depths within each domain. The horizontal structure of the radial velocity fields realized in Cases *S1* and *S3* are qualitatively similar to Case *S2*.

Figures 5.5a and 5.6a show that the largest scale of convection visible near the top of both Cases *S2* and *D2* is associated with a connected network of downflow lanes (green-blue colors) having a spatial scale of about 200 Mm. The large areas enclosed by the downflow lanes contain a number of smaller-scale upflows (orange-red tones) each measuring about 15–30 Mm across. Although the upflow cells in the shallow shell (Case *S2*) tend to be slightly larger than those in the deeper shell (Case *D2*), this general surface pattern of a network of connected downflow lanes enclosing several distinct smaller upflows appears to be a robust property of convection within our thin shells. We also note that the size of the smaller upflows in these simulations is approximately

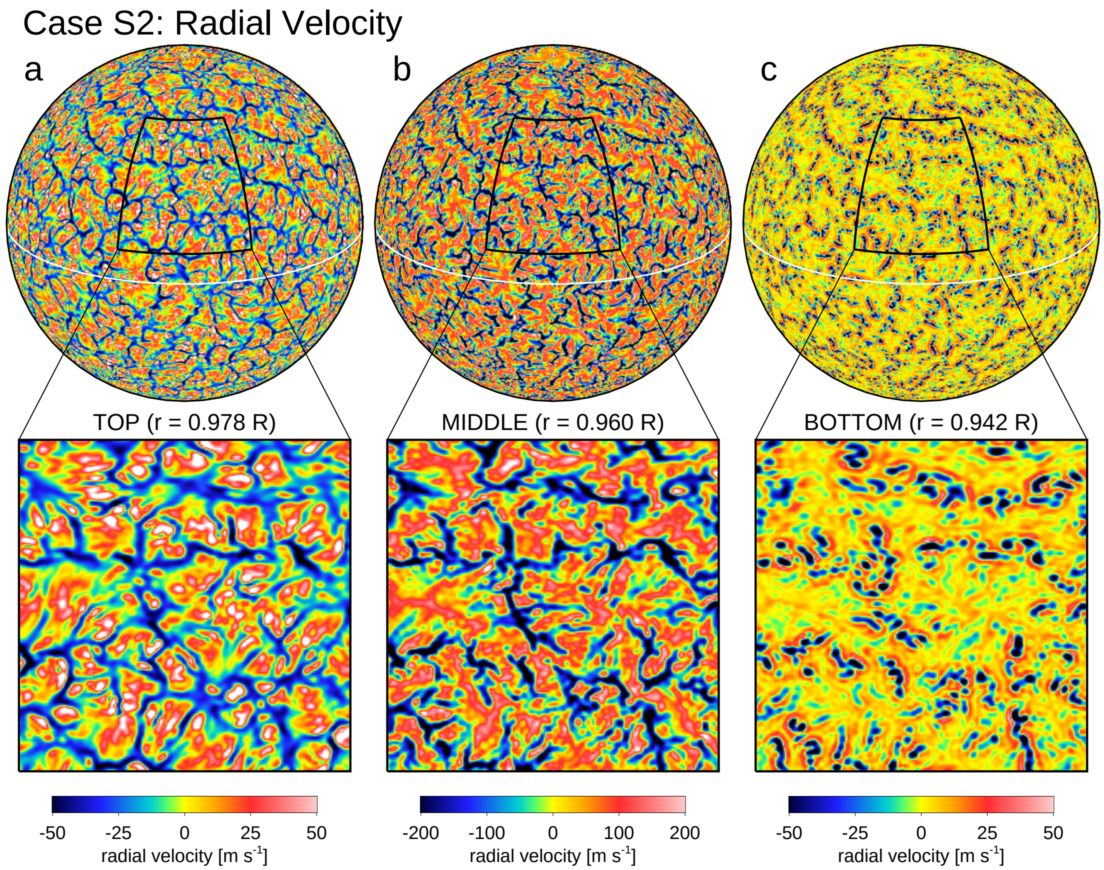

Figure 5.5: Instantaneous snapshots of radial velocity for Case *S2* near the (*a*) top, (*b*) middle, and (*c*) bottom of the domain. Positive radial velocities (orange-red colors) denote upflows and negative radial velocities (green-blue colors) denote downflows. Each image in the top row is an orthographic projection of the velocity field, with the north pole tilted 20° toward the observer and the equator indicated by a white line. Each enlarged image in the bottom row shows a rectangular (latitude-longitude) projection of a 45°-square portion of the corresponding velocity field in the top row. The four-fold azimuthal periodicity is most noticeable near the north pole.

equal to the horizontal size scale of solar supergranulation.

Figures 5.5*b*,*c* and 5.6*b*,*c* illustrate how the horizontal planforms change with depth for Cases *S2* and *D2* respectively. As the downwelling fluid reaches deeper layers, these convective structures no longer form a connected network composed of downflows having roughly constant vertical velocities along each lane. Although it is possible near the bottom to make out much of the pattern of downflow lanes seen near the

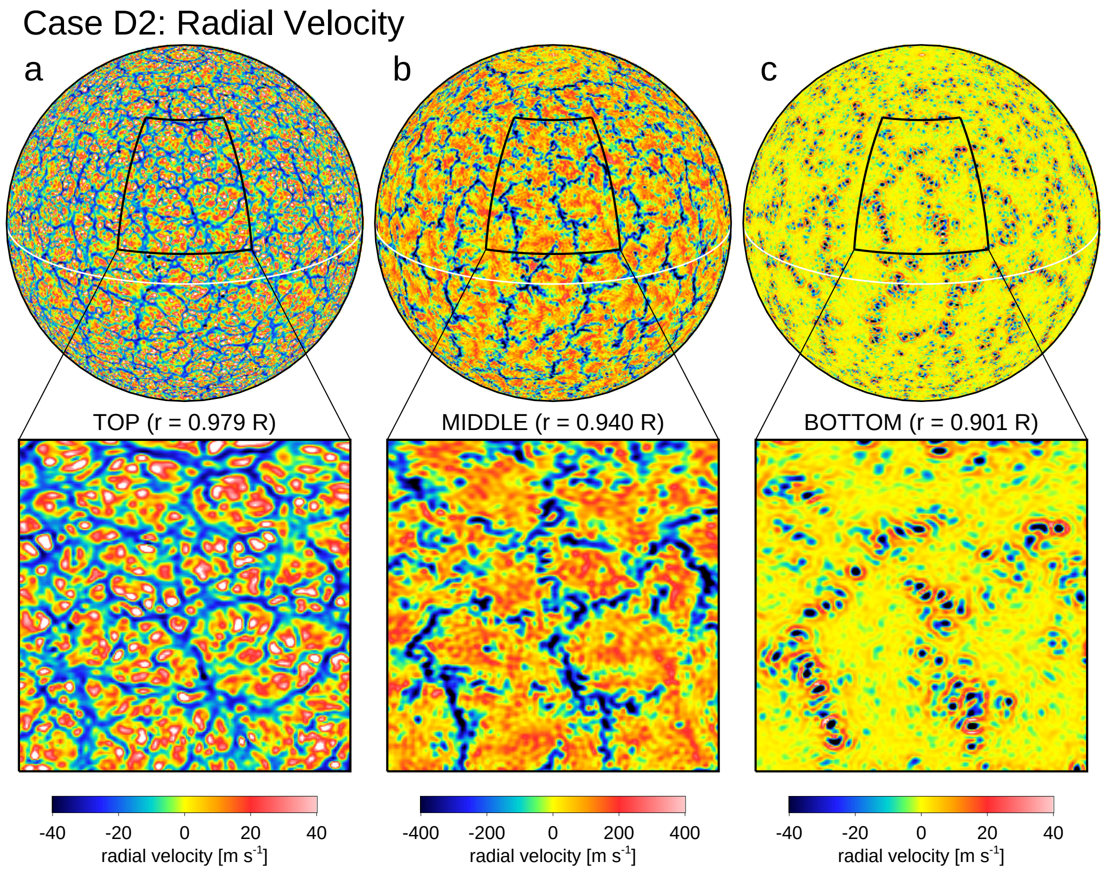

Figure 5.6: Same as in Fig. 5.5 except for Case *D2*, showing the radial velocity structure sampled near the (a) top, (b) middle, and (c) bottom of the deep shell simulation.

surface, the vertical velocities along each lane become increasingly less uniform, such that the downflows fragment into more isolated and compact plume-like structures with depth. This narrowing of scale is likely related to the larger densities found near the bottom of each domain. In addition, the strongest downflow lanes in the equatorial region of Case *D2* possess a noticeable north-south orientation that is reminiscent of the banana-cell modes evident in earlier, more laminar, spherical shell convection simulations (e.g. Miesch 1998). The columnar structures seen in Case *D2* are much thinner and have quite a bit more variation than the banana cells in the more laminar cases, as a result of the strong small-scale convection driven throughout the domain.

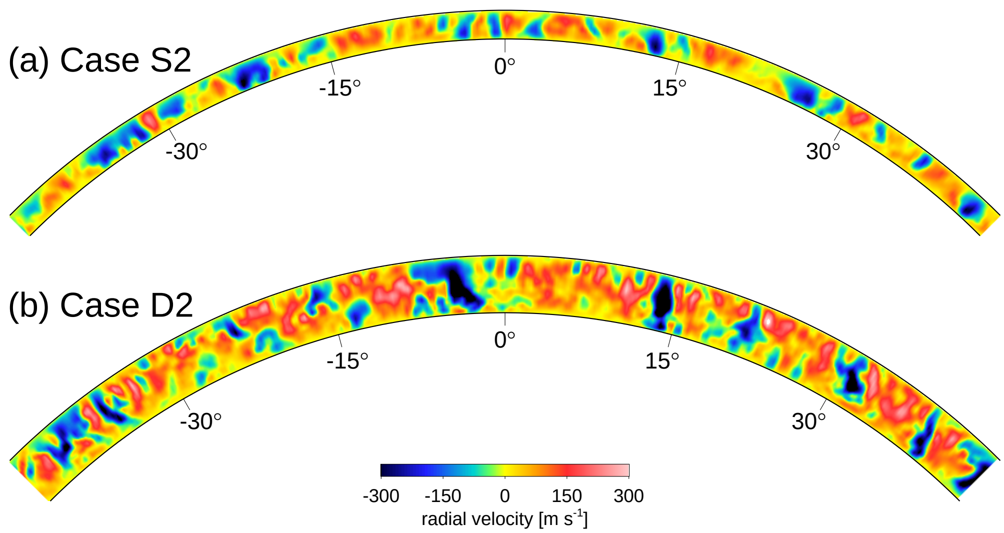

Figure 5.7: Images of the instantaneous radial velocity for Cases *S2* and *D2* as a function of latitude and radius in a cut of fixed longitude, showing the vertical structure of the pattern of upflows and downflows within each domain.

The pattern of smaller-scale upflows visible near the upper boundary of these simulations also changes its character with depth. The distinct upflows enclosed by downflow lanes seen in the upper layers gradually become more uniform, forming broad regions of upwelling fluid surrounded by an incomplete network of downflow lanes. Near the lower boundary, these broad upflow regions have largely disappeared, except for partial shrouds of upwelling fluid surrounding each of the stronger downflows. Figure 5.7 contains vertical cuts of the radial velocity field showing the variation with latitude and radius for Cases *S2* and *D2*. The radial structure of the broad upflow regions is most evident in Case *D2* (Fig. 5.7*b*), where the broad regions of upward moving fluid fragment into smaller-scale yet faster upflows as the top of the domain is approached.

Figure 5.8 shows the time evolution of the radial velocity field of Case *S2*. Such movie sequences illustrate the tendency for smaller flow features to be systematically advected by larger-scale velocity patterns. One small upflow (indicated by the arrow) as well as the downflow lane immediately to its left are both advected laterally by the

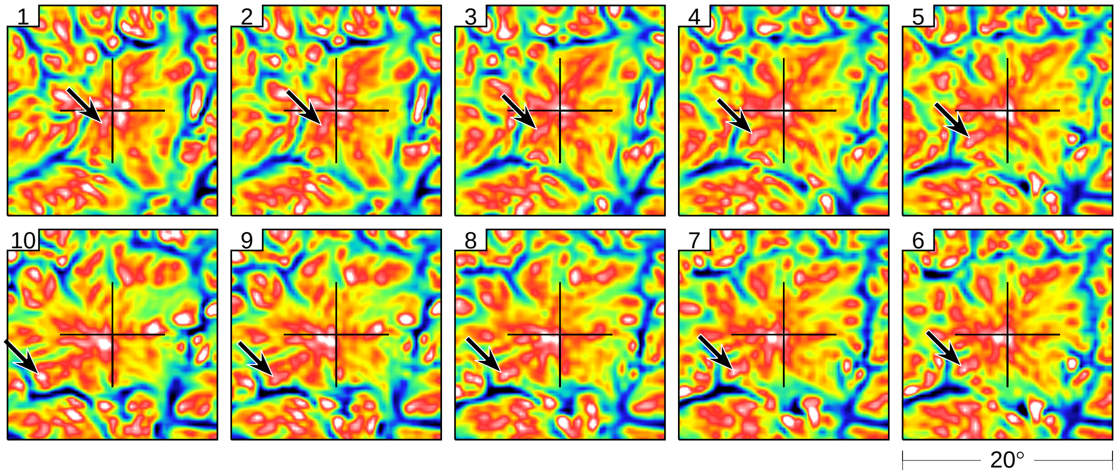

Figure 5.8: A time series of images showing a 20°-square region of Case *S2* near the upper boundary showing small-scale features in radial velocity being laterally advected by larger-scale horizontal motions. The arrow points to one such small-scale upflow which is advected away from the center of the broader upflow (indicated by the dark cross). The time index of each image is indicated in the upper-left corner, and the cadence is about 1.3 days between images.

horizontal outflow motions associated with the broader cell. The center of this broad outflow cell is indicated by a cross. Such lateral transport of velocity features by larger scales of convection is most apparent in movie sequences showing the time evolution of the radial velocity field.

In Figure 5.9 we present space-time diagrams of radial velocity sampled in time for four specific latitudes (and all longitudes) at a radius of 0.978 R for Case *S2*, plotted with respect to the rotation rate of the computational frame Ω_0. The advection of radial velocity structures appear as slanted features in each panel, with the higher latitudes rotating more slowly (retrograde) than those near the equator. The mean advection rate of the radial velocity patterns at the surface approximately equals the differential rotation rate of the fluid for the same depth. The latitudinal variation of angular velocity shown in the figure results largely from the imposed differential rotation at the lower boundary. It is interesting to note from Figure 5.9 that the pattern speed of

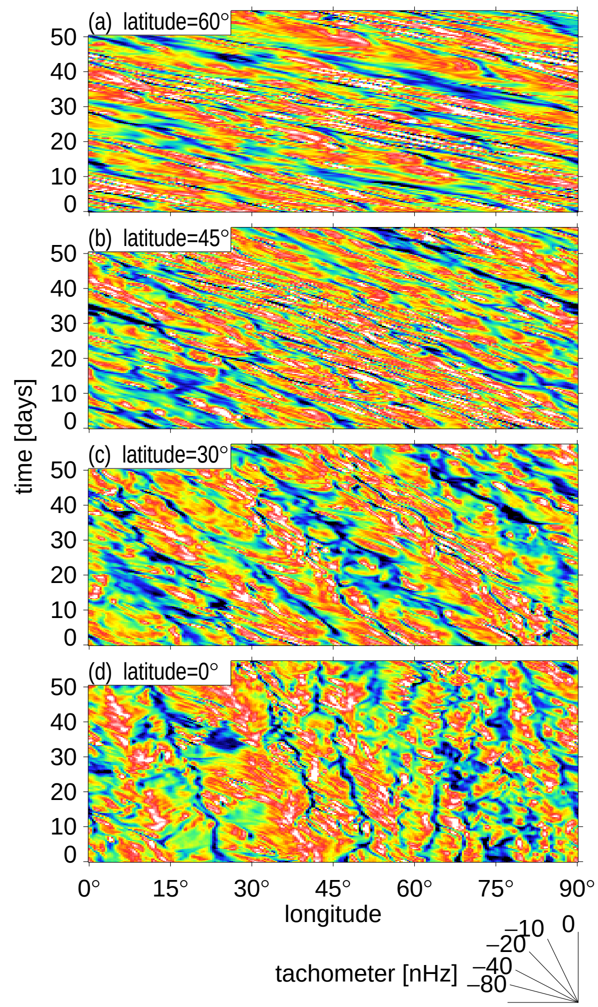

Figure 5.9: Near-surface radial velocity structures at four specific latitudes from Case *S2*, plotted as a function of time and latitude. As labeled, the four panels correspond to latitudes of 0°, 30°, 45°, and 60°. The retrograde propagation rate of these features, quantified by the tachometer, is a reflection of the no-slip differential lower boundary.

the advected structures varies somewhat with longitude, as structures having the same latitude but separated in longitude may exhibit different propagation rates.

The characteristic size scales of the convective structures near the top of these thin shell simulations are sensitive to the degree of driving they experience. We find that adjusting either the diffusivities or the superadiabaticity within the domain will alter the appearance of the convection. The superadiabaticity depends on the functional form

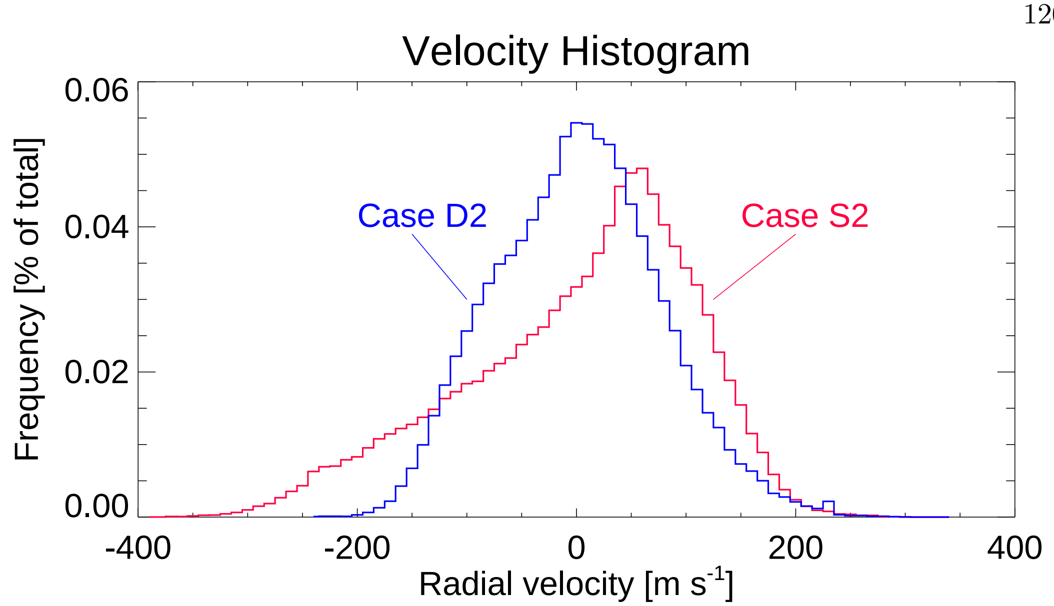

Figure 5.10: The distribution of radial velocities for the shallow and deep shells (Cases *S2* and *D2*) attained at mid-shell as shown in Figs. 5.5*b* and 5.6*b* respectively. The corresponding rms velocities are 105 m s^{-1} for Case *S2* and 140 m s^{-1} for Case *D2*. Positive radial velocities denote upflows and negative radial velocities denote downflows.

of the spherically symmetric κ_s profile, set upon the initialization of each simulation. The functional form of this profile in essence determines how much energy needs to be transported via convection near the top of the domain, which in turn feeds back on the entropy gradient. We have chosen a somewhat gentle κ_s function, as suggested by the profile of F_u in Figure 5.4, initialized to have an e-folding depth away from each boundary of about 0.01 R for both the shallow and deep shell cases.

The peak radial velocities attained by the convective structures at mid-shell in Cases *S2* and *D2* are 300 m s^{-1} and 400 m s^{-1} respectively, as shown in the radial velocity distributions of Figure 5.10. The distribution of radial velocity for Case *S2* at 0.96 R is noticeably asymmetric, such that mean downward velocities are much faster than the mean upward velocities. The fastest downward velocities correspond to the downflow lane network evident in the middle of the shell, as illustrated in Figure 5.5*b*. The radial velocity distribution for Case *D2* is more symmetric, indicating that the flow

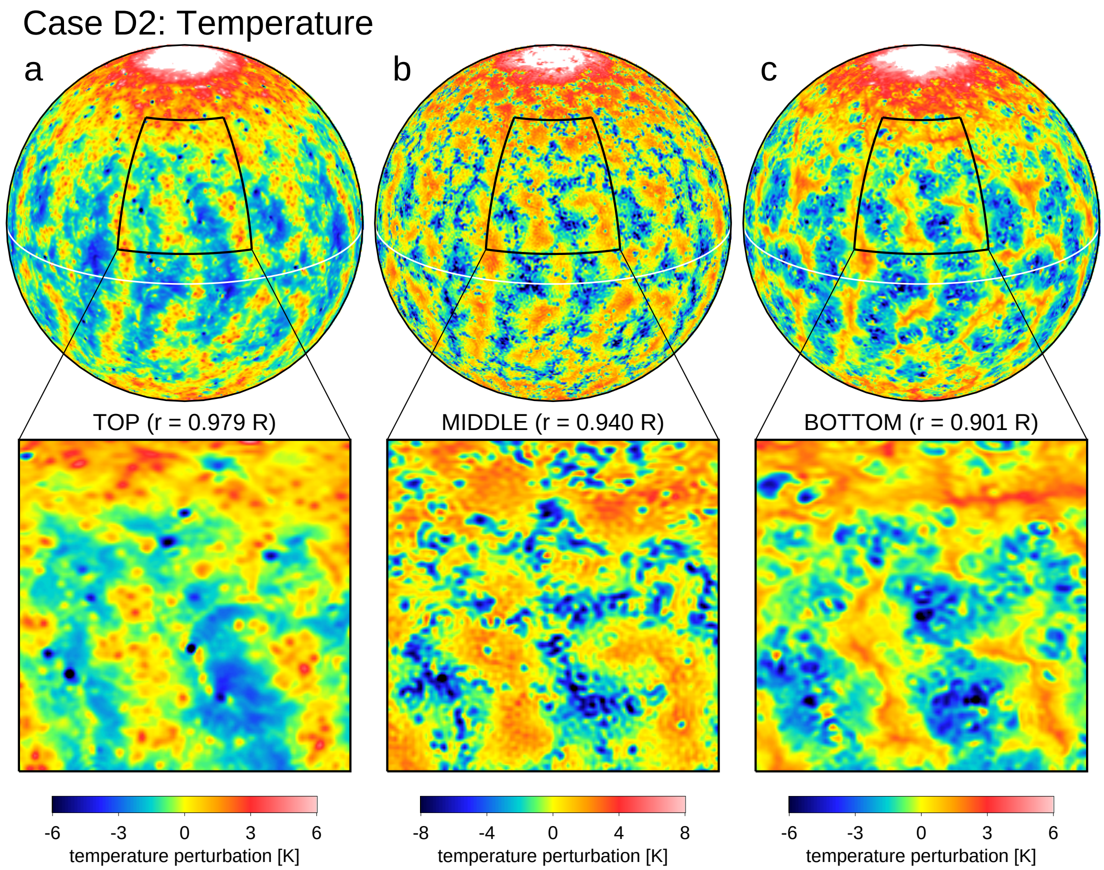

Figure 5.11: Similar to Fig. 5.6, but showing the horizontal structure of the temperature perturbation sampled near the (*a*) top, (*b*) middle, and (*c*) bottom of the domain, with the mean temperature for each level removed. Orange-red colors denote warmer fluid, green-blue colors denote cooler fluid.

patterns at 0.94 R are more homogeneous than for higher levels.

The rms velocities associated with the radial velocity distributions of Figure 5.10 are 105 m s^{-1} for Case *S2* and 140 m s^{-1} for Case *D2*, equivalent to an overturning time on the order of 6–10 days, depending on the shell depth. These overturning times suggest that the large-scale convective pattern is weakly sensitive to rotational effects, as both Cases *S2* and *D2* are rotating at the solar-like mean rate of one rotation per 28 days. We will discuss the rotational influence of these convective overturning motions in more detail in §5.4.

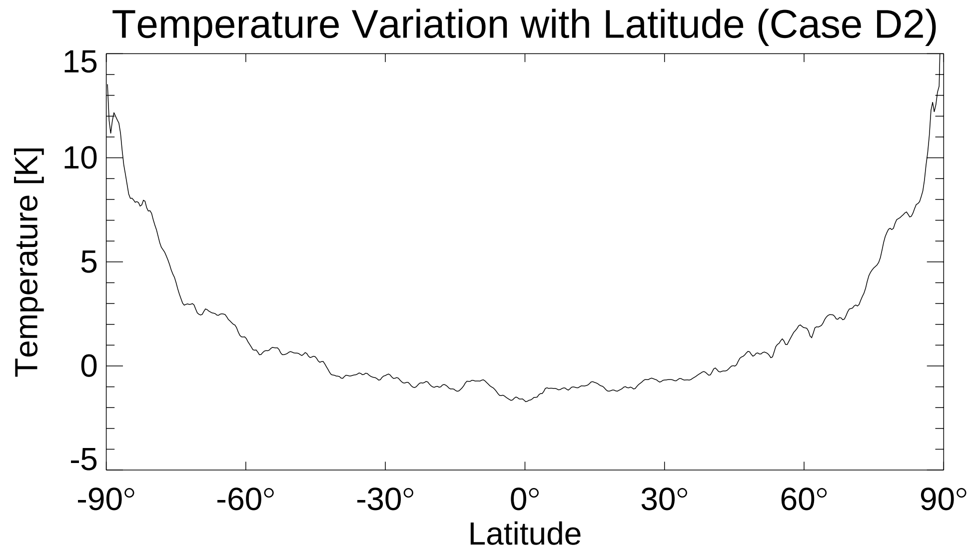

Figure 5.12: The zonally averaged fluctuating temperature near the top of the domain (r=0.979 R) for Case *D2*.

Figure 5.11 shows the fluctuating temperature field for Case *D2*, corresponding to the velocity planforms of Figure 5.6. The mean temperature at each radius has been subtracted out. We find that the locations of the large regions of warm and cool temperatures correlate well with the locations of the broad upflows and narrow downflow lanes visible in the radial velocity field, with the primary difference being that the cooler regions tend to be much broader than their radial velocity counterparts. Near the equator, the temperature field is dominated by columns of alternating warm and cold fluid associated with the weak banana-cell-like structures visible in the radial velocity images. In both temperature and radial velocity, these structures are sheared slightly by the differential rotation within the domain, and extend up to about $\pm 30°$ of latitude. These large-scale columnar temperature structures are broken up by smaller-scale variations on the temperature field which also tend to correlate well with some of the small-scale radial velocity features. For example, the localized hot and cold spots particularly evident in the close-up views of Figure 5.11a are coincident with some of the fastest fluid motions visible in the radial velocity image of Figure 5.6.

At all radii within Case *D2*, there exists a significant latitudinal temperature contrast between the equator and the poles, as shown in Figure 5.12. The temperatures in the near-polar regions are about 10–15 K warmer than near the equator, although over half of the total equator-to-pole difference occurs within 10° of the pole. As stated earlier, we believe that many characteristics of the fluid in the near-polar regions are most likely artifacts of the four-fold azimuthal periodicity imposed in these simulations, and should be interpreted with care.

5.3.2 Time-Averaged Axisymmetric Flows

The time-averaged axisymmetric (zonally averaged) profiles of angular velocity $\frac{\Omega}{2\pi}$ within all four domains are shown in Figure 5.13, with the angular velocity of the computation frame $\frac{\Omega_0}{2\pi}$ subtracted out. Note that we have chosen to have the equatorial rate imposed at the lower boundary be equal to the computational frame rate, such that $\frac{\Omega}{2\pi} = 0$ nHz there. The differentially rotating lower boundary imposed in Cases *D2*, *S2*, and *S3* decreases from 0 nHz at the equator to about -120 nHz at a latitude of 75°, and is similar in contrast and functional form to the latitudinal variation of the photospheric plasma rate measured by Snodgrass (1984). In contrast, the no-slip lower boundary imposed in Case *S1* is not differentially rotating.

With the exception of the poles, the angular velocity profiles within all four simulations are retrograde with respect to the rotating coordinate system specifying the equatorial rate, with the fastest rotation rates occurring near the bottom of each shell. Cases *S1* and *S2* show a largely constant negative radial gradient of angular velocity with radius at each point (e.g. Fig. 5.18), with the overall magnitude of Ω determined by the rotation rate imposed at the no-slip lower boundary at the corresponding latitude. Within Cases *S3* and *D2*, the negative radial gradients in angular velocity throughout the bulk of each shell are smaller, with the exception of the thin viscous boundary layer

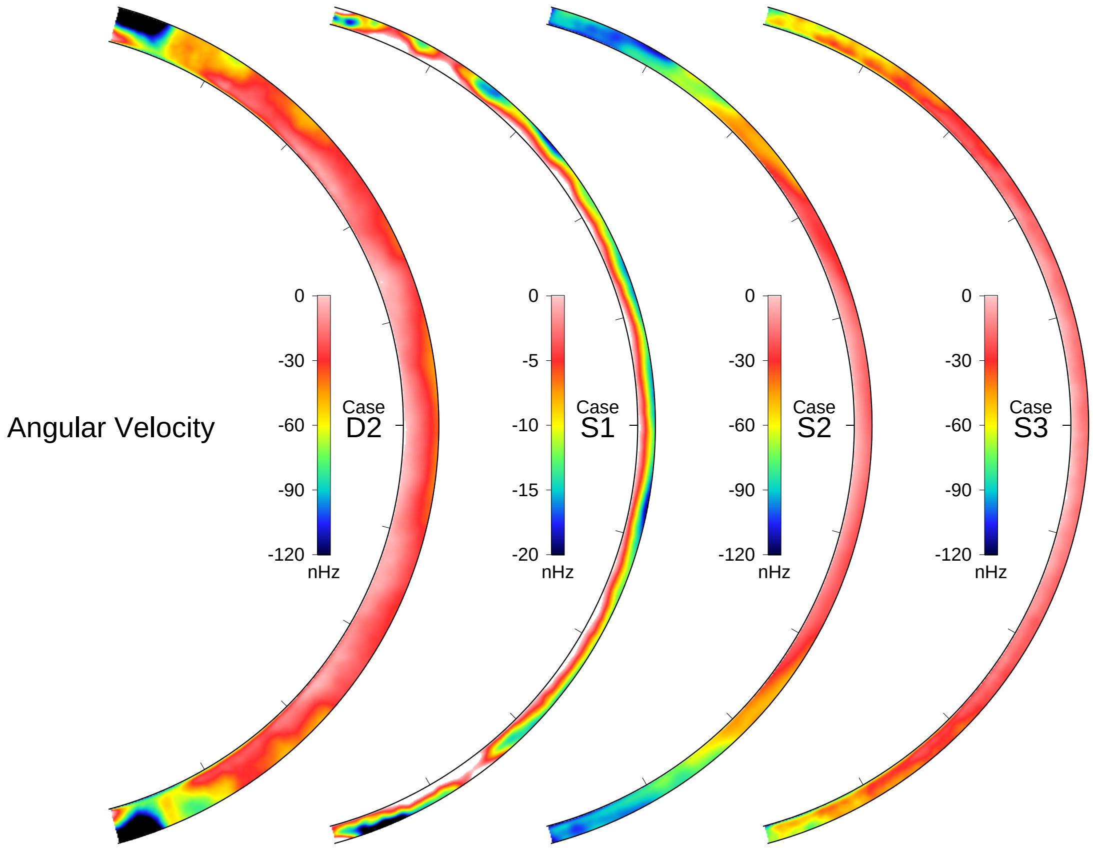

Figure 5.13: Angular velocity $\Omega/2\pi$ relative to the rotating coordinate system as a function of latitude and radius for all four cases, averaged over longitude and time. A no-slip differentially rotating lower boundary is imposed in Cases *D2*, *S2*, and *S3*. That imposed angular velocity decreases from 0 nHz at the equator to about -120 nHz at a latitude of 75°. Case *S1* has a uniformly rotating no-slip lower boundary. The tick marks are separated by 15° of latitude.

present near the lower boundary in each case.

The regions poleward of 75° of latitude are not shown in Figure 5.13 due to the high angular velocities present there. Even though these regions exhibit reasonable (linear) zonal velocities, the short moment arm produces higher values of Ω than seen elsewhere within the domain at lower latitudes. In addition, the polar regions are dominated by effects related to the four-fold azimuthal periodicity imposed in these simulations, producing dynamics which may not be otherwise present in similar simulations

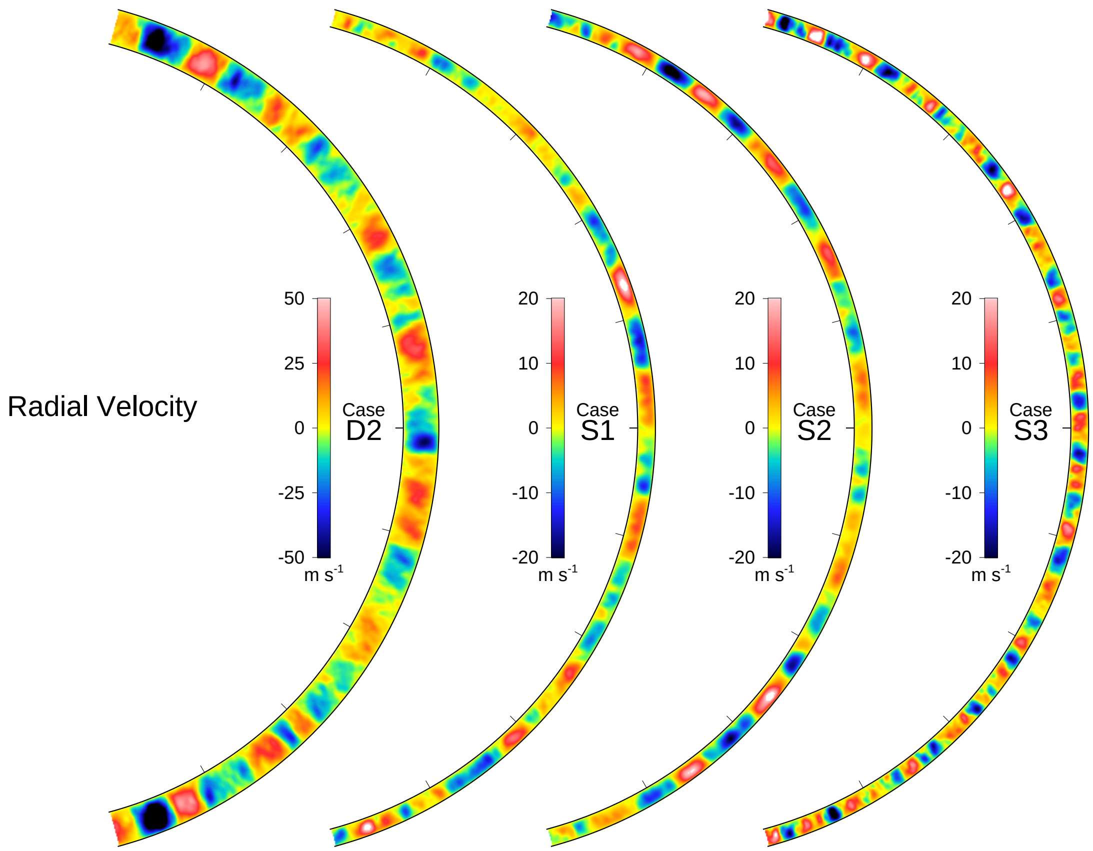

Figure 5.14: Axisymmetric radial velocity profiles for all cases. Positive values represent upward moving fluid.

without such an imposed periodicity.

The time-averaged meridional circulation is illustrated in Figures 5.14 and 5.15, showing the axisymmetric profiles of u_θ and u_ϕ. In all cases, the dominant mode driven in these simulations is that of axisymmetric rolls that occupy the entire depth of the domain. Cases *S1*, *S2*, and *D2* contain several 15°-wide rolls located between latitudes of $-75°$ and $+75°$ with typical flow speeds of 50–75 m s^{-1}. Rolls which have a poleward surface component seem to be preferred, as they are generally more extended horizontally and possess faster fluid velocities. In Case *S3*, the rolls are smaller in size but are otherwise similar to the larger rolls of the other three simulations. We will show in §5.4

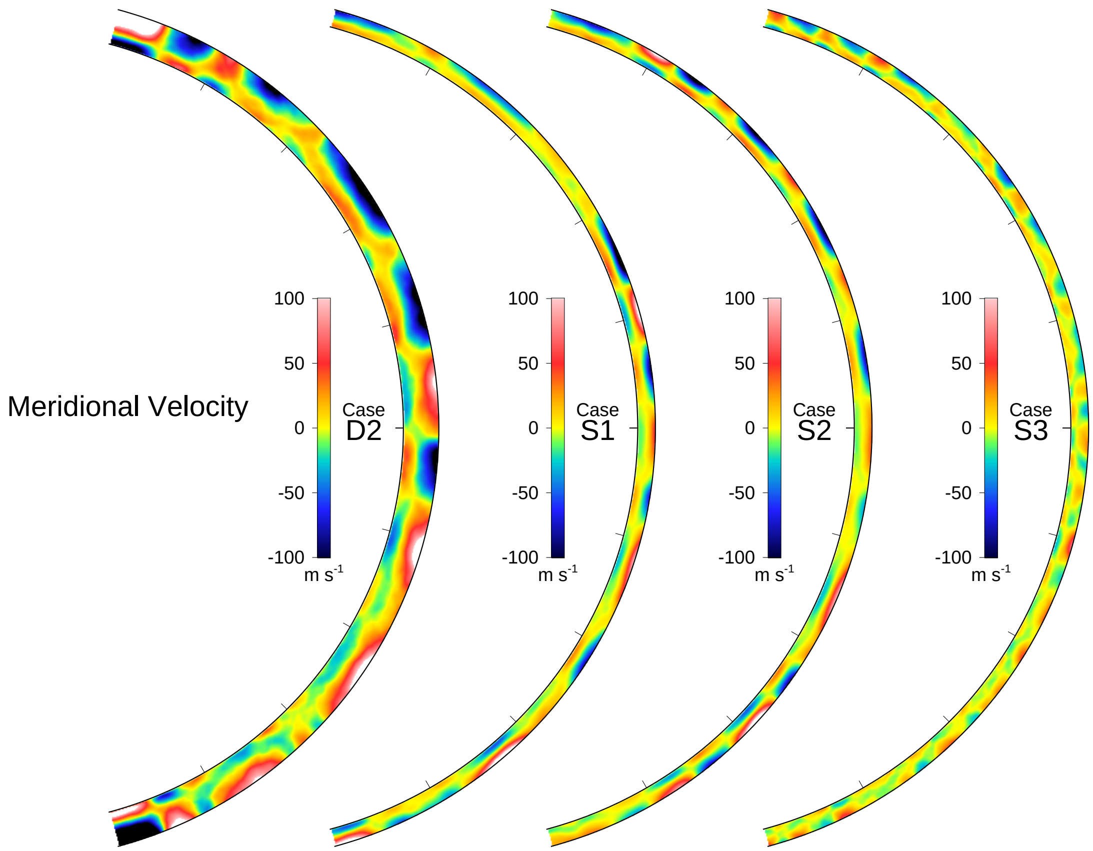

Figure 5.15: Axisymmetric meridional velocity profiles for all cases. Positive values represent southward flows.

that the rolls are primarily buoyantly driven.

In order to examine the form achieved by the differential rotation and meridional circulation in each of the four cases, we derive equations describing the kinetic energy balance within the system. Throughout the remainder of this chapter, the axisymmetric or longitudinally averaged component of a quantity $A(r,\theta,\phi)$ is denoted by an overbar, and is given by

$$\overline{A}(r,\theta) = \frac{1}{2\pi}\int_0^{2\pi} d\phi\, A(r,\theta,\phi), \tag{5.7}$$

allowing the decomposition

$$A = \overline{A}(r,\theta) + A'(r,\theta,\phi) \qquad \text{such that} \qquad \overline{A'} = 0, \tag{5.8}$$

where the prime on A' denotes the non-axisymmetric part of A. By noting that the axisymmetric component of a product $\overline{AB}$ is equal to

$$\overline{AB} = \overline{A}\,\overline{B} + \overline{A'B'}, \tag{5.9}$$

we can therefore decompose the axisymmetric kinetic energy $\overline{\mathcal{E}_k}$ into three parts:

$$\overline{\mathcal{E}_k} = \frac{\hat{\rho}\left(\overline{u_r^2} + \overline{u_\theta^2} + \overline{u_\phi^2}\right)}{2} \tag{5.10}$$

$$= \underbrace{\frac{\hat{\rho}\,\overline{u_\phi}^2}{2}}_{\text{DRKE}} + \underbrace{\frac{\hat{\rho}\left(\overline{u_r}^2 + \overline{u_\theta}^2\right)}{2}}_{\text{MCKE}} + \underbrace{\frac{\hat{\rho}\left(\overline{{u'_r}^2} + \overline{{u'_\theta}^2} + \overline{{u'_\phi}^2}\right)}{2}}_{\text{NAKE}}, \tag{5.11}$$

where

$$\text{DRKE} = \text{differential rotation kinetic energy}, \tag{5.12}$$

$$\text{MCKE} = \text{meridional circulation kinetic energy}, \tag{5.13}$$

$$\text{NAKE} = \text{non-axisymmetric (convective) kinetic energy}. \tag{5.14}$$

The balance of DRKE, MCKE, and NAKE within the shell models is now discussed in more detail.

5.4 ENERGETICS OF AXISYMMETRIC FLOWS

5.4.1 Axisymmetric Differential Rotation Balance

We will now show that the radial gradients of Ω realized in each of the four simulations are supported against diffusion by Reynolds stresses associated with non-axisymmetric convective motions. This behavior is likely caused by the tendency of convective fluid elements to partially conserve their angular momentum per unit mass $\lambda = \Omega r^2 \cos^2\theta$ as they move toward or away from the axis of rotation.

As suggested by Foukal & Jokipii (1975), possible constancy of λ along radial lines may also explain why surface magnetic tracers on the sun have a faster rotation rate relative to the surface fluid, if one assumes that the magnetic features are anchored at a radius slightly below the photosphere where the rotation rate is faster. Gilman & Foukal (1979) tested this notion by numerically modeling Boussinesq convection confined to a thin shell, and found that angular momentum was roughly conserved along local radii for such an incompressible fluid. They demonstrated that the convective motions were able to transport angular momentum inward, thereby maintaining the negative radial gradient of rotation rate with radius. The models presented here suggest that compressible convection behaves in a similar manner.

To quantify these ideas, we examine the evolution equation for the DRKE,

$$\frac{\partial\,(\mathrm{DRKE})}{\partial t} = \mathrm{RCF} + \mathrm{LCF} + \mathrm{RRS} + \mathrm{LRS} + \mathrm{ADV} + \mathrm{VT} + \mathrm{DIFF} + \mathrm{CURV}, \tag{5.15}$$

where the abbreviations signify contributions by different physical mechanisms in a manner similar to Gilman (1977). In a statistical steady state, the eight work terms in equation (5.15) above must sum to zero. These work terms are:

$$\mathrm{RCF} = \text{Coriolis forces on radial motions} = -2\Omega\,\hat{\rho}\,\overline{u_r}\;\overline{u_\phi}\,\sin\theta$$

$$\mathrm{LCF} = \text{Coriolis forces on latitudinal motions} = -2\Omega\,\hat{\rho}\,\overline{u_\theta}\;\overline{u_\phi}\,\cos\theta$$

$$\mathrm{RRS} = \text{radial Reynolds stresses} = \hat{\rho}\,\overline{u_r u_\phi}\,\frac{\partial\,\overline{u_\phi}}{\partial r}$$

$$\mathrm{LRS} = \text{latitudinal Reynolds stresses} = \hat{\rho}\,\overline{u_\theta u_\phi}\,\frac{\partial\,\overline{u_\phi}}{\partial \theta}$$

$$\mathrm{ADV} = \text{DRKE advection} = -\left[\frac{1}{r^2}\frac{\partial}{\partial r}\left(r^2\,\hat{\rho}\,\overline{u_\phi}\;\overline{u_r\,u_\phi}\right) + \frac{1}{r\sin\theta}\frac{\partial}{\partial\theta}\left(\sin\theta\,\hat{\rho}\,\overline{u_\phi}\;\overline{u_\theta u_\phi}\right)\right]$$

$$\begin{aligned}\mathrm{VT} &= \text{viscous transport} \\ &= \frac{1}{r^2}\frac{\partial}{\partial r}\left(r^2\,\nu\,\hat{\rho}\,\overline{u_\phi}\left[r\,\frac{\partial}{\partial r}\left(\frac{\overline{u_\phi}}{r}\right)\right]\right) + \frac{1}{r\sin\theta}\frac{\partial}{\partial\theta}\left(\sin\theta\,\nu\,\hat{\rho}\,\overline{u_\phi}\left[\frac{\sin\theta}{r}\frac{\partial}{\partial\theta}\left(\frac{\overline{u_\phi}}{\sin\theta}\right)\right]\right)\end{aligned}$$

$$\mathrm{DIFF} = \text{viscous losses} = -\nu\hat{\rho}\left\{\left[r\,\frac{\partial}{\partial r}\left(\frac{\overline{u_\phi}}{r}\right)\right]^2 + \left[\frac{\sin\theta}{r}\,\frac{\partial}{\partial\theta}\left(\frac{\overline{u_\phi}}{\sin\theta}\right)\right]^2\right\}$$

$$\mathrm{CURV} = \text{curvature effects} = -\frac{\overline{u_\phi}}{r\sin\theta}\left(\hat{\rho}\,\overline{u_r u_\phi}\,\sin\theta + \hat{\rho}\,\overline{u_\theta u_\phi}\,\cos\theta\right).$$

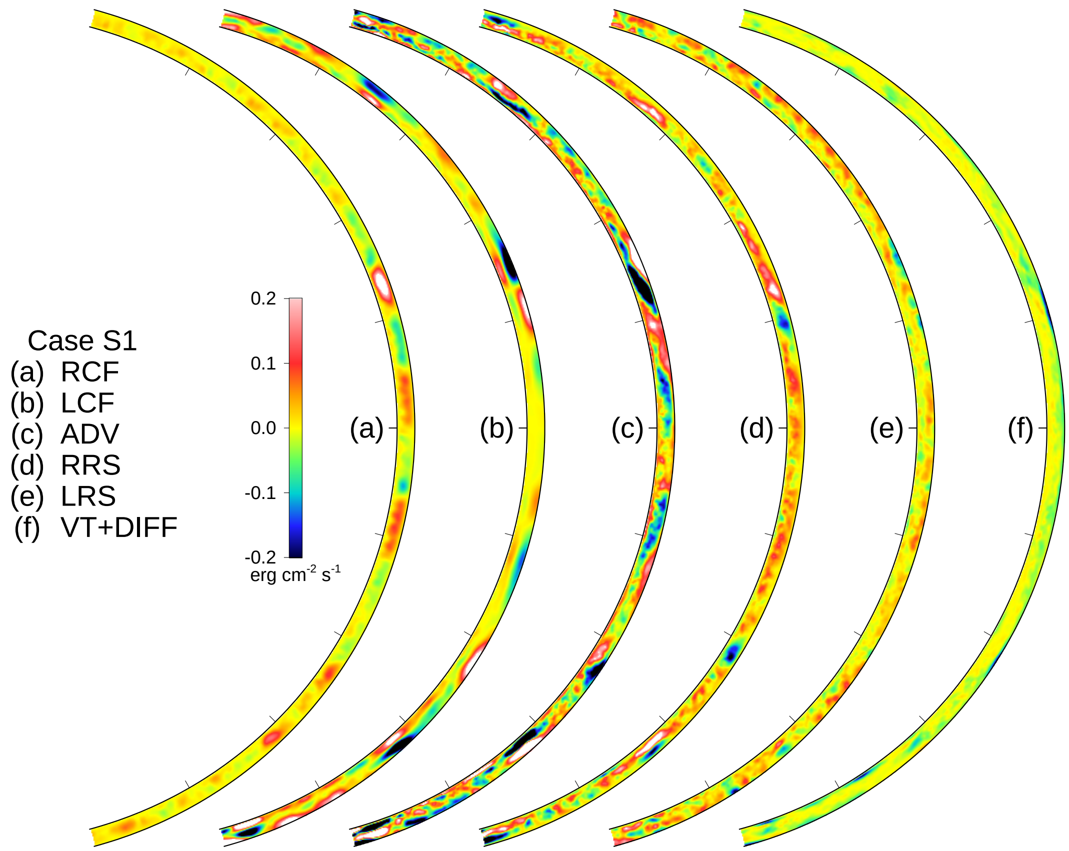

Figure 5.16: DRKE source terms for Case *S1*.

5.4.2 The Radial Shear Layer Within Case *S1*

We begin by examining the DRKE balance within Case *S1*, as it contains many of the important elements of angular momentum transfer in these simulations without the additional effects related to the differentially rotating lower boundary condition imposed in the other three simulations. The contributions from each of the terms in the DRKE balance equation (5.15) are illustrated in Figure 5.16 (with the exception of CURV, which is negligible), with Figure 5.17 showing the total DRKE and $\dfrac{\partial\,\mathrm{DRKE}}{\partial t}$ for Case *S1* as a function of radius and latitude. With respect to the rotating frame, $\overline{u_\phi} < 0$ throughout most of the domain, such that a positive contribution by any of the

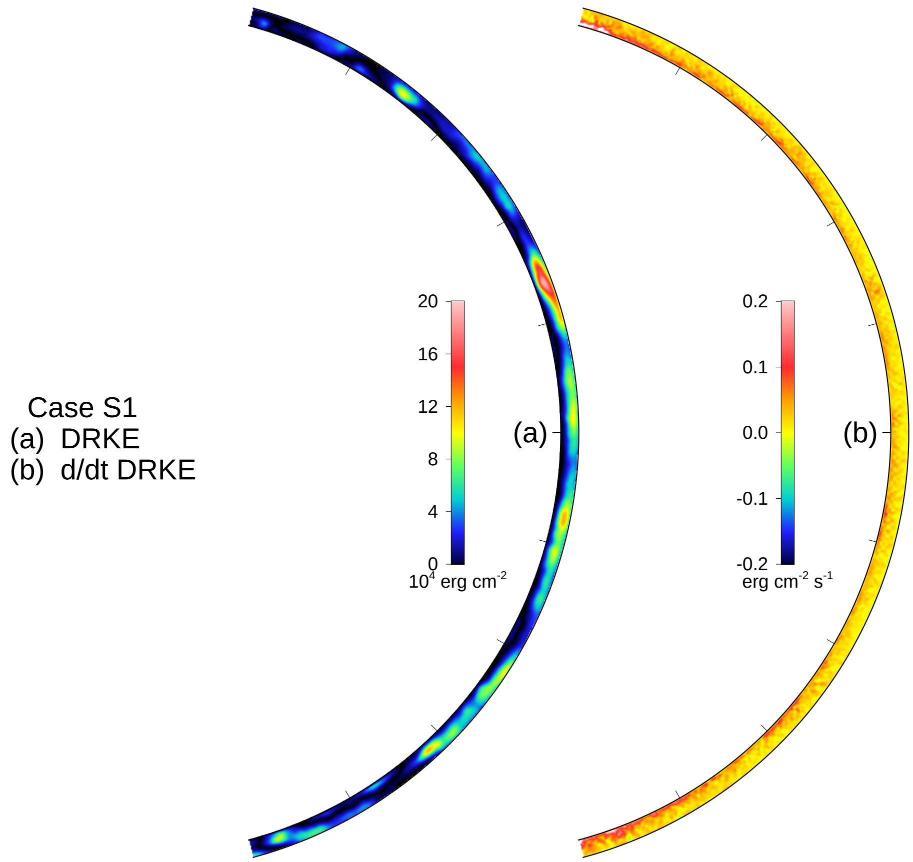

Figure 5.17: Total DRKE and change for Case *S1*. The ratio between typical values contained in (b) to those of (a) indicates the time scale on which the DRKE energetics within Case *S1* is changing.

source terms of equation (5.15) represents a source of DRKE which in isolation would decrease $\overline{u_\phi}$ over time to more negative values. Likewise, a negative contribution to DRKE represents an increase (to less negative values) in $\overline{u_\phi}$ over time. Figure 5.17 shows that Case *S1* is evolving on a time scale of at least 10^6 s or 12 days, as indicated by the sum total of all work terms (Fig. 5.17b) divided by the DRKE throughout the shell (Fig. 5.17a).

In the absence of convection, the DRKE profile shown in Figure 5.17a would achieve solid body rotation (that is, relax to zero) due to viscous dissipation in the system. Such dissipation accounts for the negative values of the VT+DIFF profile

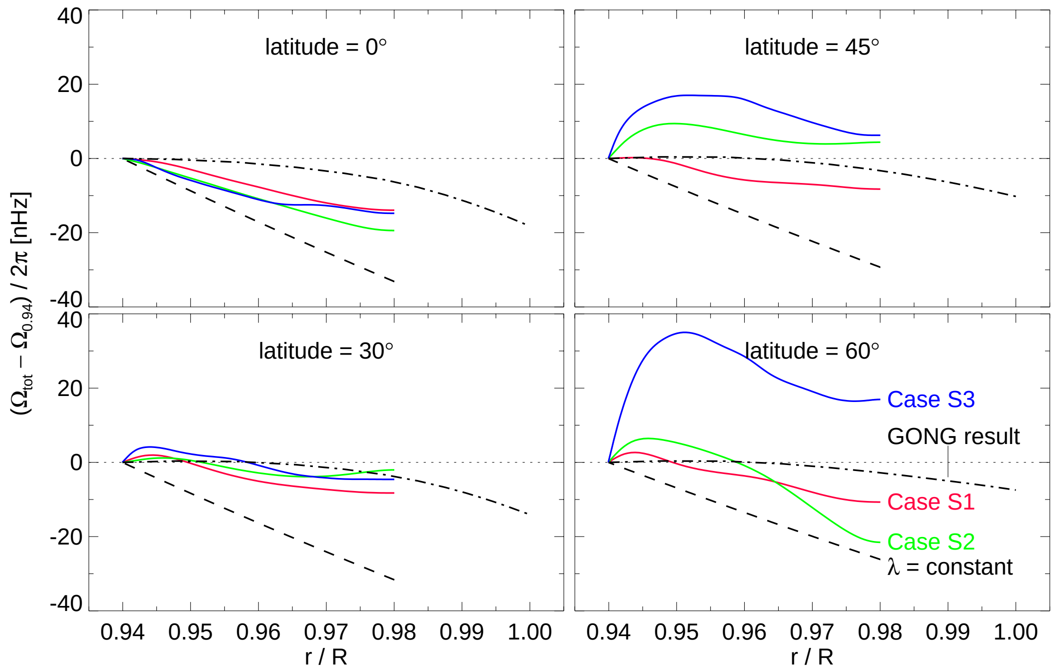

Figure 5.18: Angular velocity profiles for Cases *S1* (*red*), *S2* (*green*), and *S3* (*blue*) as a function of radius for latitudes 0°, 30°, 45°, and 60° as indicated. The dashed line in each panel represents the angular velocity of a radially moving fluid parcel for which its angular velocity per unit mass λ is conserved, while the dash-dot lines correspond to the GONG data plotted in Fig. 5.1.

shown in Figure 5.16*f*. The goal is therefore to determine which forcing terms maintain the radial shear in $\overline{u_\phi}$ against viscous diffusion. The convective motions present in the domain drive an axisymmetric meridional circulation, as well as create non-zero velocity correlations on smaller scales which produce axisymmetric Reynolds stresses. Contributions from one or both of these sources, which collectively make up the forcing terms in equation (5.15), must therefore be responsible for maintaining the non-zero radial gradient of $\overline{u_\phi}$.

The Coriolis force terms, RCF and LCF, represent exchanges between the DRKE and MCKE equations in the form of fluid parcels tending to preserve their overall angular momentum as they move toward or away from the axis of rotation. As a result, the RCF profile shown in Figure 5.16*a* is well correlated with the axisymmetric radial velocity profile (shown in Fig. 5.14), such that local upflows (downflows) in $\overline{u_r}$ tend to reduce (increase) $\overline{u_\phi}$ and thus cause a local increase (decrease) of DRKE. In a similar fashion, the LCF term shown in Figure 5.16*b* is correlated to $\overline{u_\theta}$ where now equatorward (poleward) flows produce a local increase (decrease) of DRKE.

Both the RCF and LCF contributions to the DRKE balance result from global fluid motions conserving angular momentum as they move throughout the domain. Such transport will spin down the portions of the domain farther away from the axis of rotation, which naturally tends to make $\dfrac{\partial \overline{u_\phi}}{\partial r} < 0$ everywhere. However, the strong axisymmetric flows associated with the persistent latitudinal banding in $\overline{u_r}$ and $\overline{u_\theta}$ also advect DRKE quite efficiently, such that regions of global convergence or divergence will respectively increase or decrease their DRKE content in response. This effect is captured in the DRKE transport term, ADV, shown in Figure 5.16*c*. There it can be seen that such transport effectively balances out the contributions to DRKE from the RCF and LCF terms.

We find that it is the Reynolds stress terms, RRS and LRS, that are primarily responsible for maintaining the radial shear in $\overline{u_\phi}$. These terms represent exchanges between the DRKE and NAKE equations, where the average tilt of non-axisymmetric convective structures (similar to the downflow plumes of Case *S2* discussed earlier in §5.3.1) in the $r\phi$- or $\theta\phi$-planes in the presence of gradients of $\overline{u_\phi}$ can produce contributions to DRKE. Figure 5.16*d* shows that the RRS profile is mainly positive, suggesting that the $\overline{u_r u_\phi}$ velocity correlation tends to be negative throughout the domain and thus implies a retrograde tilt among small-scale radial motions. Such a tendency is exactly what one would expect if the non-axisymmetric convection were to partially conserve its angular momentum per unit mass λ in radial motion.

The LRS term (Fig. 5.16*e*) is lesser in magnitude then RRS but also plays a role in maintaining the DRKE profile, especially at higher latitudes. The LRS term possesses a bimodal structure in radius which contains positive contributions to DRKE in the upper half of the domain and negative contributions in the lower half. Such a structure will tend to reinforce negative radial gradients in $\overline{u_\phi}$ in cases where $\overline{u_\phi} < 0$, as is the case here (see Fig. 5.17*a*).

Figure 5.18 shows the drop in total angular velocity $\Omega_{\rm tot} = \Omega + \Omega_0$ with radius realized in Case *S1* (plotted in red) for several latitudes between 0° and 60°. The dashed lines indicate the angular velocity an isolated fluid parcel moving in a purely radial direction would have if $\lambda =$ constant (that is, $\Omega_{\rm tot} \propto r^{-2}$). There is some tendency for fluid parcels in Case *S1* to conserve λ as they move radially throughout the shell, except near the bottom of the domain where $\frac{d\Omega}{dr}$ is larger (less negative). For comparison, the dash-dot lines in Figure 5.18 indicate the helioseismic inferences of Ω within the near-surface shear layer of the sun. The tendency to conserve λ is also apparent in the sun but to a lesser degree than in the models between 0.94–0.98 R, although the helioseismic results suggest that this effect may play a larger role closer to the photosphere where the convection is more vigorous.

The thin viscous boundary layer near the bottom of Case *S1* is formed in response to the no-slip lower boundary. The greater influence of viscous dissipation within this layer flattens out the angular velocity gradient at low latitudes and even produces a positive $\frac{d\Omega}{dr}$ at higher latitudes (e.g. at 60° in Fig. 5.18).

5.4.3 Differential Rotation Within Cases *S2*, *S3*, and *D2*

Turning to Cases *S2*, *S3*, and *D2*, we find that the angular velocity Ω possesses radial gradients similar to those achieved within Case *S1*, though there is substantially different behavior at high latitudes. The green and blue lines of Figure 5.18, corresponding to Cases *S2* and *S3*, along with Figure 5.19, illustrate this behavior. In this section, we show that these other three simulations are similar to Case *S1*, in which these radial gradients of Ω are primarily maintained against diffusion by Reynolds stresses associated with convective motions. The primary difference is that the latitudinal structure

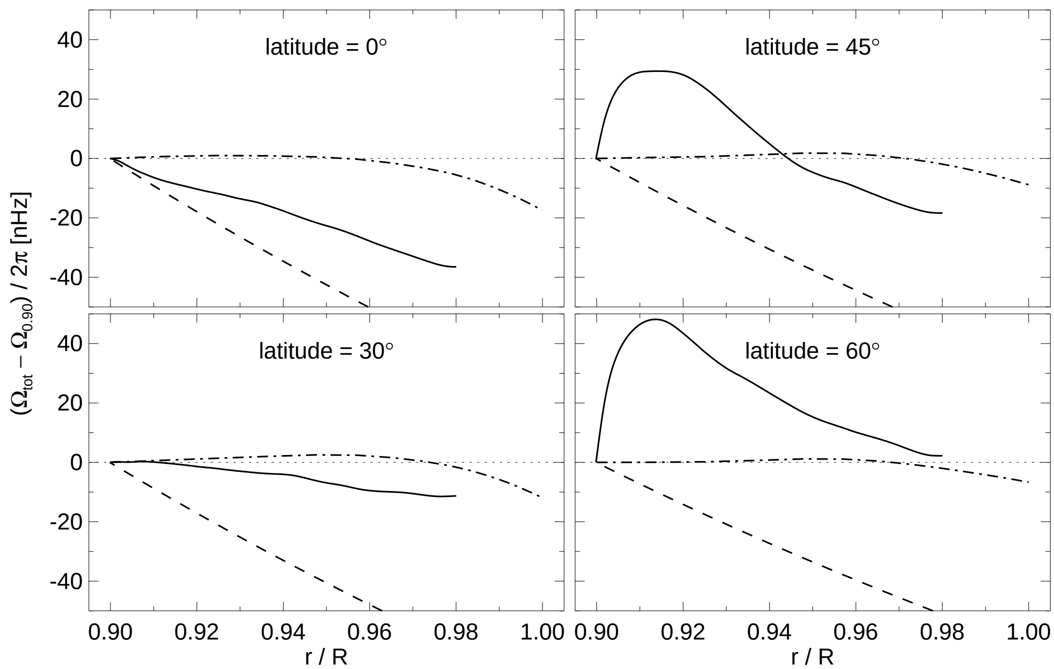

Figure 5.19: Similar to Fig. 5.18, except for the deeper shell simulation, Case *D2*. As before, the dashed line in each panel represents the angular velocity of a radially moving fluid parcel for which its angular velocity per unit mass λ is conserved, while the dash-dot lines correspond to the GONG data plotted in Fig. 5.1.

of DRKE has now changed, in response to the differentially rotating lower boundary applied in these three cases.

Figure 5.20 shows the DRKE source terms for Case *S2*, which, aside from the differentially rotating lower boundary, is otherwise identical to Case *S1*. This boundary condition forces the fluid in contact with the lower boundary to have increasingly negative zonal velocities with latitude, thereby constituting a continual supply of angular momentum. The DRKE associated with this imposed flow is then transported in both the radial and latitudinal directions, to give the angular velocity profile seen in Figure 5.13. Some of this energy is converted into MCKE, driving the more vigorous latitudinal rolls present at high latitudes (see Figs. 5.14 and 5.15), the effects of which feed back on the DRKE balance through the RCF and LCF work terms.

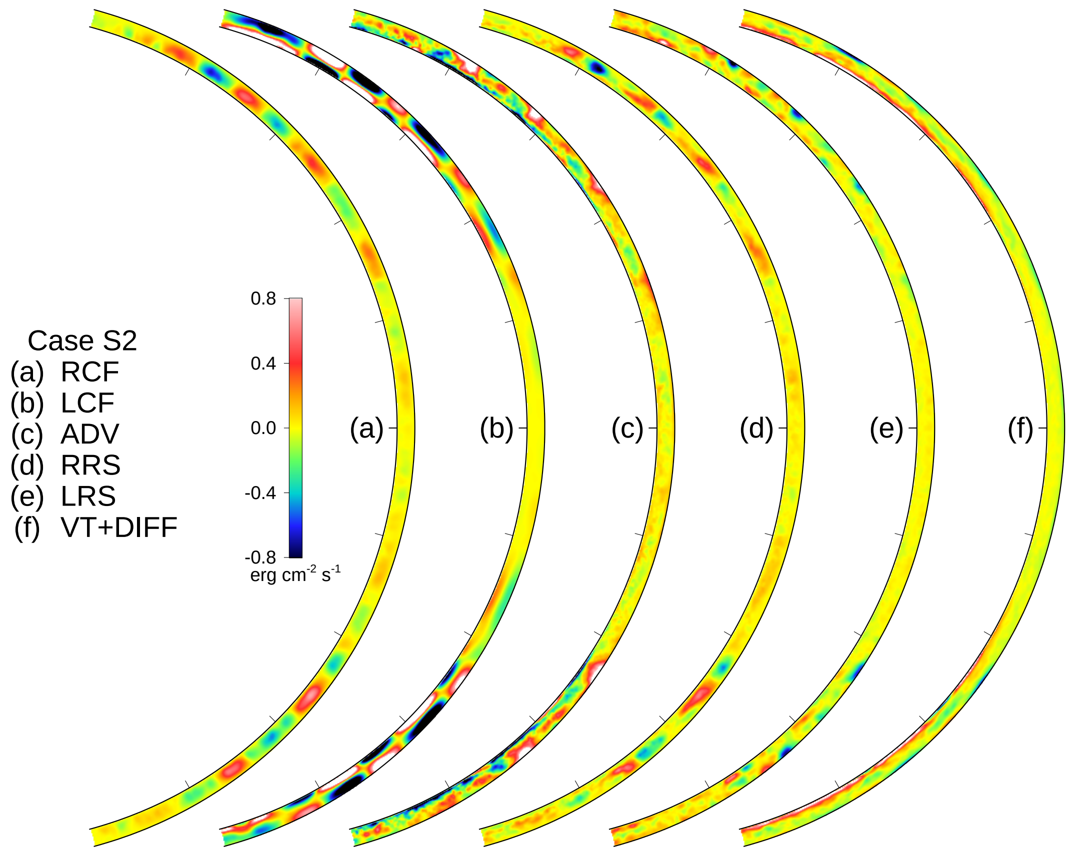

Figure 5.20: DRKE source terms for Case *S2*.

The DRKE energy balance within Cases *D2* and *S3* are shown in Figures 5.21 and 5.22 respectively. In contrast to the shallow shell (Case *S2*), these two cases possess a more moderate latitudinal gradient of $\overline{u_\phi}$. This form is achieved by a greater advection of DRKE, especially at mid to high latitudes, and is evident in the larger role the ADV term plays in the DRKE balance. A relatively lower portion of the DRKE input is converted into MCKE, as shown by the profiles of RCF and LCF.

The latitudinal rolls within Case *S3* are smaller in physical size as a consequence of the lower Prandtl number in this simulation. Both the lower viscous diffusivity and higher thermal diffusivity associated with the lower value of P_r drive more vigorous convection that occurs on smaller scales. These smaller scales are evident in the various

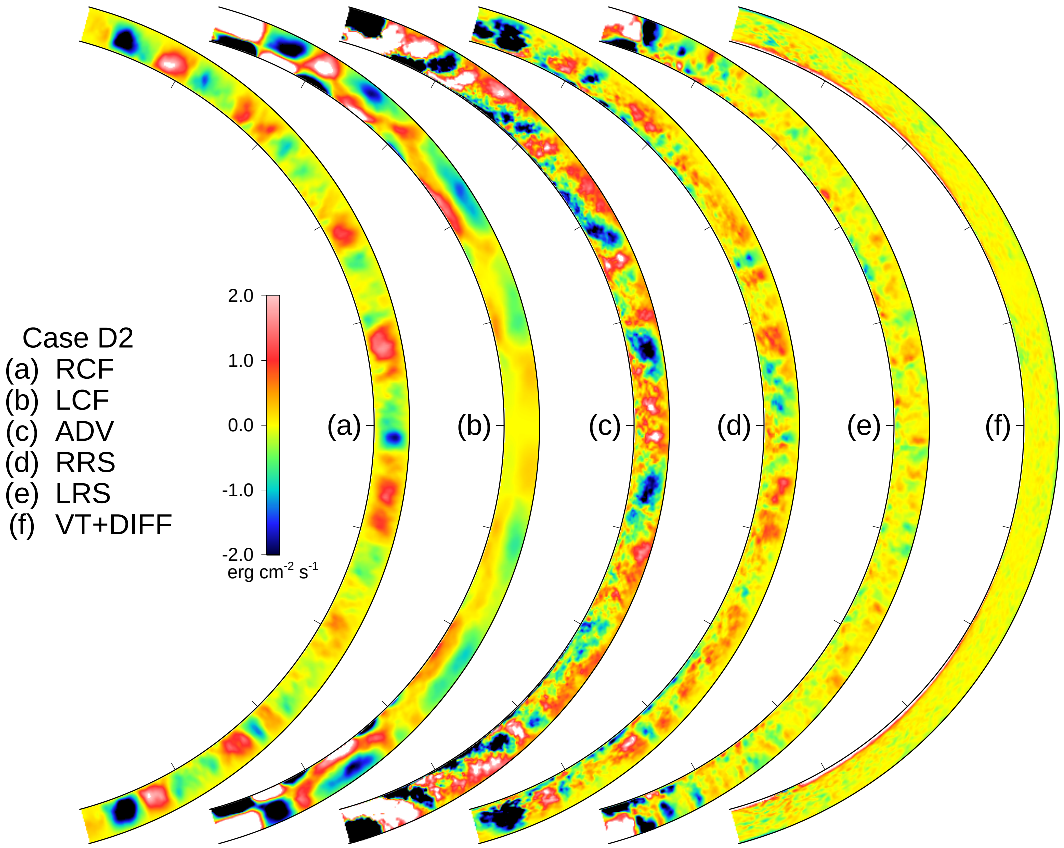

Figure 5.21: DRKE source terms for Case *D2*.

DRKE source terms, shown in Figure 5.22, but otherwise the dynamics are similar to Case *S2*.

In summary, the time scales of the largest overturning motions in our simulations suggest that they are at least weakly influenced by rotational effects, which in turn may enable Reynolds stresses to facilitate transport angular momentum inward. This inward angular momentum transport balances the outward diffusive transport, thereby maintaining a negative angular velocity gradient throughout the layer. This effect may contribute to the decrease of Ω with radius in the near-surface shear layer of the sun as deduced from helioseismic observations. Behavior at high latitudes is somewhat more complex due to the presence of a viscous boundary layer near the lower boundary, and

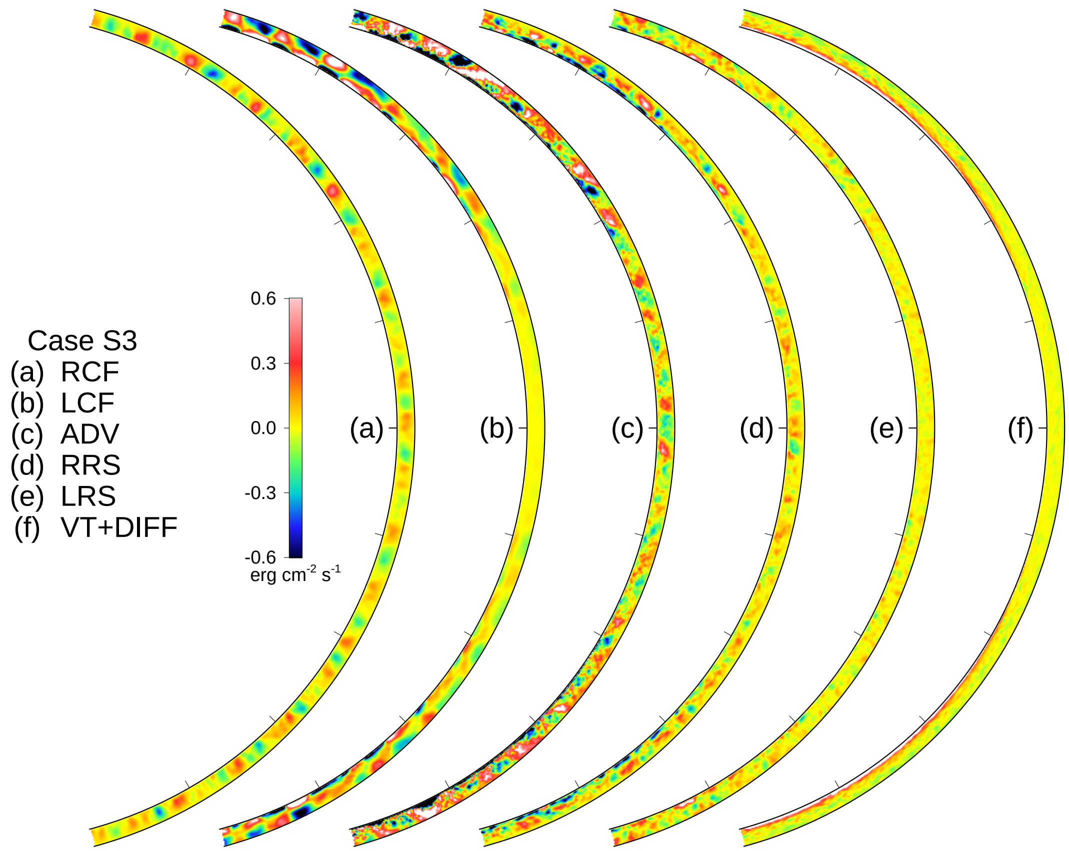

Figure 5.22: DRKE source terms for Case *S3*.

likewise there is some uncertainty in the helioseismic inferences about the radial gradient in Ω achieved at latitudes of 60° or greater.

5.4.4 Axisymmetric Meridional Circulation

We now briefly investigate the meridional circulation driven within the thin shell simulations, as these motions play an important role in the transport of DRKE (and thus angular momentum) within the shells. Schematically, the MCKE evolution equation is

$$\begin{aligned}\frac{\partial\,(\mathrm{MCKE})}{\partial t} &= \mathrm{RCF} + \mathrm{LCF} + \mathrm{RRS} + \mathrm{LRS} + \mathrm{GRAV} + \mathrm{PGF} \\ &\quad + \mathrm{ADV} + \mathrm{VT} + \mathrm{DIFF} + \mathrm{CURV},\end{aligned} \tag{5.16}$$

where the individual contributions are symbolized by:

$$\mathrm{RCF} = \text{Coriolis forces on radial motions} = 2\Omega\,\hat{\rho}\,\overline{u_r}\,\overline{u_\phi}\,\sin\theta$$

$$\mathrm{LCF} = \text{Coriolis forces on latitudinal motions} = 2\Omega\,\hat{\rho}\,\overline{u_\theta}\,\overline{u_\phi}\,\cos\theta$$

$$\mathrm{RRS} = \text{radial Reynolds stresses} = \hat{\rho}\,\overline{u_r^2}\,\frac{\partial\,\overline{u_r}}{\partial r} + \hat{\rho}\,\overline{u_r u_\theta}\,\frac{\partial\,\overline{u_\theta}}{\partial r}$$

$$\mathrm{LRS} = \text{latitudinal Reynolds stresses} = \hat{\rho}\,\overline{u_r u_\theta}\,\frac{\partial\,\overline{u_r}}{\partial\theta} + \frac{\hat{\rho}\,\overline{u_\theta^2}}{r}\,\frac{\partial\,\overline{u_\theta}}{\partial\theta}$$

$$\mathrm{GRAV} = \text{gravity/buoyancy driving} = -\overline{\rho}\,g\,\overline{u_r}$$

$$\mathrm{PGF} = \text{work done by pressure gradient forces} = -\left(\overline{u_r}\,\frac{\partial\,\overline{p}}{\partial r} + \frac{\overline{u_\theta}}{r}\,\frac{\partial\,\overline{p}}{\partial\theta}\right)$$

$$\begin{aligned}\mathrm{ADV} = \text{MCKE advection} = -\Bigg\{&\frac{1}{r^2}\frac{\partial}{\partial r}\left(r^2\left[\hat{\rho}\,\overline{u_r}\,\overline{u_r^2} + \hat{\rho}\,\overline{u_\theta}\,\overline{u_r u_\theta}\right]\right)\\ &+ \frac{1}{r\sin\theta}\frac{\partial}{\partial\theta}\left(\sin\theta\left[\hat{\rho}\,\overline{u_r}\,\overline{u_r u_\theta} + \hat{\rho}\,\overline{u_\theta}\,\overline{u_\theta^2}\right]\right)\Bigg\}\end{aligned}$$

$$\begin{aligned}\mathrm{VT} &= \text{viscous transport}\\ &= \frac{1}{r^2}\frac{\partial}{\partial r}\left[r^2\,\nu\hat{\rho}\left(2\,\overline{u_r}\,\frac{\partial\,\overline{u_r}}{\partial r} + \overline{u_\theta}\left[r\,\frac{\partial}{\partial r}\left(\frac{\overline{u_\theta}}{r}\right) + \frac{1}{r}\frac{\partial\,\overline{u_r}}{\partial\theta}\right] - \frac{2\overline{u_r}}{3}\,\overline{(\boldsymbol{\nabla\cdot u})}\right)\right]\\ &\quad + \frac{1}{r\sin\theta}\frac{\partial}{\partial\theta}\Bigg[\sin\theta\,\nu\hat{\rho}\Bigg(\overline{u_r}\left[r\,\frac{\partial}{\partial r}\left(\frac{\overline{u_\theta}}{r}\right) + \frac{1}{r}\frac{\partial\,\overline{u_r}}{\partial\theta}\right]\\ &\qquad + 2\,\overline{u_\theta}\left[\frac{1}{r}\frac{\partial\,\overline{u_\theta}}{\partial\theta} + \frac{\overline{u_r}}{r}\right] - \frac{2\overline{u_\theta}}{3}\,\overline{(\boldsymbol{\nabla\cdot u})}\Bigg)\Bigg]\end{aligned}$$

$$\begin{aligned}\mathrm{DIFF} = \text{viscous losses} = -2\nu\hat{\rho}\Bigg\{&\left[\frac{\partial\,\overline{u_r}}{\partial r} - \frac{1}{3}\,\overline{(\boldsymbol{\nabla\cdot u})}\right]^2 + \left[\frac{1}{r}\frac{\partial\,\overline{u_\theta}}{\partial\theta} + \frac{\overline{u_r}}{r} - \frac{1}{3}\,\overline{(\boldsymbol{\nabla\cdot u})}\right]^2\\ &+ \left[\frac{\overline{u_r}}{r} + \frac{\overline{u_\theta}\,\cos\theta}{r\sin\theta} - \frac{1}{3}\,\overline{(\boldsymbol{\nabla\cdot u})}\right]^2\\ &+ \frac{1}{2}\left[\frac{1}{r}\frac{\partial\,\overline{u_r}}{\partial\theta} + r\,\frac{\partial}{\partial r}\left(\frac{\overline{u_\theta}}{r}\right)\right]^2\Bigg\}\end{aligned}$$

$$\mathrm{CURV} = \text{curvature effects} = \frac{\overline{u_r}}{r}\left(\overline{u_r^2} + \overline{u_\phi^2}\right) + \frac{\overline{u_\theta}}{r\sin\theta}\left(\hat{\rho}\,\overline{u_r u_\theta}\,\sin\theta - \hat{\rho}\,\overline{u_\phi^2}\,\cos\theta\right).$$

We first examine the maintenance of the meridional circulation within Case *S1*, corresponding to the profiles of $\overline{u_r}$ and $\overline{u_\theta}$ shown previously in Figures 5.14 and 5.15. Most of the kinetic energy associated with these axisymmetric flows is contained in the 15°-wide latitudinal rolls distributed across the mid latitude and equatorial regions.

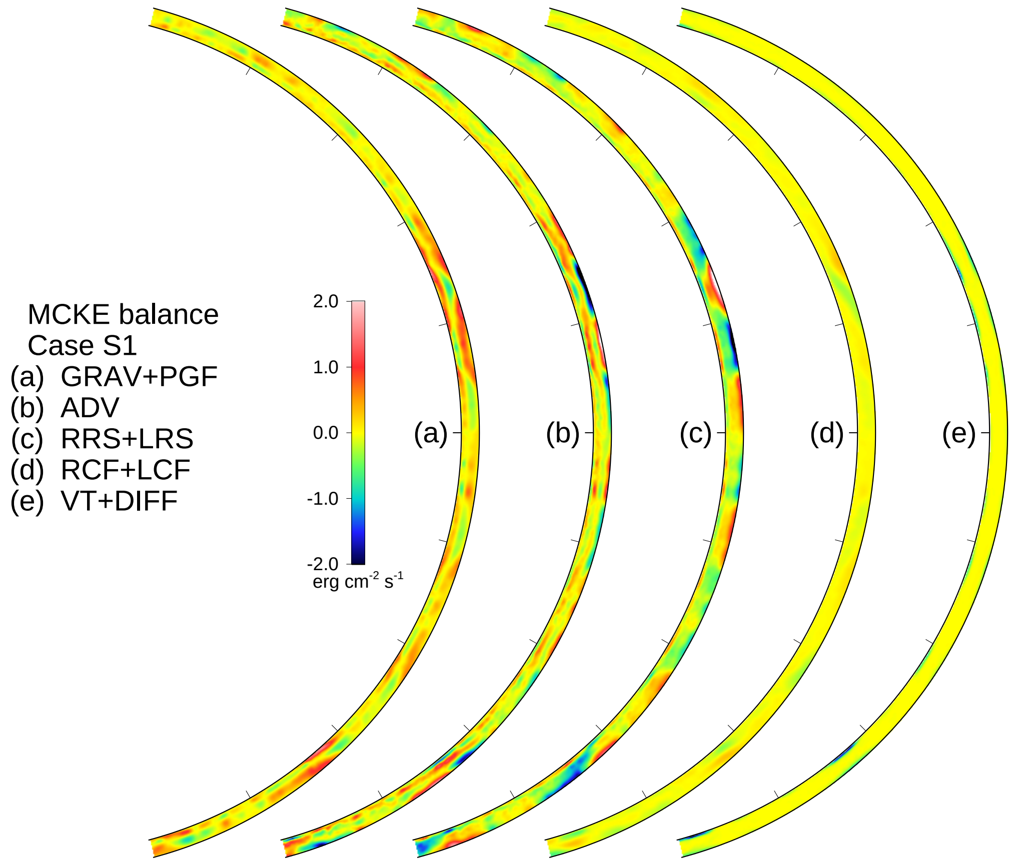

Figure 5.23: MCKE source terms for Case *S1*.

Rolls having poleward velocities near the surface are preferred over cells which have the opposite rotational sense, especially in the mid latitude regions.

The main contributions to the MCKE balance within Case *S1* are illustrated in Figure 5.23. We find that the energetics within the latitudinal rolls are achieved by a near balance between the work done by buoyancy and pressure gradients (Fig. 5.23*a*) and by Reynolds stresses (Fig. 5.23*c*). In places where the body forces drive the meridional flows (e.g. in radial upflows) the Reynolds stresses oppose it, and conversely when the body forces oppose the motion the Reynolds stresses act in such a way as to maintain it.

The RCF and LCF source terms represent the conversion of DRKE to MCKE

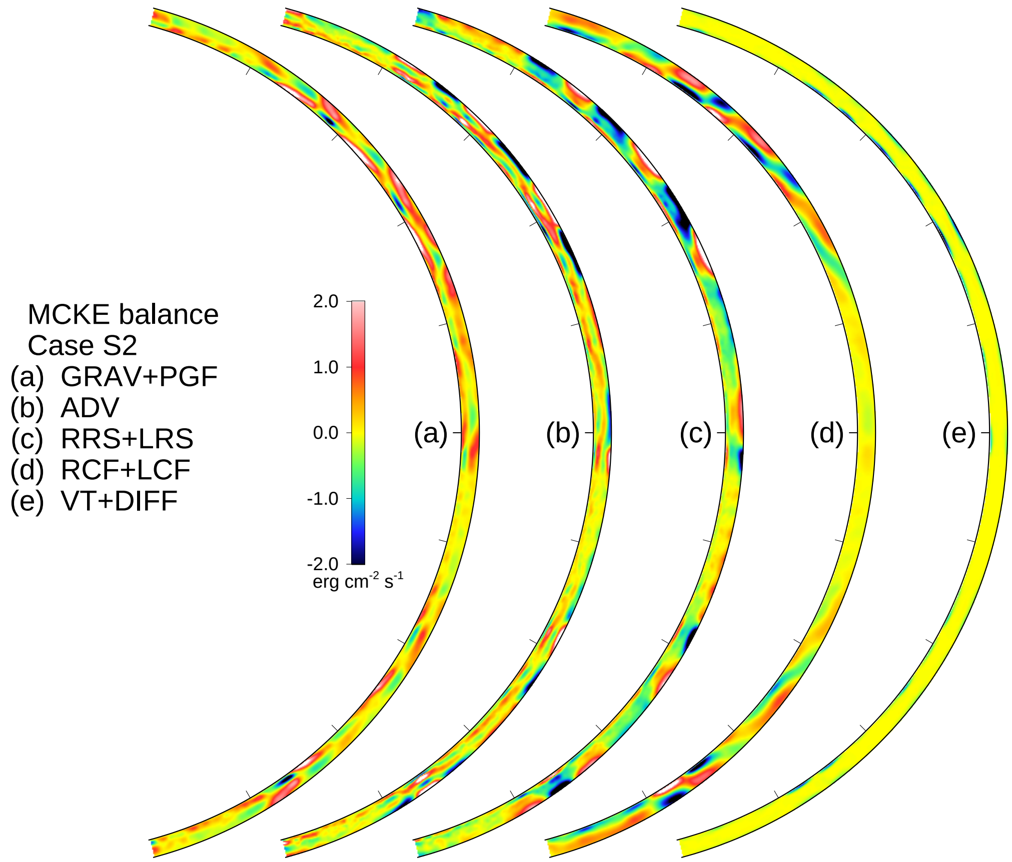

Figure 5.24: MCKE source terms for Case *S2*.

through Coriolis forces acting on the differential rotation. Because $\overline{u_\phi} < 0$ throughout most of the domain, the RCF and LCF terms will tend to enhance poleward or inward flows associated with the latitudinal rolls, and counteract any flows moving outward in radius or toward the equator. Figure 5.23*d* shows that the contributions by Coriolis forces acting on the differential rotation in Case *S1* are small relative to the body forces and Reynolds stresses.

The differentially rotating lower boundary imposed in Cases *S2*, *S3*, and *D2* affects the dynamics within these domains by driving latitudinal rolls with faster velocities than are present when the lower boundary is uniformly rotating (as in Case *S1*). This energy, added to the system as DRKE, is subsequently converted to MCKE through the

Coriolis work terms RCF and LCF. This effect is illustrated in Figure 5.24*d* for Case *S2*, showing a more prominent driving by Coriolis forces than for Case *S1* in these regions.

5.5 CONCLUSION

We have presented results of high-resolution numerical simulations of turbulence confined to thin spherical shells, seeking to understand some of the effects of supergranular scales of motion within a thin shearing layer nominally located near the top of the solar convection zone. These simulations represent the first global simulations of solar-like convection possessing horizontal scales on the order of supergranulation. In a series of four closely related simulations, we find in all cases that the convection is organized into a connected network of fast downflow lanes separating broad regions of warm more slowly rising fluid. With depth, we find that the downflow network loses some of its connectivity, instead forming more plume-like structures in the deeper layers.

Near the surface, the broad regions of upwelling fluid segment into more isolated, smaller-scale upflows, each with velocities comparable to the larger-scale network of fast downflows. These smaller upflow cells possess a spatial scale comparable to that of solar supergranulation and only appear near the upper boundary, suggesting that their origin stems from the more superadiabatic stratification present near the top of the shells. That such convective structures appear in both the shallow and deep shell simulations further suggests that it is the nature of the driving, rather than the depth of the shell, that influences the morphology of the convection near the surface.

The angular velocity within the thin shells decreases with radius throughout each domain, with the exception of the thin viscous boundary layer near the lower boundary in each case. We find that such negative radial gradients of angular velocity are maintained against diffusion by correlations between small-scale velocity components. The net effect of such Reynolds stresses suggests that fluid motions associated with both the broad upflows and strong downflow network tend to conserve their angular momentum per unit mass as they move radially throughout the shell. We believe these Reynolds stresses are an effect of the weak influence of rotation on the coherent convective structures realized in the simulations. We further speculate that supergranular convection in the sun behaves in a similar fashion, thereby contributing to the near-surface shear layer occupying the upper 5% of the sun by radius as inferred from helioseismic analyses.

Chapter 6

CONCLUDING REMARKS

We have presented the results of two complementary studies, one observational and the other theoretical, of turbulent convection of supergranular scales of motion within the upper solar convection zone in order to better understand the dynamical role of such convection in shearing layers within the sun. Complex convective patterns possessing a wide range of spatial scales are evident both in observations of supergranular outflows visible at the solar surface as well as in global numerical simulations of turbulence within thin spherical shells, and are likely to influence the dynamics of the deeper convection zone below as well as the more tenuous photosphere, chromosphere, and corona above. We now briefly summarize our findings from both studies, and conclude with a discussion of future directions in §6.2.

6.1 SUMMARY OF RESEARCH PRESENTED IN THIS THESIS

Chapter 3 describes an observational study entailing the characterization of cell sizes and evolution associated with solar supergranulation, as determined from the life histories of several thousand supergranules individually identified by their horizontal outflow signatures. The near-surface horizontal flow fields were measured by applying correlation tracking methods to mesogranular flow structures within a time series of MDI full-disk ($2''$ pixels) line-of-sight velocity images of the solar photosphere. This time series contains over 8000 images separated by one minute, sampling a $45°$-square region of quiet sun for a duration of about six days, and represents the first study of solar supergranulation at such high combined temporal and spatial resolution. Sites of strong horizontal outflow were identified as supergranules using a pattern recognition algorithm, from which the life history of all cells in the six-day dataset was recorded.

We find that supergranular outflow cells in this quiet sun region have a broad range of sizes, distributed in an approximate Gaussian fashion, with typical length scales of 14–20 Mm after image smoothing effects are accounted for. The supergranular pattern appears to be surface-filling, with individual cells separated by a connected network of thin convergence lanes that covers the entire field of view. The complex evolution of the supergranular pattern is embodied in the wide spectrum of cell lifetimes, ranging from time scales as long as several days down to the temporal resolution limit of 6 hr. Such evolution typically occurs via merging and splitting of individual supergranules, coupled with the emergence and disappearance of the associated interstitial convergence lanes. In other instances, segments of the convergence lane network are observed to be advected laterally as existing supergranular outflows grow or contract.

The supergranular pattern can therefore be characterized as an evolving network of thin convergence lanes separating broad outflow cells, and is most likely the surface manifestation of vigorous overturning motions occurring in the near-surface layers directly below the photosphere. In addition, the hierarchy of fluid motions in the upper convection zone is not limited to supergranular scales of motion, but also encompasses the smaller-scale patterns of mesogranulation and granulation as well as larger scales such as banded zonal flows and weak meridional currents. To elucidate the role such dynamics may play within the upper solar convection zone, we have constructed detailed three-dimensional numerical simulations of a compressible fluid, confined to thin rotating spherical shells positioned near the top of the solar convection zone.

The simulations presented in Chapter 5 constitute the highest resolution simulation of solar-like convection within a spherical shell computed to date. Spherical harmonic modes with $\ell \leq 340$ are explicitly resolved, allowing structures of order 10 Mm to be realized within the simulations. In all cases, a four-fold angular periodicity was used to reduce the computational workload. Solar-like stratification, thermal forcing, and differential rotation profiles are imposed on the fluid, in order to approximate the conditions present in the layers where solar supergranulation is thought to be driven. The ASH computer code, operating in a massively parallel computing environment, is used to advance in time the anelastic equations of motion. These equations allow us to include the effects of compressibility, yet filter out acoustic waves which would otherwise severely limit the size of the computational time step. The dynamical effects of turbulent motions not explicitly resolved in these simulations are accounted for by simple parameterizations of energy and momentum transport included in the anelastic equations.

The simulations suggest that convection on multiple scales may be a natural consequence of a compressible fluid experiencing a rapidly changing stratification. Convection within both shallow and deep shell cases having identical stratification near their respective upper boundaries (both located at 0.98 R) show a prominent network of narrow downflow lanes having a length scale of about 200 Mm near the top of each shell. The broad regions in between contain rising fluid that is further segmented into more localized sites of fast upflows each measuring about 15–30 Mm across, or about equal to the horizontal scale associated with solar supergranulation. With depth, the network of fast downflows becomes less uniform, forming plume-like structures that extend the full depth of each shell, while the small-scale upflows evident near in the upper layers gradually disappear altogether to form broad regions of upwelling fluid.

In all cases studied here, the latitudinal dependence of the differential rotation within these thin shell simulations reflects the angular velocity profile Ω imposed at the lower boundary. Negative radial gradients of angular velocity persist throughout each domain, and are maintained by the transport of angular momentum by the convective motions. Reynolds stresses associated with such motions, in particular the broad regions of upflowing fluid and the surrounding network of downflows, are found to transport angular momentum inward, balancing the outward transport achieved by diffusion. These dynamics may be interpreted as the tendency for radially moving fluid parcels to partially conserve their angular momentum per unit mass as they move radially throughout the shell, and are likely induced by the influence of rotation on the convective motions. These results suggest that the dynamical effects of rotation, while relatively weak given the short overturning time scales associated with the convection, are still strong enough to create the necessary velocity correlations that account for the observed angular momentum transport.

These simulations suggest that the upper shear layer of the sun may behave similarly, with the network of narrow downflow lanes associated with the supergranulation pattern facilitating the inward transport of angular momentum. Such transport would than contribute to the decrease of angular velocity with radius, as seen in helioseismic inferences of Ω. As a result, the depth of the upper shear layer may be loosely related to the radial extent of convection associated with the supergranulation pattern visible at the surface.

6.2 FUTURE OUTLOOK

The research presented in this thesis represents a detailed look at the intricate convection within the upper shear layer of the solar convection zone. We have sought to understand what scales of convection are driven, what determines the depth of the shear layer, and what are the dynamical effects of this convection in maintaining the shear layer. Since both the observational project and numerical simulations can be viewed as initial building blocks toward such understanding, we now present some possible future directions this research might take.

The correlation tracking algorithm outlined in §2.3 used to determine the supergranular flow field was shown to have systematic errors on the order of 10% for shifts between 0.005 pixels and 0.05 pixels. The magnitude of such errors suggest that the algorithm can be made more accurate by using an interpolation scheme of a higher order, thereby reducing the systematic errors generated by the algorithm.

We have left unexplored the large body of work regarding pattern formation in turbulent systems. The ever-changing near-surface velocity field appears to evolve in a remarkably ordered fashion, especially given the level of turbulence that must be present a short distance below. Consequently, it may be possible to create an evolving field of cells using a rule-based system that produces statistical area and lifetime distributions similar to those of solar supergranulation, thereby isolating the important length and time scales operating within the system.

The mean differential rotation and meridional circulation profiles deduced from the large-scale flow study of §3.4, wherein correlation tracking was applied to the supergranular flow field, contain a large degree of scatter. Determining these mean flows within many additional regions available to MDI will likely reduce this scatter.

The supergranular flow field has been shown to readily advect small-scale emergent magnetic flux toward convergence lanes, thereby concentrating the flux on relatively larger scales. This behavior is common to regions of quiet sun, such as the 45°-square field presented here. A logical extension of this research is therefore to investigate the effects of more intense magnetism on supergranular flows, such as within active regions and near sunspots. The character of supergranulation is likely to change under the influence of stronger magnetic fields, as the stabilizing effects of such magnetism affects the overturning motions associated with the convectively unstable fluid.

The numerical models possess several attributes that are drastically different than the upper solar convection zone. Foremost, the sun does not possess an impermeable lower boundary in the middle of its convection zone. Allowing mass to pass through the lower boundary would be more realistic, as the current simulations require the convective overturning motions as well as any large-scale meridional circulations to close within the confines of the thin shell domains. As an alternative to allowing permeable boundaries, we are in the process of constructing a simulation of the entire convection zone with a spatial resolution adequate to deal with a surface layer containing the small-scale convective structures seen in the simulations presented here. It will be interesting to see if a shearing boundary layer near the top of these domains forms naturally.

As computing technology increases, it will become possible to construct simulations of fluid with even higher spatial resolution, which in turn would allow convection at higher R_a and R_e to be studied. Whereas attaining solar values of R_a and R_e within simulations of convection is unlikely in the foreseeable future, it is of great interest to see whether the dynamical trends presented here also operate within more turbulent flows.

We recognize that the representation of sub-grid scale (SGS) effects in these simulations, achieved by simply enhancing the thermal and molecular diffusivities, greatly simplifies their true effects. As more coherent small-scale structures form within more turbulent fluid, the inaccuracies associated with using a simplified SGS treatment are likely to grow. It has been shown that small-scale features in the flows will not only dissipate momentum and heat, but are also able to advectively transport these quantities. More sensible treatments of the SGS terms in the ASH code would capture more of the dynamical effects associated with fluid motions not explicitly resolved.

The advent of continuous imaging of the solar surface carried out at high spatial and temporal resolution has led to remarkable ways to probe the dynamics of the intensely turbulent convection zone. Such efforts will be carried to new levels with the planned Solar Dynamics Observatory mission, and likewise the upgrades to GONG will provide uninterrupted Doppler imaging from the ground. The continuous rapid advances with massively parallel computing architectures will enable even more detailed simulations of turbulent convective fluids analogous to the solar convection zone. We thus foresee complementary paths coupling major observational and theoretical efforts in studying the complex evolving dynamics within the solar convection zone.

Bibliography

Basu, S., Antia, H. M., & Tripathy, S. C. 1999, *ApJ*, 512, 458

Beck, J. T., Duvall, J. T. L., & Scherrer, P. H. 1998, *Nature*, 394, 653

Berger, T. E., Löfdahl, M. G., Shine, R. A., & Title, A. M. 1998, *ApJ*, 506, 439

Bray, R. J., Loughhead, R. E., & Durrant, C. J. 1984, The Solar Granulation (Cambridge: Cambridge University Press)

Brummell, N., Cattaneo, F., & Toomre, J. 1995, *Science*, 269, 1370

Brummell, N. H., Hurlburt, N. E., & Toomre, J. 1996, *ApJ*, 473, 494

—. 1998, *ApJ*, 493, 955

Brun, A. S. & Toomre, J. 2001, in *Helio- and Asteroseismology at the Dawn of the Millennium*, Proceedings of the SOHO 10/GONG 2000 Workshop, ESA SP–464, ed. A. Wilson, 619–624

Brun, A. S., Turck-Chièze, S., & Zahn, J. P. 1999, *ApJ*, 525, 1032

Burr, I. W. 1974, Applied Statistical Methods (New York: Academic Press)

Canuto, V. M. 1996, *ApJ*, 467, 385

Canuto, V. M. & Christensen-Dalsgaard, J. 1998, *Ann. Rev. Fluid Mech.*, 30, 167

Cattaneo, F. 1999, *ApJ*, 515, L39

Cattaneo, F., Brummell, N. H., Toomre, J., Malagoli, A., & Hurlburt, N. E. 1991, *ApJ*, 370, 282

Charbonneau, P. & MacGregor, K. B. 1997, *ApJ*, 486, 502

Christensen-Dalsgaard, J., Proffitt, C. R., & Thompson, M. J. 1993, *ApJ*, 403, L75

Clune, T. C., Elliott, J. R., Miesch, M. S., & Toomre, J. 1999, *Parallel Comp.*, 25, 361

DeRosa, M., Duvall, Jr., T. L., & Toomre, J. 2000, *Sol. Phys.*, 192, 349

DeRosa, M. L. & Toomre, J. 1998, in *Structure and Dynamics of the Interior of the Sun and Sun-Like Stars*, Proceedings of the SOHO 6/GONG 98 Workshop, ESA SP–418, ed. S. Korzennik & A. Wilson, 753–758

Dikpati, M. & Charbonneau, P. 1999, *ApJ*, 518, 508

D'Silva, S. 1996, *ApJ*, 469, 964

D'Silva, S. & Choudhuri, A. R. 1993, *A&A*, 272, 621

Durney, B. R. & Roxburgh, I. W. 1971, *Sol. Phys.*, 16, 3

Duvall, Jr., T. L., D'Silva, S., Jefferies, S. M., Harvey, J. W., & Schou, J. 1996, *Nature*, 379, 235

Duvall, Jr., T. L., Kosovichev, A. G., Scherrer, P. H., Bogart, R. S., Bush, R. I., De Forest, C., Hoeksema, J. T., Schou, J., Saba, J. L. R., Tarbell, T. D., Title, A. M., Wolfson, C. J., & Milford, P. N. 1997, *Sol. Phys.*, 170, 63

Duvall, Jr., T. L., M., J. S., Harvey, J. W., & Pomerantz, M. A. 1993, *Nature*, 362, 430

Elliott, J. R., Miesch, M. S., & Toomre, J. 2000, *ApJ*, 533, 546

Fan, Y., Fisher, G. H., & DeLuca, E. E. 1993, *ApJ*, 405, 390

Fan, Y., Zweibel, E. G., Linton, M. G., & Fisher, G. H. 1999, *ApJ*, 521, 460

Foukal, P. & Jokipii, J. R. 1975, *ApJ*, 199, L71

Giles, P. M. 1999, PhD thesis, Stanford University

Giles, P. M., Duvall, Jr., T. L., Scherrer, P. H., & Bogart, R. S. 1997, *Nature*, 390, 52

Giles, P. M., Duvell, Jr., T. L., & Scherrer, P. H. 1998, in *Structure and Dynamics of the Interior of the Sun and Sun-Like Stars*, Proceedings of the SOHO 6/GONG 98 Workshop, ESA SP–418, ed. S. Korzennik & A. Wilson, 775–780

Gilman, P. A. 1977, *GAFD*, 8, 93

—. 1978a, *GAFD*, 11, 157

—. 1978b, *GAFD*, 11, 181

—. 1983, *ApJS*, 53, 243

Gilman, P. A. & Foukal, P. V. 1979, *ApJ*, 229, 1179

Gilman, P. A. & Glatzmaier, G. A. 1981, *ApJS*, 45, 335

Gilman, P. A. & Miller, J. 1981, *ApJS*, 46, 211

—. 1986, *ApJS*, 61, 585

Glatzmaier, G. A. 1984, J. Comp. Phys., 55, 461

—. 1985, *ApJ*, 291, 300

Glatzmaier, G. A. & Gilman, P. A. 1981, *ApJS*, 45, 351

Gough, D. & Toomre, J. 1991, *ARA&A*, 29, 627

Gough, D. A. 1969, J. Atmos. Sci., 26, 448

Haber, D. A., Hindman, B. W., Toomre, J., Bogart, R. S., & Hill, F. 2001, in *Helio- and Asteroseismology at the Dawn of the Millennium*, Proceedings of the SOHO 10/GONG 2000 Workshop, ESA SP–464, ed. A. Wilson, 213–218

Haber, D. A., Hindman, B. W., Toomre, J., Bogart, R. S., Thompson, M. J., & Hill, F. 2000, *Sol. Phys.*, 192, 335

Hagenaar, H. J., Schrijver, C. J., & Title, A. M. 1997, *ApJ*, 481, 988

Hagenaar, H. J., Schrijver, C. J., Title, A. M., & Shine, R. A. 1999, *ApJ*, 511, 932

Hansen, C. J. & Kawaler, S. D. 1994, Stellar Interiors: Physical Principles, Structure, and Evolution (New York: Springer-Verlag)

Hathaway, D. H., Gilman, P. A., Harvey, J. W., Hill, F., Howard, R. F., Jones, H. P., Kasher, J. C., Leibacher, J. W., Pintar, J. A., & Simon, G. W. 1996, *Science*, 272, 1306

Hill, F. 1988, *ApJ*, 333, 996

Howard, R., Gilman, P. A., & Gilman, P. I. 1984, *ApJ*, 283, 373

Howard, R. & Harvey, J. 1970, *Sol. Phys.*, 12, 23

Howard, R. & LaBonte, B. J. 1980, *ApJ*, 239, L33

Howe, R., Christensen-Dalsgaard, J., Hill, F., Komm, R. W., Larsen, R. M., Schou, J., Thompson, M. J., & Toomre, J. 2000, *Science*, 287, 2456

Hurlburt, N. E., Schrijver, C. J., Shine, R. A., & Title, A. M. 1995, in Proceedings of the Fourth SOHO Workshop, ESA SP–376, 239–243

Kitchatinov, L. L. & Rüdiger, G. 1993, *A&A*, 276, 96

—. 1995, *A&A*, 299, 446

LaBonte, B. J. & Howard, R. 1982, *Sol. Phys.*, 75, 161

Leighton, R. B., Noyes, R. W., & Simon, G. W. 1962, *ApJ*, 135, 474

Lesieur, M. 1997, Turbulence in Fluids (Dordrecht: Kluwer Academic Publishers)

Libbrecht, K. G. & Zirin, H. 1986, *ApJ*, 308, 413

Linton, M. G., Longcope, D. W., & Fisher, G. H. 1996, *ApJ*, 469, 954

Lisle, J., DeRosa, M., & Toomre, J. 2000, *Sol. Phys.*, 197, 21

Longcope, D. W., Fisher, G. W., & Arendt, S. 1996, *ApJ*, 464, 999

Miesch, M. S. 1998, PhD thesis, University of Colorado

Miesch, M. S., Elliott, J. R., Toomre, J., Clune, T. L., Glatzmaier, G. A., & Gilman, P. A. 2000, *ApJ*, 532, 593

Moreno-Insertis, F. 1986, *A&A*, 166, 291

November, L. J. 1994, *Sol. Phys.*, 154, 1

November, L. J., Toomre, J., & Gebbie, K. B. 1981, *ApJ*, 245, L123

Parker, E. N. 1955a, *ApJ*, 122, 293

—. 1955b, *ApJ*, 121, 491

—. 1979, Cosmical Magnetic Fields: Their Origin and Activity (Oxford: Clarendon Press)

—. 1993, *ApJ*, 408, 707

Roudier, T., Muller, R., Mein, P., Vigneau, J., Malherbe, J. M., & Espagnet, O. 1991, *A&A*, 248, 245

Scherrer, P. H., Bogart, R. S., Bush, R. I., Hoeksema, J. T., Kosovichev, A. G., Schou, J., Rosenberg, W., Springer, L., Tarbell, T. D., Title, A., Wolfson, C. J., Zayer, I., & the MDI Engineering Team. 1995, *Sol. Phys.*, 162, 129

Schou, J., Antia, H. M., Basu, S., Bogart, R. S., Bush, R. I., Chitre, S. M., Christensen-Dalsgaard, J., DiMauro, M. P., Dziembowski, W. A., Eff-Darwich, A., Gough, D. O., Haber, D. A., Hoeksema, J. T., Howe, R., Korzennik, S. G., Kosovichev, A. G., Larsen, R. M., Pijpers, F. P., Scherrer, P. H., Sekii, T., Tarbell, T. D., Title, A. M., Thompson, M. J., & Toomre, J. 1998, *ApJ*, 505, 390

Schou, J. & Bogart, R. S. 1998, *ApJ*, 504, L131

Schrijver, C. J., Title, A. M., van Ballegooijen, A. A., Hagenaar, H. J., & Shine, R. A. 1997, *ApJ*, 487, 424

Schüßler, M. 1979, *A&A*, 71, 79

Shine, R. A., Simon, G. W., & Hurlburt, N. E. 2000, *Sol. Phys.*, 193, 313

Simon, G. W. & Leighton, R. B. 1964, *ApJ*, 140, 1120

Singh, J. & Bappu, M. K. V. 1981, *Sol. Phys.*, 71, 161

Snodgrass, H. B. 1984, *Sol. Phys.*, 94, 13

Snodgrass, H. B. & Ulrich, R. K. 1990, *ApJ*, 351, 309

Spiegel, E. A. & Zahn, J.-P. 1992, *A&A*, 265, 106

Spitzer, L. 1962, Physics of Fully Ionized Gases (New York: Interscience Publishers)

Spruit, H. C., Nordlund, Å., & Title, A. M. 1990, *ARA&A*, 28, 263

Stein, R. F. & Nordlund, Å. 1998, *ApJ*, 499, 914

—. 2000, *Sol. Phys.*, 192, 91

Stix, M. 1976, *A&A*, 47, 243

Strous, L. H. & Simon, G. W. 1998, in Astronomical Society of the Pacific Conference Series, Vol. 140, 161–169

Tassoul, J.-L. 1978, Theory of Rotating Stars (Princeton: Princeton University Press)

Thompson, M. J., Toomre, J., Anderson, E. R., Antia, H. M., Berthomieu, G., Burton-clay, D., Chitre, S. M., Christensen-Dalsgaard, J., Corbard, T., DeRosa, M. Genovese, C. R., Gough, D. O., Haber, D. A., Harvey, J. W., Hill, F., Howe, R., Korzennik, S. G., Kosovichev, A. G., Leibacher, J. W., Pijpers, F. P., Provost, J., Rhodes, Jr., E. J., Schou, J., Sekii, T., Stark, P. B., & Wilson, P. R. 1996, *Science*, 272, 1300

Title, A. M., Hurlburt, N., Schrijver, C., Shine, R., & Tarbell, T. 1995, in Proceedings of the Fourth SOHO Workshop, ESA SP–376, 113–120

Tobias, S. M., Brummell, N. H., Clune, T. L., & Toomre, J. 1998, *ApJ*, 502, L177

Ulrich, R. 1970, *ApJ*, 162, 993

Ulrich, R. K. 1998, in *Structure and Dynamics of the Interior of the Sun and Sun-Like Stars*, Proceedings of the SOHO 6/GONG 98 Workshop, ESA SP–418, ed. S. Korzennik & A. Wilson, 851–855

Wang, H. & Zirin, H. 1989, *Sol. Phys.*, 120, 1

Ward, F. 1966, *ApJ*, 145, 416

Zappalà, R. A. & Zuccarello, F. 1991, *A&A*, 242, 480

Appendix A

CORRELATION TRACKING ALGORITHM DETAILS

A.1 SETTING UP THE GRIDPOINT ARRAY

In §2.3, it is stated that the correlation tracking algorithm is applied to two equally sized images $I_1(x, y)$ and $I_2(x, y)$. Our notation is such that integer values of the pixel coordinates x and y index the pixels in the two images, though we will also need to refer to fractional pixel values in what follows. An array of N gridpoints at which local displacements are to be detected is denoted by the coordinates (x_n, y_n), where $n = 1, 2, \cdots, N$. By the following method, local displacements are calculated so that the pixels in the neighborhood of (x_n, y_n) in image I_1 optimally coincide with the pixels in the neighborhood of (x_n, y_n) in image I_2 when shifted by the relative amount $(\delta x, \delta y)$.

Before calculating the optimal displacement, we formally define the neighborhood of each gridpoint as those pixels contained in a square subimage centered on the gridpoint in question. For example, if the subimages have $2p + 1$ pixels on a side (that is, p is the subimage half-width), the subimage centered on the gridpoint (x_n, y_n) extracted from image I_1 is thus comprised of all pixels $I_1(x_i, y_j)$ with

$$x_i = x_n - p + i \qquad \text{and} \qquad y_j = y_n - p + j, \tag{A.1}$$

where the indices i and j run from $i, j = 0, 1, \cdots, 2p$. Therefore, this subimage is bounded horizontally by $x = x_n - p$ and $x = x_n + p$ and bounded vertically by $y = y_n - p$

and $y = y_n + p$ inclusive. As shorthand, we define S_1^n as the subimage centered on the measurement gridpoint (x_n, y_n) extracted from image I_1. The conventions defined above are equally applicable to image I_2.

A.2 THE MERIT FUNCTION

Given the two corresponding subimages S_1^n and S_2^n centered on the same gridpoint (x_n, y_n) extracted from I_1 and I_2, we now wish to determine the relative shift between the two subimages such that the topology of the two subimages maximally coincides. To calculate this optimal displacement, we determine the displacement vector $(\delta x, \delta y)$ such that the following merit function is minimized:

$$\begin{aligned} m(\delta x, \delta y) = \sum_{i=0}^{2p-1} \sum_{j=0}^{2p-1} \Bigg\{ & W\left(x_i - x_n + \frac{1}{2}, y_j - y_n + \frac{1}{2}\right) \\ & \times \left[I_1\left(x_i + \frac{1}{2} + \frac{\delta x}{2}, y_j + \frac{1}{2} + \frac{\delta y}{2}\right)\right. \\ & \left. - I_2\left(x_i + \frac{1}{2} - \frac{\delta x}{2}, y_j + \frac{1}{2} - \frac{\delta y}{2}\right)\right]^2 \Bigg\}. \end{aligned} \tag{A.2}$$

In its essence, the merit function $m(\delta x, \delta y)$ in equation (A.2) above is a weighted sum of the squares of the differences between the pixel values of the two corresponding subimages after shifting the two subimages with respect to each other by the relative offset $(\delta x, \delta y)$.

The merit function is arranged so that the fractional pixel shifts are measured with respect to a position a half-pixel above and a half-pixel to the right of the pixels in the subimages; that is, the fractional pixel shifts are measured with respect to the points $\left(x_i + \frac{1}{2}, y_j + \frac{1}{2}\right)$. This formulation explains the presence of the various $\frac{1}{2}$'s added to the pixel indices, as well as the upper limit of $2p - 1$ for each of the sums.

Additionally, the merit function is set up so that the subimages are shifted in a symmetric fashion. For given horizontal and vertical displacements δx and δy, S_1^n and S_2^n are each shifted by the same amounts $\frac{\delta x}{2}$ and $\frac{\delta y}{2}$ but in opposite directions. This symmetric shifting stabilizes the behavior of $m(\delta x, \delta y)$ near the point $(\delta x, \delta y) = (0, 0)$.

Both the one-half pixel offset and the symmetric shift simplify the computational task of evaluating I_1 and I_2 at interpixel values. This scheme guarantees that the interpolating point always falls within the square framed by the four pixels (x_i, y_j), $(x_i, y_j + 1)$, $(x_i + 1, y_j)$, and $(x_i + 1, y_j + 1)$, as long as only shifts of less than one pixel are considered. For this condition to be true, we require

$$|\delta x| \leq 1 \qquad \text{and} \qquad |\delta y| \leq 1. \tag{A.3}$$

For the magnitudes of the velocities we hope to measure in this work, this condition is always met.

The function W in equation (A.2) above is a weighting function multiplying the squared pixel differences so that the terms in the double sum arising from points closer to the subimage center (x_n, y_n) are weighted more heavily in the sum than those farther away. We use a Gaussian function for W,

$$W(x, y) = \exp\left(-\frac{x^2 + y^2}{\sigma^2}\right), \tag{A.4}$$

although any tapered function will suffice. The adjustable parameter σ is the e-folding distance of the Gaussian, which in turn determines the spatial resolution of the resulting velocity field. The parameter p introduced above, which characterizes the size of the subimages, should be chosen such that the subimages extend far enough out to encompass the peak and falloff of W. Choosing p too large will only increase the computational workload while the extra outlying points contribute little to the weighted sum in equation (A.2). Conversely, choosing p too small may not encompass all of the points surrounding the measurement gridpoint which have any significant weighting in the double sum. In this work, p is chosen to be slightly larger than σ. Typically, $p = 11$ pixels for $\sigma = 8$ pixels.

As seen by inspecting equation (A.2), minimizing the merit function requires a method for evaluating I_1 and I_2 at fractional pixel coordinates. In general, if we know the value of a function f at the four bounding points (x_1, y_1), (x_2, y_1), (x_1, y_2), and (x_2, y_2), we can bilinearly interpolate between the abscissae to estimate the value of f at any point interior to the bounding points:

$$\begin{aligned} f(x_1 + \Delta x, y_1 + \Delta y) = (1 - A)(1 - B)\, f(x_1, y_1) + A(1 - B)\, f(x_2, y_1) \\ + (1 - A)B\, f(x_1, y_2) + AB\, f(x_2, y_2), \end{aligned} \tag{A.5}$$

where the scaled coordinates A and B are defined

$$A \equiv \frac{\Delta x}{x_2 - x_1} \qquad \text{and} \qquad B \equiv \frac{\Delta y}{y_2 - y_1}. \tag{A.6}$$

For the point $(x_1 + \Delta x, y_1 + \Delta y)$ to be interior to the bounding points, we must have

$$0 \leq A \leq 1 \qquad \text{and} \qquad 0 \leq B \leq 1, \tag{A.7}$$

otherwise we would be *extrapolating* rather than *interpolating*.

The bilinear interpolation formula (A.5) is used to evaluate I_1 and I_2 at fractional pixel coordinates. Identifying the indices x_1, x_2, y_1, and y_2 in equation (A.5) with the pixel indices x_i, x_{i+1}, y_j, and y_{j+1}, respectively, and setting $\Delta x = \frac{1}{2} + \frac{\delta x}{2}$ and $\Delta y = \frac{1}{2} + \frac{\delta y}{2}$, we obtain the following expression for the I_1 term in equation (A.2) above:

$$\begin{aligned} I_1\left(x_i + \frac{1}{2} + \frac{\delta x}{2}, y_j + \frac{1}{2} + \frac{\delta y}{2}\right) = \left(\frac{1}{2} - \frac{\delta x}{2}\right)\left(\frac{1}{2} - \frac{\delta y}{2}\right) I_1(x_i, y_j) \\ + \left(\frac{1}{2} + \frac{\delta x}{2}\right)\left(\frac{1}{2} - \frac{\delta y}{2}\right) I_1(x_{i+1}, y_j) \\ + \left(\frac{1}{2} - \frac{\delta x}{2}\right)\left(\frac{1}{2} + \frac{\delta y}{2}\right) I_1(x_i, y_{j+1}) \\ + \left(\frac{1}{2} + \frac{\delta x}{2}\right)\left(\frac{1}{2} + \frac{\delta y}{2}\right) I_1(x_{i+1}, y_{j+1}). \end{aligned} \tag{A.8}$$

Likewise for I_2, where now $\Delta x = \dfrac{1}{2} - \dfrac{\delta x}{2}$ and $\Delta y = \dfrac{1}{2} - \dfrac{\delta y}{2}$, we have

$$\begin{aligned} I_2\left(x_i + \frac{1}{2} - \frac{\delta x}{2}, y_j + \frac{1}{2} - \frac{\delta y}{2}\right) = {} & \left(\frac{1}{2} + \frac{\delta x}{2}\right)\left(\frac{1}{2} + \frac{\delta y}{2}\right) I_2(x_i, y_j) \\ & + \left(\frac{1}{2} - \frac{\delta x}{2}\right)\left(\frac{1}{2} + \frac{\delta y}{2}\right) I_2(x_{i+1}, y_j) \\ & + \left(\frac{1}{2} + \frac{\delta x}{2}\right)\left(\frac{1}{2} - \frac{\delta y}{2}\right) I_2(x_i, y_{j+1}) \\ & + \left(\frac{1}{2} - \frac{\delta x}{2}\right)\left(\frac{1}{2} - \frac{\delta y}{2}\right) I_2(x_{i+1}, y_{j+1}). \end{aligned} \tag{A.9}$$

Note that the restrictions on A and B given above in equation (A.7) imply that $|\delta x| \leq 1$ and $|\delta y| \leq 1$, as already assumed by equation (A.3). We now substitute equations (A.8) and (A.9) into equation (A.2) to obtain

$$\begin{aligned} m(\delta x, \delta y) = \sum_{i=0}^{2p-1} \sum_{j=0}^{2p-1} \Bigg\{ & W\left(x_i - x_n + \frac{1}{2}, y_j - y_n + \frac{1}{2}\right) \\ & \times \Bigg[\left(\frac{1}{2} - \frac{\delta x}{2}\right)\left(\frac{1}{2} - \frac{\delta y}{2}\right) I_1(x_i, y_j) \\ & + \left(\frac{1}{2} + \frac{\delta x}{2}\right)\left(\frac{1}{2} - \frac{\delta y}{2}\right) I_1(x_{i+1}, y_j) \\ & + \left(\frac{1}{2} - \frac{\delta x}{2}\right)\left(\frac{1}{2} + \frac{\delta y}{2}\right) I_1(x_i, y_{j+1}) \\ & + \left(\frac{1}{2} + \frac{\delta x}{2}\right)\left(\frac{1}{2} + \frac{\delta y}{2}\right) I_1(x_{i+1}, y_{j+1}) \\ & - \left(\frac{1}{2} + \frac{\delta x}{2}\right)\left(\frac{1}{2} + \frac{\delta y}{2}\right) I_2(x_i, y_j) \\ & - \left(\frac{1}{2} - \frac{\delta x}{2}\right) - \left(\frac{1}{2} + \frac{\delta y}{2}\right) I_2(x_{i+1}, y_j) \\ & - \left(\frac{1}{2} + \frac{\delta x}{2}\right)\left(\frac{1}{2} - \frac{\delta y}{2}\right) I_2(x_i, y_{j+1}) \\ & - \left(\frac{1}{2} - \frac{\delta x}{2}\right)\left(\frac{1}{2} - \frac{\delta y}{2}\right) I_2(x_{i+1}, y_{j+1})\Bigg]^2\Bigg\}. \end{aligned} \tag{A.10}$$

This expression for $m(\delta x, \delta y)$ depends only upon the unknown displacement $(\delta x, \delta y)$ and the data values of the pixels in the two subimages extracted from I_1 and I_2.

A.3 MINIMIZING THE MERIT FUNCTION

To find the values of δx and δy which minimize the merit function (A.10), we will need to evaluate the derivatives $\dfrac{\partial m}{\partial(\delta x)}$ and $\dfrac{\partial m}{\partial(\delta y)}$. This task is simplified by first expanding the squared term in equation (A.10). To proceed, first define the quantities

$$
\begin{aligned}
d_1 &= I_1(x_j, y_k) - I_2(x_{j+1}, y_{k+1}),\\
d_2 &= I_1(x_j, y_{k+1}) - I_2(x_{j+1}, y_k),\\
d_3 &= I_1(x_{j+1}, y_k) - I_2(x_j, y_{k+1}),\\
d_4 &= I_1(x_{j+1}, y_{k+1}) - I_2(x_j, y_k),
\end{aligned}
$$

and then substitute these differences into equation (A.10):

$$
\begin{aligned}
m(\delta x, \delta y) = \sum_{i=0}^{2p-1} \sum_{j=0}^{2p-1} \Bigg\{ \frac{W_{ij}}{16} \Big[&(1-\delta x)(1-\delta y)\, d_1 + (1-\delta x)(1+\delta y)\, d_2 \\
&+ (1+\delta x)(1-\delta y)\, d_3 + (1+\delta x)(1+\delta y)\, d_4 \Big]^2 \Bigg\},
\end{aligned}
\tag{A.11}
$$

where $W_{ij} = W\left(x_i - x_n + \dfrac{1}{2}, y_j - y_n + \dfrac{1}{2}\right)$. Then, after expanding the square and regrouping we have

$$
\begin{aligned}
m(\delta x, \delta y) = \sum_{i=0}^{2p-1} \sum_{j=0}^{2p-1} \Bigg\{ \frac{W_{ij}}{16} \Big[&a_1 + a_2\, \delta x^2 + a_3\, \delta y^2 + a_4\, \delta x^2 \delta y^2 + a_5\, \delta x \\
&+ a_6\, \delta y + a_7\, \delta x\, \delta y + a_8\, \delta x^2 \delta y + a_9\, \delta x\, \delta y^2 \Big] \Bigg\},
\end{aligned}
\tag{A.12}
$$

where, after some algebra, the a-coefficients are found to be

$$
\begin{aligned}
a_1 &= (d_1 + d_2 + d_3 + d_4)^2, \\
a_2 &= (d_1 + d_2 - d_3 - d_4)^2, \\
a_3 &= (d_1 - d_2 + d_3 - d_4)^2, \\
a_4 &= (d_1 - d_2 - d_3 + d_4)^2, \\
a_5 &= -2(d_1 + d_2 + d_3 + d_4)(d_1 + d_2 - d_3 - d_4), \\
a_6 &= -2(d_1 + d_2 + d_3 + d_4)(d_1 - d_2 + d_3 - d_4), \\
a_7 &= 4(d_1^2 - d_2^2 - d_3^2 + d_4^2), \\
a_8 &= -2(d_1 + d_2 - d_3 - d_4)(d_1 - d_2 - d_3 + d_4), \\
a_9 &= -2(d_1 - d_2 + d_3 - d_4)(d_1 - d_2 - d_3 + d_4).
\end{aligned}
$$

Since the offsets δx and δy are independent of the quantities being summed over, we can pull them out of the sum and define the coefficients

$$A_m \equiv \sum_{i=0}^{2p-1} \sum_{j=0}^{2p-1} \frac{W_{ij}}{16} a_m, \tag{A.13}$$

where $m = 1, 2, \cdots, 9$. Substituting equation (A.13) into equation (A.12), we have

$$
\begin{aligned}
m(\delta x, \delta y) =& A_1 + A_2\,\delta x^2 + A_3\,\delta y^2 + A_4\,\delta x^2 \delta y^2 + A_5\,\delta x \\
&+ A_6\,\delta y + A_7\,\delta x\,\delta y + A_8\,\delta x^2 \delta y + A_9\,\delta x\,\delta y^2.
\end{aligned} \tag{A.14}
$$

Note that the A_m-coefficients can be calculated as soon as the subimages have been extracted, as they depend only upon W and the data values contained in the two subimages S_1^n and S_2^n.

To find the point $(\delta x, \delta y)$ which minimizes $m(\delta x, \delta y)$, we follow the usual procedure of setting the first partial derivatives of m equal to zero and solving the resulting system of equations:

$$\frac{\partial m}{\partial(\delta x)} = 0 \quad \Longrightarrow \quad \left(A_5 + A_7\delta y + A_9\delta y^2\right) + 2\delta x\left(A_2 + A_8\delta y + A_4\delta y^2\right) = 0, \tag{A.15}$$

$$\frac{\partial m}{\partial(\delta y)} = 0 \quad \Longrightarrow \quad \left(A_6 + A_7\delta x + A_8\delta x^2\right) + 2\delta y\left(A_3 + A_9\delta x + A_4\delta x^2\right) = 0. \tag{A.16}$$

At this point, we note that solving for either δx or δy using equation (A.15) or (A.16) and substituting the resulting expression into the other yields a quintic equation. Rather than look for zeroes in such a quintic equation, the correlation tracking algorithm uses an iterative scheme to approximate the extremal value of $(\delta x, \delta y)$. Starting with an estimate for δy, the algorithm obtains an estimate for δx by solving equation (A.15). Using this estimate for δx, a new estimate for δy is calculated by solving equation (A.16). This stepping scheme is iterated until either δx and δy differ from its previous estimate by less than 10^{-4}.

A.4 ITERATING WITH BICUBIC SHIFTS

To attain a more accurate estimate of the optimal displacement $(\delta x, \delta y)$, we could use a higher-ordered interpolation scheme (such as bicubic interpolation) to evaluate I_1 and I_2 at interpixel values in the merit function (A.2) above. However, we find it simpler to use the optimal shifts $(\delta x, \delta y)$ calculated by minimizing m given by equation (A.10), which uses bilinear shifts to estimate interpixel data values, as a guess for what the optimal displacement would be had bicubic interpolation been used in minimizing the merit function. Then one of the subimages is bicubically shifted by the known amount $(\delta x, \delta y)$ and the procedure is repeated. This iteration scheme is chosen because it is computationally faster to bicubically shift images by a known amount, as opposed to calculating an unknown displacement assuming bicubic interpolation was used to evaluate the functions I_1 and I_2 at interpixel values.

The correlation tracking algorithm therefore proceeds as follows. At each measurement gridpoint (x_n, y_n), an optimal displacement is calculated using bilinear shifts in the merit function as described in §A.2. Define this initial displacement as $(\delta x, \delta y)_{\mathrm{agg}}$. The subimage S_2^n is then shifted by this offset $(\delta x, \delta y)_{\mathrm{agg}}$ using *bicubic* interpolation. An additional optimal displacement vector $(\delta x', \delta y')$ is then calculated using the merit function containing bilinear shifts, where S_1^n and the (bicubically) shifted version of S_2^n

are now used as input images. The total displacement becomes the sum of the initial displacement and this additional displacement, so that the aggregate displacement $(\delta x, \delta y)_{\text{agg}} = (\delta x, \delta y)^{\text{old}}_{\text{agg}} + (\delta x', \delta y')$.

We now continue to add to the aggregate displacement by iterating until convergence. That is, subimage S^n_2 is now bicubically shifted by the aggregate displacement $(\delta x, \delta y)_{\text{agg}}$, and another additional displacement vector is calculated using S^n_1 and the newly shifted version of S^n_2. This new displacement vector is then added to the aggregate. Convergence occurs when the displacement vector produced using S^n_1 and a shifted version of S^n_2 has a $|\delta x|$ or $|\delta y|$ less than 10^{-4}. This aggregate shift $(\delta x, \delta y)_{\text{agg}}$ is then returned as the optimal displacement for the gridpoint in question. This bicubic iteration process provides an estimate for what the optimal displacement would have been had bicubic shifts (rather than bilinear shifts) been used to evaluate I_1 and I_2 at interpixel values in equation (A.2).

A.5 CORRELATION TRACKING PITFALLS

In determining the optimal displacement for each measurement gridpoint, several problems may befall the correlation algorithm described above. As stipulated by equation (A.3), if either aggregate offset δx_{agg} or δy_{agg} is more than one pixel in either direction, the algorithm sets the offsets to zero and the gridpoint is flagged. As stated earlier, we do not expect the motions in the time series analyzed in this these to possess displacements of more than one pixel.

Two problems may occur when iterating using the bicubic shifts. First, if more than twenty iterations occur prior to convergence, the offsets are set to zero and the gridpoint is flagged. This situation usually occurs when the merit function contains no prominent minimum causing the algorithm to wander around in $(\delta x, \delta y)$-space, as is caused by when the subimages contain no prominent topological features.

The second problem which may occur during the bicubic iteration process is a degradation of the merit function. Ideally, the value of the merit function continues to decrease as the minimum value of $(\delta x, \delta y)$ is approached. If the value of the merit function is found to increase between iterations, suggesting that the next aggregate offset is actually farther away from the minimum in $m(\delta x, \delta y)$, the current aggregate displacements are returned and the gridpoint is flagged. This problem generally occurs when the topology of the merit function near the minimum value of $(\delta x, \delta y)$ is somewhat lumpy, containing several local extrema in the neighborhood of the absolute minimum.

Appendix B

ASH CODE EQUATIONS — DETAILED DERIVATIONS

This appendix supplements Chapter 4 by providing detailed derivations of the equations presented therein. In the following section, we perform a formal scale analysis on the fully compressible fluid equations in order to determine the anelastic momentum and energy equations listed in §4.2.3. We then in §B.2 derive the energy conservation equations given in §4.2.4. Lastly, in §B.3 we incorporate the streamfunction formalism presented in §4.2.5 into the anelastic evolution equations, replacing them with the evolution equations listed in §4.2.5.

B.1 ANELASTIC FLUID EQUATIONS

We now apply the scaling outlined in §4.2.3 to the fully compressible fluid equations (4.2)–(4.4) to obtain the set of anelastic equations (4.23)–(4.33), where each of the boxed equations in §B.1.2–§B.1.4 which follow correspond to one of the anelastic equations listed in §4.2.3. The derivations presented here follow Gilman & Glatzmaier (1981).

B.1.1 Order in ϵ of All Dependent Variables

As stated in §4.2.3, we express the four thermodynamic state variables as the sum of a spherically symmetric mean quantity and a fluctuating quantity, as in equation (4.21) of §4.2.3:

$$\begin{aligned}
p_{\text{total}}(r,\theta,\phi,t) &= \hat{p}(r) + p(r,\theta,\phi,t), \\
\rho_{\text{total}}(r,\theta,\phi,t) &= \hat{\rho}(r) + \rho(r,\theta,\phi,t), \\
T_{\text{total}}(r,\theta,\phi,t) &= \hat{T}(r) + T(r,\theta,\phi,t), \\
s_{\text{total}}(r,\theta,\phi,t) &= \hat{s}(r) + s(r,\theta,\phi,t).
\end{aligned} \tag{B.1}$$

Note that in these equations we have altered the notation used in equation (4.21) by removing the primes from all fluctuating quantities.

The perturbations to the state variables result from convective motions driven by the superadiabatic stratification of the layer, which is characterized by the parameter ϵ defined in equation (4.12). We therefore assume for $\frac{f}{\hat{f}}$ is of order ϵ for any quantity f in equation (B.1), with the anelastic approximation valid when $\epsilon \ll 1$. To filter out sound waves, we assume

$$\frac{\partial \rho}{\partial t} = 0, \tag{B.2}$$

as in equation (4.22) of §4.2.3.

Before performing the scale separation on the compressible fluid equations, we must first determine the order in ϵ of all variables and operators present. We examine variables other than the thermodynamic state variables in the remainder of this section. A summary of these results is provided in Table B.1.

It is important to note that the fluid velocity $\boldsymbol{u}$ is of order $\epsilon^{\frac{1}{2}}$, as suggested by equation (4.14). The main reason for this scaling is that since the kinetic energy of the motions is extracted from the stratification, we have $\frac{\hat{\rho}\boldsymbol{u}^2}{2} \sim \epsilon$ and therefore $\boldsymbol{u} \sim \epsilon^{\frac{1}{2}}$. Given a representative length scale λ_p and velocity $\boldsymbol{u}$, the time scale dt on which the convection modifies the stratification is thus on the order of $\Delta t = \frac{\lambda_p}{|\boldsymbol{u}|} \sim \epsilon^{-\frac{1}{2}}$, causing time derivatives to scale as $\frac{\partial}{\partial t} \sim \epsilon^{\frac{1}{2}}$.

The heuristic arguments presented above also apply to the diffusivity coefficients. Since we expect the eddy dissipation scale to be set by the scale of the convection, we

Table B.1: Order in ϵ for all quantities and operators appearing in the fully compressible fluid equations.

Order in ϵ	Quantities	Operators
ϵ^0	$\hat{p}$, $\hat{\rho}$, $\hat{T}$, $\hat{s}$, g, $\underline{\underline{\boldsymbol{\delta}}}$	$\boldsymbol{\nabla}$, $\boldsymbol{\nabla}\cdot$, $\boldsymbol{\nabla}\times$
$\epsilon^{\frac{1}{2}}$	$\boldsymbol{u}$, ν_{eff}, κ_s, $\boldsymbol{\Omega}$, $\underline{\underline{\boldsymbol{e}}}$	$\dfrac{\partial}{\partial t}$
ϵ^1	p, ρ, T, s	(none)

find that $\nu_{\text{eff}} \approx \lambda_p \boldsymbol{u}$, and thus $\nu_{\text{eff}} \sim \epsilon^{\frac{1}{2}}$ since $\boldsymbol{u} \sim \epsilon^{\frac{1}{2}}$. Similar scaling arguments also hold for κ_r and κ_s.

In the following subsections, we substitute the scaling given in equation (B.1) into the compressible fluid equations and derive the anelastic equations. As stated in §4.2.3, the diffusivities ν_{eff}, κ_r, and κ_s are assumed to be functions of $\hat{\rho}$ only, while the parameters γ and c_p are assumed constant throughout the domain.

B.1.2 Derivation of the Anelastic Mass Continuity Equation

By substituting equations (B.1) into the mass continuity equation (4.2), we obtain

$$\underbrace{\frac{\partial \rho}{\partial t}}_{\text{vanishes}} + \underbrace{\boldsymbol{\nabla} \cdot (\hat{\rho}\boldsymbol{u})}_{\sim\epsilon^{\frac{1}{2}}} + \underbrace{\boldsymbol{\nabla} \cdot (\rho\boldsymbol{u})}_{\sim\epsilon^{\frac{3}{2}}} = 0. \tag{B.3}$$

As indicated, the time derivative of ρ vanishes by equation (B.2). Retaining the highest-ordered term yields the anelastic mass continuity equation,

$$\boxed{\boldsymbol{\nabla} \cdot (\hat{\rho}\boldsymbol{u}) = 0.} \tag{B.4}$$

B.1.3 Derivation of the Anelastic Momentum Equations

By substituting equations (B.1) into the momentum equation (4.3), and using the definition of $\underline{\underline{\boldsymbol{\mathcal{D}}}}$, equation (4.5), we obtain

$$\begin{aligned}(\hat\rho+\rho)\left[\frac{\partial \boldsymbol{u}}{\partial t}+(\boldsymbol{u}\cdot\boldsymbol{\nabla})\boldsymbol{u}\right] &= -\boldsymbol{\nabla}(\hat p+p)-(\hat\rho+\rho)g\,\hat{\boldsymbol{r}}+2(\hat\rho+\rho)(\boldsymbol{u}\times\boldsymbol{\Omega})\\ &\quad+\boldsymbol{\nabla}\cdot\left\{2(\hat\rho+\rho)\nu_{\text{eff}}\left[\underline{\underline{\boldsymbol{e}}}-\frac{1}{3}(\boldsymbol{\nabla}\cdot\boldsymbol{u})\,\underline{\underline{\boldsymbol{\delta}}}\right]\right\}.\end{aligned} \tag{B.5}$$

After expanding and grouping according to their order in ϵ, we obtain

$$\begin{aligned}&\underbrace{\hat\rho\frac{\partial \boldsymbol{u}}{\partial t}+\hat\rho(\boldsymbol{u}\cdot\boldsymbol{\nabla})\boldsymbol{u}}_{\sim\epsilon^1}+\underbrace{\rho\frac{\partial \boldsymbol{u}}{\partial t}+\rho(\boldsymbol{u}\cdot\boldsymbol{\nabla})\boldsymbol{u}}_{\sim\epsilon^2}+\underbrace{\boldsymbol{\nabla}\hat p+\hat\rho g\,\hat{\boldsymbol{r}}}_{\sim\epsilon^0}\\ &\qquad=\underbrace{2\hat\rho(\boldsymbol{u}\times\boldsymbol{\Omega})-\boldsymbol{\nabla}p-\rho g\,\hat{\boldsymbol{r}}+\boldsymbol{\nabla}\cdot\left\{2\hat\rho\nu_{\text{eff}}\left[\underline{\underline{\boldsymbol{e}}}-\frac{1}{3}(\boldsymbol{\nabla}\cdot\boldsymbol{u})\,\underline{\underline{\boldsymbol{\delta}}}\right]\right\}}_{\sim\epsilon^1}\\ &\qquad\quad+\underbrace{2\rho(\boldsymbol{u}\times\boldsymbol{\Omega})+\boldsymbol{\nabla}\cdot\left\{2\rho\nu_{\text{eff}}\left[\underline{\underline{\boldsymbol{e}}}-\frac{1}{3}(\boldsymbol{\nabla}\cdot\boldsymbol{u})\,\underline{\underline{\boldsymbol{\delta}}}\right]\right\}}_{\sim\epsilon^2}.\end{aligned} \tag{B.6}$$

The mean momentum equation consists of the terms scaling as ϵ^0, of which only the $\hat{\boldsymbol{r}}$-component remains,

$$\boxed{\frac{\partial \hat p}{\partial r}+\hat\rho g=0.} \tag{B.7}$$

The first-order (ϵ^1) terms give the fluctuating momentum equation,

$$\boxed{\hat\rho\frac{\partial \boldsymbol{u}}{\partial t}=2\hat\rho(\boldsymbol{u}\times\boldsymbol{\Omega})-\hat\rho(\boldsymbol{u}\cdot\boldsymbol{\nabla})\boldsymbol{u}-\boldsymbol{\nabla}p-\rho g\,\hat{\boldsymbol{r}}+\boldsymbol{\nabla}\cdot\hat{\underline{\underline{\boldsymbol{\mathcal{D}}}}},} \tag{B.8}$$

where the anelastic viscous stress tensor $\hat{\underline{\underline{\boldsymbol{\mathcal{D}}}}}$ is defined

$$\boxed{\hat{\underline{\underline{\boldsymbol{\mathcal{D}}}}}=2\hat\rho\nu_{\text{eff}}\left[\underline{\underline{\boldsymbol{e}}}-\frac{1}{3}(\boldsymbol{\nabla}\cdot\boldsymbol{u})\,\underline{\underline{\boldsymbol{\delta}}}\right].} \tag{B.9}$$

B.1.4 Derivation of the Anelastic Energy Equation

By substituting equations (B.1) into the energy equation (4.4), and using the definition of Φ, equation (4.6), we obtain

$$\begin{aligned}(\hat\rho+\rho)(\hat T+T)&\left[\frac{\partial(\hat s+s)}{\partial t}+(\boldsymbol{u}\cdot\boldsymbol{\nabla})(\hat s+s)\right]\\ &=-\boldsymbol{\nabla}\cdot\hat{\boldsymbol{q}}_{\text{eff}}+2(\hat\rho+\rho)\left[\underline{\underline{\boldsymbol{e}}}:\underline{\underline{\boldsymbol{e}}}-\frac{1}{3}(\boldsymbol{\nabla}\cdot\boldsymbol{u})^2\right],\end{aligned} \tag{B.10}$$

where the anelastic heat flux $\hat{\boldsymbol{q}}_{\text{eff}}$ is defined

$$\boxed{\hat{\boldsymbol{q}}_{\text{eff}} = -\kappa_r \hat{\rho} c_p \boldsymbol{\nabla}(\hat{T} + T) - \kappa_s \hat{\rho} \hat{T} \boldsymbol{\nabla}(\hat{s} + s).} \tag{B.11}$$

In the above equation, we have explicitly included the contributions to the diffusive transport of internal energy by the fluctuating temperature and entropy gradients. Similarly, we also keep the fluctuating entropy gradient in the advection term, so that the anelastic energy equation becomes

$$\boxed{\hat{\rho}\hat{T}\frac{\partial s}{\partial t} = -\boldsymbol{\nabla} \cdot \hat{\boldsymbol{q}}_{\text{eff}} - \hat{\rho}\hat{T}(\boldsymbol{u} \cdot \boldsymbol{\nabla})(\hat{s} + s) + \hat{\Phi},} \tag{B.12}$$

where the anelastic viscous heating term $\hat{\Phi}$ is defined

$$\hat{\Phi} = 2\hat{\rho}\nu_{\text{eff}} \left[\underline{\underline{\boldsymbol{e}}} : \underline{\underline{\boldsymbol{e}}} - \frac{1}{3}(\boldsymbol{\nabla} \cdot \boldsymbol{u})^2 \right]. \tag{B.13}$$

Note that we have used the anelastic stress tensor $\underline{\underline{\hat{\boldsymbol{\mathcal{D}}}}}$ as defined in equation (B.9).

B.1.5 Derivation of the Anelastic Equations of State

Substituting equations (B.1) into the equation of state (4.10) yields

$$\hat{p} + p = \frac{\gamma - 1}{\gamma} c_p (\hat{\rho} + \rho)(\hat{T} + T). \tag{B.14}$$

Collecting the zeroth-order terms gives

$$\boxed{\hat{p} = \frac{\gamma - 1}{\gamma} c_p \hat{\rho}\hat{T},} \tag{B.15}$$

while the first-order terms are

$$p = \frac{\gamma - 1}{\gamma} c_p \left(\rho\hat{T} + \hat{\rho}T \right), \tag{B.16}$$

or after dividing by equation (B.15) we arrive at

$$\boxed{\frac{p}{\hat{p}} = \frac{\rho}{\hat{\rho}} + \frac{T}{\hat{T}}.} \tag{B.17}$$

Substituting equations (B.1) into the entropy equation (4.11) yields

$$\hat{s} + s = c_p \left[\frac{1}{\gamma} \ln(\hat{p} + p) - \ln(\hat{\rho} + \rho) \right], \tag{B.18}$$

$$= c_p \left[\frac{1}{\gamma} \left(\ln \hat{p} + \ln \left[1 + \frac{p}{\hat{p}} \right] \right) - \left(\ln \hat{\rho} + \ln \left[1 + \frac{\rho}{\hat{\rho}} \right] \right) \right]. \tag{B.19}$$

Since $\left| \frac{p}{\hat{p}} \right| \ll 1$ and $\left| \frac{\rho}{\hat{\rho}} \right| \ll 1$, we can use the series representation of $\ln(1 + x)$,

$$\ln(1 + x) = x - \frac{x^2}{2} + \frac{x^3}{3} - \cdots, \qquad \text{valid for } -1 < x \leq 1. \tag{B.20}$$

Keeping only the highest-order term in the series, we obtain

$$\hat{s} + s = c_p \left[\frac{1}{\gamma} \left(\ln \hat{p} + \frac{p}{\hat{p}} \right) - \left(\ln \hat{\rho} + \frac{\rho}{\hat{\rho}} \right) \right]. \tag{B.21}$$

The zeroth-order terms are

$$\hat{s} = c_p \left(\frac{1}{\gamma} \ln \hat{p} - \ln \hat{\rho} \right), \tag{B.22}$$

which after taking a radial derivative become

$$\boxed{\frac{d\hat{s}}{dr} = c_p \left(\frac{1}{\gamma \hat{p}} \frac{d\hat{p}}{dr} - \frac{1}{\hat{\rho}} \frac{d\hat{\rho}}{dr} \right),} \tag{B.23}$$

while the first-order terms give

$$\boxed{\frac{s}{c_p} = \frac{p}{\gamma \hat{p}} - \frac{\rho}{\hat{\rho}}.} \tag{B.24}$$

B.2 ANELASTIC EQUATION ENERGETICS

B.2.1 Derivation of the Kinetic Energy Conservation Equation

The equation describing the conservation of kinetic energy density $\mathcal{E}_k = \dfrac{\hat{\rho} \boldsymbol{u} \cdot \boldsymbol{u}}{2}$ is formed by taking $\boldsymbol{u}\cdot$ each term in the anelastic momentum equation (B.8),

$$\hat{\rho} \frac{\partial \boldsymbol{u}}{\partial t} = 2\hat{\rho}(\boldsymbol{u} \times \boldsymbol{\Omega}) - \hat{\rho}(\boldsymbol{u} \cdot \boldsymbol{\nabla})\boldsymbol{u} - \boldsymbol{\nabla} p - \rho g \,\hat{\boldsymbol{r}} + \boldsymbol{\nabla} \cdot \underline{\underline{\hat{\boldsymbol{\mathcal{D}}}}}. \tag{B.25}$$

Starting with the time-derivative term, we have

$$\hat{\rho} \boldsymbol{u} \cdot \frac{\partial \boldsymbol{u}}{\partial t} = \frac{\partial}{\partial t} \left(\frac{\hat{\rho} \boldsymbol{u} \cdot \boldsymbol{u}}{2} \right) = \frac{\partial \mathcal{E}_k}{\partial t}, \tag{B.26}$$

where we have made use of the fact that $\dfrac{\partial \hat{\rho}}{\partial t} = 0$.

The Coriolis term,

$$2\hat{\rho}\boldsymbol{u} \cdot (\boldsymbol{u} \times \boldsymbol{\Omega}) = 0, \tag{B.27}$$

vanishes since it acts perpendicular to the motion and thus cannot perform any work.

The inertial term is

$$\hat{\rho}\boldsymbol{u} \cdot [(\boldsymbol{u} \cdot \boldsymbol{\nabla})\boldsymbol{u}] = \boldsymbol{\nabla} \cdot \left[\boldsymbol{u}\left(\frac{\hat{\rho}\boldsymbol{u} \cdot \boldsymbol{u}}{2}\right)\right]. \tag{B.28}$$

This relation is most easily verified by using the following vector identity,

$$\boldsymbol{\nabla} \cdot (f\boldsymbol{A}) = \boldsymbol{A} \cdot (\boldsymbol{\nabla} f) + f(\boldsymbol{\nabla} \cdot \boldsymbol{A}), \tag{B.29}$$

to expand $\boldsymbol{\nabla} \cdot \left[\boldsymbol{u}\left(\dfrac{\hat{\rho}\boldsymbol{u} \cdot \boldsymbol{u}}{2}\right)\right] = \boldsymbol{\nabla} \cdot \left[\left(\dfrac{\hat{\rho}\boldsymbol{u}}{2}\right)\boldsymbol{u} \cdot \boldsymbol{u}\right]$, and showing that it equals $\hat{\rho}\boldsymbol{u} \cdot [(\boldsymbol{u} \cdot \boldsymbol{\nabla})\boldsymbol{u}]$:

$$\boldsymbol{\nabla} \cdot \left[\left(\frac{\hat{\rho}\boldsymbol{u}}{2}\right)\boldsymbol{u} \cdot \boldsymbol{u}\right] = \frac{\hat{\rho}\boldsymbol{u}}{2} \cdot [\boldsymbol{\nabla}(\boldsymbol{u} \cdot \boldsymbol{u})] + \underbrace{\frac{1}{2}(\boldsymbol{u} \cdot \boldsymbol{u})\boldsymbol{\nabla} \cdot (\hat{\rho}\boldsymbol{u})}_{\text{vanishes by equation (B.4)}} \tag{B.30}$$

$$= \underbrace{\hat{\rho}\boldsymbol{u} \cdot [\boldsymbol{u} \times (\boldsymbol{\nabla} \times \boldsymbol{u})]}_{\text{vanishes}} + \hat{\rho}\boldsymbol{u} \cdot [(\boldsymbol{u} \cdot \boldsymbol{\nabla})\boldsymbol{u}]. \tag{B.31}$$

Note that this derivation shows that the inertial term can be written as the divergence of the kinetic energy flux.

The remaining terms are simply

$$\boldsymbol{u} \cdot \boldsymbol{\nabla} p + \rho g \boldsymbol{u} \cdot \hat{\boldsymbol{r}} + \boldsymbol{u} \cdot \left(\boldsymbol{\nabla} \cdot \underline{\underline{\hat{\boldsymbol{\mathcal{D}}}}}\right). \tag{B.32}$$

Collecting terms, we obtain the kinetic energy conservation equation listed as equation (4.34) of Chapter 4,

$$\boxed{\frac{\partial \mathcal{E}_k}{\partial t} = -\boldsymbol{u} \cdot \boldsymbol{\nabla} p - \rho g \boldsymbol{u} \cdot \hat{\boldsymbol{r}} + \boldsymbol{u} \cdot \left(\boldsymbol{\nabla} \cdot \underline{\underline{\hat{\boldsymbol{\mathcal{D}}}}}\right) - \boldsymbol{\nabla} \cdot \left[\boldsymbol{u}\left(\frac{\hat{\rho}\boldsymbol{u} \cdot \boldsymbol{u}}{2}\right)\right].} \tag{B.33}$$

B.2.2 Derivation of the Internal Energy Conservation Equation

Since the time derivatives of $\hat{\rho}$ and $\hat{T}$ are zero, the equation describing the time dependence of internal energy density $\mathcal{E}_s = \hat{\rho}\hat{T}s$ is the anelastic internal energy equation (B.12),

$$\frac{\partial \mathcal{E}_s}{\partial t} = \boldsymbol{\nabla} \cdot \hat{\boldsymbol{q}}_{\text{eff}} - \hat{\rho}\hat{T}(\boldsymbol{u} \cdot \boldsymbol{\nabla})(\hat{s} + s) + \hat{\Phi}, \tag{B.34}$$

where the time derivative term $\hat{\rho}\hat{T}\dfrac{\partial s}{\partial t}$ has been replaced by $\dfrac{\partial}{\partial t}(\hat{\rho}\hat{T}s) = \dfrac{\partial \mathcal{E}_s}{\partial t}$.

Additional insight may be gained by rewriting the inertial term as follows:

$$\begin{aligned}
&- \hat{\rho}\hat{T}(\boldsymbol{u} \cdot \boldsymbol{\nabla})s \\
&\quad = -c_p\hat{\rho}\hat{T}(\boldsymbol{u} \cdot \boldsymbol{\nabla})\left[\frac{T}{\hat{T}} - \frac{\gamma - 1}{\gamma}\frac{p}{\hat{p}}\right] \\
&\quad = -c_p\hat{\rho}\hat{T}\boldsymbol{u} \cdot \left[\frac{\boldsymbol{\nabla}T}{\hat{T}} - \frac{\gamma-1}{\gamma}\frac{\boldsymbol{\nabla}p}{\hat{p}} - \frac{T}{\hat{T}^2}\frac{d\hat{T}}{dr}\hat{\boldsymbol{r}} + \frac{\gamma-1}{\gamma}\frac{p}{\hat{p}^2}\frac{d\hat{p}}{dr}\hat{\boldsymbol{r}}\right] \\
&\quad = -c_p\hat{\rho}\boldsymbol{u} \cdot \boldsymbol{\nabla}T + \boldsymbol{u} \cdot \boldsymbol{\nabla}p + c_p u_r \frac{\hat{\rho}T}{\hat{T}}\frac{d\hat{T}}{dr} - u_r\frac{p}{\hat{p}}\frac{d\hat{p}}{dr} \\
&\quad = -c_p\boldsymbol{\nabla} \cdot (\hat{\rho}T\boldsymbol{u}) + \boldsymbol{u} \cdot \boldsymbol{\nabla}p + c_p u_r\hat{\rho}T\left[\frac{1}{c_p}\frac{d\hat{s}}{dr} + \frac{\gamma-1}{\gamma\hat{p}}\frac{d\hat{p}}{dr}\right] - u_r\frac{p}{\hat{p}}\frac{d\hat{p}}{dr} \\
&\quad = -c_p\boldsymbol{\nabla} \cdot (\hat{\rho}T\boldsymbol{u}) + \boldsymbol{u} \cdot \boldsymbol{\nabla}p + u_r\hat{\rho}T\frac{d\hat{s}}{dr} + u_r\left[\frac{T}{\hat{T}} - \frac{p}{\hat{p}}\right]\frac{d\hat{p}}{dr} \\
&\quad = -c_p\boldsymbol{\nabla} \cdot (\hat{\rho}T\boldsymbol{u}) + \boldsymbol{u} \cdot \boldsymbol{\nabla}p - u_r\frac{\rho}{\hat{\rho}}\frac{d\hat{p}}{dr} + \underbrace{u_r\hat{\rho}T\frac{d\hat{s}}{dr}}_{\approx 0,\ \text{higher order}} \\
&\quad = -c_p\boldsymbol{\nabla} \cdot (\hat{\rho}T\boldsymbol{u}) + \boldsymbol{u} \cdot \boldsymbol{\nabla}p + u_r\rho g
\end{aligned}$$

where $u_r = \boldsymbol{u} \cdot \hat{\boldsymbol{r}}$, and where the mean equations (B.7), (B.15), and (B.23) as well as the dynamic equations of state (B.17) and (B.24) have been used throughout. Using this form of the inertial term, we obtain the internal energy conservation equation listed as equation (4.35) of Chapter 4,

$$\boxed{\frac{\partial \mathcal{E}_s}{\partial t} = \boldsymbol{\nabla} \cdot \hat{\boldsymbol{q}}_{\text{eff}} + \boldsymbol{u} \cdot \boldsymbol{\nabla}p + \rho g\boldsymbol{u} \cdot \hat{\boldsymbol{r}} - \boldsymbol{\nabla} \cdot (c_p\hat{\rho}T\boldsymbol{u}) + \hat{\Phi}.} \tag{B.35}$$

B.2.3 Derivation of the Total Energy Conservation Equation

Adding together the energy conservation equations (B.33) and (B.35) yields the total energy equation (4.36) of Chapter 4,

$$\boxed{\frac{\partial(\mathcal{E}_k+\mathcal{E}_s)}{\partial t} = \boldsymbol{\nabla}\cdot\left(\boldsymbol{u}\cdot\underline{\underline{\hat{\boldsymbol{\mathcal{D}}}}}\right) + \boldsymbol{\nabla}\cdot\left[\boldsymbol{u}\left(\frac{\hat{\rho}\boldsymbol{u}\cdot\boldsymbol{u}}{2}\right)\right] + \boldsymbol{\nabla}\cdot\hat{\boldsymbol{q}}_{\text{eff}} - \boldsymbol{\nabla}\cdot(c_p\hat{\rho}T\boldsymbol{u}).} \tag{B.36}$$

In the above equation, the viscous energy source term $\boldsymbol{\nabla}\cdot\left(\boldsymbol{u}\cdot\underline{\underline{\hat{\boldsymbol{\mathcal{D}}}}}\right)$ is arrived at by combining the diffusion terms in equations (B.33) and (B.35), which we now show using indicial notation in Cartesian coordinates.

$$\boldsymbol{u}\cdot\left(\boldsymbol{\nabla}\cdot\underline{\underline{\hat{\boldsymbol{\mathcal{D}}}}}\right)+\hat{\Phi} = u_i\frac{\partial\mathcal{D}_{ij}}{\partial x_j}+\mathcal{D}_{ij}\frac{\partial u_i}{\partial x_j} = \frac{\partial}{\partial x_j}(u_i\mathcal{D}_{ij}) = \boldsymbol{\nabla}\cdot\left(\boldsymbol{u}\cdot\underline{\underline{\hat{\boldsymbol{\mathcal{D}}}}}\right), \tag{B.37}$$

where the we have used the equality

$$\mathcal{D}_{ij}\frac{\partial u_i}{\partial x_j} = 2\hat{\rho}\nu_{\text{eff}}\left[e_{ij}\frac{\partial u_i}{\partial x_j}-\frac{1}{3}(\boldsymbol{\nabla}\cdot\boldsymbol{u})\frac{\partial u_i}{\partial x_j}\delta_{ij}\right] \tag{B.38}$$

$$= 2\hat{\rho}\nu_{\text{eff}}\left[e_{ij}e_{ij}-\frac{1}{3}(\boldsymbol{\nabla}\cdot\boldsymbol{u})^2\right] \qquad \text{since } \frac{\partial u_i}{\partial x_j}\delta_{ij} = \boldsymbol{\nabla}\cdot\boldsymbol{u} \tag{B.39}$$

$$= 2\hat{\rho}\nu_{\text{eff}}\left[\underline{\underline{\boldsymbol{e}}}:\underline{\underline{\boldsymbol{e}}}-\frac{1}{3}(\boldsymbol{\nabla}\cdot\boldsymbol{u})^2\right] \tag{B.40}$$

$$= \hat{\Phi}. \tag{B.41}$$

Going from equation (B.38) to (B.39) is achieved by using the fact that the doubly contracted tensor product of a symmetric tensor and an antisymmetric tensor is zero. Since the strain rate tensor $e_{ij} = \frac{1}{2}\left(\frac{\partial u_i}{\partial x_j}+\frac{\partial u_j}{\partial x_i}\right)$ is symmetric (as can be seen from its Cartesian representation), the product $\frac{\partial u_i}{\partial x_j}e_{ij}$ is equal to the product of e_{ij} and the symmetric part of $\frac{\partial u_i}{\partial x_j}$, which is simply e_{ij}.

B.3 THE NUMERICAL EVOLUTION EQUATIONS

We now proceed to derive equations (4.38)–(4.40) of Chapter 4.

B.3.1 Streamfunction Formalism

Any vector $\boldsymbol{A}$ for which $\boldsymbol{\nabla} \cdot \boldsymbol{A} = 0$ can be decomposed into poloidal and toroidal streamfunctions W and Z, respectively:

$$\boldsymbol{A} = \boldsymbol{\nabla} \times (\boldsymbol{\nabla} \times W\,\hat{\boldsymbol{r}}) + \boldsymbol{\nabla} \times Z\,\hat{\boldsymbol{r}}, \tag{B.42}$$

such that $\boldsymbol{\nabla} \cdot \boldsymbol{A} = 0$ is identically satisfied at all times. Because

$$\boldsymbol{\nabla} \cdot (\hat{\rho}\boldsymbol{u}) = 0, \tag{B.43}$$

by equation (B.4), we may write

$$\hat{\rho}\boldsymbol{u} = \boldsymbol{\nabla} \times (\boldsymbol{\nabla} \times W\,\hat{\boldsymbol{r}}) + \boldsymbol{\nabla} \times Z\,\hat{\boldsymbol{r}}. \tag{B.44}$$

The scalar quantities W and Z are the poloidal and toroidal streamfunctions for the mass flux, and it is equations describing the evolution of these quantities (along with p and s) that are solved by the ASH code. We outline the derivations of these equations in Table B.2, while presenting detailed derivations in §B.3.4–§B.3.7.

B.3.2 Streamfunction Identities

In this section, we list some identities used in the upcoming sections. Expanding the vector cross products from equation (B.42) in spherical polar coordinates, the three components of $\hat{\rho}\boldsymbol{u}$ are found to be

$$\hat{\rho}\boldsymbol{u} = -\left(\nabla_\perp^2 W\right)\,\hat{\boldsymbol{r}} + \left[\frac{1}{r}\frac{\partial^2 W}{\partial r \partial \theta} + \frac{1}{r\sin\theta}\frac{\partial Z}{\partial \phi}\right]\,\hat{\boldsymbol{\theta}} + \left[\frac{1}{r\sin\theta}\frac{\partial^2 W}{\partial r \partial \phi} - \frac{1}{r}\frac{\partial Z}{\partial \theta}\right]\,\hat{\boldsymbol{\phi}}, \tag{B.45}$$

while the curl of $\hat{\rho}\boldsymbol{u}$ is

$$\begin{aligned} \boldsymbol{\nabla} \times \hat{\rho}\boldsymbol{u} = -\left(\nabla_\perp^2 Z\right)\,\hat{\boldsymbol{r}} &+ \left[-\frac{1}{r\sin\theta}\frac{\partial}{\partial \phi}\left(\frac{\partial^2}{\partial r^2} + \nabla_\perp^2\right) W + \frac{1}{r}\frac{\partial^2 Z}{\partial r \partial \theta}\right]\,\hat{\boldsymbol{\theta}} \\ &+ \left[\frac{1}{r}\frac{\partial}{\partial \theta}\left(\frac{\partial^2}{\partial r^2} + \nabla_\perp^2\right) W + \frac{1}{r\sin\theta}\frac{\partial^2 Z}{\partial r \partial \phi}\right]\,\hat{\boldsymbol{\phi}}. \end{aligned} \tag{B.46}$$

Table B.2: Strategy employed to obtain the ASH code evolution equations.

Apply this operator	to this equation	to obtain the evolution equation for	derived in	as equation
$\hat{\boldsymbol{r}}\cdot$	(B.8)	$\dfrac{\partial}{\partial t}(\nabla_\perp^2 W)$	§B.3.4	(B.123)
$\boldsymbol{\nabla}_\perp\cdot$	(B.8)	$\dfrac{\partial}{\partial t}\left(\nabla_\perp^2 \dfrac{\partial W}{\partial r}\right)$	§B.3.5	(B.132)
$\hat{\boldsymbol{r}}\cdot\boldsymbol{\nabla}\times$	(B.8)	$\dfrac{\partial}{\partial t}(\nabla_\perp^2 Z)$	§B.3.6	(B.140)
[none]	(B.12)	$\dfrac{\partial s}{\partial t}$	§B.3.7	(B.144)

In the above two expressions, we have used the horizontal Laplacian operator,

$$\nabla_\perp^2 = \frac{1}{r^2 \sin\theta}\frac{\partial}{\partial\theta}\left(\sin\theta\frac{\partial}{\partial\theta}\right) + \frac{1}{r^2\sin^2\theta}\frac{\partial^2}{\partial\phi^2}, \tag{B.47}$$

defined such that the total Laplacian operator is

$$\nabla^2 = \frac{1}{r^2}\frac{\partial}{\partial r}\left(r^2\frac{\partial}{\partial r}\right) + \nabla_\perp^2. \tag{B.48}$$

The horizontal Laplacian operator commutes with radial derivatives in the following manner:

$$\left(\frac{\partial}{\partial r}\nabla_\perp^2\right) f(r,\theta,\phi) = \nabla_\perp^2\left(\frac{\partial}{\partial r} - \frac{2}{r}\right) f(r,\theta,\phi), \tag{B.49}$$

$$\left(\frac{\partial^2}{\partial r^2}\nabla_\perp^2\right) f(r,\theta,\phi) = \nabla_\perp^2\left(\frac{\partial^2}{\partial r^2} - \frac{4}{r}\frac{\partial}{\partial r} + \frac{6}{r^2}\right) f(r,\theta,\phi), \tag{B.50}$$

$$\left(\frac{\partial^3}{\partial r^3}\nabla_\perp^2\right) f(r,\theta,\phi) = \nabla_\perp^2\left(\frac{\partial^3}{\partial r^3} - \frac{6}{r}\frac{\partial^2}{\partial r^2} + \frac{18}{r^2}\frac{\partial}{\partial r} - \frac{24}{r^3}\right) f(r,\theta,\phi). \tag{B.51}$$

B.3.3 Components of the Divergence of the Viscous Stress Tensor

In this section, we evaluate the components of the anelastic viscous stress tensor, $\boldsymbol{\nabla}\cdot\underline{\underline{\hat{\mathcal{D}}}}$, in preparation for their use in §B.3.4–§B.3.7.

B.3.3.1 Preliminaries

The anelastic stress tensor is

$$
\begin{aligned}
\underline{\underline{\hat{\boldsymbol{\mathcal{D}}}}} &= 2\hat{\rho}\nu\left[\underline{\underline{\boldsymbol{e}}} - \frac{1}{3}(\boldsymbol{\nabla}\cdot\boldsymbol{u})\,\underline{\underline{\boldsymbol{\delta}}}\right] \qquad \text{by equation (B.9)} \\
&= 2\nu\left[\hat{\rho}\underline{\underline{\boldsymbol{e}}} - \frac{\hat{\rho}}{3}(\boldsymbol{\nabla}\cdot\boldsymbol{u})\underline{\underline{\boldsymbol{\delta}}}\right] \\
&= 2\nu\left[\hat{\rho}\underline{\underline{\boldsymbol{e}}} - \frac{1}{3}\Big(\boldsymbol{\nabla}\cdot(\hat{\rho}\boldsymbol{u}) - \boldsymbol{u}\cdot\boldsymbol{\nabla}\hat{\rho}\Big)\underline{\underline{\boldsymbol{\delta}}}\right] \\
&= 2\nu\left[\hat{\rho}\underline{\underline{\boldsymbol{e}}} + \frac{\beta}{3}\,\hat{\rho}u_r\,\underline{\underline{\boldsymbol{\delta}}}\right], \qquad \text{since } \boldsymbol{\nabla}\cdot(\hat{\rho}\boldsymbol{u}) = 0 \text{ by equation (B.4)}
\end{aligned}
\tag{B.52}
$$

where β is defined below in equation (B.56) and where we have dropped the "eff" subscript from ν_{eff}, hereafter using ν instead. To evaluate $\boldsymbol{\nabla}\cdot\underline{\underline{\hat{\boldsymbol{\mathcal{D}}}}}$, we will need the individual components of the tensor $\hat{\rho}\underline{\underline{\boldsymbol{e}}}$ in spherical polar coordinates,

$$
\begin{aligned}
\hat{\rho}e_{rr} &= \frac{\partial(\hat{\rho}u_r)}{\partial r} - \beta\hat{\rho}u_r \\
\hat{\rho}e_{\theta\theta} &= \frac{1}{r}\frac{\partial(\hat{\rho}u_\theta)}{\partial\theta} + \frac{1}{r}\,\hat{\rho}u_r, \\
\hat{\rho}e_{\phi\phi} &= \frac{1}{r\sin\theta}\frac{\partial(\hat{\rho}u_\phi)}{\partial\phi} + \frac{1}{r}\,\hat{\rho}u_r + \frac{\cos\theta}{r\sin\theta}\,\hat{\rho}u_\theta, \\
\hat{\rho}e_{r\theta} &= \frac{1}{2}\frac{\partial(\hat{\rho}u_\theta)}{\partial r} - \frac{\beta}{2}\,\hat{\rho}u_\theta - \frac{1}{2r}\,\hat{\rho}u_\theta + \frac{1}{2r}\frac{\partial(\hat{\rho}u_r)}{\partial\theta}, \\
\hat{\rho}e_{r\phi} &= \frac{1}{2r\sin\theta}\frac{\partial(\hat{\rho}u_r)}{\partial\phi} + \frac{1}{2}\frac{\partial(\hat{\rho}u_\phi)}{\partial r} - \frac{\beta}{2}\,\hat{\rho}u_\phi - \frac{1}{2r}\,\hat{\rho}u_\phi, \\
\hat{\rho}e_{\theta\phi} &= \frac{1}{2r}\frac{\partial(\hat{\rho}u_\phi)}{\partial\theta} - \frac{\cos\theta}{2r\sin\theta}\,\hat{\rho}u_\phi + \frac{1}{2r\sin\theta}\frac{\partial(\hat{\rho}u_\theta)}{\partial\phi},
\end{aligned}
\tag{B.53}
$$

where we have again used the definition of β given in equation (B.56) below. It will also prove useful to have handy the expression for $\boldsymbol{\nabla}\cdot(\hat{\rho}\boldsymbol{u}) = 0$,

$$
\frac{1}{r^2}\frac{\partial(r^2\hat{\rho}u_r)}{\partial r} + \frac{1}{r\sin\theta}\frac{\partial(\sin\theta\,\hat{\rho}u_\theta)}{\partial\theta} + \frac{1}{r\sin\theta}\frac{\partial(\hat{\rho}u_\phi)}{\partial\phi} = 0,
\tag{B.54}
$$

which vanishes by equation (B.4). Finally, we define the following functions of r,

$$
\alpha = \frac{d\ln\nu}{dr}
\tag{B.55}
$$

and

$$
\beta = \frac{d\ln\hat{\rho}}{dr}.
\tag{B.56}
$$

B.3.3.2 Radial Component

For any tensor $\underline{\underline{\boldsymbol{\mathcal{T}}}}$, the radial component of its divergence is

$$\hat{\boldsymbol{r}}\cdot\left(\boldsymbol{\nabla}\cdot\underline{\underline{\boldsymbol{\mathcal{T}}}}\right)=\underbrace{\frac{1}{r^2}\frac{\partial(r^2\mathcal{T}_{rr})}{\partial r}}_{\boxed{1}}+\underbrace{\frac{1}{r\sin\theta}\frac{\partial(\sin\theta\,\mathcal{T}_{r\theta})}{\partial\theta}}_{\boxed{2}}+\underbrace{\frac{1}{r\sin\theta}\frac{\partial\mathcal{T}_{r\phi}}{\partial\phi}}_{\boxed{3}}-\underbrace{\frac{\mathcal{T}_{\theta\theta}+\mathcal{T}_{\phi\phi}}{r}}_{\boxed{4}}. \tag{B.57}$$

In this section, we evaluate equation (B.57) for $\underline{\underline{\boldsymbol{\mathcal{T}}}}=\underline{\underline{\hat{\boldsymbol{\mathcal{D}}}}}$ using the definition of $\underline{\underline{\hat{\boldsymbol{\mathcal{D}}}}}$ given in equation (B.52) along with the strain rate tensor components of equation (B.53). Starting with the first term, we have

$$\begin{aligned}\boxed{1}&=\frac{1}{r^2}\frac{\partial}{\partial r}\left[r^2\,2\nu\left(\frac{\partial(\hat{\rho}u_r)}{\partial r}-\frac{2\beta}{3}\hat{\rho}u_r\right)\right]\\&=\frac{2\nu}{r^2}\left\{\alpha r^2\left[\frac{\partial(\hat{\rho}u_r)}{\partial r}-\frac{2\beta}{3}\hat{\rho}u_r\right]+\frac{\partial}{\partial r}\left(r^2\left[\frac{\partial(\hat{\rho}u_r)}{\partial r}-\frac{2\beta}{3}\hat{\rho}u_r\right]\right)\right\}\\&=\underbrace{2\nu\alpha\left[\frac{\partial(\hat{\rho}u_r)}{\partial r}-\frac{2\beta}{3}\hat{\rho}u_r\right]}_{\boxed{1a}}+\underbrace{\frac{2\nu}{r^2}\frac{\partial}{\partial r}\left[r^2\frac{\partial(\hat{\rho}u_r)}{\partial r}\right]}_{\boxed{1b}}-\underbrace{\frac{4\nu\beta}{3r^2}\frac{\partial(r^2\hat{\rho}u_r)}{\partial r}}_{\boxed{1c}}-\underbrace{\frac{4\nu}{3}\frac{d\beta}{dr}\hat{\rho}u_r}_{\boxed{1d}}.\end{aligned} \tag{B.58}$$

The second term is

$$\begin{aligned}\boxed{2}&=\frac{1}{r\sin\theta}\frac{\partial}{\partial\theta}\left[\sin\theta\,2\nu\left(\frac{1}{2}\frac{\partial(\hat{\rho}u_\theta)}{\partial r}-\frac{\beta}{2}\,\hat{\rho}u_\theta-\frac{1}{2r}\,\hat{\rho}u_\theta+\frac{1}{2r}\frac{\partial(\hat{\rho}u_r)}{\partial\theta}\right)\right]\\&=\frac{\nu}{r\sin\theta}\frac{\partial}{\partial\theta}\left[\sin\theta\left(\frac{\partial(\hat{\rho}u_\theta)}{\partial r}-\beta\hat{\rho}u_\theta-\frac{1}{r}\,\hat{\rho}u_\theta+\frac{1}{r}\frac{\partial(\hat{\rho}u_r)}{\partial\theta}\right)\right]\\&=\underbrace{\nu\frac{\partial}{\partial r}\left[\frac{1}{r\sin\theta}\frac{\partial(\sin\theta\,\hat{\rho}u_\theta)}{\partial\theta}\right]}_{\boxed{2a}}-\underbrace{\frac{\nu\beta}{r\sin\theta}\frac{\partial(\sin\theta\,\hat{\rho}u_\theta)}{\partial\theta}}_{\boxed{2b}}+\underbrace{\frac{\nu}{r^2\sin\theta}\frac{\partial}{\partial\theta}\left[\sin\theta\frac{\partial(\hat{\rho}u_r)}{\partial\theta}\right]}_{\boxed{2c}},\end{aligned} \tag{B.59}$$

while the third term is

$$\begin{aligned}\boxed{3}&=\frac{1}{r\sin\theta}\frac{\partial}{\partial\phi}\left[2\nu\left(\frac{1}{2r\sin\theta}\frac{\partial(\hat{\rho}u_r)}{\partial\phi}+\frac{1}{2}\frac{\partial(\hat{\rho}u_\phi)}{\partial r}-\frac{\beta}{2}\,\hat{\rho}u_\phi-\frac{1}{2r}\,\hat{\rho}u_\phi\right)\right]\\&=\frac{\nu}{r\sin\theta}\frac{\partial}{\partial\phi}\left[\frac{1}{r\sin\theta}\frac{\partial(\hat{\rho}u_r)}{\partial\phi}+\frac{\partial(\hat{\rho}u_\phi)}{\partial r}-\beta\hat{\rho}u_\phi-\frac{1}{r}\,\hat{\rho}u_\phi\right]\\&=\underbrace{\nu\frac{\partial}{\partial r}\left[\frac{1}{r\sin\theta}\frac{\partial(\hat{\rho}u_\phi)}{\partial\phi}\right]}_{\boxed{3a}}+\underbrace{\frac{\nu}{r^2\sin^2\theta}\frac{\partial^2(\hat{\rho}u_r)}{\partial\phi^2}}_{\boxed{3b}}-\underbrace{\frac{\nu\beta}{r\sin\theta}\frac{\partial(\hat{\rho}u_\phi)}{\partial\phi}}_{\boxed{3c}}.\end{aligned} \tag{B.60}$$

The last term is

$$\begin{aligned}
\boxed{4} &= -\frac{2\nu}{r}\left[\frac{1}{r}\frac{\partial(\hat\rho u_\theta)}{\partial\theta} + \frac{1}{r\sin\theta}\frac{\partial(\hat\rho u_\phi)}{\partial\phi} + \frac{2}{r}\hat\rho u_r + \frac{\cos\theta}{r\sin\theta}\,\hat\rho u_\theta + \frac{2\beta}{3}\hat\rho u_r\right] \\
&= -\frac{2\nu}{r}\left[\frac{1}{r\sin\theta}\frac{\partial(\sin\theta\,\hat\rho u_\theta)}{\partial\theta} + \frac{1}{r\sin\theta}\frac{\partial(\hat\rho u_\phi)}{\partial\phi}\right] - \frac{4\nu}{r^2}\,\hat\rho u_r - \frac{4\nu\beta}{3r}\hat\rho u_r \\
&= \frac{2\nu}{r}\left[\frac{1}{r^2}\frac{\partial(r^2\hat\rho u_r)}{\partial r}\right] - \frac{4\nu}{r^2}\,\hat\rho u_r - \frac{4\nu\beta}{3r}\hat\rho u_r \qquad \text{by equation (B.54)} \\
&= \frac{2\nu}{r}\left[\frac{\partial(\hat\rho u_r)}{\partial r} + \frac{2}{r}\hat\rho u_r\right] - \frac{4\nu}{r^2}\hat\rho u_r - \frac{4\nu\beta}{3r}\hat\rho u_r \\
&= \underbrace{\frac{2\nu}{r}\frac{\partial(\hat\rho u_r)}{\partial r}}_{\boxed{4a}} - \underbrace{\frac{4\nu\beta}{3r}\hat\rho u_r}_{\boxed{4b}}\,.
\end{aligned} \tag{B.61}$$

To evaluate $\hat{\boldsymbol{r}}\cdot\left[\boldsymbol{\nabla}\cdot\underline{\underline{\hat{\boldsymbol{\mathcal{D}}}}}\right] = \boxed{1}+\boxed{2}+\boxed{3}+\boxed{4}$ by equation (B.57), we combine pieces from equations (B.58)–(B.61) as indicated in the following expressions:

$$\begin{aligned}
\boxed{1c}+\boxed{2b}+\boxed{3c}+\boxed{4b} &= -\nu\beta\left[\frac{1}{r\sin\theta}\frac{\partial(\sin\theta\,\hat\rho u_\theta)}{\partial\theta} + \frac{1}{r\sin\theta}\frac{\partial(\hat\rho u_\phi)}{\partial\phi}\right] + \boxed{1c}+\boxed{4b} \\
&= \nu\beta\left[\frac{1}{r^2}\frac{\partial(r^2\hat\rho u_r)}{\partial r}\right] + \boxed{1c}+\boxed{4b} \qquad \text{by equation (B.54)} \\
&= -\frac{\nu\beta}{3r^2}\frac{\partial(r^2\hat\rho u_r)}{\partial r} + \boxed{4b} \\
&= -\frac{\nu\beta}{3}\frac{\partial(\hat\rho u_r)}{\partial r} - \frac{2\nu\beta}{3r}\hat\rho u_r + \boxed{4b} \\
&= -\frac{\nu\beta}{3}\frac{\partial(\hat\rho u_r)}{\partial r} - \frac{2\nu\beta}{r}\hat\rho u_r,
\end{aligned} \tag{B.62}$$

$$\begin{aligned}
\boxed{1b}+\boxed{2a}+\boxed{3a} &= \nu\frac{\partial}{\partial r}\left[\frac{1}{r\sin\theta}\frac{\partial(\sin\theta\,\hat\rho u_\theta)}{\partial\theta} + \frac{1}{r\sin\theta}\frac{\partial(\hat\rho u_\phi)}{\partial\phi}\right] + \boxed{1b} \\
&= -\nu\frac{\partial}{\partial r}\left[\frac{1}{r^2}\frac{\partial(r^2\hat\rho u_r)}{\partial r}\right] + \boxed{1b} \qquad \text{by equation (B.54)} \\
&= \nu\left[\frac{\partial^2(\hat\rho u_r)}{\partial r^2} + \frac{2}{r}\frac{\partial(\hat\rho u_r)}{\partial r} + \frac{2}{r^2}\hat\rho u_r\right],
\end{aligned} \tag{B.63}$$

$$\boxed{2c}+\boxed{3b} = \nu\nabla_\perp^2(\hat\rho u_r) \qquad \text{by equation (B.47).} \tag{B.64}$$

The remaining terms are unchanged:

$$\boxed{1a}+\boxed{1d}+\boxed{4a} = 2\nu\alpha\left[\frac{\partial(\hat\rho u_r)}{\partial r} - \frac{2\beta}{3}\hat\rho u_r\right] - \frac{4\nu}{3}\frac{d\beta}{dr}\hat\rho u_r + \frac{2\nu}{r}\frac{\partial(\hat\rho u_r)}{\partial r}. \tag{B.65}$$

Combining equations (B.62)–(B.65) and grouping by derivatives of $\hat\rho u_r$, we obtain

$$\begin{aligned}\hat{\boldsymbol{r}}\cdot\left[\boldsymbol{\nabla}\cdot\underline{\underline{\hat{\boldsymbol{\mathcal{D}}}}}\right] = \nu\Bigg\{&\frac{\partial^2(\hat\rho u_r)}{\partial r^2} + \left[2\alpha - \frac{\beta}{3} + \frac{4}{r}\right]\frac{\partial(\hat\rho u_r)}{\partial r}\\ &+ \left[\nabla_\perp^2 - \frac{4\alpha\beta}{3} - \frac{4}{3}\frac{d\beta}{dr} - \frac{2\beta}{r} + \frac{2}{r^2}\right]\hat\rho u_r\Bigg\}.\end{aligned} \tag{B.66}$$

The last step is to eliminate the radial mass flux $\hat\rho u_r$ in favor of the streamfunction W by substituting $\hat\rho u_r = -\nabla_\perp^2 W$, by equation (B.45). Using the commutation identities of equations (B.49) and (B.50), equation (B.66) thus becomes

$$\boxed{\begin{aligned}\hat{\boldsymbol{r}}\cdot\left[\boldsymbol{\nabla}\cdot\underline{\underline{\hat{\boldsymbol{\mathcal{D}}}}}\right] = \nu\nabla_\perp^2\Bigg\{&\frac{\partial^2 W}{\partial r^2} + \left(2\alpha - \frac{\beta}{3}\right)\frac{\partial W}{\partial r}\\ &+ \left(\nabla_\perp^2 - \frac{4\alpha\beta}{3} - \frac{4\alpha}{r} - \frac{4}{3}\frac{\partial\beta}{\partial r} - \frac{4\beta}{3r}\right)W\Bigg\}.\end{aligned}} \tag{B.67}$$

B.3.3.3 Polar Component

For any tensor $\underline{\underline{\boldsymbol{\mathcal{T}}}}$, the polar component of its divergence is

$$\hat{\boldsymbol{\theta}}\cdot\left(\boldsymbol{\nabla}\cdot\underline{\underline{\boldsymbol{\mathcal{T}}}}\right) = \underbrace{\frac{1}{r^2}\frac{\partial(r^2\mathcal{T}_{r\theta})}{\partial r}}_{\boxed{1}} + \underbrace{\frac{1}{r\sin\theta}\frac{\partial(\sin\theta\,\mathcal{T}_{\theta\theta})}{\partial\theta}}_{\boxed{2}} + \underbrace{\frac{1}{r\sin\theta}\frac{\partial\mathcal{T}_{\theta\phi}}{\partial\phi}}_{\boxed{3}} + \underbrace{\frac{\mathcal{T}_{r\theta}}{r}}_{\boxed{4}} - \underbrace{\frac{\cos\theta}{r\sin\theta}\mathcal{T}_{\phi\phi}}_{\boxed{5}}. \tag{B.68}$$

In this section, we evaluate (B.68) for $\underline{\underline{\boldsymbol{\mathcal{T}}}} = \underline{\underline{\hat{\boldsymbol{\mathcal{D}}}}}$ using the definition of $\underline{\underline{\hat{\boldsymbol{\mathcal{D}}}}}$ given in equation (B.52) along with the strain rate tensor components of equation (B.53). Starting with the first term, we have

$$\begin{aligned}\boxed{1} &= \frac{1}{r^2}\frac{\partial}{\partial r}\left(r^2\,2\nu\,\hat\rho e_{r\theta}\right) = \nu\left(2\alpha + \frac{4}{r} + 2\frac{\partial}{\partial r}\right)(\hat\rho e_{r\theta})\\ &= 2\nu\alpha\,\hat\rho e_{r\theta} + \nu\left(\frac{4}{r} + 2\frac{\partial}{\partial r}\right)\left[\frac{1}{2}\frac{\partial(\hat\rho u_\theta)}{\partial r} - \frac{\beta}{2}\,\hat\rho u_\theta - \frac{1}{2r}\,\hat\rho u_\theta + \frac{1}{2r}\frac{\partial(\hat\rho u_r)}{\partial\theta}\right]\\ &= \underbrace{2\nu\alpha\,\hat\rho e_{r\theta}}_{\boxed{1a}} - \underbrace{\nu\left[\beta\left(\frac{\partial}{\partial r} + \frac{2}{r}\right)(\hat\rho u_\theta) + \frac{d\beta}{dr}\,\hat\rho u_\theta\right]}_{\boxed{1b}} + \underbrace{\nu\left(\frac{\partial^2}{\partial r^2} + \frac{1}{r}\frac{\partial}{\partial r}\right)(\hat\rho u_\theta)}_{\boxed{1c}}\\ &\quad + \underbrace{\frac{\nu}{r}\left[\left(\frac{\partial^2}{\partial r\,\partial\theta} + \frac{1}{r}\frac{\partial}{\partial\theta}\right)(\hat\rho u_r)\right]}_{\boxed{1d}} - \underbrace{\frac{\nu}{r^2}\,\hat\rho u_\theta}_{\boxed{1e}}.\end{aligned} \tag{B.69}$$

The second term is

$$\begin{aligned}
\boxed{2} &= \frac{2\nu}{r\sin\theta}\frac{\partial}{\partial\theta}\left[\sin\theta\left(\frac{1}{r}\frac{\partial(\hat\rho u_\theta)}{\partial\theta}+\frac{1}{r}\,\hat\rho u_r+\frac{\beta}{3}\,\hat\rho u_r\right)\right] \\
&= \underbrace{\frac{2\nu}{r^2\sin\theta}\frac{\partial}{\partial\theta}\left[\sin\theta\frac{\partial(\hat\rho u_\theta)}{\partial\theta}\right]}_{\boxed{2a}}+\underbrace{\frac{2\nu}{r^2\sin\theta}\frac{\partial(\sin\theta\,\hat\rho u_r)}{\partial\theta}}_{\boxed{2b}}+\underbrace{\frac{2\nu\beta}{3r\sin\theta}\frac{\partial(\sin\theta\,\hat\rho u_r)}{\partial\theta}}_{\boxed{2c}},
\end{aligned} \tag{B.70}$$

while the third term is

$$\begin{aligned}
\boxed{3} &= \frac{\nu}{r\sin\theta}\frac{\partial}{\partial\phi}\left[\frac{1}{r}\frac{\partial(\hat\rho u_\phi)}{\partial\theta}-\frac{\cos\theta}{r\sin\theta}\,\hat\rho u_\phi+\frac{1}{r\sin\theta}\frac{\partial(\hat\rho u_\theta)}{\partial\phi}\right] \\
&= \nu\left[\frac{1}{r^2\sin\theta}\frac{\partial^2(\hat\rho u_\phi)}{\partial\theta\,\partial\phi}-\frac{\cos\theta}{r^2\sin^2\theta}\frac{\partial(\hat\rho u_\phi)}{\partial\phi}+\frac{1}{r^2\sin^2\theta}\frac{\partial^2(\hat\rho u_\theta)}{\partial\phi^2}\right] \\
&= \underbrace{\frac{\nu}{r}\frac{\partial}{\partial\theta}\left[\frac{1}{r\sin\theta}\frac{\partial(\hat\rho u_\phi)}{\partial\phi}\right]}_{\boxed{3a}}+\underbrace{\frac{1}{r^2\sin^2\theta}\frac{\partial^2(\hat\rho u_\theta)}{\partial\phi^2}}_{\boxed{3b}}.
\end{aligned} \tag{B.71}$$

The last two terms are

$$\boxed{4} = \underbrace{\frac{\nu}{r}\frac{\partial(\hat\rho u_\theta)}{\partial r}}_{\boxed{4a}}-\underbrace{\frac{\nu\beta}{r}\,\rho\hat u_\theta}_{\boxed{4b}}-\underbrace{\frac{\nu}{r^2}\,\hat\rho u_\theta}_{\boxed{4c}}+\underbrace{\frac{\nu}{r^2}\frac{\partial(\hat\rho u_r)}{\partial\theta}}_{\boxed{4d}} \tag{B.72}$$

and

$$\boxed{5} = -\underbrace{\frac{2\nu\cos\theta}{r^2\sin^2\theta}\frac{\partial(\hat\rho u_\phi)}{\partial\phi}}_{\boxed{5a}}-\underbrace{\frac{2\nu\cos\theta}{r^2\sin\theta}\,\hat\rho u_r}_{\boxed{5b}}-\underbrace{\frac{2\nu\cos^2\theta}{r^2\sin^2\theta}\,\hat\rho u_\theta}_{\boxed{5c}}-\underbrace{\frac{2\nu\beta\cos\theta}{3r\sin\theta}\,\hat\rho u_r}_{\boxed{5d}}. \tag{B.73}$$

To evaluate $\hat{\boldsymbol\theta}\cdot\left[\boldsymbol\nabla\cdot\underline{\underline{\hat{\mathcal{D}}}}\right] = \boxed{1}+\boxed{2}+\boxed{3}+\boxed{4}+\boxed{5}$ by equation (B.68), we combine pieces from equations (B.69)–(B.73) as indicated in the following expressions:

$$\boxed{1a} = \nu\alpha\left[\frac{\partial(\hat\rho u_\theta)}{\partial r}-\beta\,\hat\rho u_\theta-\frac{1}{r}\,\hat\rho u_\theta+\frac{1}{r}\frac{\partial(\hat\rho u_r)}{\partial\theta}\right], \tag{B.74}$$

$$\boxed{1b}+\boxed{2c}+\boxed{4b}+\boxed{5d} = \nu\left[\frac{2\beta}{3r}\frac{\partial(\hat\rho u_r)}{\partial\theta}-\beta\frac{\partial(\hat\rho u_\theta)}{\partial r}-\frac{d\beta}{dr}\,\hat\rho u_\theta-\frac{3\beta}{r}\,\hat\rho u_\theta\right], \tag{B.75}$$

$$\boxed{1c} + \frac{\boxed{2a}}{2} + \boxed{3b} + \boxed{4a} = \nu \nabla^2(\hat{\rho} u_\theta), \tag{B.76}$$

$$\boxed{1d} + \frac{\boxed{2a}}{2} + \boxed{3a} + \boxed{4d} = \frac{\nu}{r}\frac{\partial}{\partial \theta} \underbrace{\left[\boldsymbol{\nabla} \cdot (\hat{\rho} \boldsymbol{u})\right]}_{=0} + \frac{\nu}{r^2 \sin^2\theta}\,\hat{\rho} u_\theta, \tag{B.77}$$

$$\boxed{1e} + \boxed{4c} + \boxed{5c} = -\frac{2\nu}{r^2 \sin^2\theta}\,\hat{\rho} u_\theta, \tag{B.78}$$

$$\boxed{2b} + \boxed{5b} = \frac{2\nu}{r^2}\frac{\partial(\hat{\rho} u_r)}{\partial \theta}, \tag{B.79}$$

along with

$$\boxed{5a} = -\frac{2\nu \cos\theta}{r^2 \sin^2\theta}\frac{\partial(\hat{\rho} u_\phi)}{\partial \phi}, \tag{B.80}$$

which is left unchanged. Combining equations (B.74)–(B.80) and regrouping, we obtain

$$\boxed{\begin{aligned} \hat{\boldsymbol{\theta}} \cdot \left[\boldsymbol{\nabla} \cdot \underline{\underline{\hat{\boldsymbol{\mathcal{D}}}}}\right] = \nu \Bigg\{ & \nabla^2(\hat{\rho} u_\theta) + \frac{1}{r}\left[\alpha + \frac{2\beta}{3} + \frac{2}{r}\right]\frac{\partial(\hat{\rho} u_r)}{\partial \theta} + (\alpha - \beta)\,\frac{\partial(\hat{\rho} u_\theta)}{\partial r} \\ & - \frac{2\cos\theta}{r^2 \sin^2\theta}\frac{\partial(\hat{\rho} u_\phi)}{\partial \phi} - \left[\alpha\beta + \frac{\alpha}{r} + \frac{d\beta}{dr} + \frac{3\beta}{r} + \frac{1}{r^2 \sin^2\theta}\right]\hat{\rho} u_\theta \Bigg\} \end{aligned}} \tag{B.81}$$

The polar component will be used in combination with the azimuthal component in §B.3.3.5 and §B.3.3.6.

B.3.3.4 Azimuthal Component

For any tensor $\underline{\underline{\boldsymbol{\mathcal{T}}}}$, the azimuthal component of its divergence is

$$\hat{\boldsymbol{\phi}} \cdot \left(\boldsymbol{\nabla} \cdot \underline{\underline{\boldsymbol{\mathcal{T}}}}\right) = \underbrace{\frac{1}{r^2}\frac{\partial(r^2 \mathcal{T}_{r\phi})}{\partial r}}_{\boxed{1}} + \underbrace{\frac{1}{r}\frac{\partial \mathcal{T}_{\theta\phi}}{\partial \theta}}_{\boxed{2}} + \underbrace{\frac{1}{r\sin\theta}\frac{\partial \mathcal{T}_{\phi\phi}}{\partial \phi}}_{\boxed{3}} + \underbrace{\frac{\mathcal{T}_{r\phi}}{r}}_{\boxed{4}} + \underbrace{\frac{2\cos\theta}{r\sin\theta}\mathcal{T}_{\theta\phi}}_{\boxed{5}}. \tag{B.82}$$

In this section, we evaluate equation (B.82) for $\underline{\underline{\boldsymbol{\mathcal{T}}}} = \underline{\underline{\hat{\boldsymbol{\mathcal{D}}}}}$ using the definition of $\underline{\underline{\hat{\boldsymbol{\mathcal{D}}}}}$ given in equation (B.52) along with the strain rate tensor components of equation (B.53).

Starting with the first term, we have

$$
\begin{aligned}
\boxed{1} &= \frac{1}{r^2}\frac{\partial}{\partial r}\left(r^2\,2\nu\,\hat{\rho}e_{r\phi}\right) = \nu\left(2\alpha + \frac{4}{r} + 2\frac{\partial}{\partial r}\right)(\hat{\rho}e_{r\phi}) \\
&= 2\nu\alpha\,\hat{\rho}e_{r\phi} + \nu\left(\frac{4}{r} + 2\frac{\partial}{\partial r}\right)\left[\frac{1}{2r\sin\theta}\frac{\partial(\hat{\rho}u_r)}{\partial\phi} + \frac{1}{2}\frac{\partial(\hat{\rho}u_\phi)}{\partial r} - \frac{\beta}{2}\,\hat{\rho}u_\phi - \frac{1}{2r}\,\hat{\rho}u_\phi\right] \\
&= \underbrace{2\nu\alpha\,\hat{\rho}e_{r\phi}}_{\boxed{1a}} \underbrace{-\,\nu\left[\beta\left(\frac{\partial}{\partial r} + \frac{2}{r}\right)(\hat{\rho}u_\phi) + \frac{d\beta}{dr}\,\hat{\rho}u_\phi\right]}_{\boxed{1b}} + \underbrace{\nu\left(\frac{\partial^2}{\partial r^2} + \frac{1}{r}\frac{\partial}{\partial r}\right)(\hat{\rho}u_\phi)}_{\boxed{1c}} \\
&\quad + \underbrace{\frac{\nu}{r\sin\theta}\left(\frac{\partial^2}{\partial r\,\partial\phi} + \frac{1}{r}\frac{\partial}{\partial\phi}\right)(\hat{\rho}u_r)}_{\boxed{1d}} \underbrace{-\,\frac{\nu}{r^2}\,\hat{\rho}u_\phi}_{\boxed{1e}}\,.
\end{aligned}
\tag{B.83}
$$

The second term is

$$
\begin{aligned}
\boxed{2} &= \frac{\nu}{r}\frac{\partial}{\partial\theta}\left[\frac{1}{r}\frac{\partial(\hat{\rho}u_\phi)}{\partial\theta} - \frac{\cos\theta}{r\sin\theta}\,\hat{\rho}u_\phi + \frac{1}{r\sin\theta}\frac{\partial(\hat{\rho}u_\theta)}{\partial\phi}\right] \\
&= \underbrace{\frac{\nu}{r^2}\left(\frac{\partial^2}{\partial\theta^2} - \frac{\cos\theta}{\sin\theta}\frac{\partial}{\partial\theta}\right)(\hat{\rho}u_\phi)}_{\boxed{2a}} + \underbrace{\frac{\nu}{r^2\sin^2\theta}\,\hat{\rho}u_\phi}_{\boxed{2b}} + \underbrace{\frac{\nu}{r^2\sin\theta}\left(\frac{\partial^2}{\partial\theta\,\partial\phi} - \frac{\cos\theta}{\sin\theta}\frac{\partial}{\partial\phi}\right)(\hat{\rho}u_\theta)}_{\boxed{2c}},
\end{aligned}
\tag{B.84}
$$

while the third term is

$$
\begin{aligned}
\boxed{3} &= \frac{2\nu}{r\sin\theta}\frac{\partial}{\partial\phi}\left[\frac{1}{r\sin\theta}\frac{\partial(\hat{\rho}u_\phi)}{\partial\phi} + \frac{1}{r}\,\hat{\rho}u_r + \frac{\cos\theta}{r\sin\theta}\,\hat{\rho}u_\theta + \frac{\beta}{3}\,\hat{\rho}u_r\right] \\
&= \underbrace{\frac{2\nu}{r^2\sin^2\theta}\frac{\partial^2(\hat{\rho}u_\phi)}{\partial\phi^2}}_{\boxed{3a}} + \underbrace{\frac{2\nu}{r^2\sin\theta}\frac{\partial(\hat{\rho}u_r)}{\partial\phi}}_{\boxed{3b}} + \underbrace{\frac{2\nu\cos\theta}{r^2\sin^2\theta}\frac{\partial(\hat{\rho}u_\theta)}{\partial\phi}}_{\boxed{3c}} + \underbrace{\frac{2\nu\beta}{3r\sin\theta}\frac{\partial(\hat{\rho}u_r)}{\partial\phi}}_{\boxed{3d}}\,.
\end{aligned}
\tag{B.85}
$$

The last two terms are

$$
\boxed{4} = \underbrace{\frac{\nu}{r^2\sin\theta}\frac{\partial(\hat{\rho}u_r)}{\partial\phi}}_{\boxed{4a}} + \underbrace{\frac{\nu}{r}\frac{\partial(\hat{\rho}u_\phi)}{\partial r}}_{\boxed{4b}} - \underbrace{\frac{\nu\beta}{r}\,\hat{\rho}u_\phi}_{\boxed{4c}} - \underbrace{\frac{\nu}{r^2}\,\hat{\rho}u_\phi}_{\boxed{4d}}
\tag{B.86}
$$

and

$$
\boxed{5} = \underbrace{\frac{2\nu\cos\theta}{r^2\sin\theta}\frac{\partial(\hat{\rho}u_\phi)}{\partial\theta}}_{\boxed{5a}} - \underbrace{\frac{2\nu\cos^2\theta}{r^2\sin^2\theta}\,\hat{\rho}u_\phi}_{\boxed{5b}} + \underbrace{\frac{2\nu\cos\theta}{r^2\sin^2\theta}\frac{\partial(\hat{\rho}u_\theta)}{\partial\phi}}_{\boxed{5c}}\,.
\tag{B.87}
$$

To evaluate $\hat{\boldsymbol{\phi}} \cdot \left[\boldsymbol{\nabla} \cdot \underline{\underline{\hat{\boldsymbol{\mathcal{D}}}}}\right] = \boxed{1} + \boxed{2} + \boxed{3} + \boxed{4} + \boxed{5}$ by equation (B.82), we combine pieces from equations (B.83)–(B.87) as indicated in the following expressions:

$$\boxed{1\mathrm{a}} = \nu\alpha \left[\frac{1}{r\sin\theta}\frac{\partial(\hat{\rho}u_r)}{\partial\phi} + \frac{\partial(\hat{\rho}u_\phi)}{\partial r} - \beta\,\hat{\rho}u_\phi - \frac{1}{r}\,\hat{\rho}u_\phi\right], \tag{B.88}$$

$$\boxed{1\mathrm{b}} + \boxed{3\mathrm{d}} + \boxed{4\mathrm{c}} = \nu \left[\frac{2\beta}{3r\sin\theta}\frac{\partial(\hat{\rho}u_r)}{\partial\phi} - \beta\frac{\partial(\hat{\rho}u_\phi)}{\partial r} - \frac{d\beta}{dr}\,\hat{\rho}u_\phi - \frac{3\beta}{r}\,\hat{\rho}u_\phi\right], \tag{B.89}$$

$$\boxed{1\mathrm{c}} + \boxed{2\mathrm{a}} + \frac{\boxed{3\mathrm{a}}}{2} + \boxed{4\mathrm{b}} + \boxed{5\mathrm{a}} = \nu\nabla^2(\hat{\rho}u_\phi), \tag{B.90}$$

$$\boxed{1\mathrm{d}} + \boxed{2\mathrm{c}} + \frac{\boxed{3\mathrm{a}}}{2} + \boxed{4\mathrm{a}} + \boxed{5\mathrm{c}} = \frac{\nu}{r\sin\theta}\frac{\partial}{\partial\phi}\left[\boldsymbol{\nabla}\cdot(\hat{\rho}\boldsymbol{u})\right] = 0, \tag{B.91}$$

$$\begin{aligned}\boxed{1\mathrm{e}} + \boxed{2\mathrm{b}} + \boxed{4\mathrm{d}} + \boxed{5\mathrm{b}} &= \frac{\nu}{r^2\sin^2\theta}\left[1 - 2\sin^2\theta - 2\cos^2\theta\right](\hat{\rho}u_\phi) \\ &= -\frac{\nu}{r^2\sin^2\theta}\,\hat{\rho}u_\phi.\end{aligned} \tag{B.92}$$

The remaining terms are unchanged:

$$\boxed{3\mathrm{b}} + \boxed{3\mathrm{c}} = \nu \left[\frac{2}{r^2\sin\theta}\frac{\partial(\hat{\rho}u_r)}{\partial\phi} + \frac{2\cos\theta}{r^2\sin^2\theta}\frac{\partial(\hat{\rho}u_\theta)}{\partial\phi}\right]. \tag{B.93}$$

Combining equations (B.88)–(B.93) and regrouping, we obtain

$$\boxed{\begin{aligned}\hat{\boldsymbol{\phi}} \cdot \left[\boldsymbol{\nabla} \cdot \underline{\underline{\hat{\boldsymbol{\mathcal{D}}}}}\right] = \nu\Bigg\{&\nabla^2(\hat{\rho}u_\phi) + \frac{1}{r\sin\theta}\left[\alpha + \frac{2\beta}{3} + \frac{2}{r}\right]\frac{\partial(\hat{\rho}u_r)}{\partial\phi} + (\alpha-\beta)\,\frac{\partial(\hat{\rho}u_\phi)}{\partial r} \\ &+ \frac{2\cos\theta}{r^2\sin^2\theta}\frac{\partial(\hat{\rho}u_\theta)}{\partial\phi} - \left[\alpha\beta + \frac{\alpha}{r} + \frac{d\beta}{dr} + \frac{3\beta}{r} + \frac{1}{r^2\sin^2\theta}\right]\hat{\rho}u_\phi\Bigg\}\end{aligned}} \tag{B.94}$$

B.3.3.5 Perpendicular Divergence

We now use the results of the previous two sections to evaluate $\boldsymbol{\nabla}_\perp \cdot \left[\boldsymbol{\nabla} \cdot \underline{\underline{\hat{\boldsymbol{\mathcal{D}}}}}\right]$, which serves as the diffusion term in the P equation. By definition,

$$\boldsymbol{\nabla}_\perp \cdot \boldsymbol{A} = \frac{1}{r\sin\theta}\frac{\partial(\sin\theta\,A_\theta)}{\partial\theta} + \frac{1}{r\sin\theta}\frac{\partial A_\phi}{\partial\phi}, \tag{B.95}$$

such that

$$\boldsymbol{\nabla} \cdot \boldsymbol{A} = \frac{1}{r^2}\frac{\partial(r^2A_r)}{\partial r} + \boldsymbol{\nabla}_\perp \cdot \boldsymbol{A}. \tag{B.96}$$

Thus,

$$\boldsymbol{\nabla}_{\perp} \cdot \left[\boldsymbol{\nabla} \cdot \underline{\underline{\hat{\boldsymbol{\mathcal{D}}}}}\right] = \frac{1}{r\sin\theta}\left[\frac{\partial}{\partial\theta}\left(\sin\theta\,\hat{\boldsymbol{\theta}} \cdot \boldsymbol{\nabla} \cdot \underline{\underline{\hat{\boldsymbol{\mathcal{D}}}}}\right) + \frac{\partial}{\partial\phi}\left(\hat{\boldsymbol{\phi}} \cdot \boldsymbol{\nabla} \cdot \underline{\underline{\hat{\boldsymbol{\mathcal{D}}}}}\right)\right]. \tag{B.97}$$

The polar and azimuthal components of $\boldsymbol{\nabla} \cdot \underline{\underline{\hat{\boldsymbol{\mathcal{D}}}}}$ are given by equations (B.81) and (B.94). We rewrite them here and label the individual terms before combining them as per equation (B.97):

$$\begin{aligned}\hat{\boldsymbol{\theta}} \cdot \left[\boldsymbol{\nabla} \cdot \underline{\underline{\hat{\boldsymbol{\mathcal{D}}}}}\right] = \nu\Bigg\{ & \underbrace{\nabla^2(\hat{\rho}u_\theta)}_{\boxed{1a}} + \underbrace{\frac{1}{r}\left[\alpha + \frac{2\beta}{3} + \frac{2}{r}\right]\frac{\partial(\hat{\rho}u_r)}{\partial\theta}}_{\boxed{1b}} + \underbrace{(\alpha-\beta)\frac{\partial(\hat{\rho}u_\theta)}{\partial r}}_{\boxed{1c}} \\ & - \underbrace{\frac{2\cos\theta}{r^2\sin^2\theta}\frac{\partial(\hat{\rho}u_\phi)}{\partial\phi}}_{\boxed{1d}} - \underbrace{\left[\alpha\beta + \frac{\alpha}{r} + \frac{d\beta}{dr} + \frac{3\beta}{r} + \frac{1}{r^2\sin^2\theta}\right]\hat{\rho}u_\theta}_{\boxed{1e}}\Bigg\}\end{aligned} \tag{B.98}$$

and

$$\begin{aligned}\hat{\boldsymbol{\phi}} \cdot \left[\boldsymbol{\nabla} \cdot \underline{\underline{\hat{\boldsymbol{\mathcal{D}}}}}\right] = \nu\Bigg\{ & \underbrace{\nabla^2(\hat{\rho}u_\phi)}_{\boxed{2a}} + \underbrace{\frac{1}{r\sin\theta}\left[\alpha + \frac{2\beta}{3} + \frac{2}{r}\right]\frac{\partial(\hat{\rho}u_r)}{\partial\phi}}_{\boxed{2b}} + \underbrace{(\alpha-\beta)\frac{\partial(\hat{\rho}u_\phi)}{\partial r}}_{\boxed{2c}} \\ & + \underbrace{\frac{2\cos\theta}{r^2\sin^2\theta}\frac{\partial(\hat{\rho}u_\theta)}{\partial\phi}}_{\boxed{2d}} - \underbrace{\left[\alpha\beta + \frac{\alpha}{r} + \frac{d\beta}{dr} + \frac{3\beta}{r} + \frac{1}{r^2\sin^2\theta}\right]\hat{\rho}u_\phi}_{\boxed{2e}}\Bigg\}.\end{aligned} \tag{B.99}$$

Combining the terms containing $\boxed{\text{1a}}$ and $\boxed{\text{2a}}$ yields:

$$
\begin{aligned}
&\frac{\nu}{r\sin\theta}\left\{\frac{\partial}{\partial\theta}\left[\sin\theta\,\boxed{\text{1a}}\right]+\frac{\partial\boxed{\text{2a}}}{\partial\phi}\right\}\\
&\quad=\frac{\nu}{r\sin\theta}\left\{\frac{\partial}{\partial\theta}\left[\sin\theta\,\nabla^2(\hat\rho u_\theta)\right]+\frac{\partial}{\partial\phi}\left[\nabla^2(\hat\rho u_\phi)\right]\right\}\\
&\quad=\frac{\nu}{r\sin\theta}\left\{\nabla^2\left[\frac{\partial\left(\sin\theta\,\hat\rho u_\theta\right)}{\partial\theta}+\frac{\partial(\hat\rho u_\phi)}{\partial\phi}\right]-\frac{2\cos\theta}{r^2}\frac{\partial^2(\hat\rho u_\theta)}{\partial\theta^2}\right.\\
&\qquad\left.+\left(\frac{4\sin\theta}{r^2}-\frac{2}{r^2\sin\theta}\right)\frac{\partial(\hat\rho u_\theta)}{\partial\theta}+\frac{2\cos\theta}{r^2}\,\hat\rho u_\theta-\frac{2\cos\theta}{r^2\sin^2\theta}\frac{\partial^2(\hat\rho u_\theta)}{\partial\phi^2}\right\}\\
&\quad=\frac{\nu}{r\sin\theta}\left\{\sin\theta\,\nabla^2\Big[r\,\boldsymbol{\nabla}_\perp\cdot(\hat\rho\boldsymbol{u})\Big]+\frac{2\cos\theta}{r^2\sin\theta}\frac{\partial^2(\hat\rho u_\phi)}{\partial\theta\,\partial\phi}-\frac{2\cos\theta}{r^2\sin^2\theta}\frac{\partial^2(\hat\rho u_\theta)}{\partial\phi^2}\right.\\
&\qquad\left.+\frac{1}{r^2\sin\theta}\frac{\partial(\hat\rho u_\theta)}{\partial\theta}-\frac{\cos\theta}{r^2\sin^2\theta}\,\hat\rho u_\theta-\frac{1}{r^2\sin^2\theta}\frac{\partial(\hat\rho u_\phi)}{\partial\phi}\right\}.
\end{aligned}
\tag{B.100}
$$

Combining the terms containing $\boxed{\text{1b}}$ and $\boxed{\text{2b}}$ yields:

$$
\frac{\nu}{r\sin\theta}\left\{\frac{\partial}{\partial\theta}\left[\sin\theta\,\boxed{\text{1b}}\right]+\frac{\partial\boxed{\text{2b}}}{\partial\phi}\right\}=\nu\left[\alpha+\frac{2\beta}{3}+\frac{2}{r}\right]\nabla_\perp^2(\hat\rho u_r).
\tag{B.101}
$$

Combining the terms containing $\boxed{\text{1c}}$ and $\boxed{\text{2c}}$ yields:

$$
\begin{aligned}
\frac{\nu}{r\sin\theta}\left\{\frac{\partial}{\partial\theta}\left[\sin\theta\,\boxed{\text{1c}}\right]+\frac{\partial\boxed{\text{2c}}}{\partial\phi}\right\}&=\frac{\nu(\alpha-\beta)}{r\sin\theta}\frac{\partial}{\partial r}\left[\frac{\partial(\sin\theta\,\hat\rho u_\theta)}{\partial\theta}+\frac{\partial(\hat\rho u_\phi)}{\partial\phi}\right]\\
&=\frac{\nu(\alpha-\beta)}{r}\frac{\partial}{\partial r}\Big[r\boldsymbol{\nabla}_\perp\cdot(\hat\rho\boldsymbol{u})\Big].
\end{aligned}
\tag{B.102}
$$

Combining the terms containing $\boxed{\text{1d}}$ and $\boxed{\text{2d}}$ yields:

$$
\begin{aligned}
&\frac{\nu}{r\sin\theta}\left\{\frac{\partial}{\partial\theta}\left[\sin\theta\,\boxed{\text{1d}}\right]+\frac{\partial\boxed{\text{2d}}}{\partial\phi}\right\}\\
&\quad=\frac{\nu}{r\sin\theta}\left[-\frac{\partial}{\partial\theta}\left(\frac{2\cos\theta}{r^2\sin\theta}\frac{\partial(\hat\rho u_\phi)}{\partial\phi}\right)+\frac{\partial}{\partial\phi}\left(\frac{2\cos\theta}{r^2\sin^2\theta}\frac{\partial(\hat\rho u_\theta)}{\partial\phi}\right)\right]\\
&\quad=\frac{\nu}{r\sin\theta}\left[-\frac{2\cos\theta}{r^2\sin\theta}\frac{\partial^2(\hat\rho u_\phi)}{\partial\theta\,\partial\phi}+\frac{2}{r^2\sin^2\theta}\frac{\partial(\hat\rho u_\phi)}{\partial\phi}+\frac{2\cos\theta}{r^2\sin^2\theta}\frac{\partial^2(\hat\rho u_\theta)}{\partial\phi^2}\right].
\end{aligned}
\tag{B.103}
$$

Finally, combining the terms containing $\boxed{\text{1e}}$ and $\boxed{\text{2e}}$ yields:

$$
\begin{aligned}
-&\frac{\nu}{r\sin\theta}\left\{\frac{\partial}{\partial\theta}\left[\sin\theta\,\boxed{\text{1e}}\right]+\frac{\partial\,\boxed{\text{2e}}}{\partial\phi}\right\} \\
&\quad=-\nu\left[\alpha\beta+\frac{\alpha}{r}+\frac{d\beta}{dr}+\frac{3\beta}{r}\right]\boldsymbol{\nabla}_\perp\cdot(\hat{\rho}\boldsymbol{u}) \\
&\qquad-\frac{\nu}{r\sin\theta}\left[\frac{\partial}{\partial\theta}\left(\frac{\hat{\rho}u_\theta}{r^2\sin\theta}\right)+\frac{\partial}{\partial\phi}\left(\frac{\hat{\rho}u_\phi}{r^2\sin^2\theta}\right)\right] \\
&\quad=-\nu\left[\alpha\beta+\frac{\alpha}{r}+\frac{d\beta}{dr}+\frac{3\beta}{r}\right]\boldsymbol{\nabla}_\perp\cdot(\hat{\rho}\boldsymbol{u}) \\
&\qquad+\frac{\nu}{r\sin\theta}\left[-\frac{1}{r^2\sin\theta}\frac{\partial(\hat{\rho}u_\theta)}{\partial\theta}+\frac{\cos\theta}{r^2\sin^2\theta}\,\hat{\rho}u_\theta-\frac{1}{r^2\sin^2\theta}\frac{\partial(\hat{\rho}u_\phi)}{\partial\phi}\right].
\end{aligned}
\tag{B.104}
$$

Summing together the terms in equations (B.100)–(B.104) yields

$$
\begin{aligned}
\boldsymbol{\nabla}_\perp\cdot\left[\boldsymbol{\nabla}\cdot\hat{\underline{\underline{\boldsymbol{\mathcal{D}}}}}\right]=\nu\Bigg\{&\underbrace{\frac{1}{r}\nabla^2\Big[r\,\boldsymbol{\nabla}_\perp\cdot(\hat{\rho}\boldsymbol{u})\Big]}_{\boxed{\text{3a}}}-\underbrace{\left[\alpha\beta+\frac{\alpha}{r}+\frac{d\beta}{dr}+\frac{3\beta}{r}\right]\boldsymbol{\nabla}_\perp\cdot(\hat{\rho}\boldsymbol{u})}_{\boxed{\text{3b}}} \\
&+\underbrace{\frac{\alpha-\beta}{r}\frac{\partial}{\partial r}\Big[r\boldsymbol{\nabla}_\perp\cdot(\hat{\rho}\boldsymbol{u})\Big]}_{\boxed{\text{3c}}}+\underbrace{\left[\alpha+\frac{2\beta}{3}+\frac{2}{r}\right]\nabla_\perp^2(\hat{\rho}u_r)}_{\boxed{\text{3d}}}\Bigg\}.
\end{aligned}
\tag{B.105}
$$

Using equation (B.96) and the fact that $\boldsymbol{\nabla}\cdot(\hat{\rho}\boldsymbol{u})=0$, we can make the substitution

$$
\boldsymbol{\nabla}_\perp\cdot(\hat{\rho}\boldsymbol{u})=-\frac{1}{r^2}\frac{\partial(r^2\,\hat{\rho}u_r)}{\partial r}=-\frac{\partial(\hat{\rho}u_r)}{\partial r}-\frac{2}{r}\,\hat{\rho}u_r
\tag{B.106}
$$

such that only $\hat{\rho}u_r$ remains, and then use equation (B.45) to eliminate $\hat{\rho}u_r$ in favor of W. Once in terms of W, the commutation relations (B.49)–(B.51) are used to interchange the $\nabla_\perp^2$ operator with r-derivatives. We now examine each term in equation (B.105) above, starting with the first term:

$$
\begin{aligned}
\boxed{\text{3a}}&=\frac{1}{r}\nabla^2\Big[r\,\boldsymbol{\nabla}_\perp\cdot(\hat{\rho}\boldsymbol{u})\Big] \\
&=-\frac{1}{r}\nabla^2\left[r\,\frac{\partial(\hat{\rho}u_r)}{\partial r}+2\,\hat{\rho}u_r\right] \\
&=-\frac{1}{r}\left[\frac{1}{r^2}\frac{\partial}{\partial r}\left(r^2\frac{\partial}{\partial r}\right)+\nabla_\perp^2\right]\left[r\,\frac{\partial(\hat{\rho}u_r)}{\partial r}+2\,\hat{\rho}u_r\right] \\
&=-\left[\frac{\partial^3(\hat{\rho}u_r)}{\partial r^3}+\frac{6}{r}\frac{\partial^2(\hat{\rho}u_r)}{\partial r^2}+\frac{6}{r^2}\frac{\partial(\hat{\rho}u_r)}{\partial r}+\nabla_\perp^2\frac{\partial(\hat{\rho}u_r)}{\partial r}+\frac{2}{r}\nabla_\perp^2(\hat{\rho}u_r)\right] \\
&=\nabla_\perp^2\left[\frac{\partial^3 W}{\partial r^3}+\nabla_\perp^2\frac{\partial W}{\partial r}\right].
\end{aligned}
\tag{B.107}
$$

The next two terms are

$$\begin{aligned}\boxed{\text{3b}} &= -\left[\alpha\beta + \frac{\alpha}{r} + \frac{d\beta}{dr} + \frac{3\beta}{r}\right]\boldsymbol{\nabla}_\perp\cdot(\hat{\rho}\boldsymbol{u})\\ &= \left[\alpha\beta + \frac{\alpha}{r} + \frac{d\beta}{dr} + \frac{3\beta}{r}\right]\left[\frac{\partial(\hat{\rho}u_r)}{\partial r} + \frac{2}{r}\,\hat{\rho}u_r\right]\\ &= -\nabla_\perp^2\left[\alpha\beta + \frac{\alpha}{r} + \frac{d\beta}{dr} + \frac{3\beta}{r}\right]\frac{\partial W}{\partial r}\end{aligned}\tag{B.108}$$

and

$$\begin{aligned}\boxed{\text{3c}} &= \frac{\alpha-\beta}{r}\frac{\partial}{\partial r}\Big[r\boldsymbol{\nabla}_\perp\cdot(\hat{\rho}\boldsymbol{u})\Big]\\ &= -(\alpha-\beta)\left[\frac{\partial^2(\hat{\rho}u_r)}{\partial r^2} + \frac{3}{r}\frac{\partial(\hat{\rho}u_r)}{\partial r}\right]\\ &= \nabla_\perp^2\left[(\alpha-\beta)\left(\frac{\partial^2 W}{\partial r^2} - \frac{1}{r}\frac{\partial W}{\partial r}\right)\right].\end{aligned}\tag{B.109}$$

Lastly, the fourth term is simply

$$\boxed{\text{3d}} = \left[\alpha + \frac{2\beta}{3} + \frac{2}{r}\right]\nabla_\perp^2(\hat{\rho}u_r) = -\nabla_\perp^2\left[\alpha + \frac{2\beta}{3} + \frac{2}{r}\right]\nabla_\perp^2 W.\tag{B.110}$$

Combining equations (B.107)–(B.110) and regrouping, we obtain

$$\boxed{\begin{aligned}\boldsymbol{\nabla}_\perp\cdot\left[\boldsymbol{\nabla}\cdot\underline{\underline{\hat{\boldsymbol{\mathcal{D}}}}}\right] = \nu\nabla_\perp^2\Bigg\{&\frac{\partial^3 W}{\partial r^3} + (\alpha-\beta)\frac{\partial^2 W}{\partial r^2}\\ &-\left[\alpha\beta + \frac{2\alpha}{r} + \frac{d\beta}{dr} + \frac{2\beta}{r} - \nabla_\perp^2\right]\frac{\partial W}{\partial r}\\ &-\left[\alpha + \frac{2\beta}{3} + \frac{2}{r}\right]\nabla_\perp^2 W\Bigg\}.\end{aligned}}\tag{B.111}$$

B.3.3.6 Radial Component of Curl

We now use the results of §B.3.3.3 and §B.3.3.4 to evaluate $\hat{\boldsymbol{r}}\cdot\boldsymbol{\nabla}\times\left[\boldsymbol{\nabla}\cdot\underline{\underline{\hat{\boldsymbol{\mathcal{D}}}}}\right]$, which serves as the diffusion term in the Z equation. By definition,

$$\hat{\boldsymbol{r}}\cdot\boldsymbol{\nabla}\times\left[\boldsymbol{\nabla}\cdot\underline{\underline{\hat{\boldsymbol{\mathcal{D}}}}}\right] = \frac{1}{r\sin\theta}\left[\frac{\partial}{\partial\theta}\left(\sin\theta\,\hat{\boldsymbol{\phi}}\cdot\boldsymbol{\nabla}\cdot\underline{\underline{\hat{\boldsymbol{\mathcal{D}}}}}\right) - \frac{\partial}{\partial\phi}\left(\hat{\boldsymbol{\theta}}\cdot\boldsymbol{\nabla}\cdot\underline{\underline{\hat{\boldsymbol{\mathcal{D}}}}}\right)\right].\tag{B.112}$$

The polar and azimuthal components of $\boldsymbol{\nabla}\cdot\underline{\underline{\hat{\boldsymbol{\mathcal{D}}}}}$ are given by equations (B.81) and (B.94). We rewrite them here and label the individual terms before combining them as per equation (B.112):

$$\hat{\boldsymbol{\theta}} \cdot \left[\boldsymbol{\nabla} \cdot \underline{\underline{\hat{\boldsymbol{\mathcal{D}}}}}\right] = \nu \Bigg\{ \underbrace{\nabla^2(\hat{\rho} u_\theta)}_{\boxed{1a}} + \underbrace{\frac{1}{r}\left[\alpha + \frac{2\beta}{3} + \frac{2}{r}\right]\frac{\partial(\hat{\rho} u_r)}{\partial \theta}}_{\boxed{1b}} + \underbrace{(\alpha - \beta)\frac{\partial(\hat{\rho} u_\theta)}{\partial r}}_{\boxed{1c}}$$
$$- \underbrace{\frac{2\cos\theta}{r^2\sin^2\theta}\frac{\partial(\hat{\rho} u_\phi)}{\partial \phi}}_{\boxed{1d}} - \underbrace{\left[\alpha\beta + \frac{\alpha}{r} + \frac{d\beta}{dr} + \frac{3\beta}{r} + \frac{1}{r^2\sin^2\theta}\right]\hat{\rho} u_\theta}_{\boxed{1e}} \Bigg\} \tag{B.113}$$

and

$$\hat{\boldsymbol{\phi}} \cdot \left[\boldsymbol{\nabla} \cdot \underline{\underline{\hat{\boldsymbol{\mathcal{D}}}}}\right] = \nu \Bigg\{ \underbrace{\nabla^2(\hat{\rho} u_\phi)}_{\boxed{2a}} + \underbrace{\frac{1}{r\sin\theta}\left[\alpha + \frac{2\beta}{3} + \frac{2}{r}\right]\frac{\partial(\hat{\rho} u_r)}{\partial \phi}}_{\boxed{2b}} + \underbrace{(\alpha - \beta)\frac{\partial(\hat{\rho} u_\phi)}{\partial r}}_{\boxed{2c}}$$
$$+ \underbrace{\frac{2\cos\theta}{r^2\sin^2\theta}\frac{\partial(\hat{\rho} u_\theta)}{\partial \phi}}_{\boxed{2d}} - \underbrace{\left[\alpha\beta + \frac{\alpha}{r} + \frac{d\beta}{dr} + \frac{3\beta}{r} + \frac{1}{r^2\sin^2\theta}\right]\hat{\rho} u_\phi}_{\boxed{2e}} \Bigg\}. \tag{B.114}$$

Combining the terms containing $\boxed{1a}$ and $\boxed{2a}$ yields:

$$\begin{aligned}
&\frac{\nu}{r\sin\theta}\left\{\frac{\partial}{\partial\theta}\left[\sin\theta\,\boxed{2a}\right] - \frac{\partial\,\boxed{1a}}{\partial\phi}\right\} \\
&\quad = \frac{\nu}{r\sin\theta}\left\{\frac{\partial}{\partial\theta}\left[\sin\theta\,\nabla^2(\hat{\rho} u_\phi)\right] - \frac{\partial}{\partial\phi}\left[\nabla^2(\hat{\rho} u_\theta)\right]\right\} \\
&\quad = \frac{\nu}{r\sin\theta}\Bigg\{\nabla^2\left[\frac{\partial\left(\sin\theta\,\hat{\rho} u_\phi\right)}{\partial\theta} - \frac{\partial(\hat{\rho} u_\theta)}{\partial\phi}\right] - \frac{2\cos\theta}{r^2}\frac{\partial^2(\hat{\rho} u_\phi)}{\partial\theta^2} \\
&\qquad + \left(\frac{4\sin\theta}{r^2} - \frac{2}{r^2\sin\theta}\right)\frac{\partial(\hat{\rho} u_\phi)}{\partial\theta} + \frac{2\cos\theta}{r^2}\hat{\rho} u_\phi - \frac{2\cos\theta}{r^2\sin^2\theta}\frac{\partial^2(\hat{\rho} u_\phi)}{\partial\phi^2}\Bigg\} \\
&\quad = \frac{\nu}{r\sin\theta}\Bigg\{\sin\theta\,\nabla^2\left[r\,\hat{\boldsymbol{r}}\cdot\boldsymbol{\nabla}\times\hat{\rho}\boldsymbol{u}\right] - \frac{2\cos\theta}{r^2\sin\theta}\frac{\partial^2(\hat{\rho} u_\theta)}{\partial\theta\,\partial\phi} - \frac{2\cos\theta}{r^2\sin^2\theta}\frac{\partial^2(\hat{\rho} u_\phi)}{\partial\phi^2} \\
&\qquad + \frac{1}{r^2\sin\theta}\frac{\partial(\hat{\rho} u_\phi)}{\partial\theta} - \frac{\cos\theta}{r^2\sin^2\theta}\hat{\rho} u_\phi + \frac{1}{r^2\sin^2\theta}\frac{\partial(\hat{\rho} u_\theta)}{\partial\phi}\Bigg\}.
\end{aligned} \tag{B.115}$$

Combining the terms containing $\boxed{1b}$ and $\boxed{2b}$ yields:

$$\frac{\nu}{r\sin\theta}\left\{\frac{\partial}{\partial\theta}\left[\sin\theta\,\boxed{2b}\right] - \frac{\partial\,\boxed{1b}}{\partial\phi}\right\} = 0. \tag{B.116}$$

Combining the terms containing $\boxed{\text{1c}}$ and $\boxed{\text{2c}}$ yields:

$$\begin{aligned}
\frac{\nu}{r\sin\theta}\left\{\frac{\partial}{\partial\theta}\left[\sin\theta\,\boxed{\text{2c}}\right]-\frac{\partial\boxed{\text{1c}}}{\partial\phi}\right\} &= \frac{\nu(\alpha-\beta)}{r\sin\theta}\frac{\partial}{\partial r}\left[\frac{\partial(\sin\theta\,\hat{\rho}u_\phi)}{\partial\theta}-\frac{\partial(\hat{\rho}u_\theta)}{\partial\phi}\right] \\
&= \frac{\nu(\alpha-\beta)}{r}\frac{\partial}{\partial r}\Big[r\,\hat{\boldsymbol{r}}\cdot\boldsymbol{\nabla}\times\hat{\rho}\boldsymbol{u}\Big]. \qquad \text{(B.117)}
\end{aligned}$$

Combining the terms containing $\boxed{\text{1d}}$ and $\boxed{\text{2d}}$ yields:

$$\begin{aligned}
&\frac{\nu}{r\sin\theta}\left\{\frac{\partial}{\partial\theta}\left[\sin\theta\,\boxed{\text{2d}}\right]-\frac{\partial\boxed{\text{1d}}}{\partial\phi}\right\} \\
&\quad= \frac{\nu}{r\sin\theta}\left[\frac{\partial}{\partial\theta}\left(\frac{2\cos\theta}{r^2\sin\theta}\frac{\partial(\hat{\rho}u_\theta)}{\partial\phi}\right)+\frac{\partial}{\partial\phi}\left(\frac{2\cos\theta}{r^2\sin^2\theta}\frac{\partial(\hat{\rho}u_\phi)}{\partial\phi}\right)\right] \\
&\quad= \frac{\nu}{r\sin\theta}\left[\frac{2\cos\theta}{r^2\sin\theta}\frac{\partial^2(\hat{\rho}u_\theta)}{\partial\theta\,\partial\phi}-\frac{2}{r^2\sin^2\theta}\frac{\partial(\hat{\rho}u_\theta)}{\partial\phi}+\frac{2\cos\theta}{r^2\sin^2\theta}\frac{\partial^2(\hat{\rho}u_\phi)}{\partial\phi^2}\right] \qquad \text{(B.118)}
\end{aligned}$$

Finally, combining the terms containing $\boxed{\text{1e}}$ and $\boxed{\text{2e}}$ yields:

$$\begin{aligned}
&\frac{\nu}{r\sin\theta}\left\{\frac{\partial}{\partial\theta}\left[\sin\theta\,\boxed{\text{2e}}\right]-\frac{\partial\boxed{\text{1e}}}{\partial\phi}\right\} \\
&\quad= -\nu\left[\alpha\beta+\frac{\alpha}{r}+\frac{d\beta}{dr}+\frac{3\beta}{r}\right]\hat{\boldsymbol{r}}\cdot\boldsymbol{\nabla}\times\hat{\rho}\boldsymbol{u} \\
&\qquad -\frac{\nu}{r\sin\theta}\left[\frac{\partial}{\partial\theta}\left(\frac{\hat{\rho}u_\phi}{r^2\sin\theta}\right)+\frac{\partial}{\partial\phi}\left(\frac{\hat{\rho}u_\theta}{r^2\sin^2\theta}\right)\right] \\
&\quad= -\nu\left[\alpha\beta+\frac{\alpha}{r}+\frac{d\beta}{dr}+\frac{3\beta}{r}\right]\hat{\boldsymbol{r}}\cdot\boldsymbol{\nabla}\times\hat{\rho}\boldsymbol{u} \\
&\qquad +\frac{\nu}{r\sin\theta}\left[\frac{\cos\theta}{r^2\sin^2\theta}\hat{\rho}u_\phi+\frac{1}{r^2\sin^2\theta}\frac{\partial(\hat{\rho}u_\theta)}{\partial\phi}-\frac{1}{r^2\sin\theta}\frac{\partial(\hat{\rho}u_\phi)}{\partial\theta}\right]. \qquad \text{(B.119)}
\end{aligned}$$

Summing together the terms in equations (B.115)–(B.119) yields

$$\begin{aligned}
\hat{\boldsymbol{r}}\cdot\boldsymbol{\nabla}\times\left[\boldsymbol{\nabla}\cdot\underline{\underline{\hat{\boldsymbol{\mathcal{D}}}}}\right] = \nu\Bigg\{&\frac{1}{r}\nabla^2\Big[r\,\hat{\boldsymbol{r}}\cdot\boldsymbol{\nabla}\times\hat{\rho}\boldsymbol{u}\Big]-\left[\alpha\beta+\frac{\alpha}{r}+\frac{d\beta}{dr}+\frac{3\beta}{r}\right]\hat{\boldsymbol{r}}\cdot\boldsymbol{\nabla}\times\hat{\rho}\boldsymbol{u} \\
&+\frac{\alpha-\beta}{r}\frac{\partial}{\partial r}\Big[r\,\hat{\boldsymbol{r}}\cdot\boldsymbol{\nabla}\times\hat{\rho}\boldsymbol{u}\Big]\Bigg\}.
\end{aligned} \qquad \text{(B.120)}$$

We now eliminate $\hat{\rho}\boldsymbol{u}$ in favor of Z by substituting $\hat{\boldsymbol{r}}\cdot\boldsymbol{\nabla}\times\hat{\rho}\boldsymbol{u} = -\nabla_\perp^2 Z$ by equation (B.46) to obtain

$$\begin{aligned}
\hat{\boldsymbol{r}} \cdot \boldsymbol{\nabla} \times \left[\boldsymbol{\nabla} \cdot \underline{\underline{\hat{\boldsymbol{\mathcal{D}}}}}\right] &= -\nu \left\{ \frac{1}{r} \nabla^2 \left[r \nabla_\perp^2 Z \right] - \left[\alpha\beta + \frac{\alpha}{r} + \frac{d\beta}{dr} + \frac{3\beta}{r} \right] \nabla_\perp^2 Z \right. \\
&\qquad \left. + \frac{\alpha - \beta}{r} \frac{\partial}{\partial r} \left[r \nabla_\perp^2 Z \right] \right\} \\
&= -\nu \left\{ \frac{1}{r} \left[\frac{1}{r^2} \frac{\partial}{\partial r} \left(r^2 \frac{\partial}{\partial r} \right) + \nabla_\perp^2 \right] \left[r \nabla_\perp^2 Z \right] \right. \\
&\qquad \left. - \nabla_\perp^2 \left[\alpha\beta + \frac{\alpha}{r} + \frac{d\beta}{dr} + \frac{3\beta}{r} \right] Z + \frac{\alpha - \beta}{r} \frac{\partial}{\partial r} \left[r \nabla_\perp^2 Z \right] \right\} \\
&= -\nu \left\{ \left[\frac{\partial^2}{\partial r^2} + \frac{4}{r} \frac{\partial}{\partial r} + \frac{2}{r^2} + \nabla_\perp^2 \right] \nabla_\perp^2 Z \right. \\
&\qquad \left. - \nabla_\perp^2 \left[\alpha\beta + \frac{\alpha}{r} + \frac{d\beta}{dr} + \frac{3\beta}{r} \right] Z + (\alpha - \beta) \left[\frac{\partial}{\partial r} + \frac{1}{r} \right] \nabla_\perp^2 Z. \right\}
\end{aligned}$$

Using the commutation identities (B.49) and (B.50), we finally obtain

$$\boxed{\begin{aligned}
\hat{\boldsymbol{r}} \cdot \boldsymbol{\nabla} \times \left[\boldsymbol{\nabla} \cdot \underline{\underline{\hat{\boldsymbol{\mathcal{D}}}}}\right] = -\nu \nabla_\perp^2 &\left\{ \frac{\partial^2 Z}{\partial r^2} + (\alpha - \beta) \frac{\partial Z}{\partial r} \right. \\
&\left. - \left[\alpha\beta + \frac{2\alpha}{r} + \frac{d\beta}{dr} + \frac{2\beta}{r} + \nabla_\perp^2 \right] Z \right\}.
\end{aligned}} \tag{B.121}$$

B.3.4 Derivation of the W Equation

The evolution equation for W is obtained by taking $\hat{\boldsymbol{r}}\cdot$ each term in the anelastic momentum equation (B.8). Applying $\hat{\boldsymbol{r}}\cdot$ to the time-derivative term gives

$$\hat{\rho}\, \hat{\boldsymbol{r}} \cdot \left(\frac{\partial \boldsymbol{u}}{\partial t} \right) = \frac{\partial}{\partial t} (\hat{\boldsymbol{r}} \cdot \hat{\rho} \boldsymbol{u}) = -\frac{\partial}{\partial t} (\nabla_\perp^2 W) = -\nabla_\perp^2 \frac{\partial W}{\partial t}, \tag{B.122}$$

where we have used equation (B.45). As a result, a schematic representation of the W equation is

$$\boxed{-\nabla_\perp^2 \frac{\partial W}{\partial t} = W_{\mathrm{PG}} + W_{\mathrm{GRAV}} + W_{\mathrm{DIFF}} + W_{\mathrm{COR}} + W_{\mathrm{ADV}}.} \tag{B.123}$$

We now compute the five terms on the right-hand side.

The pressure gradient and gravitational force terms are simply

$$W_{\mathrm{PG}} = \hat{\boldsymbol{r}} \cdot \Big(-\boldsymbol{\nabla} p \Big) = -\frac{\partial p}{\partial r}, \tag{B.124}$$

and

$$W_{\text{GRAV}} = \hat{\boldsymbol{r}} \cdot \left(-\rho g\, \hat{\boldsymbol{r}}\right) = -\rho g. \tag{B.125}$$

Equation (B.67) gives the diffusion term in terms of W:

$$\begin{aligned} W_{\text{DIFF}} &= \hat{\boldsymbol{r}} \cdot \left[\boldsymbol{\nabla} \cdot \underline{\underline{\hat{\boldsymbol{\mathcal{D}}}}}\right] \\ &= \nu_{\text{eff}} \nabla_\perp^2 \left\{ \frac{\partial^2 W}{\partial r^2} + \left(2\alpha - \frac{\beta}{3}\right) \frac{\partial W}{\partial r} + \left(\nabla_\perp^2 - \frac{4\alpha\beta}{3} - \frac{4\alpha}{r} - \frac{4}{3}\frac{\partial \beta}{\partial r} - \frac{4\beta}{3r}\right) W \right\}, \end{aligned} \tag{B.126}$$

where $\alpha = \dfrac{d \ln \nu_{\text{eff}}}{dr}$ and $\beta = \dfrac{d \ln \hat{\rho}}{dr}$. The Coriolis term can also be expanded in terms of the streamfunctions:

$$\begin{aligned} W_{\text{COR}} &= 2\hat{\rho}\, \hat{\boldsymbol{r}} \cdot (\boldsymbol{u} \times \boldsymbol{\Omega}) \\ &= 2\Omega \sin\theta\, \hat{\rho} u_\phi \\ &= \frac{2\Omega}{r}\left[\frac{\partial^2 W}{\partial r \partial \phi} - \sin\theta \frac{\partial Z}{\partial \theta}\right]. \qquad \text{by equation (B.45)} \end{aligned} \tag{B.127}$$

Finally, the advection term can be expanded in terms of the three components of $\boldsymbol{u}$:

$$\begin{aligned} W_{\text{ADV}} &= -\hat{\rho}\, \hat{\boldsymbol{r}} \cdot \left[(\boldsymbol{u} \cdot \boldsymbol{\nabla})\boldsymbol{u}\right] \\ &= -\hat{\rho}\left[(\boldsymbol{u} \cdot \boldsymbol{\nabla}) u_r - \frac{u_\theta^2}{r} - \frac{u_\phi^2}{r}\right] \\ &= -\hat{\rho}\left[\left(u_r \frac{\partial}{\partial r} + \frac{u_\theta}{r}\frac{\partial}{\partial \theta} + \frac{u_\phi}{r\sin\theta}\frac{\partial}{\partial \phi}\right) u_r - \frac{u_\theta^2}{r} - \frac{u_\phi^2}{r}\right]. \end{aligned} \tag{B.128}$$

B.3.5 Derivation of the P Equation

The evolution equation for P is obtained by taking $\boldsymbol{\nabla}_\perp \cdot$ each term in the anelastic momentum equation (B.8), where the expression $\boldsymbol{\nabla}_\perp \cdot \boldsymbol{A}$ equals

$$\boldsymbol{\nabla}_\perp \cdot \boldsymbol{A} = \frac{1}{r\sin\theta}\frac{\partial(\sin\theta\, A_\theta)}{\partial \theta} + \frac{1}{r\sin\theta}\frac{\partial A_\phi}{\partial \phi}, \tag{B.129}$$

such that

$$\boldsymbol{\nabla} \cdot \boldsymbol{A} = \frac{1}{r^2}\frac{\partial(r^2 A_r)}{\partial r} + \boldsymbol{\nabla}_\perp \cdot \boldsymbol{A}. \tag{B.130}$$

The time-derivative term simplifies to

$$\begin{aligned}
\boldsymbol{\nabla}_{\perp} \cdot \left(\hat{\rho}\frac{\partial \boldsymbol{u}}{\partial t}\right) &= \frac{\partial}{\partial t}\Big[\boldsymbol{\nabla}_{\perp} \cdot (\hat{\rho}\boldsymbol{u})\Big] \\
&= \frac{\partial}{\partial t}\left[\boldsymbol{\nabla} \cdot (\hat{\rho}\boldsymbol{u}) - \frac{1}{r^2}\frac{\partial(r^2\hat{\rho}u_r)}{\partial r}\right] \qquad \text{by equation (B.130)} \\
&= -\frac{\partial}{\partial t}\left[\frac{\partial(\hat{\rho}u_r)}{\partial r} + \frac{2\hat{\rho}u_r}{r}\right] \qquad \text{by equation (B.4)} \\
&= \frac{\partial}{\partial t}\left[\frac{\partial(\nabla_{\perp}^2 W)}{\partial r} + \frac{2}{r}\nabla_{\perp}^2 W\right] \qquad \text{by equation (B.45)} \\
&= \nabla_{\perp}^2 \frac{\partial}{\partial t}\left(\frac{\partial W}{\partial r}\right). \qquad \text{by equation (B.49)}
\end{aligned} \tag{B.131}$$

Therefore, the P equation is represented by

$$\boxed{\nabla_{\perp}^2 \frac{\partial}{\partial t}\left(\frac{\partial W}{\partial r}\right) = P_{\mathrm{PG}} + P_{\mathrm{DIFF}} + P_{\mathrm{COR}} + P_{\mathrm{ADV}}.} \tag{B.132}$$

Note that there is no gravity term since the quantity $\boldsymbol{\nabla}_{\perp} \cdot (\rho g\,\hat{\boldsymbol{r}})$ vanishes. We now list the remaining terms on the right-hand side in order.

The pressure gradient term simplifies to

$$P_{\mathrm{PG}} = -\boldsymbol{\nabla}_{\perp} \cdot (\boldsymbol{\nabla} p) = -\left[\boldsymbol{\nabla} \cdot (\boldsymbol{\nabla} p) - \frac{1}{r^2}\frac{\partial}{\partial r}\left(r^2\frac{\partial p}{\partial r}\right)\right] = -\nabla_{\perp}^2 p, \tag{B.133}$$

by equations (B.47) and (B.130). The diffusion term is given by equation (B.111):

$$\begin{aligned}
P_{\mathrm{DIFF}} &= \boldsymbol{\nabla}_{\perp} \cdot \Big[\boldsymbol{\nabla} \cdot \underline{\underline{\hat{\boldsymbol{\mathcal{D}}}}}\Big] \\
&= \nu_{\mathrm{eff}}\nabla_{\perp}^2\Bigg\{\frac{\partial^3 W}{\partial r^3} + (\alpha - \beta)\frac{\partial^2 W}{\partial r^2} - \left[\alpha\beta + \frac{2\alpha}{r} + \frac{d\beta}{dr} + \frac{2\beta}{r} - \nabla_{\perp}^2\right]\frac{\partial W}{\partial r} \\
&\qquad - \left[\alpha + \frac{2\beta}{3} + \frac{2}{r}\right]\nabla_{\perp}^2 W\Bigg\}.
\end{aligned} \tag{B.134}$$

The Coriolis term can be simplified by using

$$\begin{aligned}
\boldsymbol{\nabla} \times \boldsymbol{\nabla} \times Z\,\hat{\boldsymbol{r}} &= \boldsymbol{\nabla} \times \left(\frac{1}{r\sin\theta}\frac{\partial Z}{\partial \phi}\,\hat{\boldsymbol{\theta}} - \frac{1}{r}\frac{\partial Z}{\partial \theta}\,\hat{\boldsymbol{\phi}}\right) \\
&= -\left[\frac{1}{r^2\sin\theta}\frac{\partial}{\partial \theta}\left(\sin\theta\frac{\partial Z}{\partial \theta}\right) + \frac{1}{r^2\sin^2\theta}\frac{\partial}{\partial \phi}\left(\frac{1}{r\sin\theta}\frac{\partial Z}{\partial \phi}\right)\right]\hat{\boldsymbol{r}} \\
&\qquad + \frac{1}{r}\frac{\partial^2 Z}{\partial r\partial \theta}\,\hat{\boldsymbol{\theta}} + \frac{1}{r\sin\theta}\frac{\partial^2 Z}{\partial r\partial \phi}\,\hat{\boldsymbol{\phi}} \\
&= -(\nabla_{\perp}^2 Z)\,\hat{\boldsymbol{r}} + \boldsymbol{\nabla}\left(\frac{\partial Z}{\partial r}\right) - \frac{\partial^2 Z}{\partial r^2}\,\hat{\boldsymbol{r}}
\end{aligned} \tag{B.135}$$

and

$$\boldsymbol{\nabla}\times\boldsymbol{\nabla}\times\boldsymbol{\nabla}\times W\,\hat{\boldsymbol{r}} = \boldsymbol{\nabla}\times\left[-(\nabla_\perp^2 W)\,\hat{\boldsymbol{r}} + \boldsymbol{\nabla}\left(\frac{\partial W}{\partial r}\right) - \frac{\partial^2 W}{\partial r^2}\,\hat{\boldsymbol{r}}\right]$$
$$= -\frac{1}{r\sin\theta}\frac{\partial}{\partial\phi}\left[\nabla_\perp^2 W + \frac{\partial^2 W}{\partial r^2}\right]\hat{\boldsymbol{\theta}} + \frac{1}{r}\frac{\partial}{\partial\theta}\left[\nabla_\perp^2 W + \frac{\partial^2 W}{\partial r^2}\right]\hat{\boldsymbol{\phi}} \tag{B.136}$$

so that

$$\begin{aligned}
P_{\mathrm{COR}} &= \boldsymbol{\nabla}_\perp\boldsymbol{\cdot}\left[2\hat{\rho}\boldsymbol{u}\times\boldsymbol{\Omega}\right] \\
&= 2\boldsymbol{\Omega}\boldsymbol{\cdot}\left[\boldsymbol{\nabla}\times(\hat{\rho}\boldsymbol{u})\right] - \left(\frac{\partial}{\partial r}+\frac{2}{r}\right)\left[\hat{\boldsymbol{r}}\boldsymbol{\cdot}(2\hat{\rho}\boldsymbol{u}\times\boldsymbol{\Omega})\right] \\
&= 2\Omega(\cos\theta\,\hat{\boldsymbol{r}} - \sin\theta\,\hat{\boldsymbol{\theta}})\boldsymbol{\cdot}\left[\boldsymbol{\nabla}\times\boldsymbol{\nabla}\times\boldsymbol{\nabla}\times W\,\hat{\boldsymbol{r}} + \boldsymbol{\nabla}\times\boldsymbol{\nabla}\times Z\,\hat{\boldsymbol{r}}\right] \\
&\quad - \left(\frac{\partial}{\partial r}+\frac{2}{r}\right)\left[2\Omega\sin\theta\,\hat{\rho}u_\phi\right] \\
&= 2\Omega\left[\frac{1}{r}\left(\nabla_\perp^2 + \frac{\partial^2}{\partial r^2}\right)\frac{\partial W}{\partial\phi} - \cos\theta\,\nabla_\perp^2 Z - \frac{\sin\theta}{r}\frac{\partial^2 Z}{\partial r\partial\theta}\right] \\
&\quad - \left(\frac{\partial}{\partial r}+\frac{2}{r}\right)\left[\frac{2\Omega}{r}\left(\frac{\partial^2 W}{\partial r\partial\phi} - \sin\theta\frac{\partial^2 W}{\partial r\partial\theta}\right)\right].
\end{aligned} \tag{B.137}$$

The advection term can be expanded in terms of the three components of $\boldsymbol{u}$:

$$\begin{aligned}
P_{\mathrm{ADV}} &= -\boldsymbol{\nabla}_\perp\boldsymbol{\cdot}\left[\hat{\rho}(\boldsymbol{u}\boldsymbol{\cdot}\boldsymbol{\nabla})\boldsymbol{u}\right] \\
&= -\frac{\hat{\rho}}{r\sin\theta}\left\{\frac{\partial}{\partial\theta}\left[\sin\theta\,\hat{\boldsymbol{\theta}}\boldsymbol{\cdot}\left[(\boldsymbol{u}\boldsymbol{\cdot}\boldsymbol{\nabla})\boldsymbol{u}\right]\right] + \frac{\partial}{\partial\phi}\left[\hat{\boldsymbol{\phi}}\boldsymbol{\cdot}\left[(\boldsymbol{u}\boldsymbol{\cdot}\boldsymbol{\nabla})\boldsymbol{u}\right]\right]\right\} \\
&= -\frac{\hat{\rho}}{r\sin\theta}\left\{\frac{\partial}{\partial\theta}\left[\sin\theta\left((\boldsymbol{u}\boldsymbol{\cdot}\boldsymbol{\nabla})u_\theta + \frac{u_r u_\theta}{r} - \frac{u_\phi^2\cos\theta}{r\sin\theta}\right)\right]\right. \\
&\qquad\left. + \frac{\partial}{\partial\phi}\left[(\boldsymbol{u}\boldsymbol{\cdot}\boldsymbol{\nabla})u_\phi + \frac{u_r u_\phi}{r} + \frac{u_\theta u_\phi\cos\theta}{r\sin\theta}\right]\right\} \\
&= -\frac{\hat{\rho}}{r\sin\theta}\left\{\frac{\partial}{\partial\theta}\left[\sin\theta\left(u_r\frac{\partial u_\theta}{\partial r} + \frac{u_\theta}{r}\frac{\partial u_\theta}{\partial\theta} + \frac{u_\phi}{r\sin\theta}\frac{\partial u_\theta}{\partial\phi} + \frac{u_r u_\theta}{r} - \frac{u_\phi^2\cos\theta}{r\sin\theta}\right)\right]\right. \\
&\qquad\left. + \frac{\partial}{\partial\phi}\left[u_r\frac{\partial u_\phi}{\partial r} + \frac{u_\theta}{r}\frac{\partial u_\phi}{\partial\theta} + \frac{u_\phi}{r\sin\theta}\frac{\partial u_\phi}{\partial\phi} + \frac{u_r u_\phi}{r} + \frac{u_\theta u_\phi\cos\theta}{r\sin\theta}\right]\right\}.
\end{aligned} \tag{B.138}$$

B.3.6 Derivation of the Z Equation

The evolution equation for Z is obtained by taking $\hat{\boldsymbol{r}}\boldsymbol{\cdot}\boldsymbol{\nabla}\times$ each term in the anelastic momentum equation (B.8). Applying $\hat{\boldsymbol{r}}\boldsymbol{\cdot}\boldsymbol{\nabla}\times$ to the time-derivative term gives

$$\hat{\boldsymbol{r}} \cdot \boldsymbol{\nabla} \times \frac{\partial(\hat{\rho}\boldsymbol{u})}{\partial t} = \frac{\partial}{\partial t}(\,\hat{\boldsymbol{r}} \cdot \boldsymbol{\nabla} \times \hat{\rho}\boldsymbol{u}) = -\frac{\partial}{\partial t}(\nabla_\perp^2 Z) = -\nabla_\perp^2 \frac{\partial Z}{\partial t}, \tag{B.139}$$

where we have used equation (B.46). As a result, a schematic representation of the Z equation is

$$\boxed{-\nabla_\perp^2 \frac{\partial Z}{\partial t} = Z_{\mathrm{DIFF}} + Z_{\mathrm{COR}} + Z_{\mathrm{ADV}}.} \tag{B.140}$$

Note that there is no pressure gradient term since $\boldsymbol{\nabla} \times \boldsymbol{\nabla} p = 0$, and that the gravity term vanishes since $\boldsymbol{\nabla} \times (\rho g\,\hat{\boldsymbol{r}})$ has no $\hat{\boldsymbol{r}}$-component. We now compute the three terms on the right-hand side in order.

The diffusion term is given by equation (B.121):

$$\begin{aligned} Z_{\mathrm{DIFF}} &= \hat{\boldsymbol{r}} \cdot \boldsymbol{\nabla} \times \left[\boldsymbol{\nabla} \cdot \underline{\underline{\hat{\boldsymbol{\mathcal{D}}}}}\right] \\ &= -\nu_{\mathrm{eff}} \nabla_\perp^2 \left\{ \frac{\partial^2 Z}{\partial r^2} + (\alpha - \beta)\frac{\partial Z}{\partial r} - \left[\alpha\beta + \frac{2\alpha}{r} + \frac{d\beta}{dr} + \frac{2\beta}{r} + \nabla_\perp^2\right] Z \right\}. \end{aligned} \tag{B.141}$$

The Coriolis term simplifies to

$$\begin{aligned} Z_{\mathrm{COR}} &= \hat{\boldsymbol{r}} \cdot \boldsymbol{\nabla} \times \left[(2\hat{\rho}\boldsymbol{u}) \times \boldsymbol{\Omega}\right] \\ &= 2\,\hat{\boldsymbol{r}} \cdot \left[(\boldsymbol{\Omega} \cdot \boldsymbol{\nabla})(\hat{\rho}\boldsymbol{u})\right] \\ &= 2\Omega \left[\cos\theta \frac{\partial(\hat{\rho}u_r)}{\partial r} - \frac{\sin\theta}{r}\frac{\partial(\hat{\rho}u_r)}{\partial\theta} + \frac{\hat{\rho}u_\theta \sin\theta}{r}\right] \\ &= 2\Omega \left[-\cos\theta \frac{\partial}{\partial r}(\nabla_\perp^2 W) + \frac{\sin\theta}{r}\frac{\partial}{\partial\theta}(\nabla_\perp^2 W) + \frac{\sin\theta}{r^2}\frac{\partial^2 W}{\partial r\,\partial\theta} + \frac{1}{r^2}\frac{\partial Z}{\partial\phi}\right]. \end{aligned} \tag{B.142}$$

The advection term can be expanded in terms of the three components of $\boldsymbol{u}$:

$$
\begin{aligned}
Z_{\mathrm{ADV}} &= -\hat{\boldsymbol{r}} \cdot \boldsymbol{\nabla} \times \Big[\hat{\rho}(\boldsymbol{u}\cdot\boldsymbol{\nabla})\boldsymbol{u}\Big] \\
&= -\frac{\hat{\rho}}{r\sin\theta}\left\{\frac{\partial}{\partial\theta}\Big[\sin\theta\,\hat{\boldsymbol{\phi}}\cdot\Big[(\boldsymbol{u}\cdot\boldsymbol{\nabla})\boldsymbol{u}\Big]\Big]-\frac{\partial}{\partial\phi}\Big[\hat{\boldsymbol{\theta}}\cdot\Big[(\boldsymbol{u}\cdot\boldsymbol{\nabla})\boldsymbol{u}\Big]\Big]\right\} \\
&= -\frac{\hat{\rho}}{r\sin\theta}\left\{\frac{\partial}{\partial\theta}\left[\sin\theta\left((\boldsymbol{u}\cdot\boldsymbol{\nabla})u_\phi+\frac{u_r u_\phi}{r}+\frac{u_\theta u_\phi\cos\theta}{r\sin\theta}\right)\right]\right. \\
&\qquad\left.-\frac{\partial}{\partial\phi}\left[(\boldsymbol{u}\cdot\boldsymbol{\nabla})u_\theta+\frac{u_r u_\theta}{r}-\frac{u_\phi^2\cos\theta}{r\sin\theta}\right]\right\} \\
&= -\frac{\hat{\rho}}{r\sin\theta}\left\{\frac{\partial}{\partial\theta}\left[\sin\theta\left(u_r\frac{\partial u_\phi}{\partial r}+\frac{u_\theta}{r}\frac{\partial u_\phi}{\partial\theta}+\frac{u_\phi}{r\sin\theta}\frac{\partial u_\phi}{\partial\phi}+\frac{u_r u_\phi}{r}+\frac{u_\theta u_\phi\cos\theta}{r\sin\theta}\right)\right]\right. \\
&\qquad\left.-\frac{\partial}{\partial\phi}\left[u_r\frac{\partial u_\theta}{\partial r}+\frac{u_\theta}{r}\frac{\partial u_\theta}{\partial\theta}+\frac{u_\phi}{r\sin\theta}\frac{\partial u_\theta}{\partial\phi}+\frac{u_r u_\theta}{r}-\frac{u_\phi^2\cos\theta}{r\sin\theta}\right]\right\} \qquad \text{(B.143)}
\end{aligned}
$$

B.3.7 Derivation of the S Equation

The evolution equation for S is simply equation (B.12),

$$
\boxed{\hat{\rho}\hat{T}\frac{\partial s}{\partial t} = S_{\mathrm{FLUX}} + S_{\mathrm{ADV}} + S_{\mathrm{DIFF}}.} \qquad \text{(B.144)}
$$

where the entropy and radiative fluxes are given by

$$
\begin{aligned}
S_{\mathrm{FLUX}} &= -\boldsymbol{\nabla}\cdot\hat{\boldsymbol{q}}_{\mathrm{eff}} \\
&= -\kappa_r\hat{\rho}c_p\boldsymbol{\nabla}(\hat{T}+T)-\kappa_s\hat{\rho}\hat{T}\boldsymbol{\nabla}(\hat{s}+s), \qquad \text{by equation (B.11)} \qquad \text{(B.145)}
\end{aligned}
$$

the advection term is

$$
\begin{aligned}
S_{\mathrm{ADV}} &= -\hat{\rho}\hat{T}(\boldsymbol{u}\cdot\boldsymbol{\nabla})(\hat{s}+s) \\
&= -\hat{\rho}\hat{T}\left(u_r\frac{\partial}{\partial r}+\frac{u_\theta}{r}\frac{\partial}{\partial\theta}+\frac{u_\phi}{r\sin\theta}\frac{\partial}{\partial\phi}\right)(\hat{s}+s), \qquad \text{(B.146)}
\end{aligned}
$$

and the viscous heating term is

$$
\begin{aligned}
S_{\mathrm{DIFF}} &= \hat{\Phi} \\
&= 2\hat{\rho}\nu_{\mathrm{eff}}\left[\underline{\underline{\boldsymbol{e}}}:\underline{\underline{\boldsymbol{e}}}-\frac{1}{3}(\boldsymbol{\nabla}\cdot\boldsymbol{u})^2\right]. \qquad \text{by equation (B.13)} \qquad \text{(B.147)}
\end{aligned}
$$

Appendix C

ASH CODE TIME STEPPING

We discuss here in more detail the time stepping scheme employed by the ASH code. The basic problem is how one numerically solves an initial value problem of the form

$$\frac{\partial y}{\partial t} = f(y(t), t). \tag{C.1}$$

Since any higher-dimensional differential equation can be broken down into a system of one-dimensional equations, solving the one-dimensional problem is sufficient. The ASH code uses both the Crank-Nicholson and Adams-Bashforth methods to advance the solution in time, with each described in turn.

Subscripts are used here to denote the index of the time step. For example, y_i denotes the value of y at the most recently computed time step (occurring at time t_i) and y_{i+1} denotes the yet-to-be-computed value of y at the next time step. The time separation between subsequent time steps is $\Delta t_i \equiv t_{i+1} - t_i$.

C.1 THE SECOND-ORDER CRANK-NICHOLSON METHOD

As a first step in solving equation (C.1), one notices that the function f is simply the slope of y, suggesting the formula

$$\frac{y_{i+1} - y_i}{\Delta t_i} = f_i \qquad \text{or} \qquad y_{i+1} = y_i + \Delta t_i\, f_i, \tag{C.2}$$

commonly referred to as the *forward Euler* method. This method is explicit, meaning that y_{i+1} is the only unknown quantity in the formula and thus can be readily computed.

The accuracy of this method is determined by computing the local truncation error (LTE), which is simply the residual when the true values of y and f are substituted into equation (C.2):

$$\text{LTE} = y(t_i + \Delta t_i) - y(t_i) - \Delta t_i \, f(y(t_i), t_i). \tag{C.3}$$

By noting that the Taylor expansion of $y(t_i + \Delta t_i)$ is

$$y(t_i + \Delta t_i) = y(t_i) + \Delta t_i \left.\frac{dy}{dt}\right|_{t_i} + \frac{\Delta t_i^2}{2} \left.\frac{d^2y}{dt^2}\right|_{t_i} + \cdots , \tag{C.4}$$

and by using the fact that $f = \dfrac{dy}{dt}$, substituting equation (C.4) into equation (C.3) gives

$$\text{LTE} = \frac{\Delta t_i^2}{2} \left.\frac{d^2y}{dt^2}\right|_{t_i} + \cdots . \tag{C.5}$$

Since the local truncation error only contains terms of second and higher order in Δt_i, the forward Euler method is accurate to first order.

We now consider the *backward Euler* method:

$$\frac{y_{i+1} - y_i}{\Delta t_i} = f_{i+1}. \tag{C.6}$$

The only difference between the backward and forward Euler methods is the use of the unknown quantity f_{i+1} rather than the known quantity f_i on the right-hand side. Because we have to simultaneously solve for both y_{i+1} and f_{i+1}, this method is now implicit, and consequently requires a matrix inversion if f is linear in y. If f is nonlinear in y, implicit schemes such as the backward Euler become even more problematic to implement, and as a result they are generally only used to solve linear equations. As with the forward Euler method, the backward Euler method is accurate to first order.

The Crank-Nicholson method is a weighted average of the forward and backward Euler methods presented above:

$$\frac{y_{i+1} - y_i}{\Delta t_i} = \Theta f_{i+1} + (1 - \Theta) f_i, \tag{C.7}$$

where Θ is an adjustable parameter ranging from 0 (fully explicit) to 1 (fully implicit). The Crank-Nicholson method can be shown to be accurate to second order. In addition, this method is numerically stable, meaning that there is no limit on the time step size one can use (though the accuracy of the solution might decrease if too large a time step is chosen). In contrast, the forward Euler method is conditionally stable: choosing too large of a time step will cause numerical errors to grow, eventually overwhelming the actual solution.

C.2 THE SECOND-ORDER ADAMS-BASHFORTH METHOD

We now examine explicit multistep methods, where the results from more than one previous time step are used to solve equations of the form (C.1). In this case, the values of y_i, f_i and f_{i-1} (where the last quantity is either computed from a previous time step or stated as initial conditions) are already available. We now assume the unknown quantity y_{i+1} is given by the general form

$$\frac{y_{i+1} - y_i}{\Delta t_i} = \alpha f_i + \beta f_{i-1} \qquad \text{or} \qquad y_{i+1} = y_i + \Delta t_i(\alpha f_i + \beta f_{i-1}), \tag{C.8}$$

where the constant coefficients α and β will be determined to minimize the local truncation error.

For this method to be second-order accurate, we require the local truncation error to vanish through terms of order Δt_i^2. As with the forward Euler method in the previous section, the local truncation error is calculated by substituting into equation (C.8) the true values of y and f at the various time steps and calculating the residual. That is,

$$\text{LTE} = y(t_i + \Delta t_i) - y(t_i) - \Delta t_i \left[\alpha f(y(t_i), t_i) + \beta f(y(t_i - \Delta t_{i-1}), t_i - \Delta t_{i-1})\right]. \tag{C.9}$$

We first must evaluate the Taylor series expansions of y_{i+1} and f_{i-1} around t_i. These expansions are given by

$$y(t_i + \Delta t_i) = y_i + \Delta t_i \left.\frac{dy}{dt}\right|_{t_i} + \frac{\Delta t_i^2}{2}\left.\frac{d^2y}{dt^2}\right|_{t_i} + \frac{\Delta t_i^3}{6}\left.\frac{d^3y}{dt^3}\right|_{t_i} + \cdots \tag{C.10}$$

and

$$f(y(t_i - \Delta t_{i-1}), t_i - \Delta t_{i-1}) = f_i - \Delta t_{i-1} \left.\frac{df}{dt}\right|_{t_i} + \frac{\Delta t_{i-1}^2}{2} \left.\frac{d^2 f}{dt^2}\right|_{t_i} - \frac{\Delta t_{i-1}^3}{6} \left.\frac{d^3 f}{dt^3}\right|_{t_i} + \cdots . \tag{C.11}$$

Using these Taylor expansions, and the fact that $\frac{df}{dt} = y$, $\frac{d^2 f}{dt^2} = \frac{dy}{dt}$, etc., we can now write equation (C.9) in terms of the coefficients α and β, plus the dependent variable y and its derivatives evaluated at the current time step t_i. Grouping by power of Δt_i, we now have

$$\mathrm{LTE} = \Delta t_i \left.\frac{dy}{dt}\right|_{t_i} (1 - \alpha - \beta) + \Delta t_i^2 \left.\frac{d^2 y}{dt^2}\right|_{t_i} \left(\frac{1}{2} + \beta \frac{\Delta t_{i-1}}{\Delta t_i}\right) + \cdots , \tag{C.12}$$

where only terms of first and second order in Δt_i are listed explicitly. Since we require the parenthesized expressions to vanish for the method to be second-order accurate, we must have

$$\alpha = 1 + \frac{1}{2}\frac{\Delta t_i}{\Delta t_{i-1}} \qquad \text{and} \qquad \beta = -\frac{1}{2}\frac{\Delta t_i}{\Delta t_{i-1}}. \tag{C.13}$$

Substituting these values of α and β into equation (C.8), we obtain the second-order Adams-Bashforth formula:

$$\frac{y_{i+1} - y_i}{\Delta t_i} = \left(1 + \frac{1}{2}\frac{\Delta t_i}{\Delta t_{i-1}}\right) f_i - \left(\frac{1}{2}\frac{\Delta t_i}{\Delta t_{i-1}}\right) f_{i-1}. \tag{C.14}$$

Note that higher-order Adams-Bashforth formulae can be derived in a similar manner.

C.3 COMBINING THE METHODS

The ASH code evolution equations are of the form

$$\frac{\partial y}{\partial t} = \mathcal{L} + \mathcal{N}, \tag{C.15}$$

where y can represent any dependent variable in the system of equations (W, Z, p, s), and $\mathcal{L}$ and $\mathcal{N}$ respectively designate all linear and nonlinear source terms. Generally, these source terms can be a function of any of the dependent variables as well as a function of the independent variables $\vec{\boldsymbol{r}}$ and t.

Combining the two methods, equation (C.15) becomes

$$\frac{y_{i+1} - y_i}{\Delta t_i} = \left(1 + \frac{1}{2}\frac{\Delta t_i}{\Delta t_{i-1}}\right)\mathcal{N}_i - \left(\frac{1}{2}\frac{\Delta t_i}{\Delta t_{i-1}}\right)\mathcal{N}_{i-1} + \Theta\mathcal{L}_{i+1} + (1 - \Theta)\mathcal{L}_i, \tag{C.16}$$

which is equation (4.61) in Chapter 4.